Studies of Cosmic Ray Composition using a Hybrid Fluorescence Detector

by

K.M. Simpson, B.Sc.(Hons)

Department of Physics and Mathematical Physics

A Thesis Submitted to

The University of Adelaide

For the Degree of

Doctor of Philosophy

May, 2001

Table of Contents

TABLE OF CONTENTS—*Continued*

TABLE OF CONTENTS—*Continued*

TABLE OF CONTENTS—*Continued*

Abstract

This thesis describes several aspects of cosmic ray composition studies using the Utah Fly's Eye and High Resolution Fly's Eye (HiRes) detectors.

The Fly's Eye detector utilises the atmospheric fluorescence technique to measure the development of cosmic ray cascades as they pass through the atmosphere. This is complementary to the surface array technique, as used by the Akeno experiment in Japan, which measures the electromagnetic and muon content of air showers at a single observation level. For some time it was thought that Fly's Eye and Akeno gave inconsistent composition results. In Chapter 4 I will show that the inconsistency is due, for the most part, to a difference in the assumptions made about hadronic interactions.

In Chapter 5 I present analysis of the composition between 10^{17} and 10^{18} eV using the prototype High Resolution Fly's Eye (HiRes) detector in coincidence with the Michigan Muon Array (MIA). The hybrid nature of these measurements gives us more information about cosmic ray showers than either technique on its own. The consistency or otherwise of the composition measured by the two detectors is discussed.

Finally, in Chapter 6, I discuss a method of extracting the total proton–proton cross section, $\sigma_{pp}^{\rm tot}$, from the cosmic ray data. This information is of interest because it is derived at centre–of–mass energies much higher (by at least an order of magnitude) than those currently accessible by collider experiments. I present a preliminary calculation of the cross–section using the HiRes/MIA hybrid data set.

Statement of Originality

This thesis contains no material which has been accepted for the award of any other degree or diploma in any university or other tertiary institution and, to the best of my knowledge and belief, contains no material previously published or written by another person, except where due reference has been made in the text.

I give consent to this copy of my thesis, when deposited in the University Library, being available for loan and photocopy.

Ken Simpson

B.Sc.(Hons)

Acknowledgments

I would like to thank my supervisors, Drs. Roger Clay and Bruce Dawson, for their expert guidance. They ensured that I remained on track when I otherwise might have faltered. I would also like to thank the University of Utah Cosmic Ray group for their hospitality during my visits to Salt Lake City, and for giving me the opportunity to work on this most interesting experiment. Special thanks go to Brian Fick and Zhen Cao for useful physics discussions. The Australian government supported this work via an Australian Postgraduate Award (APA).

I owe many thanks to the present and former members of the Astrophysics group at the University of Adelaide for helping to keep me sane during the past five years, in particular Bruce Dawson, Greg Thornton, Paddy McGee, Hayley Bignall, Gail Higginbottom (physics groupie), Steven Dazeley, Matt Sinnott, Rishi Meyhandan, Gary Hill, Gavin Rowell, Mike Roberts, Troy Porter and Chris Wilkinson.

I also owe a debt of gratitude to those outside the group for taking my mind off physics at strategic moments, especially Alex Hemming, Christian Killow, Pip Zapris, David Polkinghorne, Simon "Rhymon" Turner, Lucas Mosey, Mark Tucker and Paul Farina. Thanks guys — you made the whole process a lot easier to cope with. The Unibar pool competition provided a welcome distraction on Thursday nights as I was writing up, in no small part thanks to the expert management of Anthony Paxton (cheers BT). If I've missed anyone, I can only apologise and offer my humble thanks and appreciation for your help and friendship over the years.

It would be remiss of me not to thank Shari and Steve Zinik, who ensured my trips to Utah were pleasant ones. Thanks also to the students at the U of U who made me feel at home — Ben Jones, Steffanie Moore, Ben Stokes, Tareq Abu–Zayyad and Greg Archbold.

To Jonathan and Trudi — your friendship has been very important to me. Suffice it to say that I would not have completed this *magnum opus* without your support. I can never repay the debt I owe you. Except, perhaps, with a large

amount of cash.

My family have been very supportive of my studies. To Mum, Dad, Linda, Betty, Ojīchan and Obāchan, Kōhei, Kayako, Shūhei, Yuka, Takeo, Hiroko, Miho, Hayato and Eri — どうも有難うございました。

Author's Note

The nature of a collaborative experiment is that individual efforts are not always made clear. In case it is not obvious in the text, I outline here my contributions to this work.

- I generated the simulation data for the study described in Chapter 4, as well as analysing those data to determine the parameters for input into the detector simulations. Our initial simulations revealed several inconsistencies, which turned out to be related to bugs in the simulation code used (MOCCA/Sibyll). These bugs were corrected as a direct result of this effort.

- The survey of tube pointing directions using Laserscope in Section 5.6 was my work. I analysed HiRes prototype data taken by our collaborators in Utah to determine how much the assumed pointing directions differed from the real ones.

- Laserscope data were also used to test the validity of the raytracing calculation used in the HiRes analysis software.

- The assumed atmospheric density profiles in the HiRes analysis software were compared to real data from radiosondes and found to be deficient. I showed that use of the most recent radiosonde data, normalised to the current ground pressure, gave a better estimate of the real density profile.

- I analysed a large amount of CORSIKA events (these were generated by our collaborators in Utah, who had access to better computing facilities) for the composition study in Chapter 5. I developed algorithms for taking raw event data (muon arrival times, weights and momenta) and producing a fitted lateral distribution, muon risetime and shower front curvature for each event. The results were used in the study of correlation between shower parameters.

- I did a large amount of work optimising the cuts used in the study of detector resolution (Section 5.5). The resultant cuts were applied to the real data for the composition study in Section 5.9.

- I tested several parts of the HiRes reconstruction software to determine why the observed residual distribution for profile fitting (*i.e.*, the distribution of the fitted value subtracted from the data, divided by the estimated error) was broader than expected. It eventuated that the errors were being underestimated.

- I analysed the HiRes/MIA data set to extract a value for the total proton–proton cross section from the $X_{\rm max}$ distribution. This involved careful treatment of the tail of the distribution to ensure a bias–free fit. Possible systematic effects were explored using Monte Carlo simulations.

- In addition to the above, I made several contributions to the experiment which were not appropriate to mention in the main body of this thesis. I spent a total of 8 months in Utah. This entailed many days and nights at Dugway collecting data and helping with detector construction and maintenance. I also managed the collection and first stages of analysis of atmospheric data from Dugway. I wrote software to integrate these data with the HiRes data stream.

Chapter 1

Introduction

In order to place the author's research in context, it is necessary to present a review of the history and current state of cosmic ray research. Since the material discussed here has been covered by many other authors, I shall endeavour to keep it brief. An excellent account of early cosmic ray research is given by Hillas [1]. The extremely high energy (EHE) region ($E > 10^{17}$ eV)[1], which is the focus of this thesis, has been reviewed more recently by Sokolsky *et al.* [2] and by Yoshida and Dai [3].

1.1 A Brief History of Cosmic Ray Research

The discovery of the extraterrestrial nature of cosmic rays[2] was made by Hess in 1912 [4, 5]. He made a series of flights in a balloon bearing an electrometer, which allowed him to measure the amount of ionisation as a function of height, up to 5km above sea level. His experiments showed that the mean ionisation increased with altitude, and hence that cosmic rays must originate beyond Earth. Hess' results were confirmed by Kolhörster [6], who extended the measurements up to an altitude of 9km. The measurement of a variation with geomagnetic latitude by Clay in 1927 [7] showed that cosmic rays were charged particles, and an excess of events arriving from the west compared to the east could only be explained if positively charged particles predominated[3].

[1] There appears to be some confusion over the nomenclature of cosmic rays. Some authors refer to the region above 10^{17} eV as the Ultra High Energy region. In this thesis I will always use the term Extremely High Energy for this part of the spectrum.

[2] The term "cosmic rays" was coined by Millikan in the 1920's

[3] see chapter 2 of Ref. [1], and references therein

Although the cyclotron was first built in the early 1930's, it was not until 1948 that sufficiently high beam energies to create new particles were attained. In the intervening years, cosmic rays provided an important resource for particle physicists. Anderson [8] and Blackett and Occhialini [9] discovered the positron using cloud chamber photography. The use of cloud chambers also led to the discovery of the muon by Neddermeyer and Anderson in 1937 [10]. This was originally misinterpreted as being the particle postulated by Yukawa in 1935, but the fact that it was not strongly interacting put the lie to this conclusion. It was not until the development of the emulsion chamber that the real pion was discovered [11]. In addition, the kaon, Λ, Σ^+ and Ξ^- were all discovered in emulsion or cloud chamber experiments at altitude, between 1947 and 1962. By the early 1950's accelerator technology had developed sufficiently to supersede cosmic ray physics as a means of carrying out particle physics studies. Since it was now possible to produce a well–understood primary beam in the laboratory, it was no longer an advantage to study the enigmatic cosmic radiation, which could only yield a limited amount of information regarding particle properties.

While detection of single particles in cloud chambers was instrumental in early developments in particle physics, the most important discovery for modern cosmic ray physics was made when Auger and collaborators found evidence for the existence of cosmic ray *showers* in the late 1930's [12, 13]. They found coincidences well above the accidental rate in Geiger–Müller counters placed up to 300m apart. They concluded from their observations that the showers must contain at least $\sim 10^6$ particles. Assuming an average particle energy of the order of the critical energy ($\sim$ 80 MeV), this meant, after ionisation losses had been taken into account, that the primary particle must have had an energy of $\sim 10^{15}$ eV. In the conclusion to their 1939 paper, Auger *et al.* note [13]:

> One of the consequences of the extension of the energy spectrum of cosmic rays up to 10^{15} eV is that it is actually impossible to imagine a single process able to give to a particle such an energy. It seems much more likely that the charged particles which constitute the primary

cosmic radiation acquire their energy along electric fields of a very great extension.

Auger *et al.* originally thought that these showers could best be explained by appealing to electromagnetic cascade theory, and that the primary particles were electrons, positrons or γ–rays. This was shown to be incorrect shortly after the war by Cocconi *et al.* [14] and by Daudin [15], in experiments conducted in the Alps. They measured a sizeable (a few percent) muon component in the secondary flux, with a much broader lateral distribution than electrons. They also measured a small number of nucleons. This behaviour was inconsistent with a simple electron–photon cascade, since it required nuclear interactions early in the shower. Measurements at altitude by Kaplon *et al.* [16] showed that the most likely culprits were, in fact, protons or nuclei.

With the discovery of particles arriving with energies greater than 10^{15} eV, tremendous interest developed in the precise nature and origin of the primary radiation. Since the primary flux was too low to measure directly beyond a certain point, the development of air shower arrays became a necessity. One of the earliest was built by Rossi and co–workers [17, 18] and consisted of eleven 1 m^2 plastic scintillators in a concentric circular arrangement with a radius of 230m. They demonstrated that it was possible to infer the arrival direction using timing information, and that by measuring the density of particles as a function of distance from the shower core[4], they could calculate the shower particle size and hence estimate the primary energy. An isotropic distribution of events with energies ranging from 10^{15} to 10^{18} eV and obeying a power law with a spectral index of -2.17 was observed[5]. Following this, a detector specifically designed to study the flux above 10^{17} eV was built at Volcano Ranch, New Mexico [19]. It originally consisted of nineteen 3.3 m^2 scintillators in a hexagonal grid covering 2 km^2, and was later (1960) expanded (by doubling the detector spacing) to cover 8 km^2. The

[4]the point of impact of the shower axis with the ground

[5]Throughout this thesis, I adopt the following convention: $J(>E) \propto E^{\gamma}$, where $J(>E)$ is the integral flux and $\gamma < 0$.

angular resolution[6] of this array was approximately 5°.

In 1962 the Volcano Ranch array detected a particle with an energy around 10^{20} eV [20]. A few years later, shortly after the discovery of the cosmic microwave background radiation (CMBR) by Penzias and Wilson [21], Greisen [22] and Zatsepin and Kuzmin [23] independently suggested that there should be a cutoff in the spectrum above $\simeq 6 \times 10^{19}$ eV due to interaction of cosmic ray protons with the ubiquitous CMBR photons, if the highest energy events were of extragalactic origin. This implied that the event observed at Volcano Ranch could not have originated further than $\simeq 50$ megaparsecs away. In addition, at such high energies it is anticipated that cosmic rays should be deflected by only a few degrees in intergalactic magnetic fields. To investigate the existence of the GZK cutoff and the possible anisotropy in arrival directions associated with a localised source or set of sources, several large EHE air–shower experiments were constructed:

- The Universities of Leeds, Nottingham, Durham and Imperial College, London built and operated the **Haverah Park** array from 1968 to 1987 [24]. This encompassed an area of 12 km^2 and was comprised of 34 1.2 m deep water Cherenkov detectors with areas between 1 m^2 and 34 m^2. Primary energies were estimated using the relation $E \propto \rho(600)^{\alpha}$. Simulations showed [24] that the constant of proportionality is $\simeq 10^{17}$ and $\alpha \simeq 1$. Here $\rho(600)$ is the water Cherenkov density 600m from the shower core and is used in preference to the ground–level shower size as it is less dependent on composition and fluctuations in shower development [25]. The Haverah Park detector had an angular resolution of $2.5^{\circ} \sec\theta$ for events arriving at a zenith angle θ.

- The **Sydney University Giant Airshower Recorder (SUGAR)** [26] ran for twelve years (1968–1979) and, to date, has been the only detector built for EHE cosmic rays in the southern hemisphere. It consisted of 47

[6] In this thesis, the term "angular resolution" will always refer to zenith angle, unless otherwise specified

detector stations covering an area of 70 km^2. Each station comprised two 6 m^2 liquid scintillator tanks separated by 50 m. These were buried under 1.7 m of soil and therefore measured only the muon component of air showers, with a muon energy threshold of 0.75 $\sec\theta$ GeV. The total muon number, a composition–dependent quantity, was used to estimate the primary energy. This may have been overestimated due to photomultiplier afterpulsing [26]. The quoted angular resolution is $3^\circ \sec\theta$, although this applies to events viewed by three detector stations or more. Most events were viewed by only three stations, with an angular resolution of 6° for vertical showers.

- The **Yakutsk** array in Siberia [27, 28] began operation in 1969 and has expanded from a 1 km^2 array for lower–energy events to a 10 km^2 EHE cosmic ray observatory, having at one stage (1973–1990) covered an area of 18 km^2. It is the oldest EHE cosmic ray detector still in operation. Composed mostly of plastic scintillators, it also features $\sim$ 350 m^2 of underground muon detectors near the centre of the array for composition studies (energy threshold 1.0 $\sec\theta$ GeV), as well as 50 atmospheric Cherenkov detectors. Data from the latter are used to check the $\rho(600) \rightarrow E$ conversion. Note that $\rho(600)$ in this case is fundamentally different to that measured at Haverah Park — here it will consist mostly of low–energy electrons, whereas in the Haverah Park case the predominant contribution comes from high–energy muons [24]. Yakutsk quote a $\rho(600)$ resolution of 25% at 10^{17} eV, decreasing slowly with energy, and an angular resolution of $\simeq 2^\circ \sec\theta$ at 10^{19} eV [28].

- The large array at **Akeno**, near Tokyo, has been operated since 1979 by a collaboration led by the University of Tokyo. In its original configuration (usually referred to as **A1**), it was a 1 km^2 detector sensitive to showers between 10^{14} and 10^{18} eV. Over 200 plastic scintillators were used in tandem with 500 m^2 of muon counters and a proportional counter used for shower core calorimetry [29]. Energy was estimated using the shower size. The array was expanded to 20 km^2 (**A20**) in 1984 with the deployment of 19

additional 2.25 m^2 scintillators with a 1 km spacing, as well as four large muon counters [30]. The $\rho(600)$ method was used to determine energy, with a resolution of 30%. The estimated angular resolution of A20 is 3° for vertical showers [31]. The Akeno experiment was further expanded in 1991, in the same manner as the A20 extension, to form a 100 km^2 detector consisting of 111 2.2 m^2 scintillators and 27 muon counters of various sizes. This arrangement, known as **AGASA** (Akeno Giant Air Shower Array) [32], has the same $\rho(600)$ resolution as A20, but a superior angular resolution (1.6°) [33]. It has a muon energy threshold of 0.5 $\sec\theta$ GeV, compared to 1.0 $\sec\theta$ GeV for A1 and A20.

- The **Fly's Eye** detector, situated on the Dugway Proving Ground in the Western Utah desert, operated from 1981 to 1992 and was the first of its type — a detector which measured the fluorescence light emitted by charged shower particles traversing the atmosphere [34]. The method was first proposed by Suga [35] and by Greisen and co–workers in the 1960's [36], but was not successfully implemented until 1976, when the University of Utah built a 3–mirror prototype overlooking the Volcano Ranch array [37]. This led to the construction of the first Fly's Eye detector in 1981, comprising 67 spherical mirrors of 1.5 m diameter and with either 12 or 14 photomultiplier tubes (each viewing a $5° \times 5°$ area of the sky) at the focus. In 1986 a second 36–mirror detector, 3.4 km away, was added to enable stereo measurements of EAS. Fly's Eye II viewed only the half of the sky in the direction of Fly's Eye I. The aperture of the stereo detector was approximately 1000 km^2sr at 10^{20} eV, but it had only a 10% duty cycle since it could only be operated on clear moonless nights. The Fly's Eye measured the longitudinal development of cascades initiated by EAS, *i.e.* the number of charged particles in the cascade as a function of atmospheric depth. The energy of the primary particle was then, by calorimetric arguments, simply proportional to the integral of the longitudinal profile. The shower geometry was determined by

the pointing directions and trigger times of the hit PMTs. The monocular energy resolution was 30%, and that for stereo events was 20%. The angular resolution for stereo events was between 1° and 10° depending on the shower geometry [38]. The Fly's Eye viewed the most energetic cosmic ray seen so far, with an energy (3.2×10^{20} eV) well above the GZK cutoff [39].

In 1993 the Fly's Eye was superseded by the **High Resolution Fly's Eye** (HiRes). Until 1997 a prototype detector (14 mirrors at one site, 4 mirrors at the other, 256 1°$\times$ 1°pixels at the focus of each mirror) was in operation. These mirrors were redeployed to form what is now HiRes I, and a second 42–mirror site has now been added. At the time of writing (July 2000), HiRes II is almost fully operational, with some debugging of the electronics yet to be done.

- The **Pierre Auger Observatory** was first proposed in the early 1990's and will be the first large–scale hybrid detector, with two sites of four fluorescence detectors overlooking a 3000 km^2 array of 1600 water Cherenkov detectors [40]. Funding has been approved for the Southern Hemisphere site, in Malargüe (Argentina), but is still pending for the Northern Hemisphere site (Millard County, Utah). With a collaboration numbering over 250 researchers and a budget of over $100 million, it will be the largest cosmic ray experiment yet. Construction of the Malargüe site is expected to be complete by 2003 [41].

Aspects of the AGASA and Fly's Eye/HiRes experiments pertinent to this work will be discussed more fully in Chapters 4 and 5. Note that I have only discussed the development of detectors for the EHE regime; details of the many lower energy EAS experiments are not included here.

1.2 Current knowledge of EHE Cosmic Ray Physics

The primary objectives of observational cosmic ray physics are to measure the energy spectrum, the chemical composition and the anisotropy in arrival directions of the primary particles. The spectrum and anisotropy are, relatively speaking, straightforward to measure, while composition measurements are complicated by the lack of particle physics knowledge at the relevant centre–of–mass (COM) system energies.

1.2.1 The Energy Spectrum

The cosmic ray spectrum spans 10 orders of magnitude and extends up to 10^{20} eV and beyond, in a remarkably smooth fashion — see Figure 1.1. The flux below 10^{11} eV is suppressed due to the magnetic field of the sun (solar modulation) and tracks the solar cycle, but above this the spectrum is a good fit to a power law. It is usually expressed as

$$J(E) = \frac{\frac{dN(E)}{dE}}{A\Omega(E)T} = J_0 \left(\frac{E}{E_0}\right)^{\gamma}, \tag{1.1}$$

where $dN(E)/dE$ is the raw energy distribution, and the denominator is the exposure of the detector (aperture, $A\Omega(E)$, multiplied by integration time, T) as a function of energy.

Since the spectrum is steeply falling, it is usual to plot the differential flux multiplied by $E^{2.7}$ in order to more clearly distinguish any features, as in Figure 1.2. When this is done, two features immediately become evident: a break and subsequent steepening near 3×10^{15} eV, termed the "knee", and a flattening above approximately 3×10^{18} eV, termed the "ankle". Figure 1.3 shows the flux multiplied by E^3 and better illustrates the structure near the ankle.

These features are not simply artefacts of the detection process, since they are evident in experiments that measure shower energy in quite different ways. Conjuring a plausible explanation for them is a challenging task. Although a flattening of the spectrum can be naturally explained by the transition from one

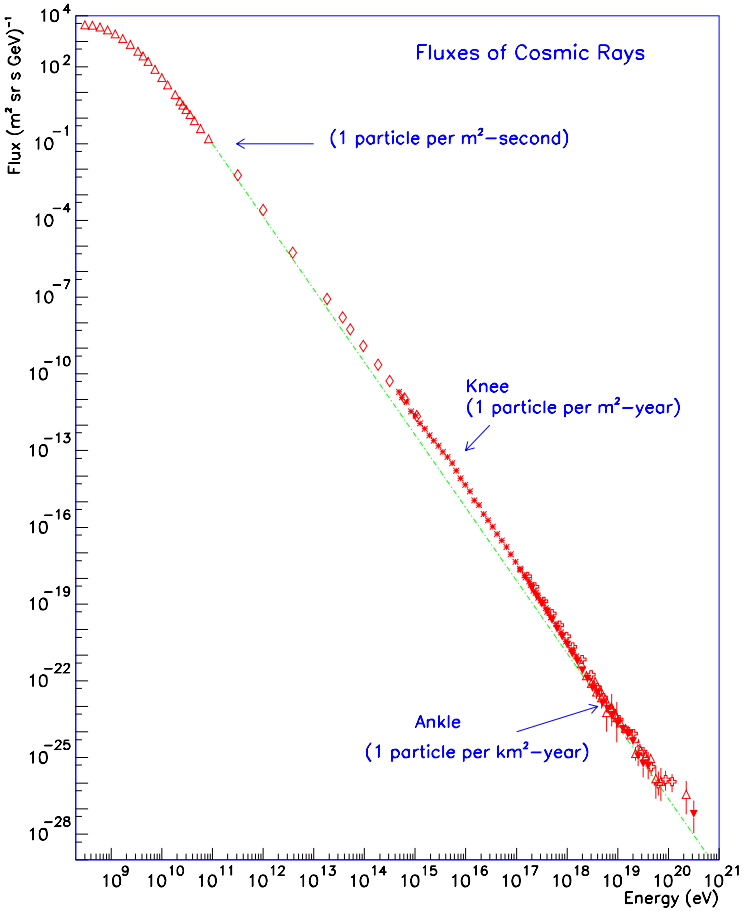

FIGURE 1.1. The differential cosmic ray energy spectrum, from [40]. The spectral index is approximately -2.7 up to the knee, and about -3.1 between the knee and the ankle.

type of power–law source to another, a knee–type feature cannot be reconciled in the same manner unless a "cosmic conspiracy" occurs; the first source must switch off at the same energy as the second turns on, and the intensities must be equal at the transition point. It therefore seems likely that there is one source type only, at least up to $\sim 10^{18}$ eV. A popular interpretation is that cosmic rays are galactic up to the ankle, and extragalactic thereafter. The extragalactic hypothesis is supported by the fact that a proton with an energy of 10^{18} eV has a Larmor radius which is greater than the thickness of the galactic disk, and can therefore not be contained within the galaxy. There is additional reason for believing that the highest energy cosmic rays do not originate in our galaxy, as will be discussed

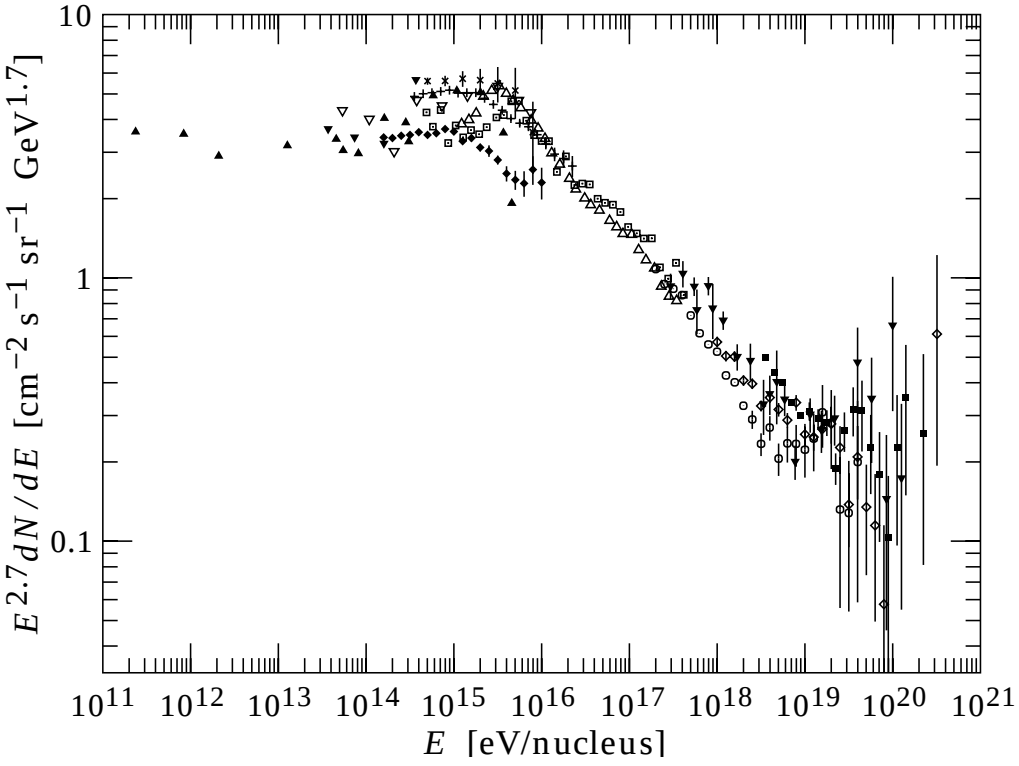

FIGURE 1.2. The all–particle spectrum, multiplied by $E^{2.7}$ to accentuate the knee and ankle [42]. The data are from Akeno (□), JACEE (▼), Proton–4 (▲), Tien Shan (▽), MSU (△), Tibet (+), HEGRA (×), CASA–MIA (⧫), Fly's Eye (stereo (○), mono (◇)), and Haverah Park (■). The high energy data points indicated by ▼ are from AGASA. See Ref. [42] for references to the original papers.

below.

The observation of events with energies exceeding 6×10^{19}, although not yet providing compelling evidence for a flux above the GZK cutoff, suggests that their source(s) must lie within 100 Mpc. As can be seen in Figure 1.4, protons with $E > 10^{20} eV$ arriving from further than this distance will have lost energy at a rapid rate due to pion photoproduction, until they are degraded to sub–GZK energies.

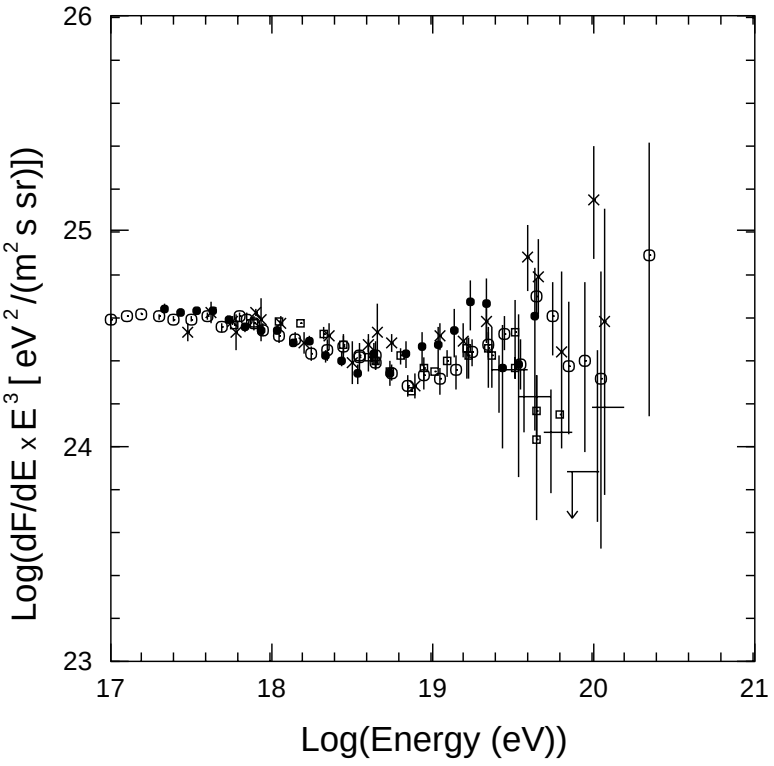

FIGURE 1.3. The portion of the differential spectrum (multiplied by E^3) above 10^{17} eV [40], as measured by Haverah Park ($\times$), the Fly's Eye (stereo, $\bullet$), Yakutsk ($\square$) and AGASA ($\odot$). The data are normalised to the AGASA flux at 10^{18} eV.

1.2.2 Anisotropy

The flux below 10^{17} eV has been well measured and is known to be almost isotropic. This is unsurprising as the galactic magnetic field washes out directional information for charged particles at these energies. Recent results in the EHE region are somewhat more interesting. The AGASA group has measured a 4.5σ excess from a direction approximately 10° from the galactic centre, in the energy range $10^{18.0}$ — $10^{18.4}$ eV [44]. In addition, they see a 3.9σ excess from the direction of the Cygnus region. This energy range has not been selected *a priori* but rather after a search to determine the range in which the anisotropy is greatest. The overall anisotropy in the galactic plane in this energy range, from a harmonic analysis, is 4%.

Recently Bellido *et al.* [45] have performed a reanalysis of SUGAR data and

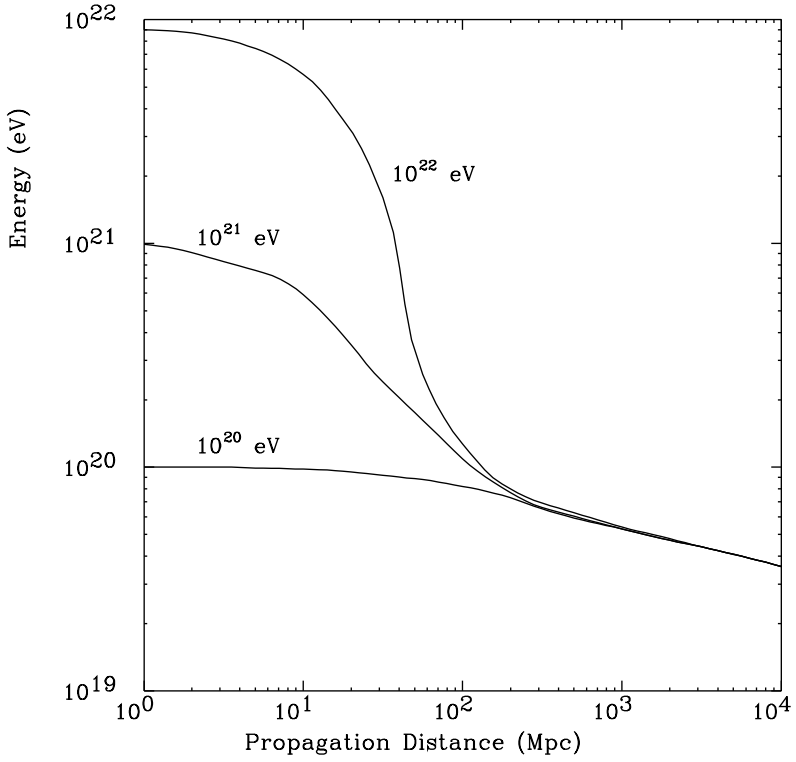

FIGURE 1.4. Proton energy as a function of propagation distance, from Ref. [43].

found a marginally significant excess around 7.5° from the galactic centre, close to that found by AGASA. They widened the energy range slightly (to $10^{17.9} \rightarrow 10^{18.5}$ eV) for their search to allow for possible systematic errors in the SUGAR energy determination (see section 1.1). The chance probability (*i.e.* the probability that the excess was due purely to a statistical fluctuation) of finding this excess was estimated at 0.005. The location of the excess region on their sky map is consistent with the AGASA result within the angular resolution of the SUGAR detector ($3^\circ \sec\theta$), although the apparent size of the source region is not. The authors argue that, since the size of the excess region is of the order of the SUGAR angular resolution, it can be interpreted as being due to a point source.

The Fly's Eye group have searched for large–scale anisotropy in their data and have found a small galactic plane enhancement (chance probability 0.06%, corresponding to a 3.2σ excess for monocular data) [46]. The enhancement is strongest in the range $10^{17.6}$ — $10^{18.0}$.

None of the aforementioned studies report a statistically significant excess from the supergalactic plane. Stanev *et al.* [47] have claimed, based on a 1995 study of 143 events above 2×10^{19} eV from three Northern Hemisphere experiments (Haverah Park, Yakutsk, AGASA), that there is evidence for clustering of the highest energy events near the supergalactic plane. However, the evidence is not strong, and is not confirmed by the only Southern Hemisphere results [48]. The AGASA group also do not see any statistically significant clustering towards the supergalactic plane, although there is tenuous evidence for correlated pairs of events at the highest energies [49]. Better statistics are required to formulate a convincing argument.

1.2.3 Composition

At energies up to the order of 10^{14} eV, it is possible to measure cosmic ray composition directly with balloon or satellite–borne detectors, generally emulsion chambers. JACEE [50] and RUNJOB [51, 52] are two recent examples of such experiments. Beyond 100 TeV the flux becomes too low for a balloon–type experiment, since the payload and exposure time required would be enormous. Instead, measurements of the secondary particles from EAS must be made. Interpreting such measurements to infer the composition of the primary particles is a challenging task. In most cases the best that can be done is to measure one or more composition–sensitive shower parameters and compare the mean results, as a function of energy, to the average behaviour expected from Monte Carlo shower simulations. It is not possible to obtain the composition on an event–by–event basis due to fluctuations in shower development. In addition, the hadronic models used in shower simulations rely on extrapolations of accelerator data obtained at much lower energies, and uncertainties in the models can have dramatic effects on the inferred composition, as will be seen in Chapter 4.

A summary of recent composition measurements near the knee of the spectrum ($\sim$ 1–10 $\times 10^{15}$ eV) is given in Table 1.1. The disagreement between the conclusions of the different experimenters is clear. If there is a general trend it is towards

a heavier composition through the knee. This may indicate a rigidity–dependent cutoff at the source; since shock acceleration models predict a maximum energy proportional to the charge (see Section 1.3.1), heavy nuclei are able to be accelerated to higher energies than protons, and would therefore be more abundant with increasing energy up to the maximum allowed. For acceleration by supernova remnants (SNR), this is of the order of 10^{15} eV, roughly the energy at which the knee is situated.

Experiment	**Technique**	**Result**
DICE	Cherenkov Imaging	mixed $\rightarrow$ light
AIROBICC	Cherenkov lateral distribution, N_e	mixed throughout
VULCAN	Cherenkov lateral distribution	mixed $\rightarrow$ heavy
CASA–MIA	N_e and N_μ	mixed $\rightarrow$ heavy
EAS–TOP	muon lateral distribution, N_e	mixed $\rightarrow$ heavy
MSU	10 GeV muon lateral distribution	light $\rightarrow$ heavy
Frejus	Deep (TeV) muons	light
KASCADE	Hadrons	mixed $\rightarrow$ heavy
KASCADE	N_e and N_μ	light $\rightarrow$ mixed
BLANCA	Cherenkov lateral distribution	mixed $\rightarrow$ heavy

TABLE 1.1. Composition near the knee (see Fowler [53, and references therein]).

Resolving the composition above 10^{17} eV is even more problematic than at the knee, due to poorer statistics and larger uncertainties in the particle physics. The problem of EHE composition will be discussed extensively in Chapters 4 and 5, but I will briefly discuss some (pre–1996) composition results here.

Composition studies are usually couched in terms of a two–component model, as originally proposed by the Fly's Eye group [54]. EAS experiments lack the ability to measure the actual mass to any degree of precision, due to intrinsic shower fluctuations. We therefore speak in terms of protons and iron nuclei (equivalently, "light" and "heavy"), as these are the most likely extremes of the flux of hadronic

cosmic rays.

The composition–sensitive parameters usually studied are the muon content of the shower (either the particle density at 600m from the core, or the total number of muons in the shower) and the depth of maximum shower development. The former is measurable only by surface arrays such as AGASA, while the latter is directly measurable by fluorescence detectors and may possibly be inferred (in a highly model–dependent way) by surface array measurements. Composition measurements above 10^{17} eV are summarised in Table 1.2.3.

Experiment	**Technique**	**Hadronic Model**	**Result**
AGASA	$\rho_\mu(600)/\mathrm{S}(600)$	scaling	heavy
Fly's Eye	$X_{\max}$	KNP	heavy $\rightarrow$ light
Haverah Park	D_{10} (μ risetime)	scaling	constant (mixed?)
Yakutsk	$X_{\max}$	QGS	mixed $\rightarrow$ light
Yakutsk	$\rho_\mu(600)/\mathrm{S}(600)$	QGS	mixed $\rightarrow$ light
Yakutsk	$X_{\max}$	scaling	>Fe $\rightarrow$ heavy
Yakutsk	$\rho_\mu(600)/\mathrm{S}(600)$	scaling	heavy $\rightarrow$ >Fe

TABLE 1.2. Summary of EHE composition trends, as discussed in the text. D_{10} is the elongation rate (rate of change of $X_{\max}$ with $\log E$). >Fe means that the data imply a composition heavier than iron according to the hadronic model used.

The AGASA group infer composition by measuring $\rho_\mu(600)$, the density of muons 600m from the shower core, as a function of energy. This choice is justified by the fact (deduced from shower simulations) that the fluctuations in the particle density at a given energy due to those in shower development are minimised at 600m. The charged particle density at this distance is used to determine the primary energy, via the relation [55]

$$E = 2.0 \times 10^{17} S_0(600)^{1.0}\,\mathrm{eV}, \tag{1.2}$$

where $S_0(600)$ is the actual density, $S(600)$, corrected to what would be observed for a vertical shower.

The measured values of $\rho_\mu(600)$ are then compared to the expectation from simulations of proton and iron showers. In their 1995 paper [55], the AGASA group find that their $\rho_\mu(600)$ measurements are consistent with an unchanging composition from $10^{16.5}$ up to 10^{19} eV.

The Fly's Eye experiment directly measured the depth of shower maximum, $X_{\rm max}$, by imaging the fluorescence light which is emitted isotropically by air showers. $X_{\rm max}$ has been shown to be a good indicator of composition; on average, proton–initiated showers will develop later than those due to nuclei, and will suffer greater fluctuations. $X_{\rm max}$ for a particular species can be parametrised by

$$X_{\rm max} = \alpha \log E + \beta, \tag{1.3}$$

where the parameter α is termed the "elongation rate" (usually denoted as D_{10}). In model calculations it has been shown to have a very mild energy dependence and can be regarded as constant over the range considered here.

By comparing their $X_{\rm max}$ results to the predictions of a QCD Pomeron model (the KNP model [56]), the Fly's Eye group [54] found that the mean values and elongation rate below 3×10^{17} eV corresponded to the expectation for an iron composition. Near this energy an increase in elongation rate occurred, and at the highest energies the absolute values were consistent with the predictions for proton showers. They therefore concluded that there was a change from a purely heavy composition at 10^{17} eV to a purely light one at 3×10^{19} eV.

The Yakutsk group [28] use several different shower parameters in their composition studies. They measure the muon and charged particle densities and the Cherenkov light lateral distribution directly, and infer $X_{\rm max}$ from the Cherenkov lateral distribution function. The predictions of a quark–gluon–string model [57, 58] for various ratios of parameters (*e.g.* total muons to integrated Cherenkov flux, muon density to charged particle density at fixed core distance) and for $X_{\rm max}$ are compared to the data. The conclusion is that the composition changes from a mixed one to a protonic one at higher energies. If a scaling [7] model is used, incon-

[7] Throughout this thesis, "scaling" refers to Feynman scaling, a property of scattering cross

sistencies result; for example, the $X_{\rm max}$ measurements now imply a change from a composition heavier than iron to something iron–like, whereas the $\rho_\mu(600)$ results suggest the opposite trend, from a heavy composition to a super–heavy one. This highlights a possible problem with either the scaling model or with systematics in the $X_{\rm max}$ measurement. The Yakutsk results should be regarded with caution, since they did not use a detector Monte Carlo to take account of possible systematic effects or biases in their experiment.

Although the Haverah Park group [59] were unable to measure $X_{\rm max}$ directly, they were able to calculate the elongation rate by measuring the charged particle risetime (in their case, due almost entirely to muons) at a fixed core distance as a function of energy. This is possible because the risetime exhibits a linear correlation with $X_{\rm max}$ (this is a geometrical effect which will be discussed in a later chapter). In addition, the absolute value of $X_{\rm max}$ can be inferred, but the conversion is model–dependent. Their measurement of $D_{10} = 73 \pm 5$ g.cm^{-2}.decade^{-1} is consistent with the Fly's Eye value of 69 ± 5, but they reach a different conclusion regarding composition. The hadronic model they used, contained in the MOCCA shower simulation, predicts the elongation rate for a homogeneous composition (as opposed to a mixture of protons and nuclei) to be 70 g.cm^{-2}.decade^{-1}, consistent with their measurement. Based on this, the conclusion is that the composition is constant between 10^{17} and 3×10^{18} eV. To further resolve whether the composition is mixed or homogeneous over this range would require an absolute determination of $X_{\rm max}$. There is tentative evidence for a change in the elongation rate above 3×10^{18} eV, but the errors are large and preclude a definitive statement.

Clearly the question of composition is a difficult one, as shown by the disagreement between the various EHE observatories. This is largely due to the different systematics of the experiments and the different hadronic models used to inter-

sections at high energies. Models incorporating scaling are often at odds with the cosmic ray data, while the introduction of scaling violations can help to bring them into better agreement. Experimental evidence of such violations is elusive, due to the difficulty of measuring such an effect at accelerators. This will be further elaborated upon in a later chapter.

pret the results. I will show in Chapter 4 that consistency can be attained in the framework of a single hadronic model.

1.3 Models of Origin and Propagation

A detailed discussion of source theories is beyond the scope of this thesis, but I will outline here the main proposed mechanisms. Overviews of source models are given by Hillas [60] and, more recently, Biermann [61]. Another recent review by Bhattacharjee and Sigl [62] places particular emphasis on Topological Defect models.

1.3.1 Models of cosmic ray origin

The multitude of models for cosmic ray production may be broken down into two major classes: acceleration and "top–down" models. The former is the more conventional hypothesis but struggles to reach the highest energies observed. Top–down models, in which cosmic rays begin at energies at and preferably well above those observed, are rather speculative in nature, and many rely on new fundamental physics.

Figure 1.5, the famous "Hillas diagram", displays potential acceleration sites on a magnetic field *vs.* size plot.

Broadly speaking, cosmic rays may be accelerated in two ways, either gradually in a "statistical" manner, or in so–called "one-shot" mechanisms. The former involves magnetic fields while the latter generally entails direct acceleration by electric fields.

The potential sources in which direct acceleration may take place lie in the top left quadrant of Figure 1.5. The difficulty with these objects is that although they may be able to accelerate particles to the required energies, the intense radiation in their vicinity is likely to degrade cosmic ray energies via pion photoproduction and synchrotron losses in the associated strong magnetic fields. In addition, it is

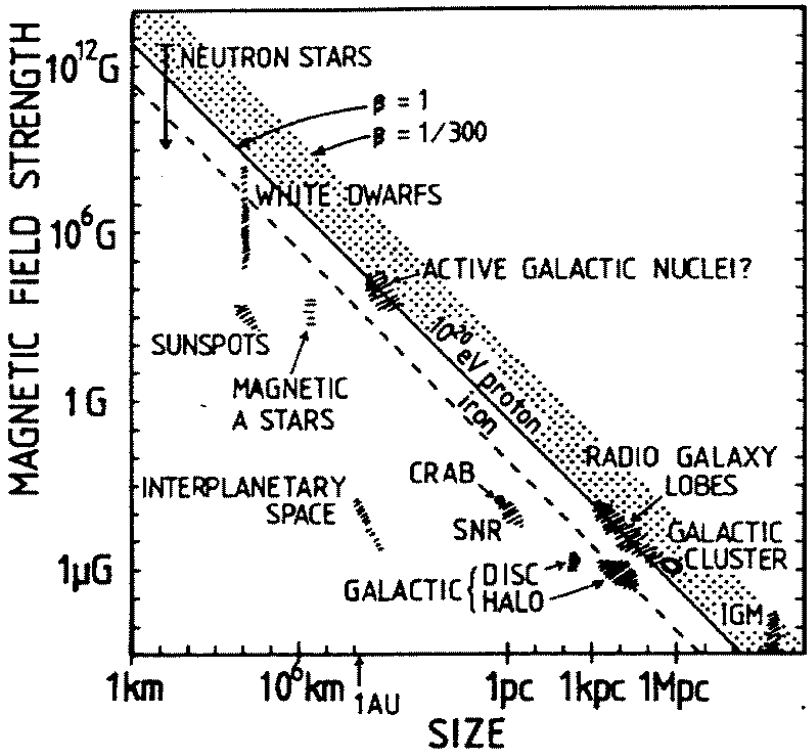

FIGURE 1.5. Potential acceleration sites, from ref. [60]. In order to be able to accelerate protons to above 10^{20} eV, an astrophysical object must lie above the solid line. The top of the shaded band represents $\beta = 1/300$, a more realistic shock velocity than the limit of $\beta = 1$.

difficult to explain how this type of mechanism can produce a power–law spectrum of particles [60].

The idea of a statistical acceleration process was first proposed by Fermi [63]. He suggested that charged particles could scatter off magnetised clouds in the interstellar medium, gaining or losing energy depending on the angle at which they enter the clouds. After many such encounters there is a net energy gain proportional to β^2 ($\beta = v/c$, v being the typical cloud velocity). This leads naturally to a power–law spectrum, but is too slow to accelerate cosmic rays to sufficiently high energy, since $\beta \sim 10^{-4}$ in general [64]. A faster mechanism is one in which particles are accelerated by astrophysical shocks. In this scenario there is a net energy gain per cycle proportional to β (the speed of the shock

front, divided by c) because the particles undergo only head–on collisions and therefore gain energy each time they cross the shock front (see, *e.g.* Ref. [65] for a pedagogical discussion). The scattering centres in this instance are magnetic irregularities on either side of the shock front. This process is referred to as first–order Fermi acceleration (*i.e.*, first–order in β), or diffusive shock acceleration[8].

Fairly simple arguments show that the maximum possible energy (in units of 10^{18} eV) able to be reached by shock acceleration is [67]

$$E_{\rm max} \approx \varepsilon \times \beta \times Z \times B_{\mu\rm G} \times L_{\rm kpc}, \tag{1.4}$$

where β is the shock speed, $B_{\mu\rm G}$ is the magnetic field in units of microgauss and $L_{\rm kpc}$ is the size of the acceleration region in kiloparsecs. The quantity ε lies between 0 and 1 and reflects the efficiency of the acceleration process. A 100% efficient process is extremely unlikely; for most cosmic accelerators, it is possible that $\varepsilon \ll 1$ [61].

Eq. 1.4 can be used to rule out some of the objects in Figure 1.5 as potential accelerators of the highest energy cosmic rays. The dashed line delineates the region above which objects must lie to accelerate iron nuclei to 10^{20} eV, and the line immediately above it corresponds to the lower limit for protons. These assume ultrarelativistic shocks ($\beta \approx 1$), rather unrealistically. It is probable that the line should lie somewhere in the shaded region, the top of which corresponds to $\beta = 1/300$, a more realistic value for most astrophysical situations. It is immediately obvious that very few source candidates remain. Among those ruled out are supernova remnants (SNR), believed to be responsible for cosmic ray acceleration up to the knee. The remaining candidates are further depleted by the fact that cosmic rays will lose energy by photoproduction in their vicinity. Figure 1.6 shows that the most promising sources are hot–spots of radiogalaxies. These are compact regions of highly luminous radio emission seen in the lobes of a class of galaxies known as Fanaroff–Riley class II (FR–II) galaxies. Rachen and Biermann [68] first proposed FR–II galaxies as potential acceleration sites, and estimated an upper

[8] see *e.g.* Ref. [66] for a detailed review of the theory.

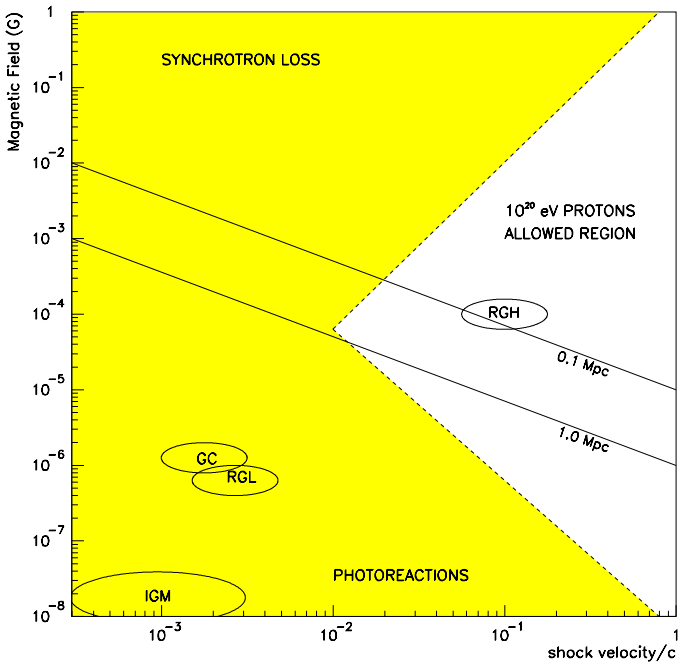

FIGURE 1.6. A plot of magnetic field strength against shock velocity, from Ref. [40]. IGM = Intergalactic Medium, RGL = Radio Galaxy Lobes, GC = Galactic Cluster, RGH = Radio Galaxy Hotspots.

limit of $\approx 3 \times 10^{21}$ eV for protons borne of this environment. If FR–II galaxies, and radiogalaxies in general, are responsible for the highest energy flux, the cosmic ray data should exhibit a supergalactic plane enhancement above 10^{19} eV, increasing with energy. Statistics are still too poor to make a conclusion regarding this point (see section 1.2.2).

Topological Defects (TD) are associated with spontaneous symmetry breaking in Grand Unified Theories (GUTs). TD models of cosmic ray origin generally hypothesise that some superheavy particles ("X" particles) with mass of the order of the GUT symmetry breaking scale ($m_X \sim 10^{25}$ eV) can become trapped in these artefacts of the early Universe, and are released at some later time due to TD decays or annihilation. The X particles then decay to quarks and leptons; the quarks subsequently hadronise and produce mostly pions, with a small ($\sim 3\%$ of

the total decay products) nucleonic component [61]. The further decay of these products means that the bulk of the flux is in neutrinos, gamma rays, electrons and positrons. The EHE cosmic rays can therefore be explained in this framework if they are nucleons or (most probably) gamma rays. Some authors [69, 70] suggest that it is also possible for neutrinos to contribute if they have masses of order 1 eV, since in this case the relic neutrinos may cluster in the galactic halo to provide a target for protons and gamma rays to be created (via resonant Z production: $\nu\,\nu_{\rm background} \longrightarrow Z^* \longrightarrow$ hadrons)[9]. Strong constraints on this class of TD models would be provided by measurements of the diffuse gamma ray and neutrino fluxes. A heavy nuclear composition would also rule out this type of model, since these processes cannot produce nuclei.

In addition to decays of X particles, it is possible that the highest energy cosmic rays are themselves topological defects. The most popular scenario is for a monopole, which is easily accelerated in the Galactic magnetic field, to cause an air shower which mimics a hadronic one. However, there are problems with this scheme; it is difficult to get monopoles to interact inelastically enough (*i.e.*, to deposit enough energy) to initiate an EAS, and there ought to be a strong anisotropy in arrival directions, which is not observed [62].

It should be noted that while most acceleration models have difficulty in reaching the highest observed energies, they must account for at least part, and probably all, of the flux at lower energies. Even if topological defects are responsible for the highest energy events, some other sources such as radiogalaxies are required to produce the spectrum between, for example, 3×10^{18} and 5×10^{19} eV [61].

1.3.2 Cosmic Ray Propagation

As well as searching for potential sources of cosmic rays, it is necessary to consider what happens to them when they travel over interstellar or intergalactic distances. As already mentioned, energetic protons have a relatively short (cosmologically

[9] interestingly, Fargion *et al.* [69] note that this would result in a new cutoff energy of the order of 10^{23} eV

speaking!) mean free path through the cosmic microwave background. The mean free path for nuclei is even shorter, due to photodisintegration. Protons and nuclei will be deflected in magnetic fields. At sufficiently high energies, the deflection is small and on average is approximately equal to

$$\theta \approx 0.3^{\circ} \frac{L_{\rm Mpc}^{1/2} l_{\rm Mpc}^{1/2} Z B_{\rm nG}}{E_{20}}, \tag{1.5}$$

where $L_{\rm Mpc}$ is the distance to the source in Mpc, $B_{\rm nG}$ is the magnetic field in nanogauss, $l_{\rm Mpc}$ is the coherence length of the field, Z is the charge and E_{20} is the particle energy in units of 10^{20} eV [40]. This means, for example, that a 10^{20} eV proton propagating through a 1 nG field with a 1 Mpc coherence length (perhaps typical of the extragalactic field), arriving from 50 Mpc, will be deflected by 2.1° on average. This is encouraging insofar as point source searches go, as long as sufficient statistics and good detector angular resolution are achieved.

Gamma rays do not suffer deflection in magnetic fields, but are subject to severe energy losses due to interactions with the infrared, radio and microwave backgrounds. Neutrinos are also undeflected, but due to their low interaction cross sections with hadronic matter, are unlikely to cause atmospheric cascades unless they arrive horizontally and therefore traverse a large amount of atmosphere. This difficulty may be overcome if they interact with the relic neutrino background, as described above.

1.4 Summary

The cosmic ray spectrum extends smoothly over 11 orders of magnitude, with only three noticeable features: the "knee" around 10^{15} eV, the "dip" or second knee around 10^{18} eV, and the "ankle" near 10^{19} eV. The sources of cosmic rays are still unknown. It is probable that for energies up to and possibly slightly beyond the knee, the observed flux can be accounted for by acceleration in supernova remnants. The ankle in the spectrum may signal a change from galactic to extragalactic sources, especially as it occurs at an energy where cosmic ray protons

can no longer be confined in the galactic disk. If the highest energy particles are protons, the sources cannot be located more than ~ 100 Mpc away, since protons suffer large energy losses due to pion photoproduction on the cosmic microwave background and are thereby prevented from reaching us from that distance. The unambiguous detection of a GZK cutoff would prove the extragalactic origin of the highest energy particles. AGASA and (preliminary) HiRes results seem to indicate that the spectrum extends smoothly beyond the expected cutoff, although not enough events have been detected to make a definitive statement. Much better statistics are required to establish the composition of the highest energy events, and whether there is any anisotropy in their arrival directions. This will enable stronger constraints to be placed on potential sources of these particles. Future measurements by HiRes, AGASA and the Auger detector should achieve this goal.

Chapter 2

Physics of Extensive Air Showers

The fact that high energy cosmic rays cascade in the atmosphere makes their detection possible. Interpreting the cosmic ray data therefore requires a deep understanding of the underlying shower physics. In this chapter I give an overview of processes contributing to air shower development.

Much of the difficulty in interpreting EAS measurements stems from uncertainties in the hadronic physics beyond a centre of mass (COM) energy of ~ 1 TeV. Various models have been devised to describe hadronic interactions at energies well above those attainable at accelerators. I will outline the main features of some of these models and describe how they are implemented in EAS simulations.

2.1 A simple model of air showers

A simple model, due originally to Heitler [71], can be used to illustrate some of the main features of EAS development. Consider, as a concrete example, an electromagnetic cascade (although the arguments here apply equally well to any type of interaction), as depicted in Figure 2.1.

In this example, a high–energy primary photon produces an e^+e^- pair. Each secondary then undergoes bremsstrahlung to produce further high–energy photons, which in turn pair produce, and so forth. Note that each of these processes must take place in some external field (*i.e.* the electromagnetic field of a nucleus), in order to conserve 4–momentum. In this simplified treatment, it is assumed that each interaction takes place after a fixed length λ, and that the energy is divided equally among the secondaries.

The multiplication continues until the mean particle energy reaches some crit-

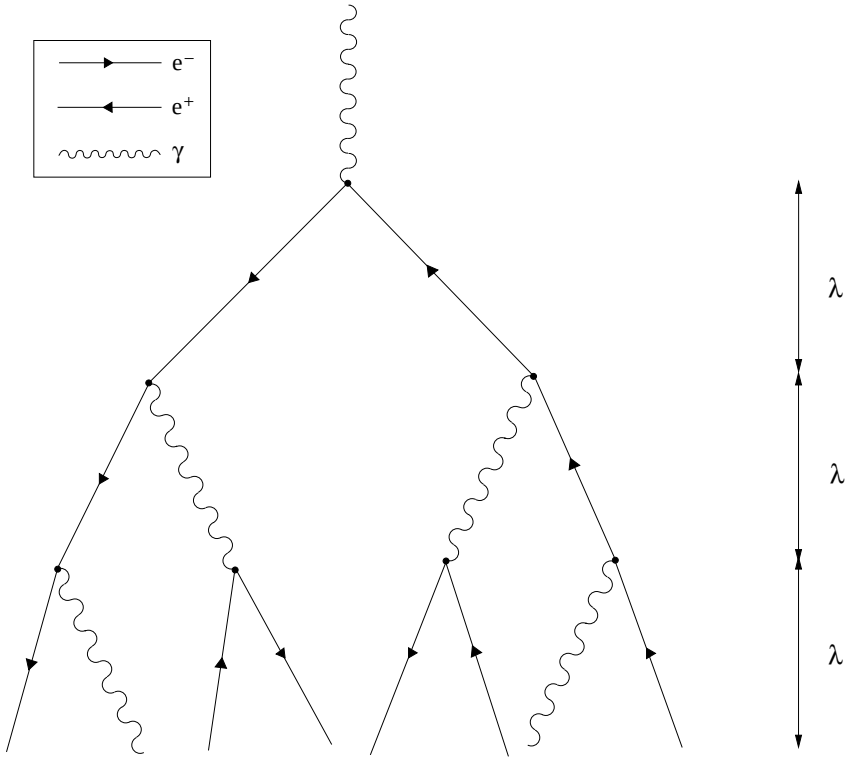

FIGURE 2.1. A purely electromagnetic cascade, initiated by a γ–ray. Scattering angles are exaggerated for clarity.

ical value, E_c, at which point energy losses due to ionisation, Compton scattering and the photoelectric effect begin to dominate over the multiplicative processes mentioned above. Below this energy particle production grinds to a halt, and the cascade begins to attenuate.

A couple of important features of cascades may be extracted by noting that at shower maximum, when the mean particle energy is E_c, the number of shower particles is $N(X_{\max}) = E_0/E_c$, E_0 being the primary energy and $X_{\max}$ the depth of shower maximum. At a depth X, the cascade has gone through X/λ generations, and the number of particles is therefore $N(X) = 2^{X/\lambda}$. Hence it can be seen that $X_{\max} = \lambda \frac{\ln(E_0/E_c)}{\ln 2}$. We therefore have the results

$$\begin{aligned} N(X_{\max}) \equiv N_{\max} &\propto E_0 \\ X_{\max} &\propto \ln E_0. \end{aligned} \tag{2.1}$$

These results hold exactly for electromagnetic cascades, and are approximately

true for hadronic ones [72].

2.2 Components of an EAS

There are three major components of atmospheric cascades initiated by cosmic rays: a hadronic core, a set of electromagnetic subshowers due primarily to π^0 decay, and a muonic component which arises mostly due to $\pi^{\pm}$ decay. These are illustrated schematically in Figure 2.2. In addition, a large number of Cherenkov and fluorescence photons are generated.

2.2.1 The hadronic core

A primary cosmic ray, whether a nucleon or a nucleus, will interact with an air nucleus to produce a number of secondary hadrons. The most common products are pions and kaons, as well as nucleons produced in decays of nucleonic resonances. At sufficiently high energies, strange baryons and some charmed hadrons may be produced. The production angles are generally quite small, particularly early in the shower, and the resultant hadronic cascade forms an energetic core (lateral extent of the order of a few metres) for the EAS. The hadronic core continues to feed the electromagnetic and muon components of the shower until it is exhausted, *i.e.* at the point where the mean hadron energy falls below the threshold for pion production. The rate at which energy is dissipated into the electromagnetic component depends on the details of the hadronic interactions, as will be discussed in section 2.3.

2.2.2 The electromagnetic component

In the terminology of air showers, the "electromagnetic (EM) component" refers to that part of the shower composed of electrons, positrons and photons. e^+e^- are usually referred to collectively as electrons, and I will adopt this convention here. In an extensive air shower, the EM component is generated predominantly

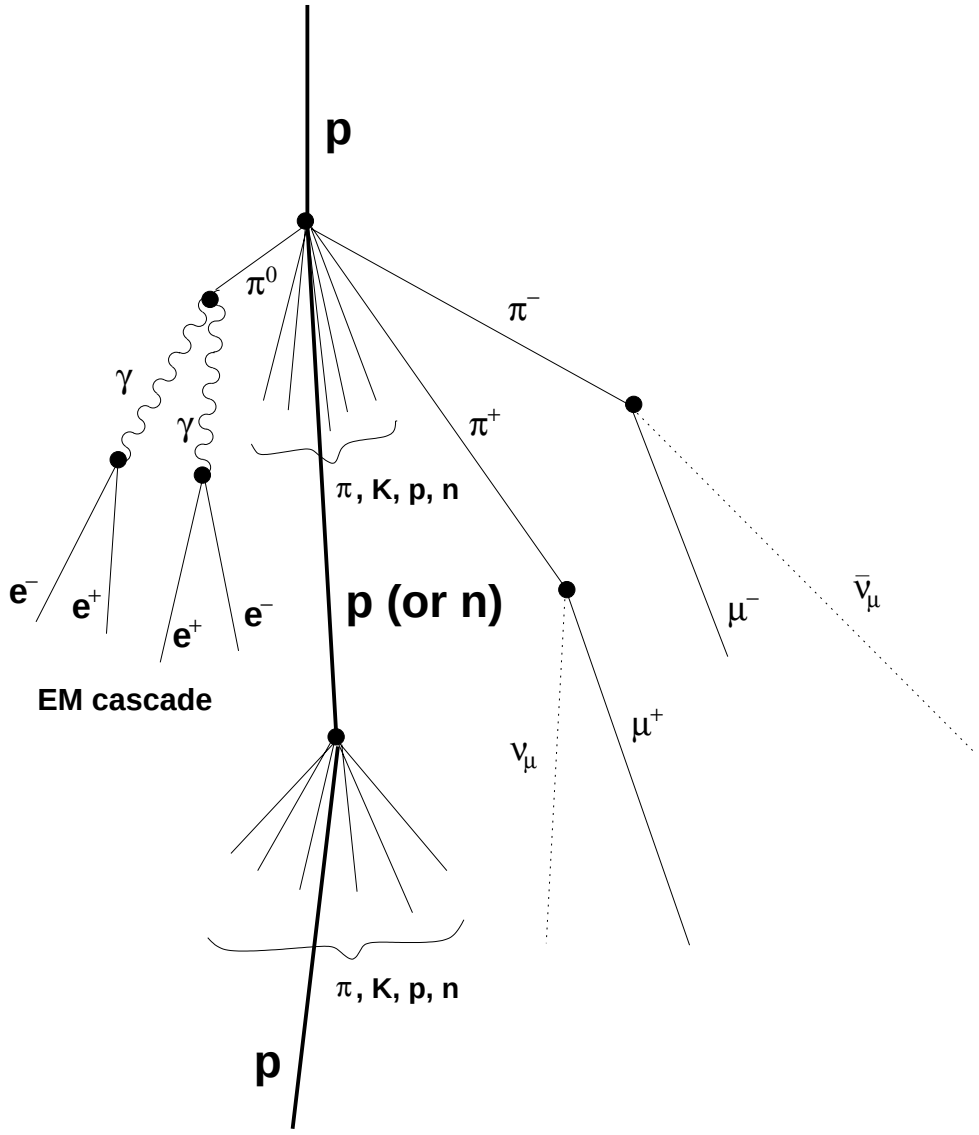

FIGURE 2.2. Anatomy of an air shower initiated by a high energy proton, illustrating the three major components of EAS. Scattering angles are (greatly) exaggerated for clarity.

by π^0 decays ($\pi^0 \longrightarrow 2\gamma$, branching ratio (BR) 98.4%). These are either produced directly in high–energy hadron collisions or via decays of secondary kaons, particularly the following processes:

$$\begin{aligned} K^{\pm} &\longrightarrow \pi^{\pm} + \pi^0 \quad (\mathrm{BR}\,21.2\%) \\ K^0_S &\longrightarrow 2\pi^0 \quad (\mathrm{BR}\,31.4\%) \\ K^0_L &\longrightarrow 3\pi^0 \quad (\mathrm{BR}\,21.8\%) \end{aligned}$$

In addition, pions may be produced in two–body decays such as those of the Δ, ρ and ω resonances, and the strange baryons (Σ, Λ, Ξ, Ω). η decays, either directly to γs or to π^0s, are another generator of EM cascades.

Each high–energy photon emerging from one of the above decay processes generates an EM cascade along lines similar to the toy model described in section 2.1. The EM component of an extensive air shower is therefore a superposition of a large number of smaller sub–showers generated at different heights, continually fed by an energetic core of hadrons. Approximately 90% of the primary energy eventually finds its way into the EM component of the shower, with the rest being carried by neutrinos, muons and low–energy hadrons.

EM cascade theory is well understood — the review article of Rossi and Greisen [73], written some 60 years ago, remains the standard reference work[1]. The method generally employed, as first implemented by Carlson and Oppenheimer [75], is to solve the coupled cascade equations [74]:

$$\begin{aligned} \frac{\partial \pi(E,t)}{\partial t} &= -\frac{\pi(E,t)}{\lambda_\pi(E)} + \int_E^\infty \pi(E',t)\varphi_{\pi\pi}(E',E)dE' \\ &+ \int_E^\infty \gamma(E',t)\varphi_{\gamma\pi}(E',E)dE' + \frac{\partial[\pi(E,t)\epsilon(E)]}{\partial E} \\ \frac{\partial \gamma(E,t)}{\partial t} &= -\frac{\gamma(E,t)}{\lambda_\gamma(E)} + \int_E^\infty \pi(E',t)\varphi_{\pi\gamma}(E',E)dE' \\ &+ \int_E^\infty \gamma(E',t)\varphi_{\gamma\gamma}(E',E)dE', \end{aligned} \tag{2.2}$$

[1]The book by Rossi [74] also contains an excellent discussion of the subject.

with the following definitions:

$\pi(E,t)$	total number of e^+ and e^- with energy E at depth t
$\gamma(E,t)$	number of photons with energy E at depth t
$\lambda_\pi(E)$	mean free path of e^+/e^-
$\lambda_\gamma(E)$	mean free path of γ
$\varphi_{ij}(E,E')dE'$	probability per radiation length that particle i of energy E produces particle j with energy between E' and $E'+dE'$
$\epsilon(E)$	rate of continuous energy loss per radiation length

Equations 2.2 can be solved analytically if appropriate approximations are employed. In **Approximation A**, $\varphi_{\gamma\gamma}$ and $\epsilon(E)$ are set to zero, and λ_π and λ_γ are the mean free paths for bremsstrahlung and pair production, respectively. **Approximation B** also takes continuous energy loss by ionisation into account by setting $\epsilon(E) = E_c = \text{constant}$. E_c is the critical energy and is $\simeq 80$ MeV for air. In both cases, complete screening of the nucleus by atomic electrons is assumed.

Under Approximation B, the total number of electrons at depth X resulting from a cascade initiated by a photon with energy E_0 is [72]

$$N_e(E_0,t) \simeq \frac{0.31}{\sqrt{t_{\max}}} \exp\left[t\left(1-\frac{3}{2}\ln s\right)\right], \tag{2.3}$$

where

$$\begin{aligned} t &\equiv X/x_0 \quad \text{(depth in units of radiation length, } x_0\text{)} \\ t_{\max} &= \ln(E_0/E_c) \\ s &\equiv \frac{3t}{t+2t_{\max}}. \end{aligned} \tag{2.4}$$

The parameter s is termed the "shower age" and has the following properties: $s=0$ at the start of the cascade, $s=1$ at maximum, and $s=2$ when the cascade has completely attenuated, *i.e.* no particles remain. It is clear from Eqs. 2.3 and 2.4 that the results of Approximation B are qualitatively in agreement with those of the Heitler model of Section 2.1.

The angular spread of the EM component is due predominantly to multiple Coulomb scattering of low–energy electrons. The mean square deflection for an electron with energy E through a thickness δt is

$$\langle \delta\theta^2 \rangle = \left(\frac{E_s}{E} \right)^2 \delta t, \tag{2.5}$$

where $E_s \approx 21$ MeV. An approximate calculation due to Greisen [76] and Kamata and Nishimura [77] yields the following expression for the lateral distribution of electrons:

$$\rho(N_e, r) = \frac{N_e}{r_M^2} f_{\mathrm{NKG}}(r/r_M), \tag{2.6}$$

with the NKG function f_{NKG} defined by

$$f_{\mathrm{NKG}}(r/r_M) = C(s) \left(\frac{r}{r_M} \right)^{s-2} \left(1 + \frac{r}{r_M} \right)^{s-4.5}. \tag{2.7}$$

$C(s)$ is an age-dependent normalisation factor, and $r_M = x_0(E_s/E_c)$ is the Moliére unit, the characteristic length scale for the spread of the shower electrons.

This functional form assumes azimuthal symmetry for the particle density. In reality, the lateral distribution of inclined showers will have an asymmetry due to purely geometrical effects; there is also distortion of the lateral distribution due to the geomagnetic field. Pryke [78] has attempted to quantify these effects using Monte Carlo simulations, and has found that they are significant at large core distances and for inclined showers. Analysis of ground array data does not generally attempt to correct for these distortions; they can be ignored so long as the array spacing is not too large.

The NKG function does not adequately describe the lateral distribution for a hadronic air shower, since a hadronic EAS is a superposition of EM cascades initiated at different depths. The age parameter s is no longer well–defined. Surface scintillator array measurements of the lateral distribution show that the NKG function is too steep near the core, and too flat at large core distances [72]. The AGASA collaboration have found a better fit to their data by using the following modified form [79]:

$$\rho(r) = C \left(\frac{r}{r_M} \right)^{-1.2} \left(1 + \frac{r}{r_M} \right)^{-(\eta-1.2)} \left(1 + \left(\frac{r}{1000} \right)^2 \right)^{-\delta}, \tag{2.8}$$

where $\delta = 0.6 \pm 0.1$ and

$$\eta = (3.97 \pm 0.13) - (1.79 \pm 0.62)(\sec\theta - 1). \tag{2.9}$$

It is not possible to calculate the longitudinal development of an EAS in a simple way, as can be done for EM cascades. Instead one must resort to parametrisations, such as the following due to Gaisser and Hillas [80]:

$$N(X) = N_{\max}\left(\frac{X - X_0}{X_{\max} - X_0}\right)^{\frac{X_{\max}-X_0}{\lambda}} \exp\left[\frac{X_{\max} - X}{\lambda}\right], \tag{2.10}$$

where $N_{\max}$ is the shower size at maximum, and λ is a parameter which is dependent on the proton–air cross–section (and which was originally equated with the proton mean free path). X_0 is the point of first interaction, not to be confused with the radiation length x_0.

The energy dependence of the depth of shower maximum can be parametrised using the following argument due to Linsley [81]: supposing that the proton mean free path and the composition of the primary spectrum are energy independent, the increase of $X_{\max}$ with energy is mostly due to the increase in energy of the neutral pions in the fragmentation region. By analogy with Eq. 2.1, we write

$$X_{\max} = x_0 \ln(E_{\pi^0}) + \text{const.} \tag{2.11}$$

Assuming the available energy E is divided evenly amongst the secondary pions, then $E_{\pi^0} = E/\langle n\rangle_{\text{frag}}$ where $\langle n\rangle_{\text{frag}}$ is the mean multiplicity in the fragmentation region. As a result,

$$X_{\max} = (1 - \alpha)x_0 \ln E + \text{const.}, \tag{2.12}$$

where α is the logarithmic derivative of $\langle n\rangle_{\text{frag}}$. This result holds for nucleon primaries. For nuclei, one can appeal to the superposition theorem, which states that, on average, an EAS initiated by a nucleus of mass number A and energy E is equivalent to one initiated by A independent nucleons of energy E/A, *i.e.*

$$\langle X_{\max}\rangle = (1 - \alpha)x_0(\ln E - \langle \ln A\rangle) + \text{const.} \tag{2.13}$$

A quantity often used in discussion of air showers is the elongation rate D_e, which is defined as the logarithmic derivative of the mean depth of maximum:

$$D_e = x_0 \left[(1-\alpha) \left(1 - \frac{\partial \langle \ln A \rangle}{\partial \ln E} \right) + \frac{\partial \alpha}{\partial \ln E} (\langle \ln A \rangle - \ln E) \right]. \tag{2.14}$$

This is Linsley's famous "elongation rate theorem" [81]. Here I have allowed for energy dependence of α. In most models α is constant, and so the second derivative term can be omitted. Note that α is bounded by zero below (scaling models) and by 1/2 above (energy conservation) [81]. Gaisser *et al.* modified Eq. 2.14 to take account of the energy dependence of the hadronic cross–sections, viz.

$$D_e = \left(1 - \alpha - \beta \frac{\partial (\lambda_N + \lambda_\pi)}{\partial \ln E} \right) \left(1 - \frac{\partial \langle \ln A \rangle}{\partial \ln E} \right), \tag{2.15}$$

where βx_0 is a dimensionless constant of order unity and $\lambda_{N,\pi}$ are the mean free paths of nucleons and pions respectively [82].

Eq. 2.15 highlights a major difficulty of cosmic ray physics, namely the need to disentangle astrophysical information ($\langle \ln A \rangle$) from particle physics information ($\alpha, \lambda_{N,\pi}$) in order to interpret the data.

2.2.3 Muons

Muons in EAS are produced mainly via $\pi^\pm$ and $K^\pm$ decay, fed by the hadronic core just as the EM component is. However, unlike the EM component, muons do not multiply. By the same token, attenuation of the muon component is slow.

The energy losses of muons can be written as

$$-\frac{dE}{dx} = a(E) + b(E)E, \tag{2.16}$$

where $a(E)$ is the loss rate by continuous mechanisms, *i.e.* ionisation, and $b(E)$ is a function which describes discrete losses. b contains contributions from muon bremsstrahlung, pair production in the field of a nucleus ($Z + \mu^\pm \longrightarrow Z' + \mu^\pm + e^+e^-$), or by a muon interacting directly with a nucleon (a process which has almost no effect on air shower development). Cillis and Sciutto [83] have recently done a Monte Carlo calculation of the discrete energy losses. They show that the

mean free path for bremsstrahlung is of the order 10^5 g/cm^2 at a muon energy of 1 GeV, slowly decreasing with energy. Since the atmosphere only spans $\sim$ 1000 g/cm^2, the effect on air showers is completely negligible. Pair production has a similar mean free path at 1 GeV, but decreases to $\sim$ few hundred g/cm^2 at 1 TeV and continues to fall with energy. This becomes the dominant energy loss process for high energy ($>$ 1 TeV) muons, but only for showers at large zenith angles[2]. Below this energy, ionisation losses, which are constant at around 2 MeV/(g/cm^2), tend to predominate. Since typical muon energies are of the order of a GeV, the rate of relative energy loss is slow, and so the muon component tends to reach a plateau when the hadrons in the core fall below the pion production threshold. Muon decay can also become important when the energy drops below 10 GeV.

Muons tend to be far less numerous than electrons, as is easily seen by the following rough argument [72]. Assuming charged and neutral pions are produced in equal proportion (a statement which is approximately true), then there will be a GeV photon corresponding to each GeV muon, since $N_{\pi^0}/N_{\pi_\pm} = 1/2$ and $\pi^0 \longrightarrow 2\gamma$. According to the Heitler model, each GeV photon produces approximately 10 electrons; hence $N_e/N_\mu \sim 10$. In reality the ratio can be much larger, and is energy–dependent.

Because of the slow attenuation of the muon component, the total muon number N_μ is sometimes used as an energy estimator for ground arrays, *e.g.* in the SUGAR experiment (see Chapter 1). There are two immediate problems with this; showers of a given energy that happen to develop later and reach ground level before maximum will have their energy underestimated, and showers initiated by nuclei will, in general, produce more muons than those initiated by protons of the same energy, and therefore have their energy overestimated. I will return to this point later. Quite generally, the dependence of N_μ on primary energy can

[2] At large enough zenith angles, pair production can contribute to the extreme tail of the longitudinal development profile, but has very little effect elsewhere [83].

be written as

$$N_\mu(> E_{\text{threshold}}) = AB\left(\frac{E_0}{A}\right)^{p_\mu}, \tag{2.17}$$

where $E_{\text{threshold}}$ is the threshold energy of the muon counter, A is the mass number of the nucleus, and B and p_μ are hadronic model–dependent constants. Most models yield p_μ values between 0.78 and 0.86 [72]. Here the superposition approximation has been employed. It gives approximately the correct average results, but underestimates fluctuations. The AGASA collaboration [84] obtain for this relation

$$N_\mu = 10^{8.38\pm0.35} E_0^{0.84\pm0.02} \tag{2.18}$$

for vertical showers.

Air shower muons have a much harder spectrum than electrons (and $m_\mu \gg m_e$), and therefore suffer minimal Coulomb deflections (see Eq. 2.5). The lateral spread of muons is therefore mostly due to their production angles. Particles near the core tend to be from decays of "local" low energy pions produced near the ground, while particles far from the core generally result from decays of pions produced early in the shower. The transverse momentum distribution of secondary pions (and kaons) is therefore an important quantity when discussing the transverse structure of the muon component.

The lateral distribution for muon energies ≥ 1 GeV was first parametrised by Greisen [85] as

$$\rho_\mu(R) = N_\mu\left(\frac{C_\mu}{R_0^2}\right)\left(\frac{R}{R_0}\right)^{-\alpha}\left(1+\frac{R}{R_0}\right)^{-\beta}, \tag{2.19}$$

where $\rho_\mu(R)$ is the number of muons per square metre at a core distance R, R_0 is a zenith angle–dependent scale factor and C_μ is a normalisation constant. As for the EM component, azimuthal symmetry of the lateral distribution is (incorrectly) assumed.

The AGASA group found Eq. 2.19 to be inadequate for core distances beyond 800m, and incorporated a further factor to correctly describe the large–distance

behaviour [84]:

$$\rho_\mu(R) = N_\mu \left(\frac{C'_\mu}{R_0^2}\right)\left(\frac{R}{R_0}\right)^{-\alpha}\left(1+\frac{R}{R_0}\right)^{-\beta}\left[1+\left(\frac{R}{800\text{m}}\right)^3\right]^{-\delta}, \qquad (2.20)$$

where for vertical showers they obtain $\alpha = 0.75$, $\beta = 2.52$, $\delta = 0.6$, $R_0 = 266$ m, and $C'_\mu = 0.325$ for this parameter set.

To illustrate some of the points above, I plot the results from Monte Carlo–generated air showers (10^{17} eV protons) in Fig. 2.3.

2.2.4 Cherenkov photons

Cherenkov radiation is emitted by any charged particle traversing a dielectric medium at a speed greater than the local speed of light, *i.e.* for $nv/c > 1$ where n is the refractive index of the material. The large number of charged particles in an EAS generates an enormous amount of Cherenkov light. Using the approximate formula in the Fly's Eye NIM paper [34], a shower which has a local size N_e at some depth in the atmosphere will generate of the order N_e Cherenkov photons per metre. The angular dependence has the form

$$\frac{dN}{d\Omega} = \frac{\exp\left(-\theta/\theta_0\right)}{2\pi\sin\theta}, \qquad (2.21)$$

with $\theta_0 = aE_{\text{th}}^{-b}$, E_{th} being the threshold energy (in MeV) for Cherenkov emission. E_{th} is ~ 21 MeV at sea level and increases approximately exponentially with height [85]. a and b are generally small and of order 1. It is easily seen from 2.21 that the angular dependence diverges as $1/\theta$ for small θ. Hence the Cherenkov component is a very narrow intense cone of photons (mostly visible or UV) with a continuous energy spectrum. This light can be imaged, as is done by gamma ray telescopes (HEGRA, Whipple), or cosmic ray experiments (BLANCA, DICE). In the latter case it is possible to infer the cosmic ray energy and composition by studying the lateral distribution of Cherenkov light (see Ref. [53], for example). For a fluorescence detector like HiRes, Cherenkov photons form an unwanted background. I shall explain why in Chapter 3.

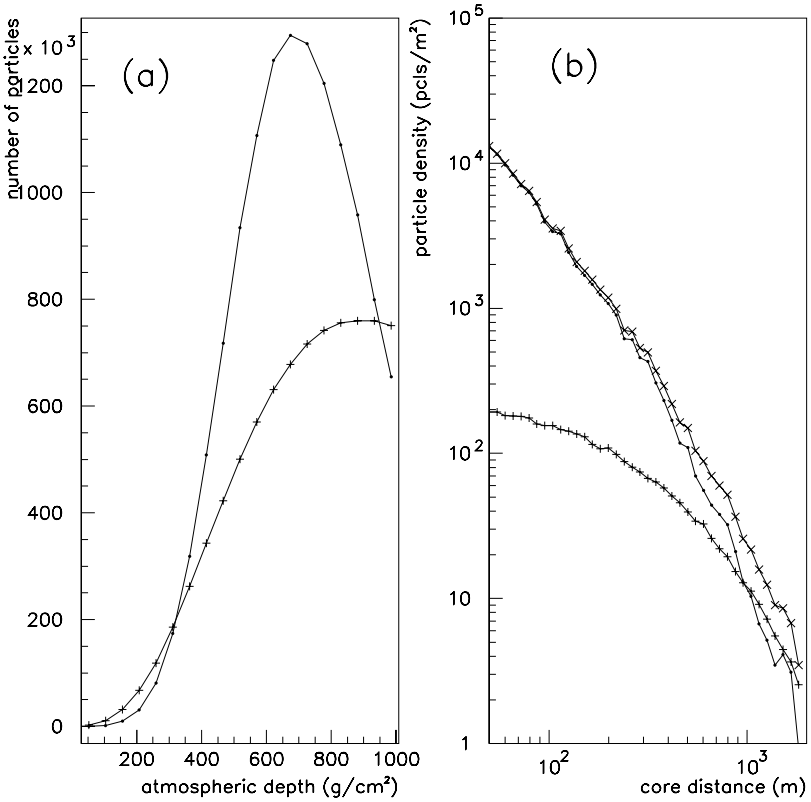

FIGURE 2.3. Electromagnetic ($\cdot$) and muon ($+$) components of EAS initiated by 10^{17} eV protons at a zenith angle of 30°, as simulated by the AIRES code with QGSJet hadronic model: (a) longitudinal profile (electrons scaled down by a factor of 50), (b) lateral distribution. In (b) the distribution of all charged particles ($\times$) is also shown. The "bumpiness" of the electron lateral distribution is not intrinsic, but rather is due to sampling fluctuations.

2.3 Hadronic interactions at high energies

Although a detailed discussion of hadronic physics is beyond the scope of this work, it will be useful to highlight the features that have the most bearing on air shower development[3]. This will be of relevance when discussing the interpretation of EAS measurements.

The most important kinematic region at energies relevant to cosmic ray experiments ($E_{\rm lab} > 10^{14}$ eV, *i.e.* $E_{\rm COM} \gtrsim 500$ GeV) is the fragmentation region, since most of the energy is carried away by particles in this region. This corresponds to small angles between the momentum of the produced particles and the beam direction. In fixed–target experiments, it is possible to measure many quantities of interest to cosmic ray physicists, but at colliders it is very difficult to make measurements close to the beam. The highest lab energy attained for protons at a fixed–target experiment is 1 TeV, and so detailed knowledge of the fragmentation region is restricted to rather low centre–of–mass energies. This means that a significant degree of extrapolation is required, and consequently the uncertainties in hadronic models are large. In fact, they provide the bulk of the uncertainty in EAS simulations.

The longitudinal development of the cascade is controlled by the proton–air and pion–air cross sections, and by the inelasticity. The proton–air cross section determines the depth of first interaction and is therefore correlated quite strongly with the mean depth of maximum. The early part of the cascade produces a large number of pions (these are easily the most dominant secondaries), and the pion–air cross section is *ipso facto* of some relevance for further cascade development . In addition, the inelasticity plays a vital role. Higher inelasticity implies faster dissipation of energy into the secondary particles, and hence more rapid shower development, since it takes fewer generations for particle energies to degrade.

The charged multiplicity in the central region is relevant mostly from the point of view of muon production. Higher multiplicity implies lower average $\pi^{\pm}$ energies

[3]The terms used in this section are defined in Appendix A.

(for a fixed inelasticity), and therefore a greater probability of pion decay; one would therefore expect a higher number of muons per shower on average. The lateral distribution of muons measured at ground level depends on the height of production of the parent pions. Geometrical arguments lead to the conclusion that a shower that develops earlier will tend to produce a flatter lateral distribution (more muons at large distances — see Fig. 2.4). This, of course, assumes that the production angles are not too dissimilar, which they ought not to be provided that the energies of the parent pions are similar.

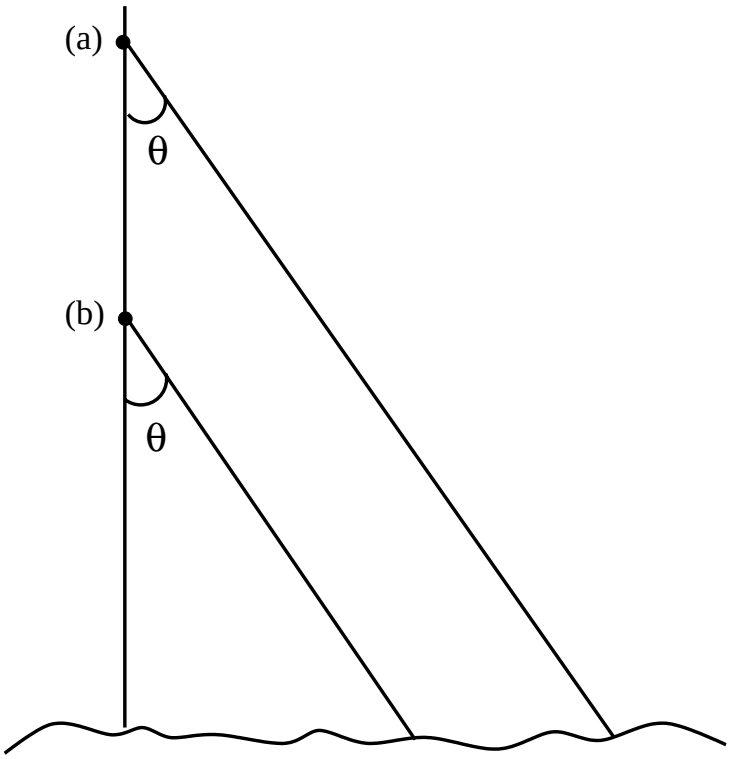

FIGURE 2.4. Effect of cascade development on muon lateral distribution. Muons arriving from point (a) will hit the ground at larger core distances than those arriving from point (b), assuming the production angles are the same.

It should be clear from the preceding discussion that there are a large number of parameters which affect development of hadronic cascades in a complicated way. It is not obvious what combination of these will produce the behaviour observed by cosmic ray experiments. As a result, we rely largely on sophisticated Monte

Carlo programs to model hadronic air showers. The hadronic generators used for the analysis in this thesis will be discussed in Section 2.3.2.

2.3.1 Phenomenology of hadron–hadron scattering

The hadronic processes relevant to air shower physics are generally characterised by small transverse momentum ("soft" hadronic interactions) and are therefore not calculable in perturbative QCD. Instead one must rely on phenomenological methods.

Most modern descriptions of soft hadron–hadron scattering utilise the framework originally developed by Gribov [86], after an idea by Regge [87], to describe low–energy scattering data. The crux of the idea is to allow the angular momentum ℓ to become complex. The scattering amplitude, which would ordinarily have poles at integer values of ℓ, may now have poles at some arbitrary position $\ell = \alpha(t)$, *i.e.* the position of the pole shifts as the 4–momentum transfer squared, t, changes. α is a complex function referred to as a *Regge trajectory*. When α takes on non–negative integer values for some value of $|t| < 0$, the corresponding energy is that of a bound state; a resonance can occur for $|t| > 0$ when $\mathrm{Re}\,\alpha(t)$ is integral and $\mathrm{Im}\,\alpha(t)$ is small. Hence, instead of considering scattering as an exchange of one or more particles, we treat it as the simultaneous exchange of a whole *trajectory* of particles. Experimentally, the mesonic resonances are found to lie on almost linear Regge trajectories [88].

Gribov–Regge theory predicts that, for the exchange of a trajectory $\alpha(t)$, the differential cross section behaves as $d\sigma/dt \sim s^{2\alpha(t)-2}$, and the total cross section as $\sigma \sim s^{\alpha(t=0)-1}$. Accelerator measurements show that cross sections rise slowly with the centre of mass energy $\sqrt{s}$ [42]. The asymptotic behaviour of the total cross section is therefore controlled by a trajectory with $\alpha_P(0) \simeq 1$. This trajectory corresponds to an object called the pomeron. If cross sections obeyed strict scaling and were asymptotically constant, we would have $\alpha_P(0) = 1$. In practice, it is a little larger than 1.

The following Regge–type fit, which provides an excellent description of all data

for total cross sections, has been performed by Donnachie and Landshoff [89]:

$$\sigma_{ab}^{\rm tot} = X_{ab} s^{\epsilon} + Y_{ab} s^{-\eta}, \tag{2.22}$$

where the first term is due to pomeron exchange and the second due to the trajectory on which the ρ, ω, f and a mesons lie. They find $\epsilon = 0.08$ and $\eta = 0.45$, implying a pomeron intercept $\alpha_P(0)$ of 1.08.

What is the connection between the pomeron and QCD? A clue is provided by the Pomeranchuk theorem, namely that the total cross sections for ab and $a\bar{b}$ scattering are aymptotically equal [90]. This means the pomeron must be an object with the quantum numbers of the vacuum. The simplest such object would be a glueball consisting of two gluons, although this gives a constant cross–section [91]. More elaborate scenarios, such as the one illustrated in Figure 2.5, feature "ladders" of soft gluons (with possible insertions of $q\bar{q}$ pairs), which can lead to rising cross sections. Such scenarios arise naturally at first order in so–called "topological expansions" of QCD [92, 93, 94].

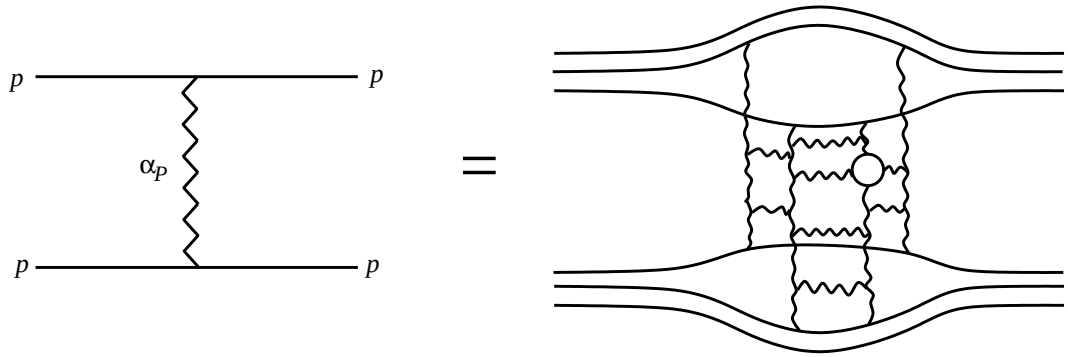

FIGURE 2.5. pp scattering via pomeron exchange (α_P). Here the pomeron is represented as a gluon ladder (squiggly lines) with a quark loop insertion (circle). Essentially after Ref. [95].

Accelerator measurements show that with rising energy, the multiplicity in the central region increases, and is correlated with transverse momentum [72]. These "minijets" imply the onset of a hard part to the cross section, due to parton–parton scattering. This is in contrast to the scenario described above, in which scattering

is described in terms of interactions of soft gluons. The minijet contribution to the cross section is small, but grows with energy [72, 96].

Multiparticle production is usually modelled by the formation and fragmentation of quark–gluon "strings". In pp scattering, for example, a valence quark from the projectile will combine with a qq state, called a diquark, from the target, and vice versa. The quark and diquark are joined by gluons, which tighten themselves into a "colour flux tube" due to the fact that the gluon is self–interacting. As the target and projectile move apart, the string tension continues to increase (infrared slavery) up to the point where it fragments. At each break in the string, a $q\bar{q}$ pair forms; this process is referred to as "hadronisation". Hadronic generators used in cosmic ray calculations differ mostly in the way in which string formation and fragmentation are implemented.

2.3.2 Implementations of hadronic models

The hadronic models currently used in shower simulations have many common features. These are summarised in Table 2.1.

Of the models listed in Table 2.1, only QGSJet [101], SIBYLL [96] and DPMJet [102] are applicable at sufficiently high energies for this study. QGSJet and DPMJet share almost identical major characteristics; I have chosen to use the former rather than the latter for this work, mainly for reasons of computational economy. For example, at 10^{15} eV, QGSJet is approximately 3 times as fast as DPMJet, and uses roughly a fifth of the memory [103].

The major differences between QGSJet and SIBYLL affecting cascade development are illustrated below. Figs. 2.6 and 2.7 show the energy dependence of the hadron–air and nucleus–air cross sections. Note the sharp rise with energy of the proton–air and pion–air cross sections for SIBYLL, due to the increasing minijet contribution, and the significant divergence from the corresponding QGSJet quantities at the highest energies. This difference is not reflected in the iron–air cross section.

In Fig. 2.8 the elasticity distributions for the two models are shown. The

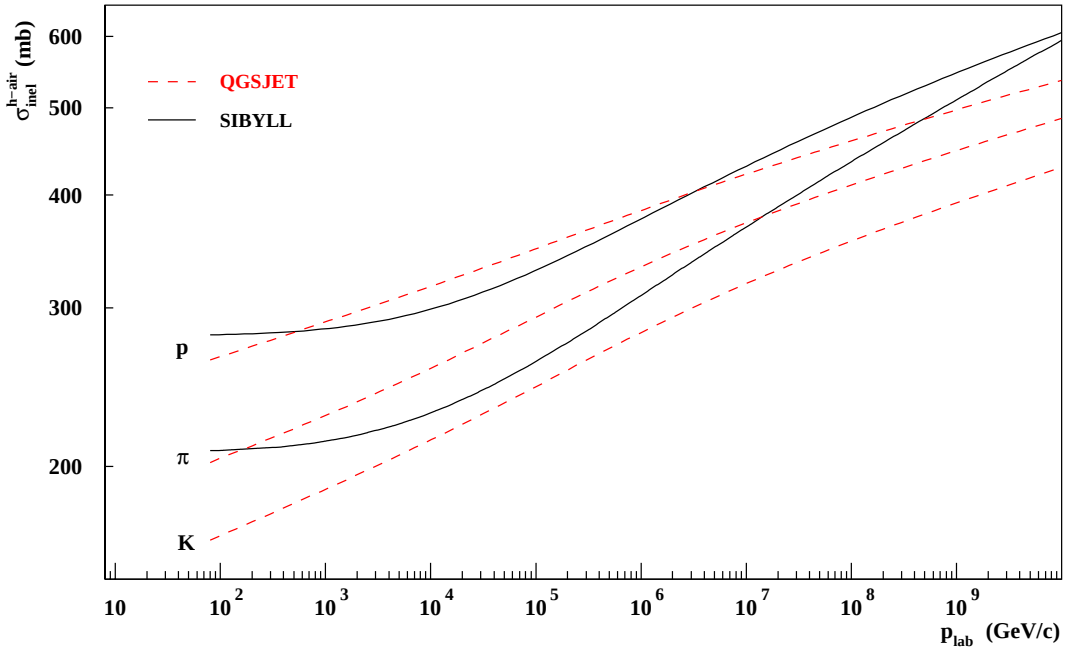

FIGURE 2.6. Inelastic hadron–air cross sections for QGSJet and SIBYLL. In the latter, the cross section for kaons on air is taken to be the same as that for pions. Figure adapted from Fig. 2 of Ref. [99].

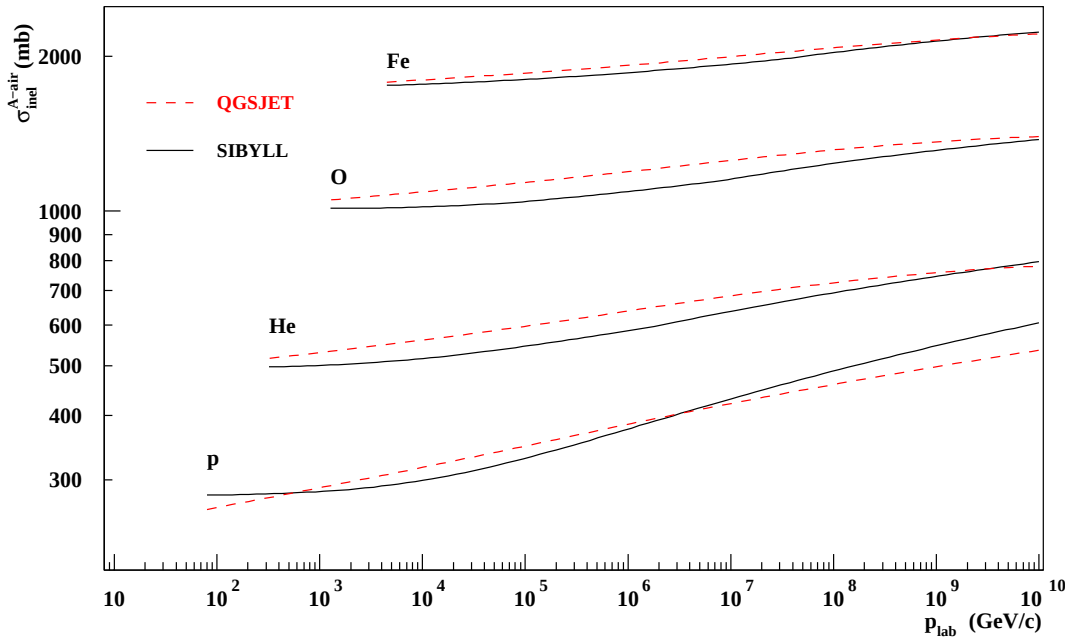

FIGURE 2.7. Inelastic nucleus–air cross sections for QGSJet and SIBYLL, for four different nuclei: protons (hydrogen), helium, oxygen and iron. Figure adapted from Fig. 4 of Ref. [99].

	VENUS	QGSJet	SIBYLL	HDPM	DPMJet
Gribov–Regge	√	√			√
$\alpha_P(0)$	1.07	1.07	1.0		1.05
minijets		√	√		√
diffractive scattering	√	√	√	√	√
secondary interactions	√				√
nucleus–nucleus ints.	√	√			√
superposition			√	√	
residual nuclei		√			√
max. energy (GeV)	10^7	10^{11}	10^{11}	10^8	10^{12}

TABLE 2.1. Characteristics of hadronic models used in air shower calculations. Essentially after Refs. [97] and [98]. "secondary interactions" refers to re–interaction of produced and spectator hadrons; "residual nuclei" means that fragments of target and projectile nuclei are properly accounted for.

distribution for SIBYLL remains relatively constant with changing energy, while the QGSJet distribution becomes harder (more inelastic) with increasing energy. One would therefore anticipate an increasing difference in $X_{\max}$ distributions from the two models [100].

2.4 Cascade Simulators

It is possible to write down a large set of coupled cascade equations such as Eqs. 2.2 for each species in the shower, but it is not practical to attempt a wholly analytical solution for physically interesting cases. Instead, large Monte Carlo programs are used to simulate EAS. The most commonly used cascade simulation codes are MOCCA, AIRES and CORSIKA.

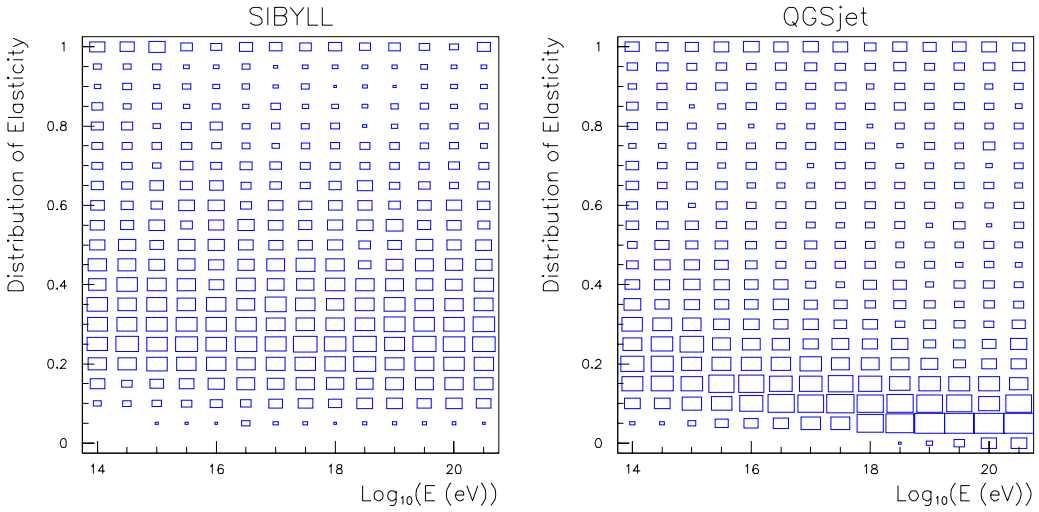

FIGURE 2.8. Elasticity distributions for SIBYLL and QGSJet [100]. The side length of the boxes is proportional to the bin contents.

2.4.1 MOCCA

The MOCCA (**MO**nte **C**arlo **CA**scade) code was developed originally by Michael Hillas at Leeds [104, 105] in the Pascal programming language. Up until a few years ago, it was the most widely used EAS simulation code; it has largely been supplanted by AIRES and CORSIKA.

MOCCA was the first cascade simulation to introduce the notion of thin sampling, or "thinning". In this scheme, the many low energy particles are not treated in detail; instead, some small fraction below the thinning energy $E_{\rm thin}$ are followed and assigned a weight (greater than 1) according to their energies. $E_{\rm thin}$ is generally taken as some fraction (called the thinning level) of the primary cosmic ray energy. The CPU time required per shower scales with the thinning level — for example, a shower thinned at 10^{-4} will take roughly an order of magnitude longer than one thinned at 10^{-3}. The penalty for increasing thinning to speed up simulations is a large increase in artificial (non–statistical) fluctuations. Pryke [100] has shown that one can obtain unbiased results for $X_{\rm max}$ with a thinning level as severe as $10^{-3.5}$, although one suspects that the lateral distributions of electrons

and muons would be unlikely to be bias–free in this case. For most applications, a thinning level of 10^{-5} is considered sufficient.

The hadronic model incorporated in the 1992 version of MOCCA employs a simple "splitting" strategy [105]. This reproduces some features of accelerator data up to a few hundred GeV, but fails at higher energies, particularly since it produces only pions. The splitting model leads naturally to scaling in the fragmentation region. An interface to allow MOCCA to use the SIBYLL hadronic generator has been written; this combination was widely used until recently.

2.4.2 AIRES

The original implementation of AIRES (**AIR** Shower **E**xtended **S**imulations) [106] was essentially a Fortran rewrite of the 1992 version of MOCCA. The underlying physics was the same, and the two codes have been shown to be completely consistent [107]. Although later versions of AIRES diverge somewhat, particularly with respect to the implementation of thin sampling, the physics is still largely the same [106].

AIRES is much more modular in structure than MOCCA, thereby allowing different hadronic drivers to be easily incorporated. In addition, it enables greater control over shower input parameters. It also has advantages in terms of speed and efficiency.

2.4.3 CORSIKA

CORSIKA (**CO**smic **R**ay **SI**mulations for **KA**scade) [98] is the most widely used and comprehensive EAS code available. It supports a number of different hadronic interaction codes. For lab energies below a few hundred GeV, detailed simulations are done for hadronic interactions via the GHEISHA subroutines [108]. Electromagnetic subshowers are simulated at all energies using the EGS4 code [109]. GHEISHA and EGS4 are known to give very good reproductions of experimental data. Thin sampling is implemented in a similar way to MOCCA.

Chapter 3

Experimental Techniques

I provide here a brief description of the physics behind the techniques employed by Fly's Eye/HiRes (fluorescence) and MIA and AGASA (charged particle detection) to measure EAS. Details of the detector operation and analysis techniques will be given in Chapters 4 and 5.

3.1 Surface Arrays

Until the advent of the fluorescence technique in the late 1970s, the use of ground based detectors was the only method by which cosmic ray air showers were measured. There are two giant arrays still in operation (Yakutsk, which also employs an array of photomultiplier tubes to measure atmospheric Cherenkov emission, and AGASA). The Pierre Auger Project will feature the largest array yet, covering an area of some 3000 km^2 overlooked by four fluorescence detectors [40].

Ground arrays[1] directly sample shower particles by several different methods, each involving a large number of detector stations separated by some appropriate distance, optimally tens of metres for arrays to measure low–energy showers and hundreds of metres up to a kilometre or so for EHE arrays. In the EHE region, there are two favoured detector types, namely scintillation counters and water Cherenkov detectors. The former usually employs detectors composed of a photomultiplier tube (PMT) viewing a slab of plastic scintillator and encased in a light–tight enclosure. In addition, thin lead sheeting may be employed to boost, via pair–production, the number of electrons available for scintillation. The latter type consists of tanks filled with water of high purity and viewed by one or more PMTs, which record the Cherenkov light produced by shower electrons, photons

[1] The terms "ground array" and "surface array" will be used interchangeably in this section.

and muons. The biggest difference between the two types of detector is the nature of the signal that they measure. Scintillation counters are equally sensitive to electrons and muons, while water Cherenkov detectors will measure much more signal from typical muons than electrons. The former have a much harder spectrum and can traverse the entire detector, while the latter are quickly absorbed. In addition, low–energy photons, which are much more numerous than either electrons or muons, can be converted to an observable signal in a water Cherenkov tank and produce a sizeable contribution. These comments are borne out by Fig. 3.1.

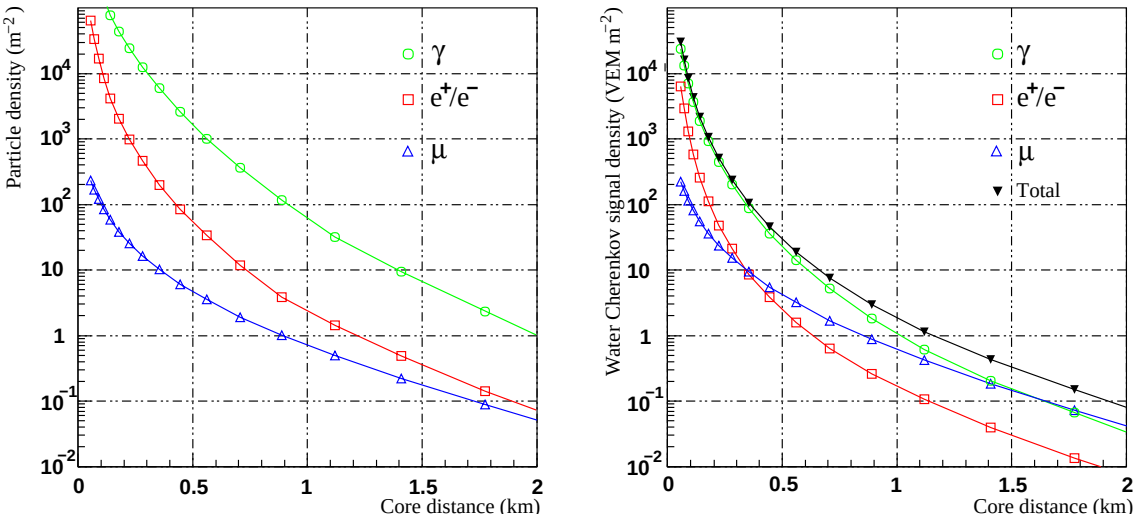

FIGURE 3.1. The simulated lateral distributions of shower components (left hand plot) and the corresponding contribution to the water Cherenkov signal (right hand plot). Adapted from Ref. [40].

The detectors relevant to this thesis are of the scintillation type. I will subsequently refer only to this type of detector. The term "ground array" will therefore be understood to mean an array of scintillators. A discussion of water Cherenkov detectors may be found in, for example, the Pierre Auger Project Design Report [40].

Event reconstruction for ground arrays proceeds roughly along the following lines. The shower front is initially assumed to be planar. Using the times of the hits recorded by each counter and the measured particle densities, and assuming azimuthal symmetry in the plane of the shower front (reasonable enough in most

situations — see Chapter 2), one can estimate the arrival direction and core location for the shower. The aim of this is to establish the initial parameter set for a fit to some lateral distribution function, *e.g.* the modified NKG form used by AGASA, Eq. 2.8. The curvature of the shower front must also be taken into account. The net result of this process is the determination of important physical properties including the shower geometry and number of charged particles at the observation level, as well as the full lateral distribution.

3.1.1 Energy determination

From Eqs. 2.3 and 2.4 it is seen that the number of particles at shower maximum, $N_{\rm max}$, is proportional to the primary cosmic ray energy. This result is derived in Approximation B of electromagnetic cascade theory, but is also borne out by more sophisticated treatments of hadron–induced showers. Unfortunately, ground arrays measure the electron size at only one atmospheric depth. It is very difficult to tell with a surface array alone what stage of longitudinal development the cascade has reached. This makes it very difficult to determine energy using surface array measurements. Even if one could determine the shower size at maximum, the constant of proportionality has some hadronic model dependence.

It has been known for some time from Monte Carlo simulations that the particle density far from the core is somewhat insensitive to fluctuations in shower development. It is also relatively independent of composition [25, 110]. The exact distance at which this becomes true is energy–dependent, but 600m is a reasonable figure over the range 10^{17}–10^{20} eV [2]. For showers of fixed energy, the density at 600m can therefore be regarded as a good indicator of the primary energy. The precise relation between $S(600)$, the scintillator density at 600m, and energy can be determined using Monte Carlo results.

An alternative method for determining energy has been developed by the CASA and MIA collaborations [111]. Using MOCCA/SIBYLL simulations, they find that the quantity $(N_e + 25 \times N_\mu)$ is proportional to energy and independent of composition. They apply this relation over the energy range 10^{14}–10^{16}

eV. CASA/MIA estimate that the mean absolute energy error resulting from this method is around 25% at 10^{14} eV, decreasing to about 16% above 10^{15} eV.

3.1.2 Composition

A shower initiated by a heavy nucleus develops faster than that initiated by a proton shower, on average. The average depth of shower maximum, $X_{\max}$, is therefore a measure of the mean composition at a given energy.

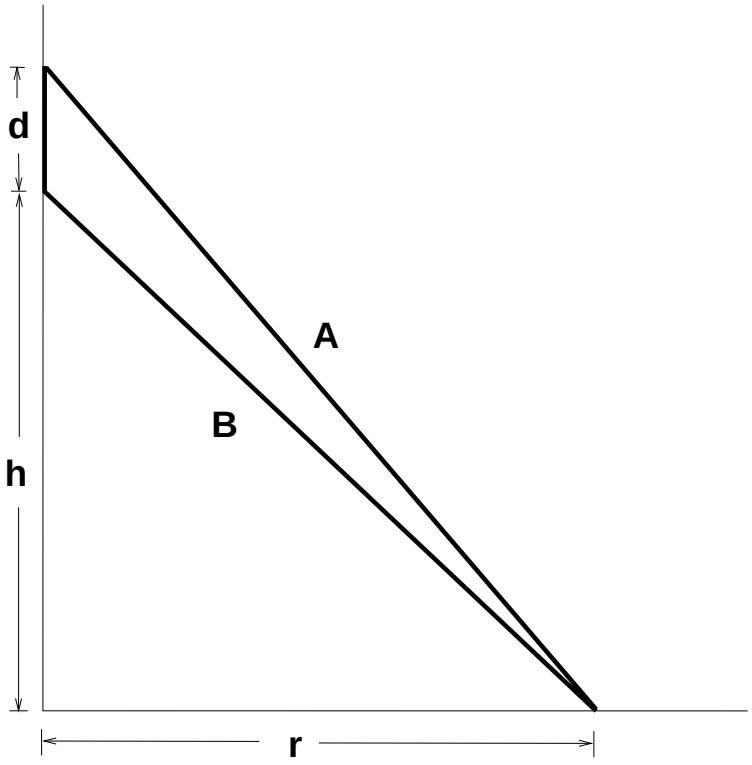

FIGURE 3.2. Geometry for the risetime calculation as described in the text.

Ground arrays are unable to measure $X_{\max}$ directly, although there are indirect methods of inferring it, *e.g.* by studying the temporal structure of the shower. Showers which develop earlier will have less time dispersion than those which develop later, as can be seen by the following simple geometrical argument. Suppose that the cascade develops over a distance d, as in Fig. 3.2. Then the path difference for particles travelling via path A differs from that for particles travelling via

path B by

$$\begin{aligned} \Delta &= (d + \sqrt{r^2 + h^2}) - \sqrt{r^2 + (h+d)^2} \\ &\simeq d + h\left(1 + \frac{1}{2}\frac{r^2}{h^2}\right) - (h+d)\left(1 + \frac{1}{2}\frac{r^2}{(h+d)^2}\right), \end{aligned} \tag{3.1}$$

where we have assumed $h >> r$ (typically, d might be of the order of a few hundred metres, while we would take r to be a few hundred metres and h of the order of a few kilometres). Simplifying this, one obtains

$$\Delta = \frac{1}{2}\left(\frac{r^2 d}{h(h+d)}\right). \tag{3.2}$$

It is therefore seen that the higher in the atmosphere the shower develops (larger h), the smaller the path difference, and hence the time dispersion at a given core distance r, will be. The risetime at r, defined as the time taken for the signal to increase from the 10% level to the 50% level (either number of muons, or water Cherenkov signal), is therefore an indirect measure of $X_{\max}$. That there is a strong correlation between risetime and distance to $X_{\max}$ can be seen from CORSIKA simulations, the results of which I plot in Fig. 3.3.

A slightly undesirable property of the risetime is that the conversion from risetime to $X_{\max}$ is model dependent, and must be determined separately for each experiment. Nonetheless, it can still be a useful indication of the stage of shower development. It might be a particularly useful parameter for a hybrid (fluorescence and surface array) detector. The $X_{\max}$–risetime relation can be fixed in a model–independent way using hybrid data, and then applied to the data for which fluorescence measurements are not available (due to the $\sim 10\%$ duty cycle of fluorescence detectors).

A more direct way of inferring composition is to measure the muon content of the shower. In the superposition approximation, a nucleus with mass A will generate a factor $A^{0.15}$ more muons than a proton when it cascades (in more rigorous treatments the ratio is smaller, but still non–negligible) [72]. Experiments therefore attempt to measure the total number of shower muons above some energy threshold (~ 1 GeV). This is done by using underground (or otherwise shielded)

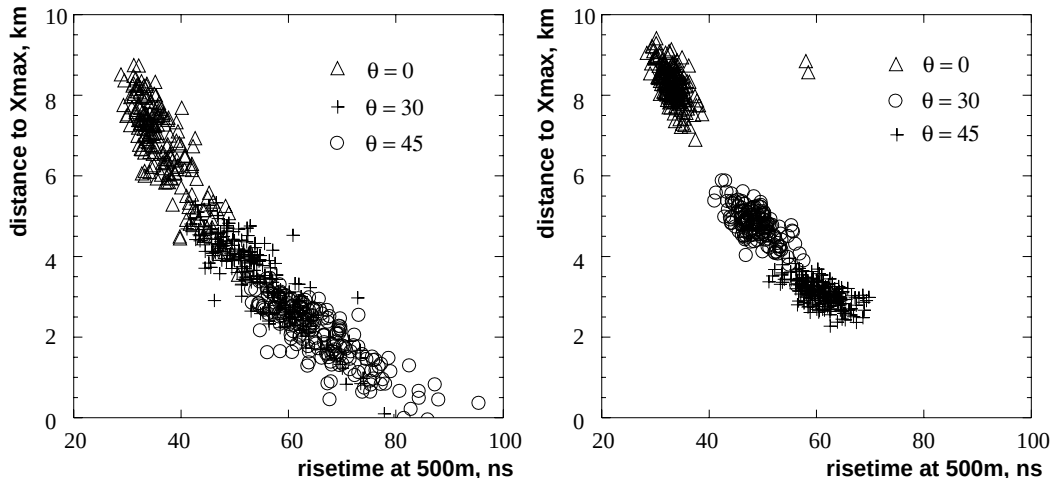

FIGURE 3.3. Correlation between distance to $X_{\max}$ and risetime at 500m from the core, for 10^{17} eV proton (left) and iron (right) showers generated by CORSIKA/SIBYLL. Three different populations are shown, these being for events with zenith angles of $0°, 30°$ and $45°$. The separation between populations is greater for iron showers due to their smaller $X_{\max}$ fluctuations.

muon detectors (usually scintillation or proportional counters) situated beneath the surface array, and looking for coincidences. In fact, this is one way of doing UHE gamma ray astronomy, since gamma initiated showers tend to contain many fewer muons than hadronic ones and a muon veto can be applied. The CASA and MIA arrays were originally built for this purpose.

The total number of muons in a shower, N_μ, is sensitive to composition; so too is the density at 600m, $\rho_\mu(600)$, and this is often used as an alternative to N_μ. In some cases $\rho_\mu(600)$ may be easier to measure than N_μ. In this thesis I will investigate the composition sensitivity of both parameters.

3.2 Atmospheric Fluorescence

The atmospheric fluorescence technique was pioneered by Greisen and co–workers in the 1960's [112, 113], after an idea by Suga [35]. They tested the technique by constructing two sites, each of 212 photomultiplier tubes arranged in a hemi-

spherical structure "like half a fly's eye". In the mid 1970's, the University of Utah built a prototype (3–mirror) "Fly's Eye" overlooking the Volcano Ranch surface array in New Mexico [37]. The full Fly's Eye detector, which is described briefly in Chapter 4, was built in Utah and began operation in 1981.

The only currently operational fluorescence detector is the High Resolution Fly's Eye (HiRes), which is the focus of the author's work and which will be discussed in more detail in Chapter 5. Proposed detectors will have the same basic design, namely an array of mirrors focussing light onto a cluster of PMTs.

The fluorescence technique relies on the fact that charged particles traversing the atmosphere excite or ionise nitrogen molecules, which then isotropically emit UV photons. The yield from this process is lowered significantly by collisional de–excitation by oxygen molecules; the yield for pure nitrogen is a factor of 5 higher than in air [114].

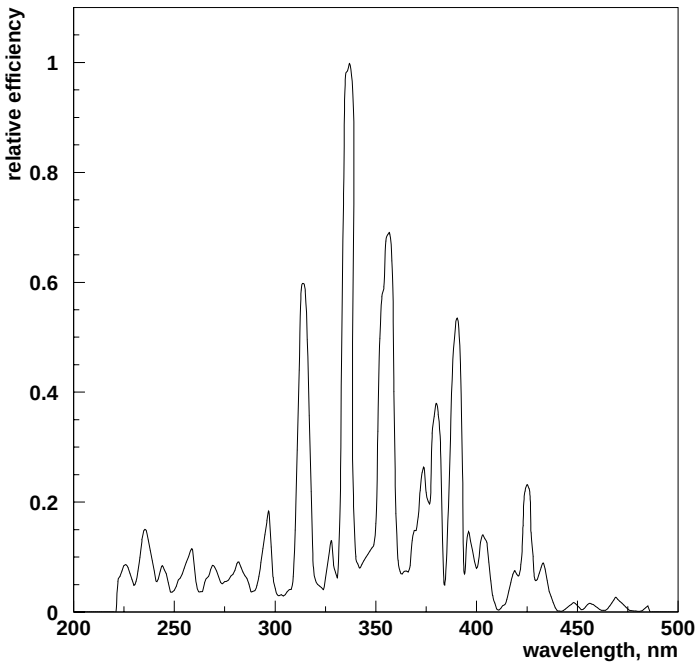

FIGURE 3.4. The fluorescence spectrum as measured by Bunner [36], normalised to the yield of the line at 337 nm.

The nitrogen fluorescence spectrum is depicted in Fig. 3.4. Most of the emission occurs between 300 and 400nm and is due to the 2P band of molecular nitrogen and the 1N band of the N_2^+ ion [36]. The efficiency is very low — only ~ 4 fluorescence photons are emitted per metre of atmosphere traversed by an electron — however, above 10^{17} eV, showers are sufficiently large to be detectable above the night sky background. The recent measurements of Kakimoto *et al.* [114] show that the fluorescence yield is almost independent of pressure and temperature, and is proportional to the ionisation energy loss, dE/dx.

Analysis of fluorescence detector data requires detailed modelling of the light production and attenuation mechanisms. The fluorescence signal can be depleted by atmospheric absorption or scattering. Conversely, the intense beam of Cherenkov photons emitted along the shower axis may add to the observed signal by being scattered towards the detector. Direct Cherenkov light can also contribute. Although the Cherenkov angle is only around 1°, the lateral spread of electrons means that there is significant Cherenkov emission out to 20° or so. This means that tubes which view the track at an angle of 20° or less will measure some direct Cherenkov light.

Although absorption is weak in the wavelength band of interest, Rayleigh scattering and Mie scattering can be significant. The former involves scattering off atmospheric molecules and is a well–understood process, being easily calculable in electromagnetic scattering theory, and requiring only knowledge of the atmospheric density profile. The cross–section for Rayleigh scattering varies with wavelength as λ^{-4} and has an angular dependence $1 + \cos^2\theta$. The effect of Mie scattering, on the other hand, is much harder to quantify. The scattering centres in this case are particles (aerosols) whose size is comparable to the wavelength of the fluorescence photons. The cross section depends on the type and size distribution of the particles, and is characterised by a weak (flat or λ^{-1}) wavelength dependence and strong forward peak. The major difficulty in quantifying this effect is an experimental rather than a theoretical one. The size distribution and density profile of aerosols is not well known, and can be highly variable from night to

night. Extensive monitoring of the atmosphere is therefore a vital task.

A further complication to the picture presented above is that multiple scattering of fluorescence and Cherenkov photons can contribute to the total signal. Photons which would ordinarily be scattered out of the beam and therefore go undetected can be re–scattered and enter the detector within the time allotted for an event trigger. The shower track therefore appears brighter than it ordinarily would at that geometry, and the usual reconstruction algorithms overestimate the shower energy. This may be especially important for distant showers. Simulations show that the correction to the reconstructed energy is of the order of 10% for showers 30km away and 5% for those 10km away, and is mildly dependent on the atmospheric model used (the figures quoted here are for a standard US desert atmosphere) [115, 116].

There are several sources of background light for a fluorescence detector. These include scattered starlight, diffuse galactic radiation, sunlight scattered by interplanetary matter and airglow [34]. Transient sources such as aeroplanes and Cherenkov radiation from low energy cosmic rays do not pose a serious difficulty. However, bright stars or planets entering the field of view can be problematic.

The signal–to–noise ratio can be estimated in the following way. The number of background photoelectrons B seen by a single PMT subtending solid angle $\Delta\Omega$ over an integration time Δt can be written as

$$B \propto \epsilon A b \Delta\Omega \Delta t, \tag{3.3}$$

where ϵ is the optical efficiency of the system, A is the area of the mirror, and b is the background flux. If the PMT is AC–coupled, only the fluctuation in the background is important, *i.e.* the number of noise photoelectrons, N, is

$$N = \sqrt{B} \propto \sqrt{\epsilon A b \Delta\Omega \Delta t}. \tag{3.4}$$

The number of signal photoelectrons S seen by the PMT in the same time is given by

$$S \propto \frac{\epsilon A n_e c\Delta t}{4\pi R^2} e^{-R/\lambda}, \tag{3.5}$$

where n_e is the shower size at that part of the track viewed by the PMT, R is the distance to the observed segment and $c\Delta t$ is the length of that segment. λ is the beam attenuation length and is composed of contributions from Rayleigh and Mie scattering. The signal–to–noise within the integration time is therefore given by

$$\frac{S}{N} \propto \frac{n_e c}{4\pi R^2}\sqrt{\frac{\epsilon A\Delta t}{b\Delta\Omega}} e^{-R/\lambda}. \tag{3.6}$$

We observe from Eq. 3.6 that the S/N ratio depends quite strongly on the distance to the shower, as expected. A detector can be optimised to measure distant (higher energy) events by increasing the mirror area and integration time, and decreasing the tube size. This was done when the Fly's Eye was superseded by HiRes. The mirror area was increased from 1.8 m to 3.1 m, and the tube size decreased from 5° to 1°, with a resultant factor of 6.6 increase in S/N [117].

3.2.1 Geometry reconstruction

For a single fluorescence eye, the shower geometry is determined by using both amplitude and timing information from the triggered tubes[2]. The first step is to determine the **shower–detector plane** or SDP, which is the plane containing the shower axis and the centroid of the detector. This is illustrated in Fig. 3.5.

The SDP is determined to first approximation by using the pointing directions of the triggered tubes. The unit normal to the SDP, $\hat{\mathbf{n}}$, can be found by minimising the quantity $\sum_i \mathbf{r}_i \cdot \hat{\mathbf{n}}$, where $\mathbf{r}_i$ is the pointing direction of the i^{th} triggered tube. Refinements can be made to this method. For example, one can construct a χ^2 where each tube is weighted by its amplitude, and minimise it to find the SDP normal. This should give a better estimate since brighter tubes are more likely to be closer to the shower axis.

[2]The detailed procedure is described in Chapter 5.

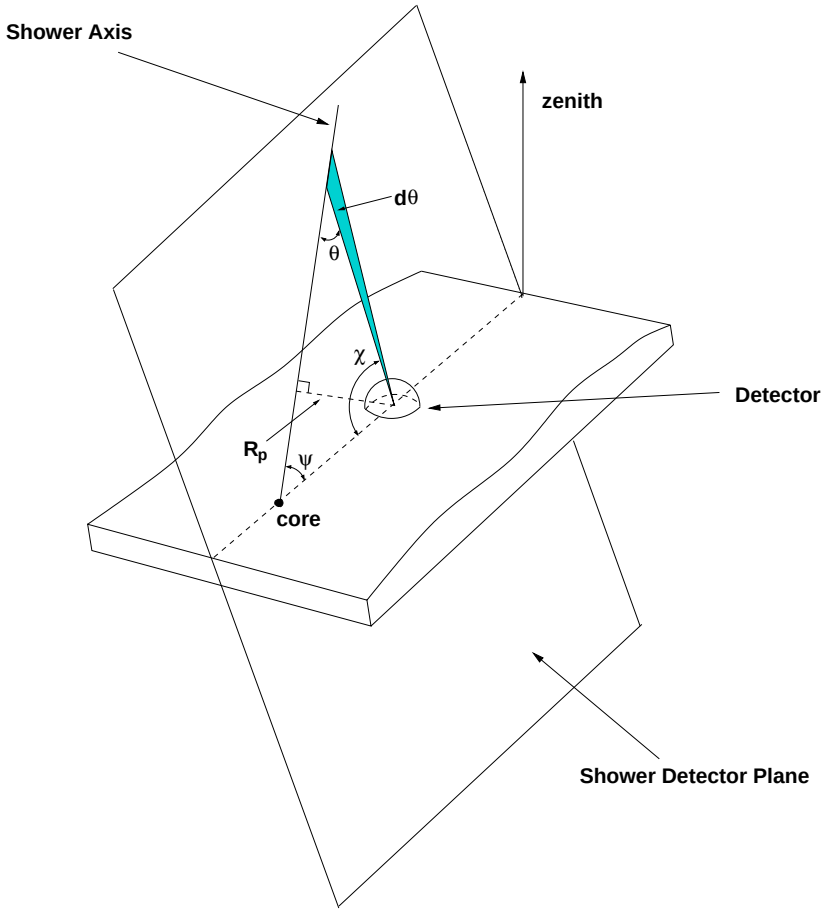

FIGURE 3.5. Geometry of an EAS detected by a fluorescence telescope, showing the Shower–Detector Plane.

If the shower is viewed by two eyes, the shower axis is simply given by the intersection of the SDP for each eye. The geometrical reconstruction accuracy can be improved further by using timing information [118]. If only one eye sees the shower (monocular observation), the orientation of the track within the SDP, as expressed by the quantities $R_{\rm p}$ and ψ (see Fig. 3.5), must be determined using the trigger times of the hit tubes.

Suppose that a PMT views light coming from point P, as in Fig. 3.6. Then the lag between the time taken for light to arrive directly at the PMT from P and the time the shower takes to reach point O is given by

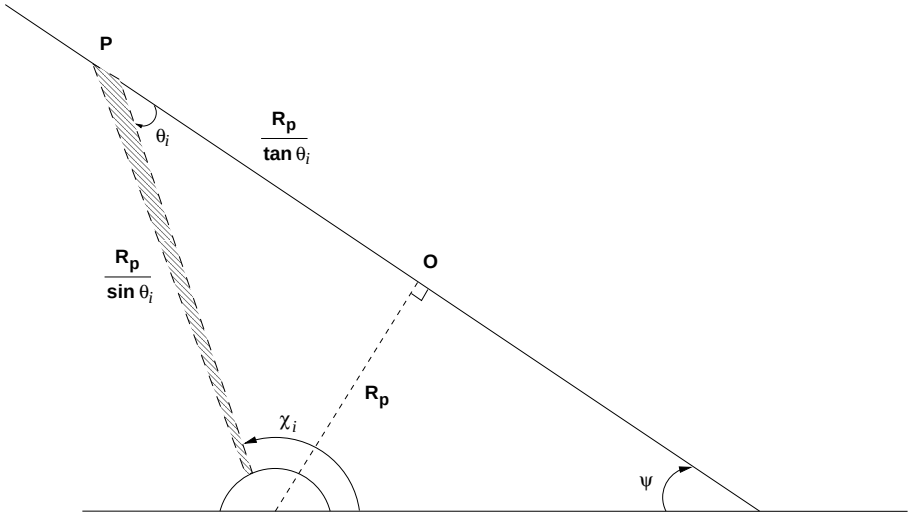

FIGURE 3.6. Determination of the shower axis using timing information.

$$\delta(\theta_i) \equiv (t_i - t_0) = \frac{R_{\rm p}}{c \sin\theta_i} - \frac{R_{\rm p}}{c \tan\theta_i} = \frac{R_{\rm p} \tan\theta_i/2}{c}. \tag{3.7}$$

Here $R_{\rm p}$ is the "impact parameter", defined as the perpendicular distance from the detector to the shower axis, t_i is the trigger time for the $i^{\rm th}$ tube viewing the shower, and t_0 is the time at which the shower front reaches point O. In Fig. 3.6, χ_i is the observation angle of the tube in the SDP. This is given by $\chi_i = \pi - \theta_i - \psi$, *i.e.*

$$\chi_i = \pi - \psi - 2\arctan\left(\frac{c(t_i - t_0)}{R_{\rm p}}\right). \tag{3.8}$$

Thus, given the tube pointing directions (and hence χ_i) and trigger times for each PMT, one can perform a fit using Eq. 3.8 to determine the parameters t_0, $R_{\rm p}$ and ψ. The track geometry is now completely specified.

Once the shower geometry is known, the shower development profile, *i.e.* the shower size as a function of atmospheric depth, can be extracted. The fluorescence light emitted at the shower axis can be calculated, after taking account of Rayleigh and Mie scattering of the beam, as well as scattering of Cherenkov light into the detector. This is an iterative process, because the Cherenkov beam strength can only be calculated once the longitudinal profile is known.

3.2.2 Energy determination

The fluorescence technique effectively uses the atmosphere as a calorimeter, since it measures energy deposition by shower electrons. Having removed the Cherenkov component, one is left with the amount of fluorescence light as a function of atmospheric depth, which then yields the number of electrons as a function of depth. This then allows determination of the shower energy.

The calorimetric energy, $E_{\rm cal}$, is given by

$$E_{\rm cal} = \alpha \int_0^\infty N_e(X) dX, \tag{3.9}$$

where $N_e(X)$ is the shower longitudinal profile. α is the mean ionisation loss rate of shower electrons and is determined from CORSIKA simulations to be 2.19 MeV/(g/cm^2) [119], almost independent of the primary composition.

Eq. 3.9 only gives the total energy loss of electrons. It does not account for neutrinos, high–energy muons and nuclear excitations, which do not produce fluorescence. One must therefore apply a "missing energy" parametrisation to obtain E_0 from $E_{\rm cal}$. The study by Song *et al.* using CORSIKA simulations gives the following result [119]:

$$E_{\rm cal}/E_0 = (0.959 \pm 0.003) - (0.082 \pm 0.003) E_{\rm cal}^{-(0.150 \pm 0.006)}, \tag{3.10}$$

The amount of missing energy differs for proton and heavy nucleus initiated showers. When applying a correction to real data, one does not know the composition *a priori*, and an "average" correction such as Eq. 3.10 must be used. The systematic effect on energy of a composition–independent correction is less than 5% [119].

3.2.3 Composition

Fluorescence detectors can measure $X_{\rm max}$ directly, and this is perhaps the only composition sensitive parameter available for study with such an instrument. Having determined the longitudinal profile as described above, the depth of maximum

can be extracted by fitting to a functional form such as Eq. 2.10. Although the composition cannot be determined on an event–by–event basis, the mean composition can be inferred by comparing the measured mean $X_{\rm max}$ to the simulated $X_{\rm max}$ for different species, as a function of energy. A measured elongation rate which is different to the elongation rate for a homogeneous composition (according to a given model) indicates a changing composition. This sort of argument formed the basis of the conclusions in the Fly's Eye composition paper [54]. Unfortunately, it is very difficult to derive a numerical value for the mean mass number $\langle A \rangle$ from $X_{\rm max}$ measurements, since the separation between the compositional extremes (proton and iron) is not much larger than the experimental resolution [100].

Another possibility is that the composition can be inferred by studying the width of the $X_{\rm max}$ distribution as a function of energy. In the superposition approximation, the energy per nucleon of a nucleus with mass number A and energy E is E/A. Iron nuclei will therefore be subject to fewer fluctuations than protons, and will have a narrower $X_{\rm max}$ distribution. The problem with this approach is that the $X_{\rm max}$ distribution is not symmetric, and the concept of "width" is therefore ill–defined. Detector resolution can also be important. The Fly's Eye stereo analysis indicated that the $X_{\rm max}$ distribution for iron was affected considerably more by instrumental biases than was that for proton [120].

In the following two chapters we investigate the issue of composition more deeply, using data from the Fly's Eye and its successor, HiRes.

Chapter 4

Comparison of Fly's Eye and Akeno composition measurements

In this chapter I describe a re–analysis of data from the Utah Fly's Eye detector and the Akeno air shower array located near Tokyo, Japan. This study was motivated by the controversy that had arisen in the field after the publication of the AGASA composition results in 1995 [55].

4.1 Detector Description

A brief description of the two experiments is included only for completeness. Fly's Eye triggering and reconstruction are discussed in the PhD thesis of Green [121]. Triggering and reconstruction for the A1 array are covered in Refs. [122, 123]. The AGASA experiment is described in Ref. [32].

4.1.1 The Fly's Eye

The Fly's Eye detector [34], situated on Dugway Proving Grounds in the Western Utah desert, operated in monocular mode (single fluorescence eye) from 1981 to 1986, at which point a second site, 3.4 km away, was installed. The two eyes (FE1 and FE2) operated in stereo mode until 1993, when the detector was shut down in preparation for the construction of HiRes.

Each Fly's Eye site consisted of a number of spherical mirrors focussing fluorescence light onto a cluster of either 12 or 14 PMTs of circular cross section, each with a 5.5° field of view, and with Winston cones employed to allow hexagonal close packing. The mirrors and associated PMT clusters were housed inside

parameter	FE1	FE2
longitude	112°50′9.25″	112°48′59.07″
latitude	40°11′47.78″	40°13′18.00″
height above sea level	1593 m	1459 m
atmospheric depth	852 g/cm^2	867 g/cm^2
number of mirrors	67	36
number of PMTs	880	464
PMT peak quantum efficiency	0.17	0.26
mirror diameter	1.575 m	1.575 m
focal length	1.52 m	1.52 m
mirror obscuration	13%	13%
Winston cone aperture	6.57×10^{-3} sr	6.57×10^{-3} sr
Winston cone efficiency	0.8	0.8
Peak filter transmission (350 nm)	0.81	0.81

TABLE 4.1. Physical parameters of the Fly's Eye detectors. Adapted from Ref. [124].

motorised 2.44 m diameter "garbage cans" which pointed downwards during periods of inactivity to protect them from the elements. FE1 viewed the whole night sky, and FE2 viewed the half of the sky in the direction of FE1 to maximise the stereo aperture. The physical parameters of the detector stations are given in Table 4.1. With the exception of the PMT preamplifier board, all electronics were housed inside a central facility. These included circuits for triggering, pulse integral measurement and arrival time latches.

Several significant changes were made to the Fly's Eye in the years that it was operational. This meant that the data analysis had to be divided into six "epochs". For example, UV filters were installed in front of the PMTs in 1986, increasing the event rate by a factor of three [117].

The data acquisition sequence for a single Fly's Eye is illustrated in Fig 4.1.

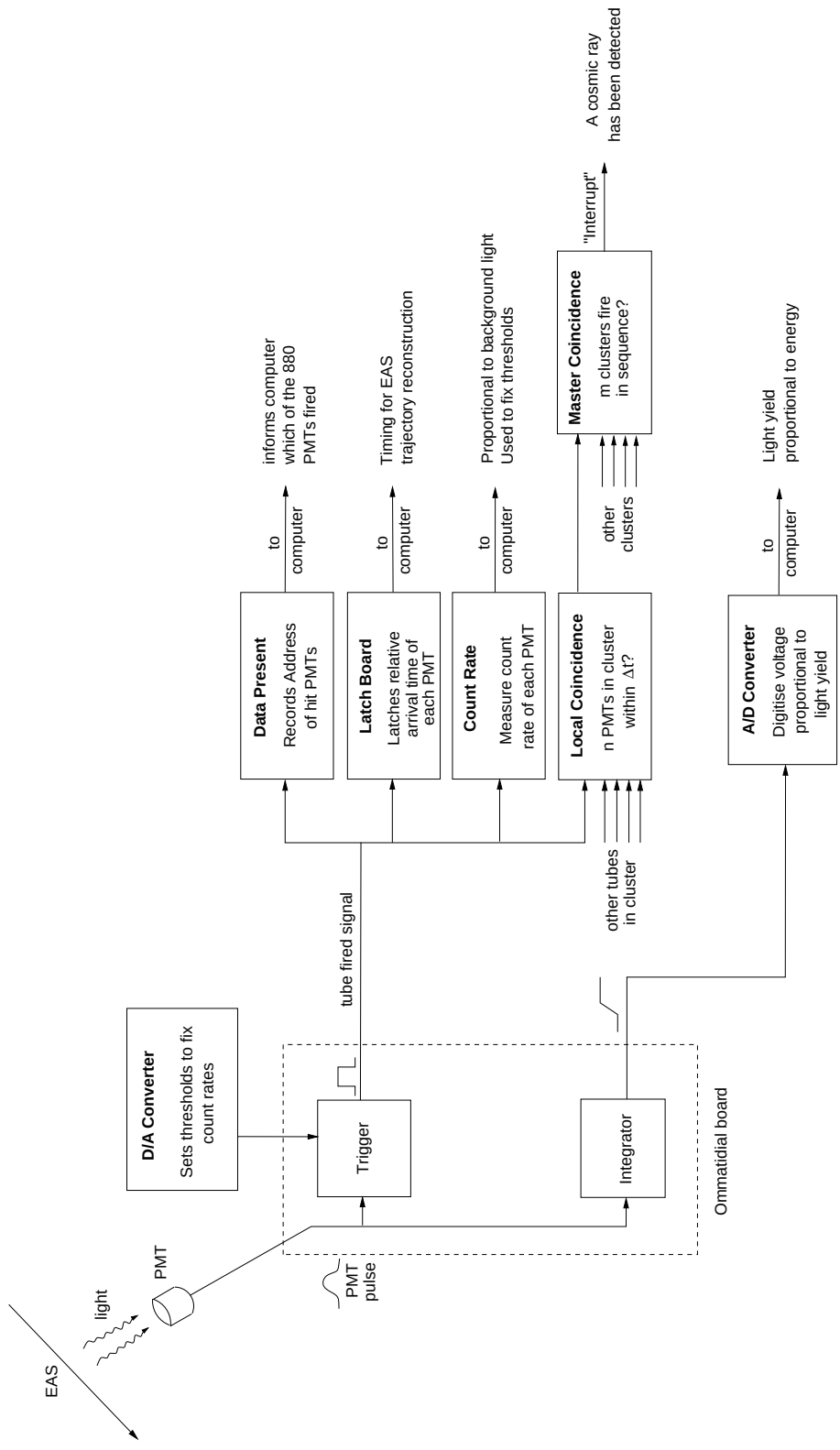

FIGURE 4.1. Block diagram of Fly's Eye data acquisition. Adapted from Ref. [34].

In addition to the scheme outlined there, each FE1 trigger was accompanied by the transmission of an infrared flash (intersite flasher) in the direction of FE2. If FE2 had also been triggered, the event was recorded as a candidate stereo event. Event times were recorded by WWVB clocks. These receive the current time (in UTC) via a radio broadcast, and are accurate to within ± 1 ms.

Calibration of the detector comprised several elements. This included the use of surveying techniques to determine the true pointing directions of each mirror, periodic measurements of the absolute reflectivity of each mirror, laboratory measurements of PMT quantum efficiency and filter transmission before deployment, and nightly electronic calibration during each run period. The section of the atmosphere viewed by the detector was monitored using a nitrogen laser fired at several different angles and from various positions. Xenon flash bulbs firing vertically were also employed for this purpose. These "upward going showers" were valuable in determining the geometrical reconstruction accuracy of the detector [34].

Event reconstruction was done in a similar manner to that described in Section 3.2, with genuine cosmic ray events (downward going) distinguished from lasers and flashers (upward going) using timing information. Once reconstructed, the data were subjected to quality cuts (see Huang [124] for details).

A comprehensive detector Monte Carlo was developed to estimate the instrumental effect on energy and $X_{\rm max}$. For the stereo data set discussed here, the $X_{\rm max}$ resolution, defined as the standard deviation of the distribution of $(X_{\rm max}^{\rm input} - X_{\rm max}^{\rm recon})$, was 65 g/cm^2, with a systematic error that was estimated to be ± 20 g/cm^2 at the most [125]. The estimated energy resolution $((E^{\rm input} - E^{\rm recon})/E^{\rm input})$ was 25%, and the angular resolution (angle between input and reconstructed directions) was 2°, rising to 4° at the highest measured energies [117].

4.1.2 Akeno arrays

A group led by the University of Tokyo has operated several ground arrays at Akeno, 100 km west of Tokyo, since 1979. The first array, known as A1, consisted of 156 scintillators of 1 m^2 area spread over 1 km^2. Eight 25 m^2 muon detectors

each comprising 50 proportional counters [126] were also employed from 1981 onwards. The muon energy threshold for these counters was $E_\mu \geq 1.0 \times \sec\theta$ GeV. The estimated uncertainty in reconstruction of the shower size N_e was 20%, and the uncertainty in muon size (N_μ) reconstruction was 20% for events in which the core landed inside the bounds of the array. The array triggered if 7 or more counters out of 37 mutually separated by 120 m triggered within the gate time. The analysis method for A1 is described in Ref. [122].

In 1984, a second array covering 20 km^2 and known as A20 was constructed, such that the A1 array was located at one of its corners. A20 consisted of 19 scintillators of 2.2 m^2 area and 4 of 1.0 m^2 area, separated by approximately 1 km. An array trigger was formed if 6 or more counters fired within the gate time, at which point there was a simultaneous readout of data from any triggered A1 counters. If any muon counters were hit, these were used in the analysis.

For A1, the total electron number N_e is used as an energy estimator. The relationship between N_e and E is [123]

$$E = 3.9 \times 10^{15} \left(\frac{N_e}{10^6} \right)^{0.9} \text{ eV}. \tag{4.1}$$

A1 and A20 no longer exist as independent entities. In 1990 they were incorporated into the A100 array, also known as the Akeno Giant Air Shower Array (AGASA) [32]. A100 composes 111 scintillators of 2.2 m^2 area, spaced 1 km apart and covering 100 km^2. It originally employed 14 muon counters of similar type to those used in A1. This number was increased to 27 in 1993. These detectors operated at a lower muon energy threshold, namely $0.5 \times \sec\theta$ GeV. The array is divided into four "branches", one of which (the Akeno Branch) contains A1 and A20. It is depicted in Fig. 4.2.

An array trigger is registered for A100 if five neighbouring counters are hit within the gate time of 25 μs [32]. A muon station will self–trigger if two proportional counters within it, not necessarily adjacent to each other, fire at the same time as an array trigger. A muon station which does not meet this requirement

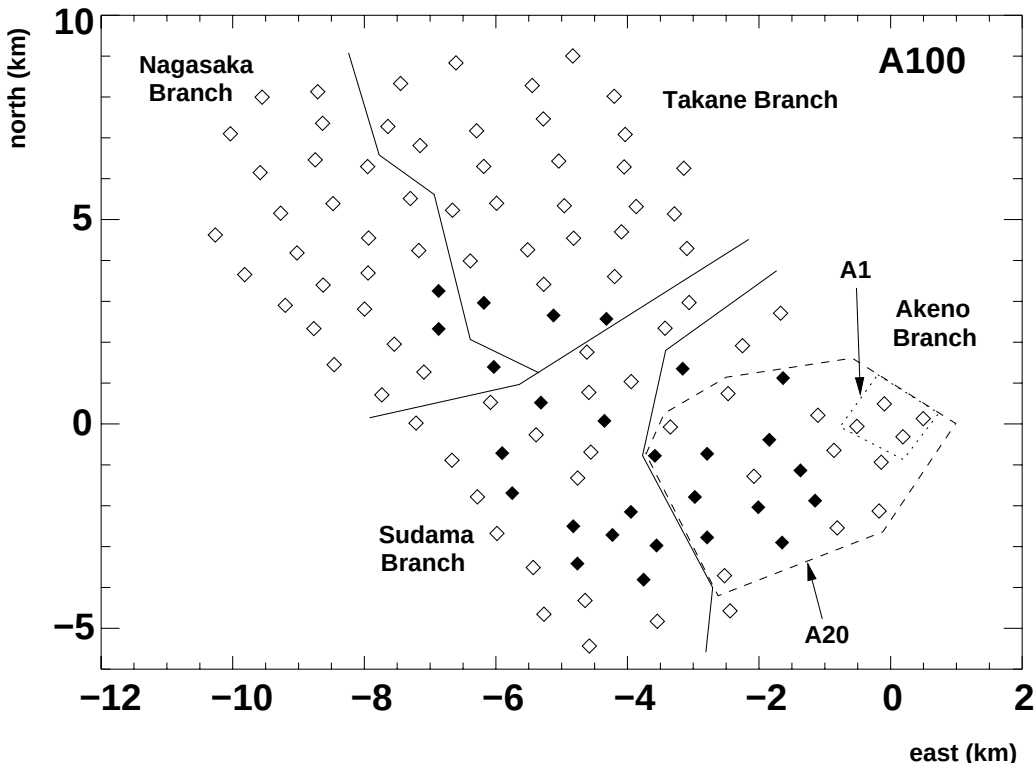

FIGURE 4.2. The layout of the A100 array at Akeno. The centre of A1 is the origin of the coordinate system. Open diamonds are scintillation counters, and closed ones are muon detectors. The boundaries of A1 and A20 are indicated. Each branch of A100 (separated by solid lines) has its own data acquisition centre, but these are not shown here. Nor is cabling between detectors.

may still undergo an "assisted trigger" if the scintillator at the same location records a signal above threshold [127]. An event is kept for further analysis if it satisfies the scintillator trigger requirement and if there is at least one self–triggered or assisted–triggered muon station. In the latter case, it may be that no muons are detected.

Because of the relative sparseness of A100, the lateral distribution is not sampled well enough to measure either N_e or N_μ. Instead, $S(600)$ is used as an energy estimator, and $\rho_\mu(600)$ is used as an indicator of composition. The measured particle densities are used in a maximum likelihood fit to determine the core location and normalisation of the lateral distribution function, Eq. 2.8. Once these

parameters are known, $S(600)$ is calculated using Eq. 2.8. The muon density ρ_μ can be calculated by two methods. The first is the so–called "on–off method" and assumes that the number of particles impinging on each counter is Poisson–distributed [55]. If n counters are hit out of m available, then the muon density is given by

$$\rho_\mu = -\frac{m \ln(1 - n/m)}{\text{Area}}, \tag{4.2}$$

where Area is the total area of the detector. This method works well for vertical showers if $n \ll m$. An alternative method is to calculate the "analogue density" by dividing the total energy loss in a counter by the average energy loss of a vertically incident muon, and then dividing by the detector area.

The relationship between energy and $S(600)$ for Akeno is [110]

$$E = 2.0 \times 10^{17} S_0(600), \tag{4.3}$$

where $S_0(600)$ is the observed density converted to the density that would be expected for a vertical shower, using the relation [128]

$$S_\theta(600) = S_0(600) \exp\left[-\frac{X_0}{500}(\sec\theta - 1) - \frac{X_0}{594}(\sec\theta - 1)^2\right], \tag{4.4}$$

where X_0=920 g/cm^2 is the atmospheric depth at Akeno and θ is the zenith angle of the shower.

4.2 Consistency between the experiments

The muon data published by the Akeno group in 1995 seemed to suggest that the EHE composition was predominantly heavy and unchanging with energy [55]. This was at odds with the result from Fly's Eye (see Fig. 4.3), namely that the composition changed rather abruptly from a predominantly heavy one (iron) at 3×10^{17} eV to become entirely light (protonic) at 10^{19} eV [54].

There are reasons for suspecting that the disagreement between the two experiments is due to a difference in the hadronic models used to interpret the data.

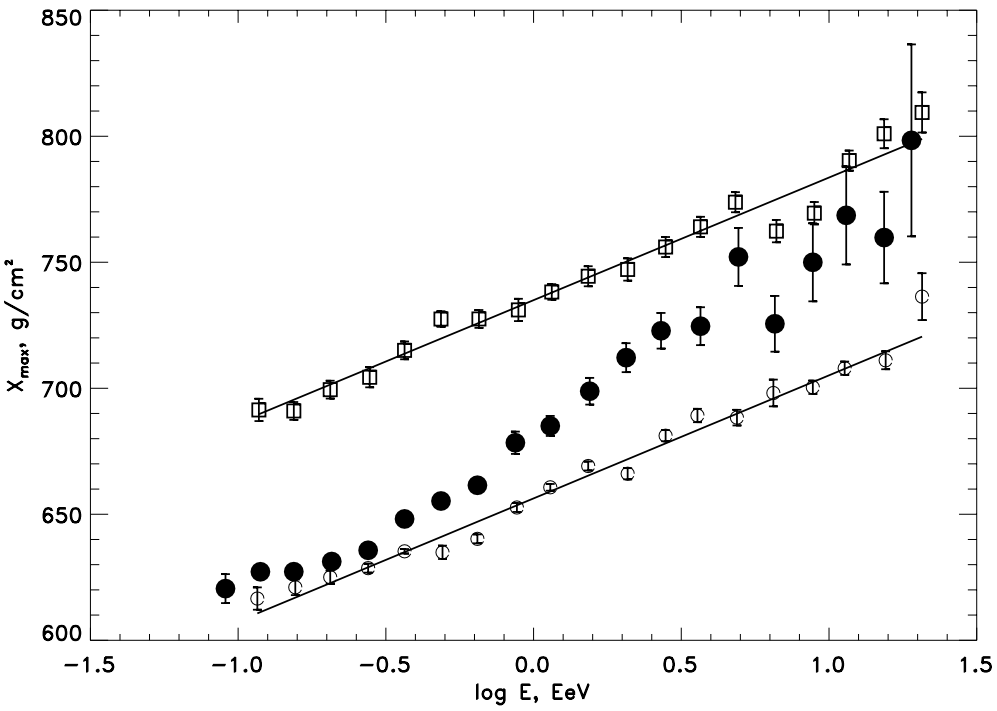

FIGURE 4.3. $X_{\max}$ as a function of energy, as measured by the Fly's Eye [54]. Data are indicated by filled circles, while the predictions of the KNP model for iron nuclei (empty circles) and protons (squares) are also shown. The solid lines are fits to the simulation points. All error bars are statistical.

The Fly's Eye conclusion was based on a comparison of their $X_{\max}$ data to Monte Carlo simulations which used a hadronic event generator based on the KNP [56] model. This model incorporates extreme violations of Feynman scaling in the fragmentation region. Akeno, on the other hand, compared the muon content of showers simulated using the 1992 version of MOCCA to their $\rho_\mu(600)$ data. As mentioned previously (see section 2.4.1), the internal hadronic model in MOCCA features scaling and an inelasticity which does not change with energy. The simulated shower development will therefore be noticeably different if this model is used. For example, the elongation rate for scaling models is approximately 70 g/cm^2, whereas an extreme model such as KNP gives an elongation rate of approximately 50 g/cm^2. This fact alone would considerably weaken the conclusion

in the Fly's Eye paper.

To eliminate some of the confusion surrounding these conflicting results, a re–analysis of Fly's Eye and Akeno data was performed [129]. The hope was that, by being consistent in the choice of hadronic model, consistency between the two experiments would be attained. The Fly's Eye data from Ref. [54], the A1 results from Ref. [55] and the A100 results from Ref. [130] were used in this analysis.

4.2.1 Investigation of detector biases

We used the MOCCA cascade simulator with the SIBYLL [96] hadronic event generator (section 2.3.2), at a thinning level of 10^{-6}. SIBYLL was chosen for its ease of availability and the fact that an interface to MOCCA had already been written. SIBYLL does feature scaling violations, but they are not as severe as those in the KNP model.

For the $X_{\max}$ part of the study, 80 vertical showers were generated at fixed energies each half–decade interval from 10^{17} to $10^{19.5}$ eV inclusive. This energy range covers the overlap between the two experiments, apart from the region above the GZK cutoff where data are still too sparse to yield useful information about the mean behaviour of composition parameters. An additional technical problem arose when we attempted to generate 10^{20} eV events using MOCCA/SIBYLL. In almost every case, the program would crash before completing the simulation of one shower. We were unable to determine the source of the problem, but can only suspect that it is related to the interface between the two codes.

In Refs. [55] and [130], the AGASA collaboration have scaled the muon densities recorded by A100 down by a factor of 1.4 to account for the fact that A1 has a higher muon energy threshold than A100 (1 GeV *cf.* 0.5 GeV). This is done to allow comparison of the two data sets to their simulations, which were performed with a threshold of 1 GeV. The correction factor is based on an experimental measurement at 10^{17} eV [131], but we have found from our simulations that the ratio $N_\mu(>1\text{GeV})/N_\mu(>0.5\text{GeV})$ is composition– and energy–dependent. That this is the case is easily seen by realising that this ratio is tied to $X_{\max}$. Showers that

develop early will have a softer spectrum of parent pions and therefore a larger number of lower energy muons. At 10^{17} eV, we found that the ratio was 1.4 for iron and 1.2 for protons. These ratios decrease with energy. We therefore thought it better to compare A1 and A100 data separately to 1.0 GeV and 0.5 GeV simulations, respectively. To this end we used the previously generated showers for the A1 study, and produced additional showers with a 0.5 GeV muon threshold for the A100 study. These were generated at a zenith angle of $\theta = 23°$, which corresponds to the mean $\sec\theta$ of 1.09 for the A100 data set [55].

When comparing the results of simulations with experimental data, it is crucial to take account of possible experimental biases. Ideally, a detector Monte Carlo should be used to simulate triggering and data acquisition, and the resultant "fake" events passed through the same reconstruction procedure as for the real data. In the case of Fly's Eye, such an analysis is complicated considerably by the change over time of the detector configuration. Several different detector epochs would have to be simulated for complete rigour. This has been done on many occasions previously, and we used the results of one such investigation by Ding *et al.* [132] to apply corrections to the simulated MOCCA/SIBYLL $X_{\max}$ results. That study generated proton and iron showers with an E^{-3} differential spectrum. These were then passed through a detailed detector simulation and reconstructed using the standard Fly's Eye analysis routines. This process takes account of effects such as triggering bias (for example, there is a small bias against the detection of iron showers near the Fly's Eye threshold of 10^{17} eV) and small systematic shifts in $X_{\max}$ introduced by the reconstruction procedure.

Ding *et al.* [132] give values for the input and reconstructed values of $X_{\max}$ for detector epoch 3. We have used these results to parametrise, in terms of $X_{\max}$ and energy, the shift in $X_{\max}$ due to reconstruction. We perform a bilinear fit to the expression

$$\begin{aligned} \Delta X_{\rm max} &= X_{\rm max}^{\rm recon} - X_{\rm max}^{\rm in} \\ &= a X_{\rm max}^{\rm in} + b \log E + c, \end{aligned} \tag{4.5}$$

where $X_{\rm max}^{\rm recon}$ is the reconstructed $X_{\rm max}$, and $X_{\rm max}^{\rm in}$ is the input value. Here E is in units of eV. The fit yields the following coefficients:

$$\begin{aligned} a &= 6.84 \pm 0.599 \\ b &= -0.204 \pm 0.00660 \text{ g/cm}^2 \\ c &= 39.7 \text{ g/cm}^2. \end{aligned} \tag{4.6}$$

Although the input $X_{\rm max}$ values in the Ding *et al.* study are slightly different to ours, we feel confident applying this parametrisation to our Monte Carlo data because of its two–dimensional nature. In addition to the shift from Eq. 4.6, we shift the simulation points down by a further 20 g/cm^2. This was done in the original Fly's Eye composition study [120], and is required here to ensure that the real data at 10^{17} eV do not imply a composition heavier than iron. A 20 g/cm^2 shift is entirely consistent with possible systematic effects in the Fly's Eye experiment [120].

The AGASA analysis is rather straightforward from the point of view of investigating triggering biases. Event reconstruction for simulated showers was complicated by the fact that thinning–induced fluctuations in MOCCA/SIBYLL lead to a deficit of particles far from the core, thus limiting our ability to fit the lateral distribution. Decreasing the thinning to 10^{-7} or 10^{-8} may have alleviated the problem somewhat, but would have been rather expensive in terms of CPU time. In the interests of speed, we opted not to follow this course. Instead, we assumed that the array correctly measures particle densities, and concentrated on the issue of triggering bias.

For both the A1 and A100 arrays, we proceeded in the following way. For each MOCCA/SIBYLL simulated shower, the muon lateral distribution and the lateral

distribution expected for 5 cm thick scintillators were obtained. Random core locations were generated for each shower, and the muon and scintillator densities were statistically fluctuated. This was done by multiplying the detector area by the input density and treating the result as the mean of a Poisson distribution from which the "measured" number of particles was sampled. The trigger conditions for both the scintillator detectors and muon detectors, as described above, were then applied.

The A1 study reveals that there is no compositional triggering bias, for either the scintillator or muon detector parts of the array. The triggering efficiency is the same for protons and iron at all energies. On the other hand, we find for A100 that iron showers trigger the array preferentially to protons, as can be seen from Fig. 4.4.

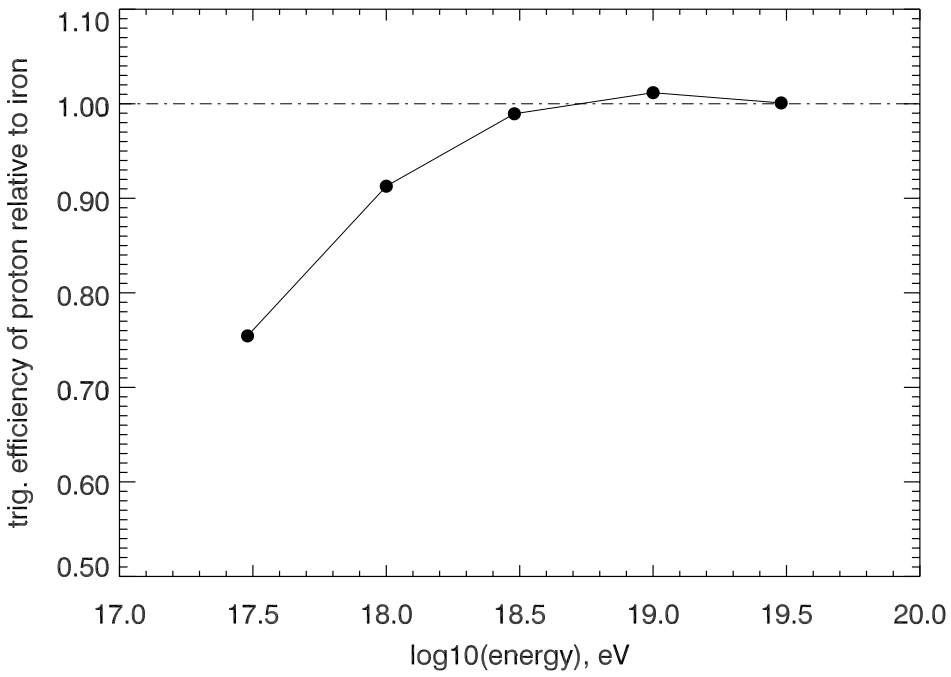

FIGURE 4.4. The simulated A100 triggering efficiency for protons relative to iron (proton efficiency divided by iron efficiency). Below 3×10^{18} eV, a bias is evident.

For each array trigger in our A100 study, we calculated $\rho_\mu(600)$ in exactly

the same way as done by the AGASA group. The core distance for each self–or assisted–triggered muon station was calculated. If this lay between 500 m and 800 m, the measured density was scaled to that at 600 m using the AGASA muon lateral distribution function, Eq. 2.20. Each triggered muon station thereby contributed to the mean $\rho_\mu(600)$ for a given $S(600)$ bin. Note that some showers would contribute a single zero to the average, these being assisted–triggered events where the only triggered muon station has a measured density of zero.

In the following section, we plot the mean $\rho_\mu(600)$ as a function of energy for A1 and A100 against the results of the above MOCCA/SIBYLL simulations. The energy scale is derived using the relation Eq. 4.3. Since the showers generated for the A1 study were all vertical, $S(600) = S_0(600)$. On the other hand, the values of $S(600)$ from the A100 simulations had to be corrected to the equivalent vertical value using the relation Eq. 4.4. We found that the energy derived using Eq. 4.3 tended to underestimate the true energy, *i.e.* it was lower than the primary energy input to MOCCA/SIBYLL. The deficit was around 30% for the vertical showers used for the A1 analysis, and around 20% for the inclined showers used for the A100 study. That there was a discrepancy is perhaps unsurprising, given the difference in models used to derive the original relationship between $S(600)$ and energy. The model dependence was noted in the original Akeno paper on this subject [110].

Recently the AGASA group have performed a comparison of their data to CORSIKA simulations, using both SIBYLL and QGSJet. They derive a new energy conversion relation

$$E = 2.15 \times 10^{17} (S_0(600))^{1.015}, \tag{4.7}$$

which has an uncertainty of approximately 10% associated with the model dependence of $S(600)$ [133].

4.2.2 Composition results

Having applied the correction implied by Eq. 4.6 to the input $X_{\max}$ values from MOCCA/SIBYLL, we are in a position to compare the simulated values to the Fly's Eye data. The data are displayed alongside the MOCCA/SIBYLL simulation points in Fig. 4.5 below.

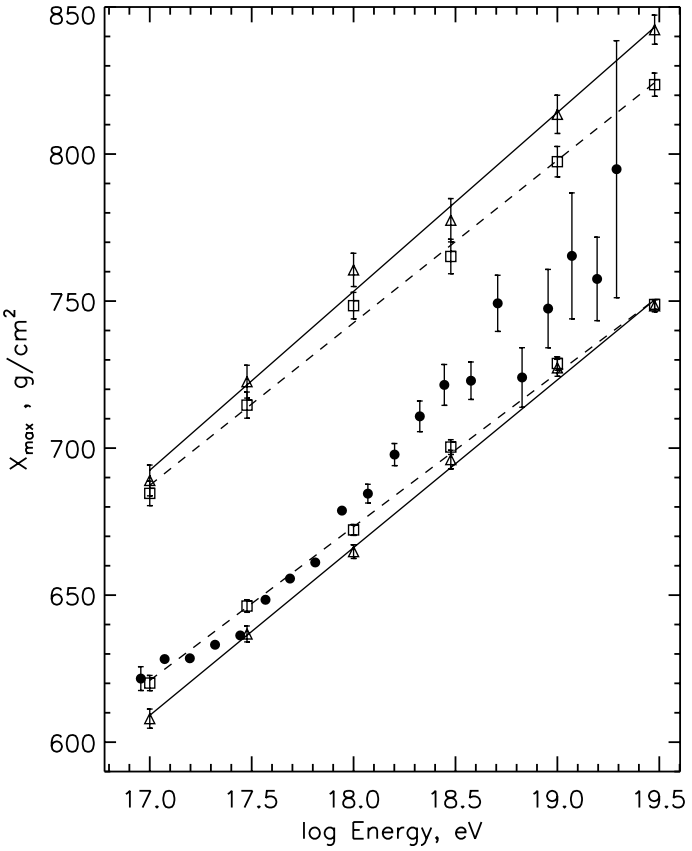

FIGURE 4.5. The Fly's Eye data, this time plotted alongside simulation results from MOCCA/SIBYLL. Solid lines (triangles) are fits to the input simulation data, while dashed lines (squares) are fits to the same data after instrumental effects have been taken into account. The 20 g/cm^2 shift discussed in the text has been applied here.

Assuming a two–component composition model, *i.e.* a primary beam containing only protons and iron nuclei, we can make a quantitative assessment of the

composition over the energy range of interest. This is done by calculating the "fraction of iron", which is derived in the following way. The mean $X_{\rm max}$ at a given energy is given by a weighted average of the proton and iron $X_{\rm max}$ values at that energy. Writing the fraction of iron as $F_{\rm i}$, we have

$$X_{\rm max} = F_{\rm i} X^{\rm i}_{\rm max} + (1 - F_{\rm i}) X^{\rm p}_{\rm max}, \tag{4.8}$$

where $X^{\rm p,i}_{\rm max}$ are the simulated values for proton and iron respectively. Rearranging this for $F_{\rm i}$ gives

$$F_{\rm i} = \frac{X_{\rm max} - X^{\rm p}_{\rm max}}{X^{\rm i}_{\rm max} - X^{\rm p}_{\rm max}}. \tag{4.9}$$

We use this equation to plot the fraction of iron as a function of energy for the Fly's Eye data. For each point, $X^{\rm p,i}_{\rm max}$ are calculated from a fit to the simulation points. The error in $F_{\rm i}$ is calculated according to

$$\sigma_{F_{\rm i}} = \sqrt{\left(\frac{\partial F_{\rm i}}{\partial X_{\rm max}}\right)^2 \sigma^2_{X_{\rm max}} + \left(\frac{\partial F_{\rm i}}{\partial X^{\rm i}_{\rm max}}\right)^2 \sigma^2_{X^{\rm i}_{\rm max}} + \left(\frac{\partial F_{\rm i}}{\partial X^{\rm p}_{\rm max}}\right)^2 \sigma^2_{X^{\rm p}_{\rm max}}}. \tag{4.10}$$

$\sigma_{X_{\rm max}}$ is the statistical error in the Fly's Eye data point, and $\sigma_{X^{\rm p,i}_{\rm max}}$ are the statistical errors in the simulation values resulting from the fit.

In Fig. 4.6 below we plot the fraction of iron as a function of energy for the Fly's Eye data. The errors are those derived using Eq. 4.10. The implication is that, under the SIBYLL model, the composition changes from 100% iron at 3×10^{17} eV to a mixed composition ($\sim 50\%$) at the highest energies. This is not as extreme as the change implied by the KNP model (see Fig. 4.3).

In Figs. 4.7 and 4.8 we show the A1 and A100 data respectively, with the MOCCA/SIBYLL predictions plotted on the same graphs. A simple interpretation of these plots is that for A1, the composition changes from mostly iron at 3×10^{17} eV to some lighter mix at higher energies. A similar conclusion is reached for A100. We can put this interpretation on a more quantitative footing by calculating the fraction of iron for the two experiments.

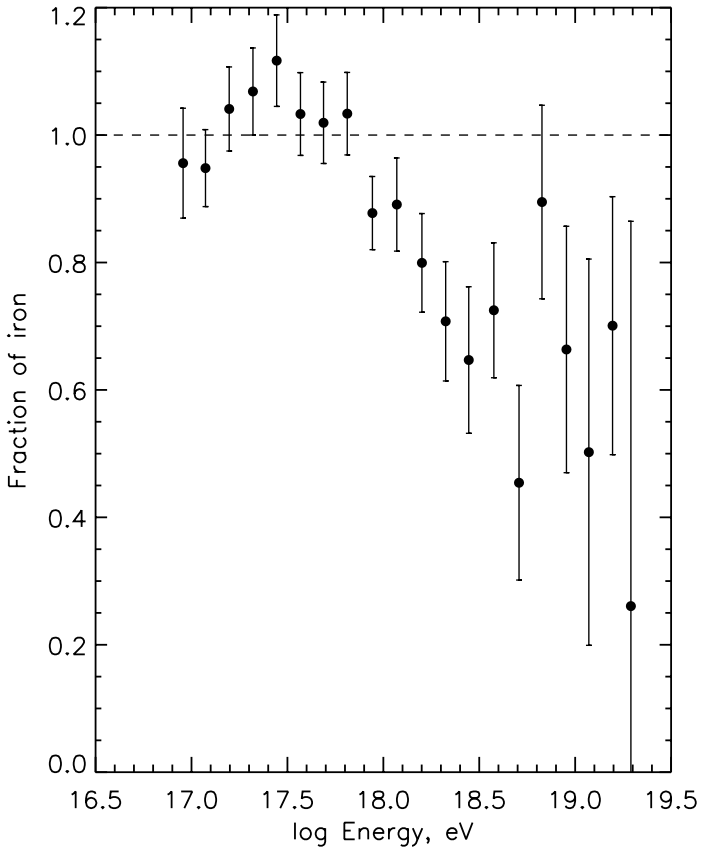

FIGURE 4.6. Fraction of iron from Fly's Eye data. Errors are calculated as described in the text.

Because A1 is free of triggering bias, the fraction of iron for A1 data can be calculated in a similar way to that for Fly's Eye data, substituting $\rho_\mu(600)$ for $X_{\max}$. However, for A100 the triggering bias must be taken into account. This is done in the following way. Suppose that the efficiency for recording an array trigger is $\epsilon_{\rm i}$ for iron showers and $\epsilon_{\rm p}$ for proton showers ($0 \leq \epsilon_{\rm i,p} \leq 1$). Some of these events will have no hit muon counters, as per the assisted triggering scheme described above. This must be taken into account. Call the efficiency for a zero–muon event (given an array trigger) $\epsilon_{\rm i}^0$ and $\epsilon_{\rm p}^0$ for iron and protons, respectively. Then the probability of recording an event with muon information is

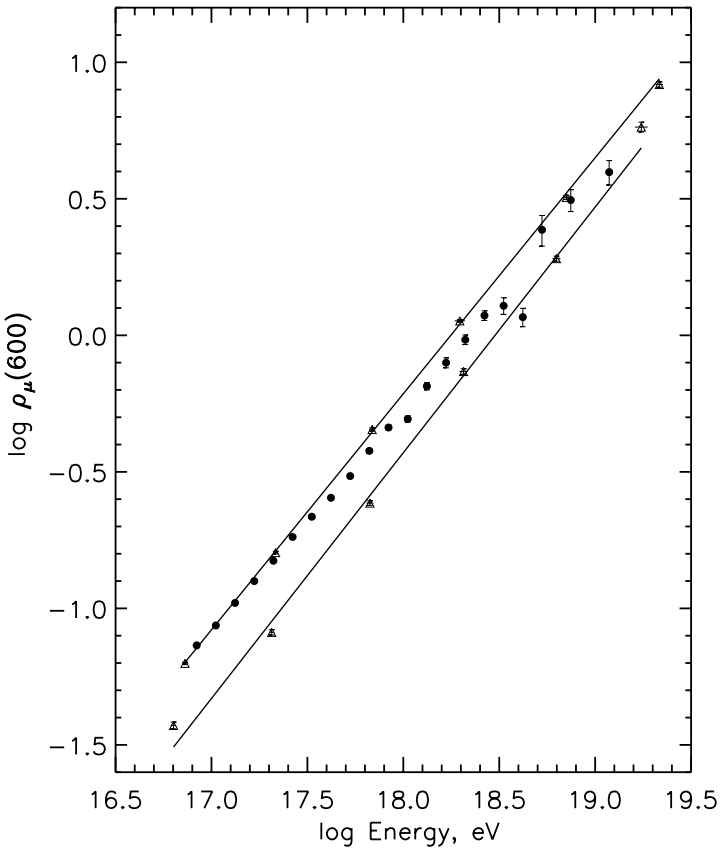

FIGURE 4.7. $\log_{10}\rho_\mu(600)$ as a function of $\log_{10}E$ for the A1 experiment (filled circles). Also shown are the predictions of MOCCA/SIBYLL for iron (top) and proton (bottom) showers. The lines are fits to the simulation points (triangles). Simulations were done at half–decade intervals from 10^{17} eV to 3×10^{19} eV inclusive.

$$\begin{aligned} P_j &= P(\text{array trigger}) \times P(\text{at least one hit muon counter}) \qquad (4.11)\\ &= P(\text{array trigger}) \times (1 - P(\text{no muons}))\\ &= \epsilon_j(1-\epsilon_j^0), \end{aligned}$$

where j is either p or i. The measured value of $\rho_\mu(600)$ at fixed $S(600)$ can therefore be written as a weighted sum of the simulated values for protons and iron nuclei, *i.e.*

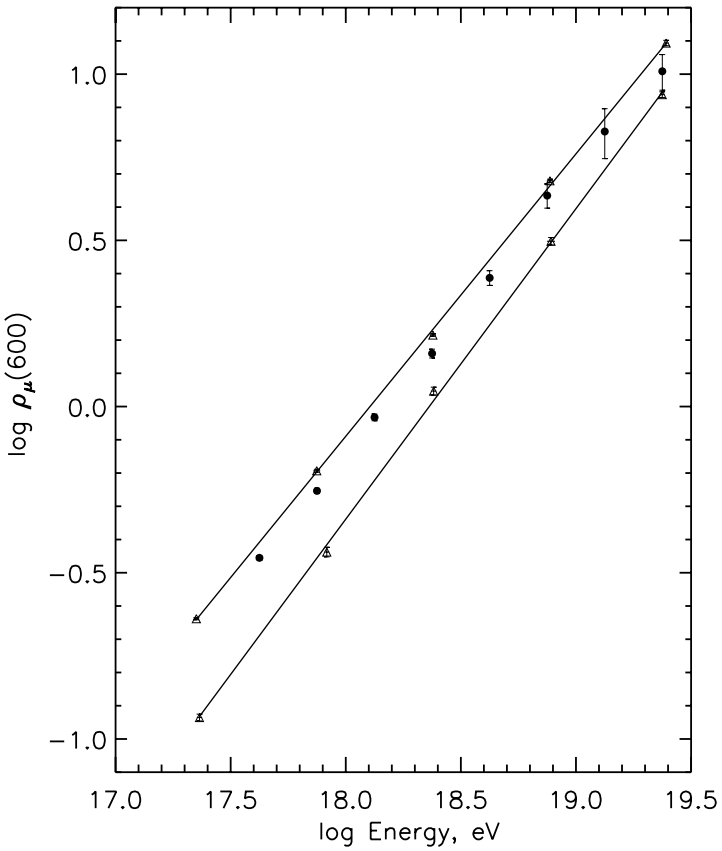

FIGURE 4.8. The same as Fig. 4.7, but for A100 data from Ref. [130], with the 1.4 factor removed. Simulation points are at half–decade intervals from 3×10^{17} eV to 3×10^{19} eV inclusive.

$$\rho_\mu(600) = \sum_{j=\mathrm{p,i}} F_j P_j \rho_j, \tag{4.12}$$

where F_j is the fraction of species j present in the primary beam, and ρ_j is the muon density for species j. F_j differs from the fraction measured by the array, due to the array triggering efficiency, by a factor ϵ_j. We therefore have the normalisation condition $F_\mathrm{i}\epsilon_\mathrm{i} + F_\mathrm{p}\epsilon_\mathrm{p} = 1$. Using this in Eq. 4.12 with the definition Eq. 4.12 yields F_i, the fraction of iron in the primary beam:

$$F_{\rm i} = \frac{\rho_\mu(600) - (1-\epsilon_{\rm p}^0)\rho_{\rm p}}{\epsilon_{\rm i}[(1-\epsilon_{\rm i}^0)\rho_{\rm i} - (1-\epsilon_{\rm p}^0)\rho_{\rm p}]}. \tag{4.13}$$

The statistical error in $F_{\rm i}$ can be calculated in the usual way, *i.e.*

$$\sigma_{F_{\rm i}} = \sqrt{\left(\frac{\partial F_{\rm i}}{\partial \rho_\mu}\right)^2 \sigma^2_{\rho_\mu} + \left(\frac{\partial F_{\rm i}}{\partial \rho_{\rm i}}\right)^2 \sigma^2_{\rho_{\rm i}} + \left(\frac{\partial F_{\rm i}}{\partial \rho_{\rm p}}\right)^2 \sigma^2_{\rho_{\rm p}}}, \tag{4.14}$$

where $\rho_\mu(600)$ has been written as ρ_μ for convenience, σ_{ρ_μ} is the statistical error in the measured ρ_μ, and $\sigma_{\rho_{\rm p}}$ and $\sigma_{\rho_{\rm i}}$ are the errors in the Monte Carlo values resulting from the fit described above. For reasons of brevity, the explicit expression for $\sigma_{F_{\rm i}}$ is not included here.

The fraction of iron from the two Akeno experiments is shown in Fig. 4.9. As for the Fly's Eye, the data interpreted in the light of the SIBYLL model suggest a change in composition from 100% iron near 10^{17} eV to $\sim 50\%$ iron at the highest energies. It is encouraging that the results from A1 and A100 are consistent, given that they are two different experiments with different muon energy thresholds and analysis methods.

By way of comparison, we plot the fit to the A1 points in Fig. 4.9 on top of the Fly's Eye points from Fig. 4.6. This is shown in Fig. 4.10 below. Several points are worth noting:

- Both AGASA and Fly's Eye support a heavy composition near 10^{17} eV.
- Both experiments require a change to a significantly lighter composition (55–70% iron in the two–component model) in the energy range up to 3×10^{18} eV. Above this energy, statistical uncertainties preclude a definitive statement.
- The way in which the composition changes is different in the two experiments. The change in the Akeno data occurs at a lower energy. It is possible that this is due to the energy calibration. For the purposes of illustration, we assume that AGASA underestimates energy by 30%. We have seen from

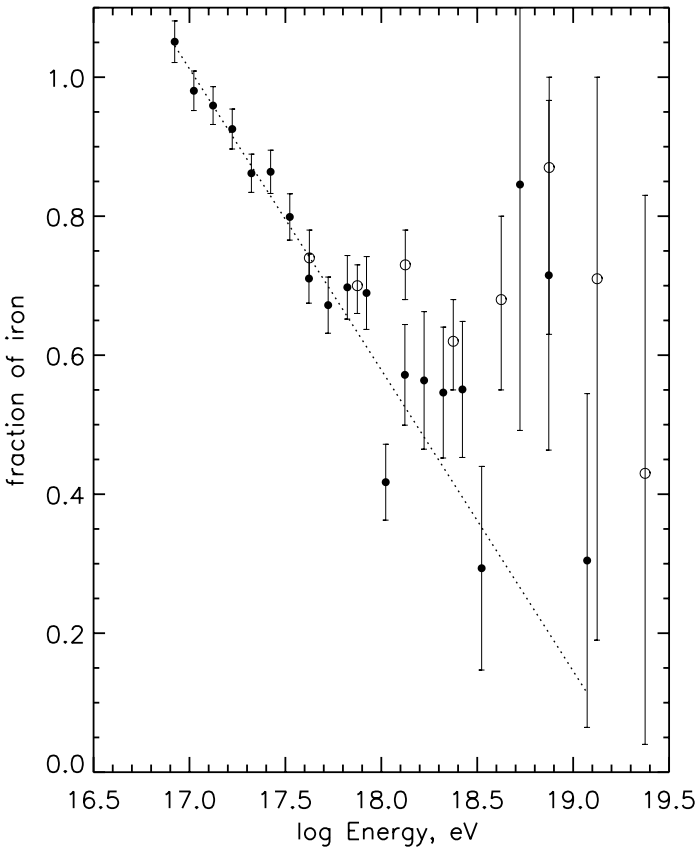

FIGURE 4.9. The fraction of iron in the primary beam implied from A1 data (filled circles) and A100 data (open circles). Error bars are a combination of statistical uncertainties in the data and those resulting from the fit to the simulation points, as discussed in the text. The dotted line is a fit to the A1 points.

MOCCA/SIBYLL simulations that this is the shortfall if the AGASA energy conversion relation is used. Of course, we could just as easily assume Fly's Eye overestimates energy by this amount. This assumption allows us to shift the A1 line of Fig. 4.9, thereby giving slightly better agreement between the two experiments.

- It is possible that the systematic error in $X_{\max}$ assignment by Fly's Eye may be as large as 30 g/cm^2, rather than the 20 g/cm^2 assumed above and in the original analysis of Gaisser *et al.* [120]. Under this assumption, the Fly's

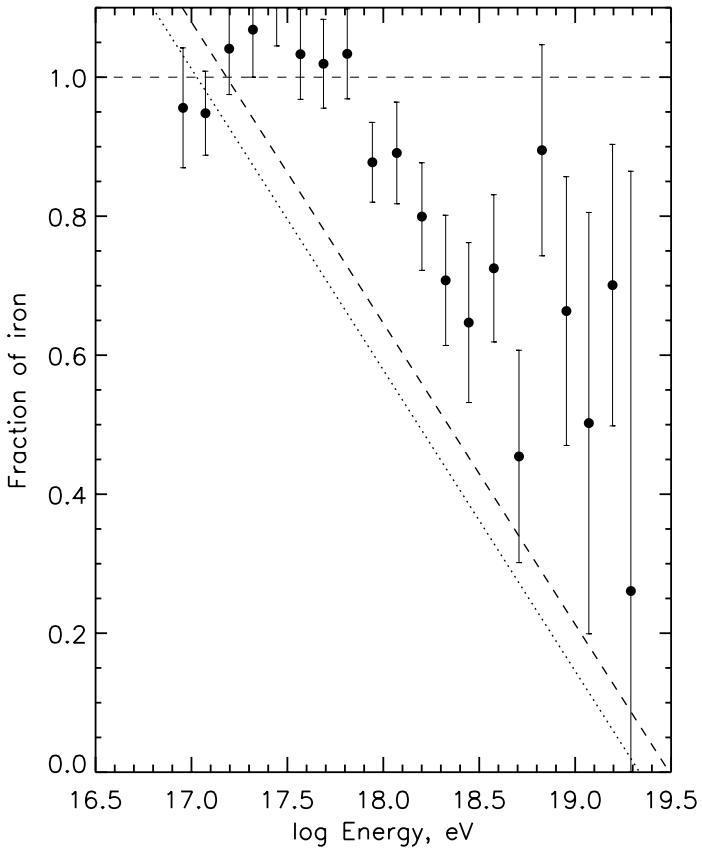

FIGURE 4.10. The fit to the A1 fraction of iron (Fig. 4.9), plotted alongside the Fly's Eye fraction of iron (Fig. 4.6). The dashed line is the A1 fit shifted under the assumption that the A1 analysis underestimates energy by 30% (see discussion in the text).

Eye fraction of iron shifts such that, if the 30% shift in the A1 energy is also applied, the results are brought into better agreement yet (Fig. 4.11.

- It is also possible that there are no experimental systematic problems with either energy or $X_{\max}$, and that the difference between the experimental results is due to the underlying physics assumptions in SIBYLL.

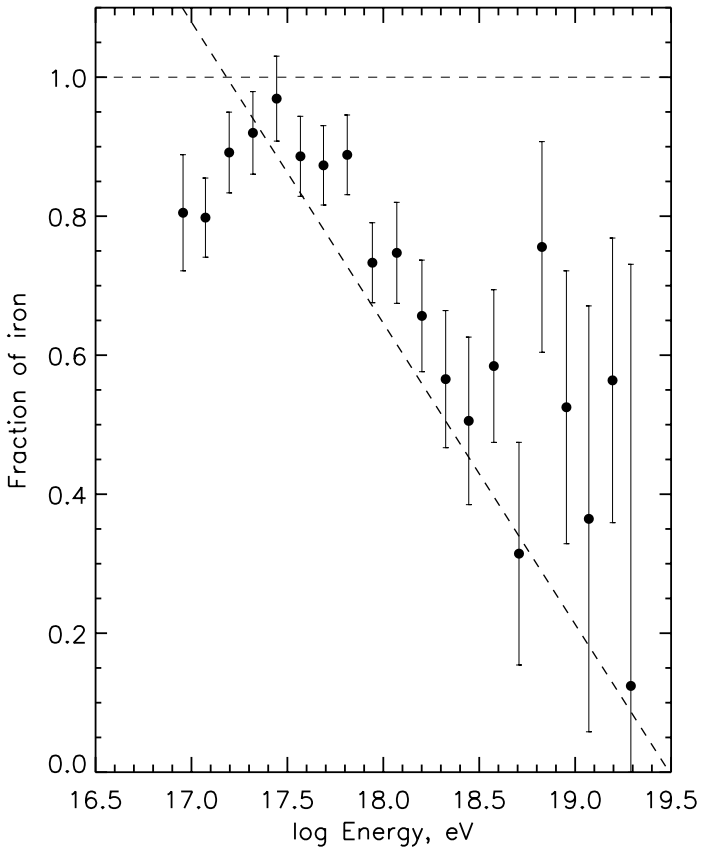

FIGURE 4.11. Similar to Fig. 4.10, but we also attempt to show the effect of possible systematics in the data or hadronic model. We assume that the A1 analysis underestimates energy by 30%, and that there is an additional 10 g/cm^2 shift required in either the Fly's eye data or the simulation results.

4.3 Summary and Discussion

When attempting to compare composition results from different experiments, it is crucial to examine them in the context of the same hadronic interaction model. We have seen that the Akeno and Fly's Eye experiments, based on comparison to *different* hadronic models, give totally irreconcilable conclusions about composition. The analysis in this chapter shows that the disagreement between the experiments can be considerably reduced if the same hadronic model (in this case, the minijet–based model contained in SIBYLL) is used in the interpretation of the

measurements. That the agreement is not complete can be explained in several ways — we have observed, for example, that the AGASA reconstruction procedure underestimates energy by 30%. It may be that the systematic error in $X_{\rm max}$ reconstruction for the Fly's Eye is larger than the 20 g/cm^2 assumed in our analysis, and by previous authors. On the other hand, the remaining disagreement may indicate a deficiency in the model, particularly in terms of the correlation between the longitudinal shower development and the muon content of the shower.

Chapter 5

Composition studies using a hybrid detector

In this chapter I present some results obtained using events measured by the HiRes 1 prototype in coincidence with MIA. This was the first "hybrid" detector (fluorescence eye plus ground array). I begin with a brief discussion of the detectors used for this work. The nature of the hybrid data set is then outlined. Finally, I describe the results of some analyses performed on the hybrid data, and their implications for cosmic ray composition and hadronic interaction models.

5.1 Detectors

Features of the HiRes prototype detector and the Michigan Muon Array (MIA) relevant to this work are described. Detailed descriptions can be found in Refs. [134, 135] and [136, 137] respectively.

5.1.1 The HiRes prototype

The prototype HiRes I detector was fully operational from March 1993 to November 1996, at which point it was reconfigured and incorporated into the full detector. 14 mirrors viewing elevation angles between 3° and 70° operated in the configuration shown in Fig. 5.1. The layout of the site atop Little Granite Mountain on Dugway Proving Ground, Utah, is shown in Fig. 5.2. The prototype was designed to overlook the CASA and MIA arrays, thus enabling the study of coincident events.

Each of 7 HiRes I buildings contained 2 mirrors and associated electronics. Two of these buildings were corn silos, used to house mirrors oriented towards

high elevation angles. The others were prefabricated buildings with electronically controlled shutter–style doors.

The detector is operated from a central facility which houses the central timing crate, computers, YAG laser used for detector calibration, and operator quarters. Communication between the mirror units and control software is achieved via a single ethernet line.

A simple schematic of the data acquisition process is shown in Fig. 5.3. Fluorescence light emitted by the shower is focussed by each mirror onto a "cluster" of 256 (16×16) PMTs. The pulses seen by the PMTs are passed to a VME crate for processing.

The mirrors employed by the prototype (and now by the full detector) are 2 m diameter composite spherical mirrors with effective area 3.75 m^2. They have a radius of curvature of 4.74 m and an f–number of 1.16. The mirrors were fabricated by slumping 4 smaller segments which were then cut to size and aluminised [138]. The segments were fitted together in a "clover" pattern.

The HiRes mirrors were designed to have a finite spot size. This was done to smooth out fluctuations in PMT response along the track which are introduced by gaps between tubes and by gain variations across the PMT face. Ray Tracing calculations show [134] that the spot shape depends quite strongly on the angle between the track and the mirror axis, as can be seen from Fig. 5.4. The effect of coma becomes more significant as the off–axis angle increases, and the central spot becomes larger.

The support structure for the prototype mirrors was an aluminium hexcell honeycomb structure which was glued to their backs. Unfortunately, this was found to have a large thermal expansion coefficient, causing a decrease of up to 3mm/C° in the radius of curvature and thereby increasing the spot size. All of the prototype data were affected by this problem. This structure was replaced by a simpler and more robust arrangement when the full detector was assembled.

Each cluster has at its face a UV bandpass filter which admits photons of wavelength between 300 and 400 nm. The peak transmission of this filter is 80%

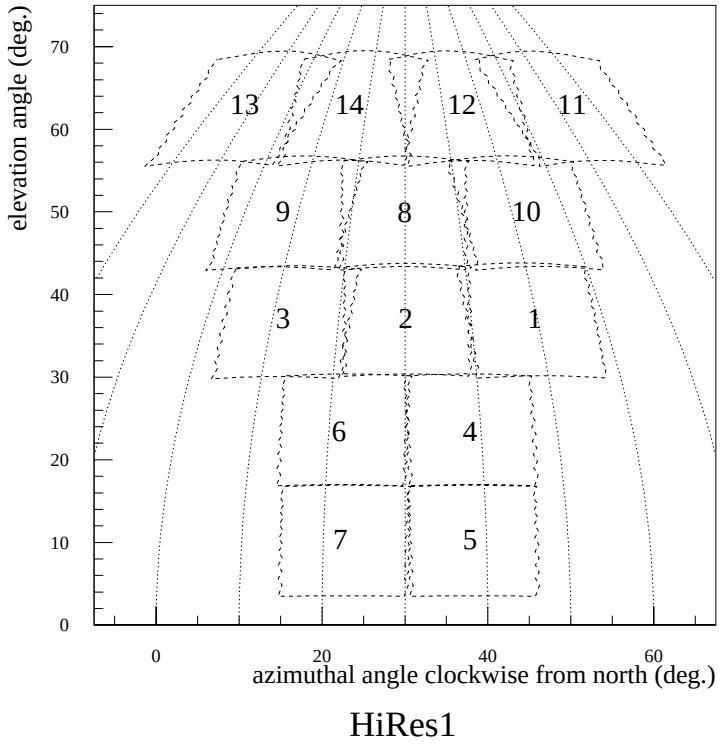

FIGURE 5.1. Field of view of the HiRes I prototype detector, with mirror numbers indicated.

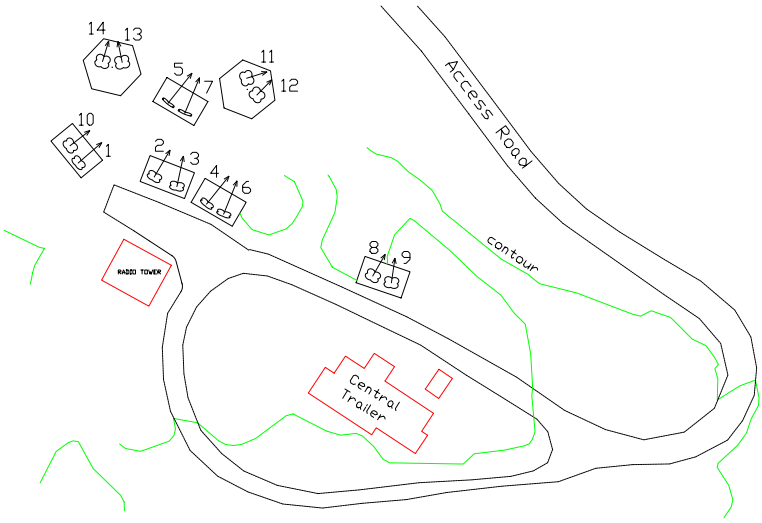

FIGURE 5.2. Layout of the HiRes I prototype.

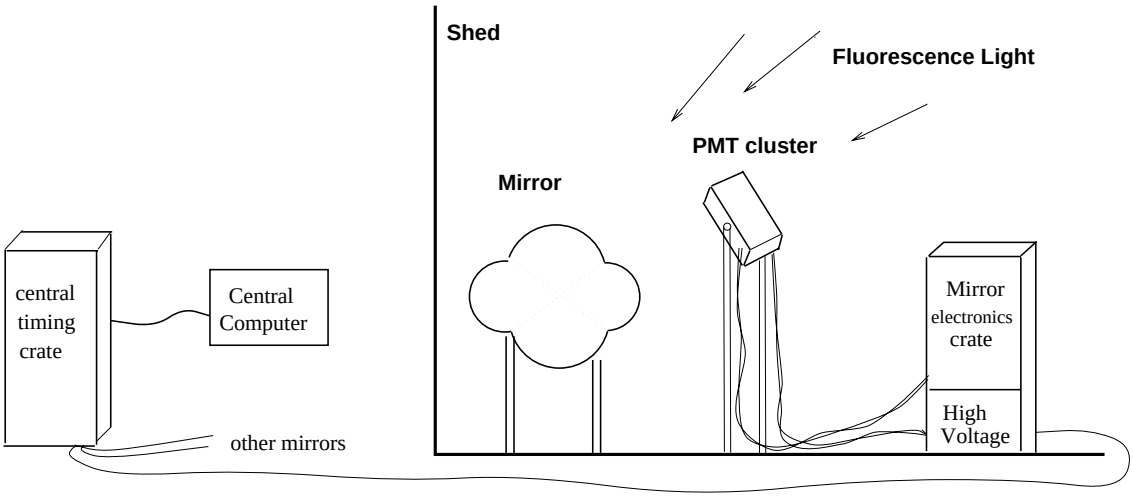

FIGURE 5.3. Simple depiction of HiRes operation.

(Fig. 5.6). Adding the filter improved the signal to noise by a factor of 1.7 [139].

A PMT cluster consists of 256 tubes having hexagonal cross–section and an approximately $1^\circ \times 1^\circ$ field of view. Hexagonal tubes were employed to allow close packing and therefore obviate the need for Winston cones. Each tube is AC–coupled, ensuring that only fluctuations in the night sky background contribute to the noise. The tubes are arranged into 16 "subclusters" of 16, as in Fig. 5.5.

Knowledge of PMT pointing directions is crucial for accurate event reconstruction. The pointing direction of a mirror can be obtained using surveying techniques, and those of individual tubes may be inferred from the overall mirror pointing. Over time, the surveyed directions will vary from the actual directions, due to small movements of mirror buildings or movement of the cluster, or even of tubes within the cluster. The change can be quantified using several methods. I will discuss one such method in Section 5.6.

The electronics for each mirror unit were contained in a single VME crate. The following components were present:

- 16 data acquisition boards, known as "ommatidial" boards[1], one for each PMT subcluster. The ommatidial boards handled triggering and signal digitisation for each PMT.

[1] An ommatidium is one of the elements of the compound eye of an arthropod.

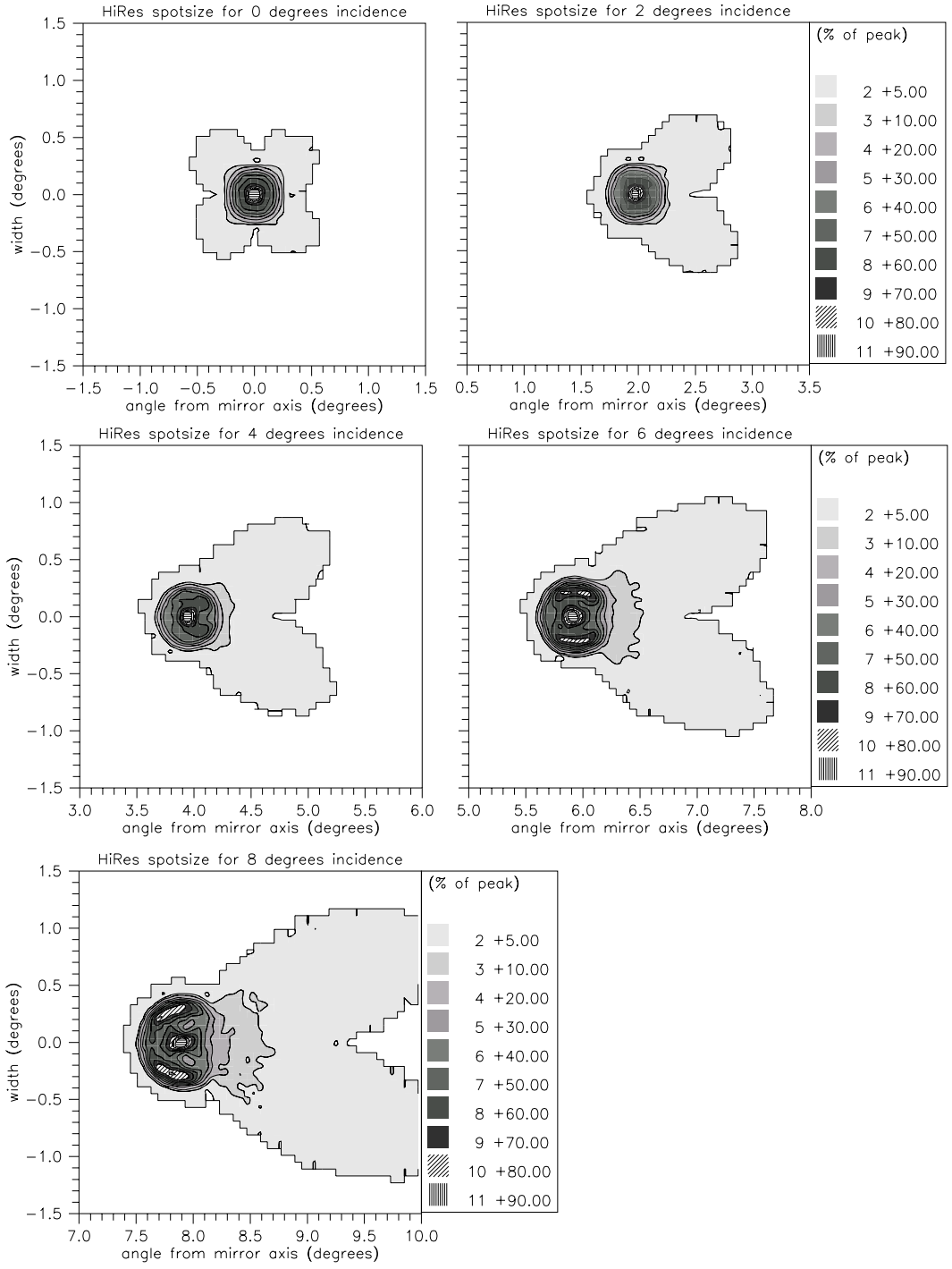

FIGURE 5.4. The spot size of a HiRes mirror as a function of the off–axis angle, from ray tracing calculations [134]. The spots for incident angles of 0°, 2°, 4°, 6° and 8° are shown.

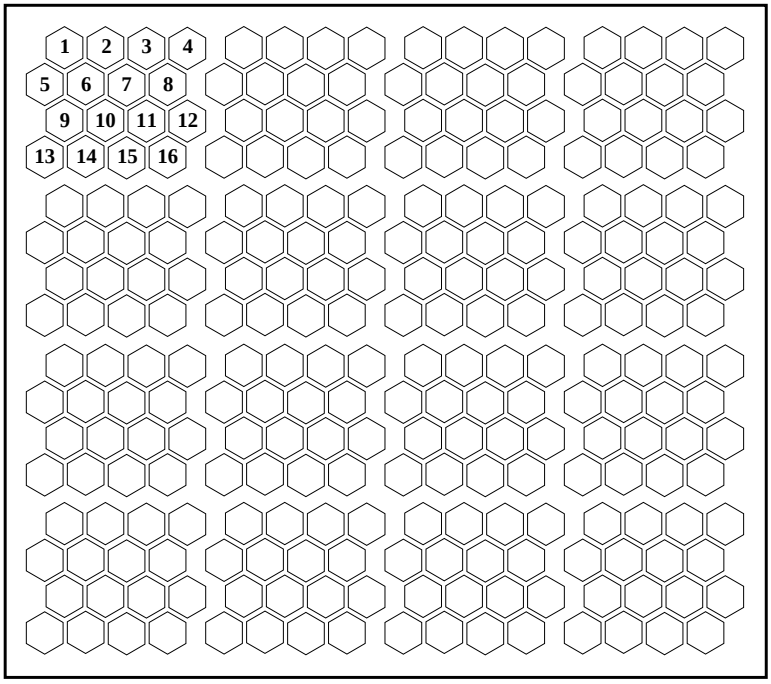

FIGURE 5.5. A HiRes PMT cluster, composed of 16 subclusters (gaps exaggerated for clarity).

The HiRes prototype used "sample and hold" electronics, *i.e.* once the integrated charge reached some threshold level, the triggering time and integrated charge at that time were stored. This threshold was dynamically adjusted every 4 seconds to allow for changes in the night sky background. The threshold adjustment was intended to maintain a trigger rate of 200 Hz [118].

- A trigger board. This determined whether subcluster and/or mirror–wide triggers had occurred. A subcluster trigger was formed when the pattern of PMT triggers within a subcluster matched a pattern in a hardware trigger lookup table. During normal data collection, three tubes with two being hexagonally adjacent were required for a subcluster trigger. Several other conditions are possible, but these are generally used for calibration purposes only [134].

  Once a subcluster trigger is formed, the output of the lookup table is re-

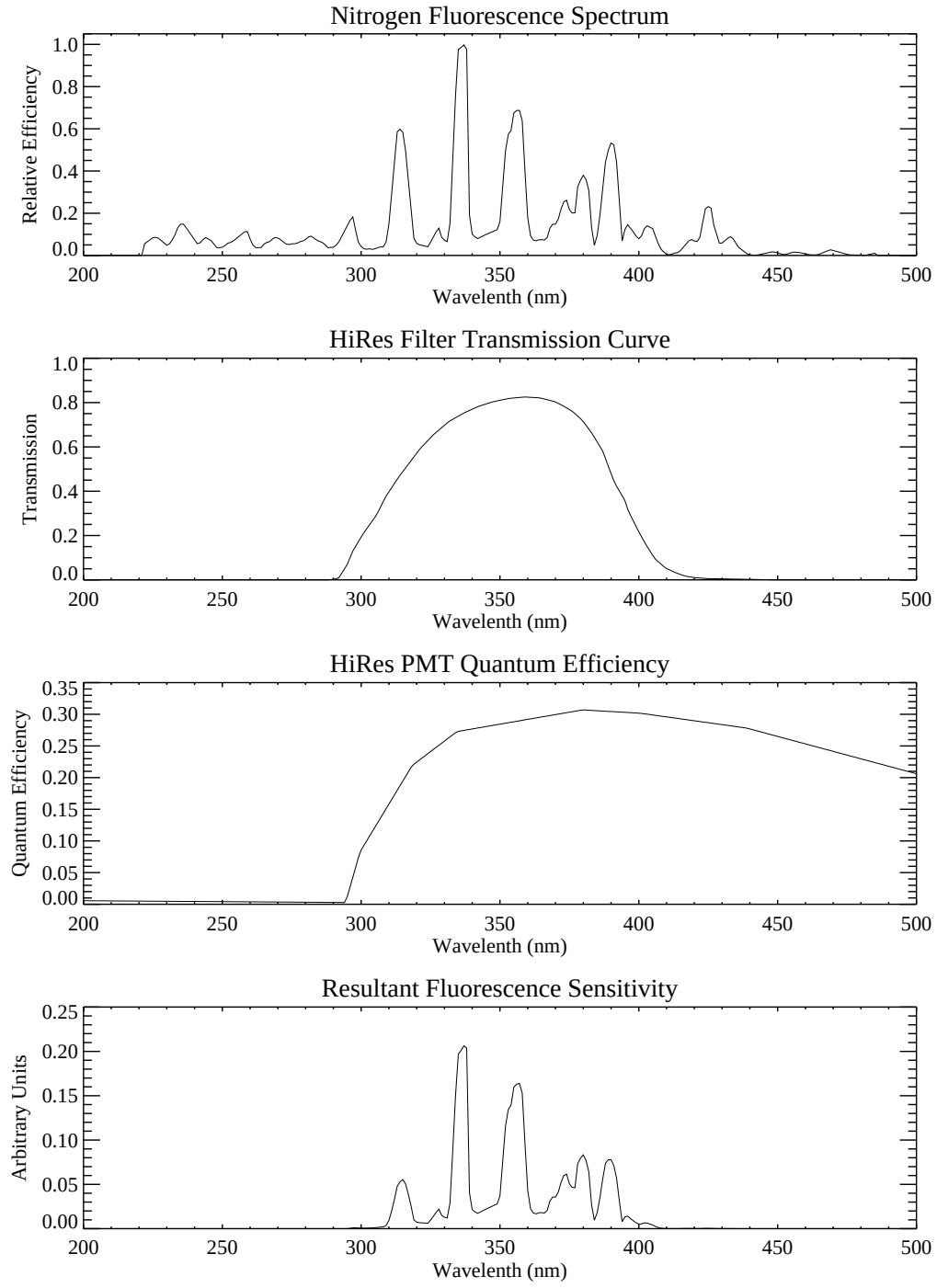

FIGURE 5.6. The fluorescence spectrum (bottom), taking into account the filter transmission function and PMT quantum efficiency.

shaped into a 25 μs pulse and used as the input for a mirror trigger lookup table. If at least two subcluster triggers have been formed, a mirror trigger is generated. A mirror trigger is also sent to adjacent mirrors. The two subcluster requirement is relaxed to a single subcluster for these to allow for tracks that clip the edge or corner of a mirror.

In the event of a mirror trigger, a mirror save condition is generated. This prevents PMT charge integrals from being cleared, and allows new PMT triggers for up to 10 μs after the mirror trigger, in order that the track may finish crossing the mirror. After a holdoff time of a further 10–25 μs, the PMT charge and time integrals are digitised and saved as a mirror event.

- CPU board. This provides the interface, via an ethernet link, between the central computer and mirror electronics. The CPU card collects TDC (time) and QDC (charge) information from each PMT and sends it to the central computer as an "event packet". Other data, such as trigger rates and thresholds, are also collected every minute.

- PPG (programmable pulse generator) board. This generates waveforms of known shape and amplitude for use in electronic calibration.

- A "garbage" board, which contains various sensors and relays (*e.g.* building door control, temperature sensors, high voltage readout)

Calibration of the prototype comprised several elements. PMT quantum efficiency and gain were measured in the laboratory for each tube before deployment. The gain has the form $\exp(\alpha)V^{\beta}$ as a function of voltage V, where α and β are determined on a tube–by–tube basis. The uniformity of response across the tube face (see Fig. 5.7) was also measured, using a translation stage.

Optical calibration was done on a nightly basis using a YAG laser. This was housed in the central facility, and its output delivered via optical fibres. For each mirror, one fibre bundle shone light from the mirror centre (through a teflon diffuser) directly onto the cluster. A further two fibre bundles located at the sides

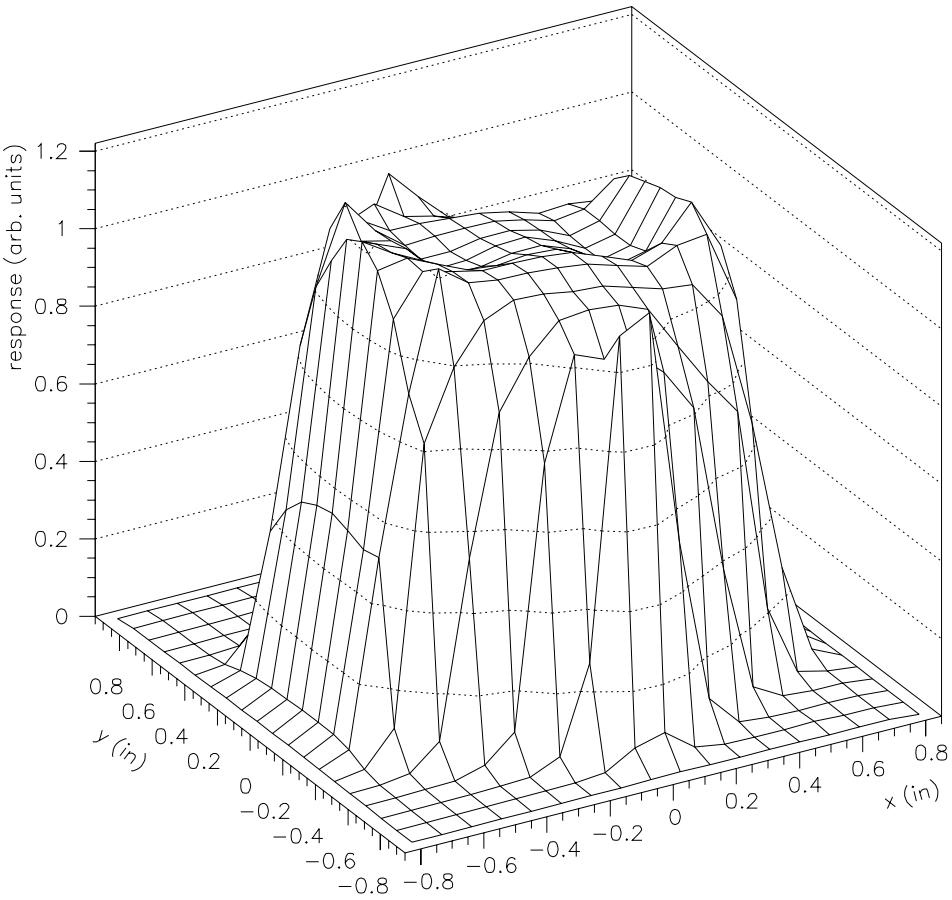

FIGURE 5.7. Tube response profile, as a function of position on the tube face (relative to the tube centre, in inches).

of the cluster box shone light onto the mirror which was then reflected onto the cluster. This procedure was followed at the beginning and end of each night, and the data were used to monitor the electronics gain for each tube. In addition, the mirror reflectivity could be measured by comparing the mean PMT response for direct laser shots to that for reflected shots. The reflectivity measured using this method was 90% when the mirrors were first washed, degrading rapidly (due to dust) to 80% after a month or two. This measurement was affected by a problem with the teflon diffusers which introduced an uncertainty of more than 10% in the

nightly light output [118].

Absolute calibration of prototype PMTs was done using a portable system consisting of 4 "standard" tubes, ommatidial board, PPG board and high voltage supply [140]. These tubes were chosen based on having similar gains and response profiles and were calibrated to within 2% [134]. The calibration was done by placing the standard tubes in each cluster and replacing the ommatidial board for the appropriate subcluster with the standard ommatidial board. The cluster was then illuminated by the YAG laser and the response of the standard tubes was compared to the other tubes in the cluster. Absolute calibration, being somewhat time consuming, was done only once a year in general.

The QDCs (charge to digital converters) were calibrated using the PPG pulser. Each tube was forced to repeatedly trigger and integrate at approximately 1.5 Hz for one minute ("snapshot" data). The resultant mean QDC was the pedestal for that tube, while the RMS deviation gave the combination of electronic and sky noise. The latter was disentangled by taking noise data with the building doors shut (electronic noise only) and open (electronic plus night sky background). This was done at the beginning and end of each night.

Atmospheric monitoring was the most difficult, but arguably most important, calibration task for the HiRes prototype. In particular, the aerosol component was (and still is) poorly measured and potentially highly variable on a nightly basis. An attempt to quantify atmospheric effects on HiRes data was made by implementing several measures. A number of vertically aligned UV light sources known as flashers were placed at various distances from HiRes I. These consisted of a Xenon flash bulb and mirror inside a weatherproof container and were operated remotely via radio control. Two "legs" of flasher units were placed at distances 1 km, 2 km, 4 km, 8 km and 10 km from HiRes I. In addition to these, a steerable YAG laser was installed at the site formerly used by Fly's Eye II, and a portable laser system called the Laserscope was developed.

Flasher and laser events can be used to infer the character of the atmosphere on a given night, primarily through measurement of the horizontal extinction length.

This is an important parameter for accurate measurement of the shower energy. In addition to atmospheric monitoring, these events also provide valuable tests of geometrical reconstruction algorithms, since the event geometry is known *a priori*.

5.1.2 MIA

The Michigan Muon Array (MIA) consisted of 16 "patches" of 64 scintillation counters, buried beneath the Chicago Air Shower Array (CASA) [137] (Fig. 5.8). Each counter was a 1.3m $\times$ 1.9m scintillator with a photomultiplier tube (inside a watertight casing) attached. The 3m of dirt above MIA acted as an absorber for the EM component of air showers. Since the counters would not be able to be maintained after burial, a simple and robust design was required. For this reason as well as for cost–efficiency, MIA did not record pulse height information, only whether a counter triggered or not, and the trigger time.

The CASA/MIA site was located approximately 3.3 km northeast of the HiRes prototype (Fig. 5.9).

Signals from the MIA PMTs were sent to a discriminator, the output of which started a TDC operating in common–stop mode. The TDC was stopped by an event trigger. If a counter was not stopped within the gate time of 5.2 μs, it was reset in preparation for the next signal.

Event triggers generally occurred in two ways. If CASA was triggered, all MIA TDC values were read out, regardless of how many MIA counters had triggered. If a HiRes trigger had occurred, a signal would be sent via a flasher unit located at 5 Mile Hill, and picked up by a receiving unit at the CASA/MIA site. A pulse would then be sent to the CASA/MIA trigger system for processing. If at least 6 MIA patches had at least 3 hit counters, a MIA readout would occur. This triggering requirement was selected in order to prevent HiRes from adding to the MIA deadtime.

Initial Monte Carlo simulations suggested that the muon energy threshold for MIA counters was 1.0 GeV for vertical muons [134]; however, a later estimate placed this figure at 0.85 GeV. The latter was used for the analysis in this thesis.

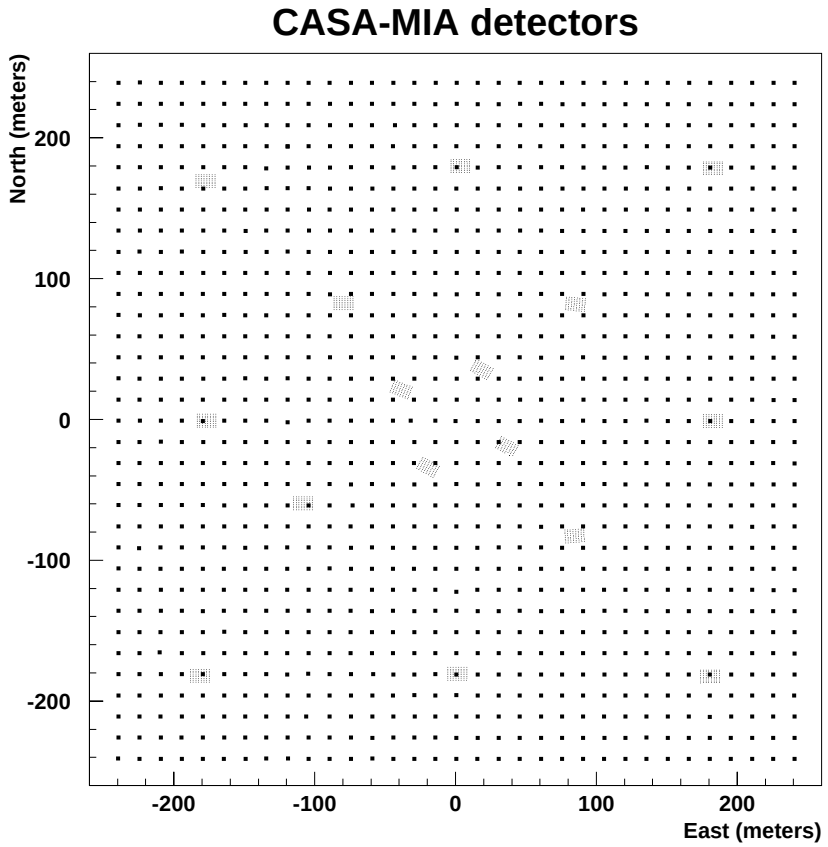

FIGURE 5.8. Layout of the CASA and MIA detectors. The grid spacing for the CASA detectors is 15 m. Squares: CASA stations, shaded rectangles: MIA patches.

The counter efficiency at the time of burial was 93% [137]. A 1995 study [141] suggested that the mean efficiency decreased by as much as 13%, although the technique used in that study left considerable doubt as to the absolute efficiency [134].

5.1.3 The Hybrid Data Set

Data taking for HiRes and CASA/MIA was done independently, apart from the HiRes–driven MIA triggers described above. At the end of each night, the raw HiRes data packets would be processed to build events. These events would then be calibrated using the nightly electronics calibration data (see above) to deter-

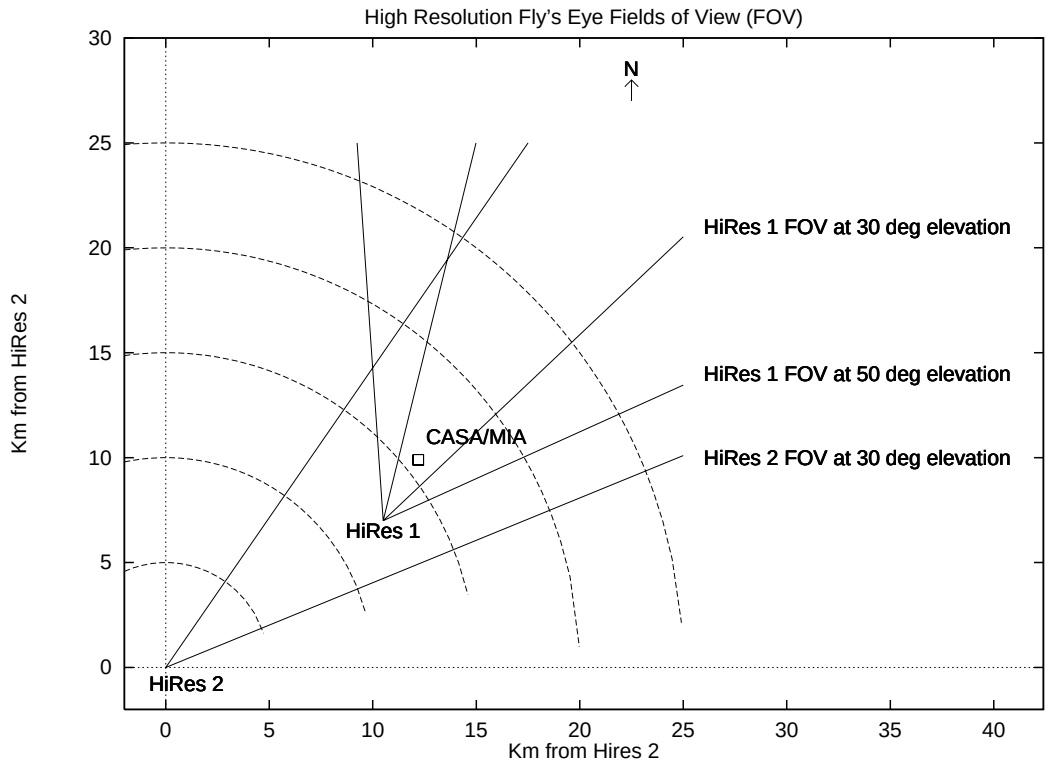

FIGURE 5.9. Position of HiRes 1 with respect to HiRes 2 and CASA/MIA.

mine photon number from QDC for each channel, and absolute firing time from TDC values.

After event building, "track–like" events would be selected by applying a Rayleigh filter. The triggered tubes in a mirror were time–ordered, and unit vectors then drawn between each pair of tubes. The unit vectors were then summed. For noise events containing n tubes, the resultant vector should have a length $\sim \sqrt{n}$, reflecting the fact that the tubes are uncorrelated and can therefore be described by a random walk in two dimensions. Cosmic ray events, on the other hand, will have Rayleigh vectors significantly longer than $\sqrt{n}$. The probability of randomly obtaining a vector of a given length by summing n unit vectors is given by the Rayleigh distribution. The criterion applied for HiRes events was that at least one mirror had a Rayleigh vector with chance probability less than 5% [118]. For borderline events, a further filter called Scanner, which was most effective for rejecting events due to Cherenkov emission from low energy cosmic

rays, was applied [134]. Scanner removes events which span a time of less than 250 ns (Cherenkov blasts), and also removes tubes which clearly trigger before or after the event (noise tubes).

Once candidate HiRes events had been selected, a list of candidate event times was assembled by the HiRes computer and ftp'ed to to the CASA/MIA computer for comparison with the event times in the raw CASA/MIA data. Coincidences were identified if the HiRes trigger occurred within 3 ms of the CASA/MIA trigger, or if the receiving unit at CASA/MIA recorded a flash within 50 μs of a MIA trigger [134]. Data for these events were appended to a file which was then passed through the first stage of the CASA/MIA event processing software, called PASS0 [111]. This essentially made a correction to the measured times to allow for delays due to signal transport along the PMT cables, as well as applying electronic calibration.

Once coincidence events were identified, the times of the matched events were sent back to the HiRes computer and used to tag the HiRes events for further processing.

The data merging process proceeded by taking CASA/MIA–HiRes coincidence data and packing the information from those events into the standard HiRes data format (DST, or Data Summary Tape). Each event has various "banks" associated with it, containing such information as raw QDC counts for each channel, inferred number of photons, and timing information for muons and HiRes PMTs.

The initial DST file for the full coincidence data set contained 43274 events. Two cuts were imposed on this data set. Each event was required to span a track length of at least 15 degrees (this being the angle subtended by the first and last tubes in the track). This eliminated events which would be fitted poorly due to there being a limited view of the track [134]. In addition, HiRes–MIA events with fewer than 40 muon counters hit, or HiRes–CASA/MIA events with fewer than 80 hits were discarded. This eliminated a large number of accidental coincidences (Fig. 5.10).

The 2881 events remaining after these two basic cuts were passed through

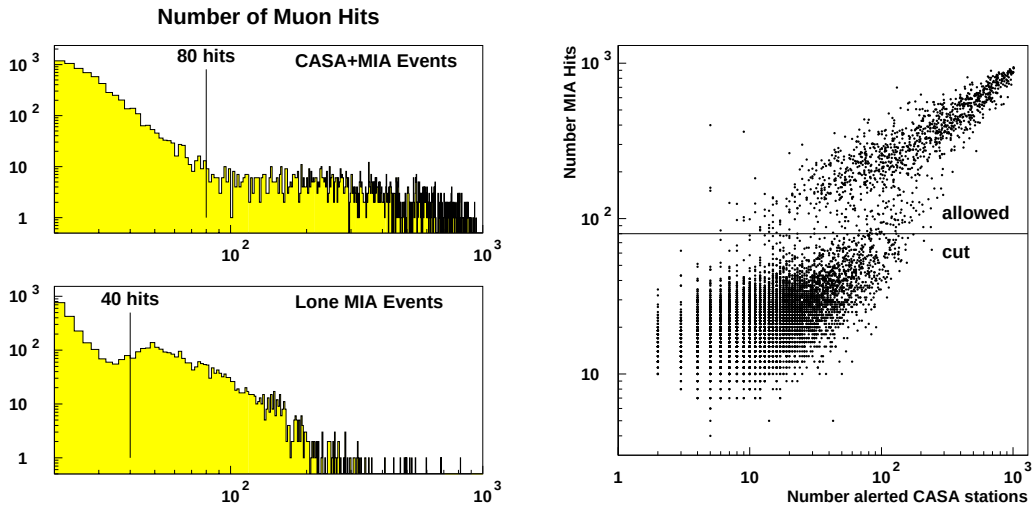

FIGURE 5.10. Number of muons for the hybrid data set described above [134]. In the right hand plot, there are clearly two populations, the lower of which constitute accidental coincidences. Most of these are removed by the 80 muon counter requirement.

several event reconstruction algorithms, originally developed (for the most part) by Kidd [134]. Several refinements were made to these programs. These will be discussed in a later section.

5.2 Hybrid Geometry Reconstruction

In this section I describe the technique used to perform geometrical reconstruction for the hybrid data set. This discussion largely follows the theses of Kidd [134] and Wilkinson [118].

5.2.1 HiRes reconstruction

For an event measured by a single HiRes eye, the first task is to determine the event geometry. This is done in two stages. The first stage yields the Shower–Detector Plane (SDP), as shown in Fig. 3.5. The pointing directions of triggered tubes in

an event define a great circle on the celestial sphere. To a first approximation, the plane containing the detector and this great circle is the Shower–Detector Plane.

A better estimate of the SDP can be obtained by weighting each tube by its signal, since the tubes with higher amplitudes should be those closest to the shower axis. The χ^2 for this **Amplitude Weighted** fit is therefore

$$\chi^2 = \sum_{i=1}^{\text{ntubes}} w_i \frac{\theta_i^2}{\sigma^2}, \tag{5.1}$$

where w_i is the signal (in photoelectrons) for the i^{th} PMT divided by the mean signal for the event, θ_i is the offplane angle of the i^{th} PMT (defined as the angular distance between the tube centre and the SDP), and σ is the "tube width", $\sigma \simeq 0.3^\circ$ [134]. The offplane angle can be written as

$$\theta_i = \frac{\pi}{2} - \cos^{-1}(\hat{n} \cdot \hat{t}_i), \tag{5.2}$$

where $\hat{n}$ is the normal to the SDP and $\hat{t}_i$ is the pointing direction of the i^{th} tube. Minimising the χ^2 therefore yields the three components of the SDP normal. In fact, one need only fit for two parameters, since $\hat{n}$ is a unit vector.

A χ^2 of the form 5.1 has the effect of forcing the fitter to concentrate on the brightest tubes in the track, thereby reducing the influence of noise tubes and atmospheric scattering. However, it does not take account of optical effects, such as the finite spot size. A more sophisticated treatment than the above, known as **Amplitude Fitting**, attempts to do precisely this. In this case the χ^2 is constructed as

$$\chi^2 = \sum_{i=1}^{\text{ntubes}} \frac{(\text{sig}_i^{\text{measured}} - \text{sig}_i^{\text{expected}})^2}{\sigma_i^2}. \tag{5.3}$$

Here $\text{sig}_i^{\text{measured}}$ is the measured amplitude for the i^{th} tube in the track, in photoelectrons. $\text{sig}_i^{\text{expected}}$ is derived for a given trial plane by calculating the response expected from ray tracing calculations. This is retrieved from a lookup table and

convolved with the laboratory–measured PMT response function (Fig. 5.19). The ray tracing response is what would be expected if the mirror were illuminated uniformly by some light source [134]. It must be scaled to the actual light flux at the time of triggering. This is estimated by averaging the signal in all tubes that lie within 3° of the triggered tube, assuming that the signal varies smoothly along the track. The expected signal is therefore $\mathrm{sig}_i^{\mathrm{expected}}$ = (ray tracing response for tube i) $\times$ (average flux at tube i).

The error in the denominator of Eq. 5.3 is estimated to be $\sigma_i^2 = \mathrm{sig}_i^{\mathrm{measured}}$ + sky noise + $0.05 \times \mathrm{sig}_i^{\mathrm{expected}}$, *i.e.* it is a sum of contributions due to poisson fluctuations in the measured signal, the night sky background, and error in the estimated amplitude. The latter is usually arbitrarily taken to be 5%.

Note that the above techniques do not take account of parallax, *i.e.* the detector is regarded as a point. For showers with small impact parameters, such as those in the hybrid data set, this is not a good assumption. A global plane fit such as those described above also relies on rather precise knowledge of tube pointing directions. Instead, it was decided to determine the geometry on a mirror by mirror basis. Further refinements such as including the intrinsic shower width were also made. These will be discussed shortly.

Once the SDP has been determined, the geometry of the shower can be completely specified by using the times of triggered tubes to determine the orientation of the track within the SDP. One constructs a χ^2

$$\chi^2 = \sum_{i=1}^{\mathrm{ntubes}} \frac{(t_i - (t_0 + \frac{R_p}{c} \tan \frac{\theta_i}{2}))^2}{(\sigma_i^t)^2}. \tag{5.4}$$

The geometry for the timing fit is shown in Fig. 3.6.

Monocular timing fits rely on precise knowledge of tube triggering times. One cannot assume that tubes trigger after 50% of the time taken for the track to traverse the tube face, since bright tracks will trigger the tube early, while dim tracks will tend to trigger late. This is referred to as "time slewing". To compensate for the effects of time slewing, one needs to know the temporal structure of

the EAS as it passes through the field of view. Unfortunately, such pulse shape information was not available with the sample–and–hold electronics employed by the HiRes prototype. The full HiRes II detector employs Flash ADC (FADC) electronics which yield the necessary information, and it should be possible in future to parametrise the effects of time slewing in terms of amplitude and shower impact parameter[2].

The timing error, σ_i^t in Eq. 5.4, is dominated by time slewing. Since no detailed time slewing studies have yet been done, it is not possible to estimate the magnitude of σ_i^t on an event by event basis. For the HiRes–MIA dataset, Kidd [134] used the RMS value of the (approximately gaussian) distribution of residuals from the timing fit, *i.e.* the measured time minus the monocular fitted time for the whole data set. This yielded $\sigma_i^t = 40$ ns.

The algorithm used in a monocular timing fit must be able to detect curvature in the tan function in Eq. 5.4. For short tracks, the tan function can appear linear over the small angular range available, and errors in R_p and ψ become correlated [134].

5.2.2 MIA reconstruction

It is relatively straightforward to reconstruct the shower axis using the times of hit MIA counters, provided that the core location of the shower is known. For CASA/MIA events, this can be found using pulse height and timing information from CASA (see *e.g.* Ref. [142] for details). For HiRes–MIA events, an iterative technique, to be described in Section 5.2.3, is employed.

The first approximation to the shower axis is calculated by assuming a planar shower front. A simple χ^2 is constructed thus:

$$\chi^2 = \sum_{i=1}^{\text{ncounters}} \frac{(t_i - \text{time}_i)^2}{\sigma_t^2}, \tag{5.5}$$

[2] A preliminary attempt to study time slewing in the prototype stereo data set was made by Wilkinson [118]

where

$$t_i = t_0 + \frac{\hat{n} \cdot \vec{x}_i}{c}. \tag{5.6}$$

Here time$_i$ is the measured time for the i^{th} counter, and $\vec{x}_i$ is its position vector relative to the centre of the array. σ_t is taken to be the resolution of the MIA TDCs, *i.e.* 4 ns [134]. Minimising this χ^2 yields the (approximate) time at which the shower core hits the ground, as well as the direction vector $\hat{n}$. Note that the precise core location is not required for this fit.

For precise determination of the axis, the curvature of the shower front must be taken into account. Analysis of the CASA/MIA data set suggests that the departure from a plane front is given as a function of core distance r by $\Delta t = 0.0655r + 0.0001199r^2$ [134]. This was derived out to a distance of 350 m, but is also assumed to hold for larger core distances. Naturally, the core location must be known for this fit. The χ^2 for the MIA "cone fit" is the same as for the plane fit, except that a term $ar + br^2$ is subtracted from the right hand side of Eq. 5.6. a and b are the CASA/MIA derived values above.

5.2.3 Hybrid reconstruction

Geometrical reconstruction for HiRes–MIA events is achieved via the following algorithm [134][3].

1. An approximate SDP is calculated from HiRes data by doing an amplitude weighted fit. Parallax is ignored, *i.e.* the detector is taken to be a point.

2. The "most vertical direction" $\hat{v}$ in the SDP is used as a first approximation to the track vector. This is obtained by taking the vector (0,0,1) and rotating it until it lies in the SDP.

3. The vector obtained in step 2 is used to reject obvious accidental muon hits. A plane front with normal vector $\hat{v}$ is assumed, and the measured times

[3]The program used for reconstruction is called hbrd_traj

are recalculated relative to the plane. Any muons arriving more than a microsecond from the resultant median arrival time are rejected.

4. The times of the remaining ("intime") muons are used to perform a MIA plane fit, as above. The arrival times are recalculated relative to the new plane, and any muons which arrive within a range (-172.5, +132.5) ns of the median time are flagged as intime and retained for further analysis.

5. The intime muons are used for a further MIA plane fit. If the resultant track vector lies further than 10° from the trial SDP, the event is most likely an accidental coincidence, and is rejected.

6. The direction found in step 5 is projected into the SDP. This yields the angle ψ (see Fig. 3.5.

7. R_p and t_0 (the HiRes reference time) are determined by doing a monocular timing fit with ψ fixed.

8. With R_p and ψ known, a rough core location can be calculated. This is then used as the input to a MIA cone fit.

9. The new MIA direction vector is projected into the SDP to calculate ψ. The fit of step 7 is repeated to find R_p.

10. The program iterates between steps 7 and 9 until the incremental change in R_p is less than 10 m, or until the maximum number of iterations is exceeded. In the latter case, the event is rejected.

11. The SDP is re–determined using an amplitude weighted fit, this time taking account of the different mirror positions (parallax).

12. The iterative procedure, step 10, is repeated.

Once the shower geometry has been fixed according to the prescription above, other physically important parameters may be extracted. HiRes is used to determine the shower energy via the calorimetric method discussed in Section 3.2.2.

The depth of maximum, $X_{\max}$, is also determined from the longitudinal profile. MIA measurements yield the total muon number, N_μ, and the muon density as a function of core distance. The techniques for calculating these parameters are discussed in the next section.

5.3 Extracting composition parameters

5.3.1 Muon number

The muon content of the shower is calculated using an "on–off" method similar to that employed by AGASA (see Ch. 4). The aim is to maximise the log likelihood function

$$\mathcal{L} = \sum_{i=1}^{\mathrm{N_{hit}}} \ln p_i + \sum_{i=1}^{\mathrm{N_{unhit}}} \ln q_i, \tag{5.7}$$

where q_i is the probability that the i^{th} counter is unhit, and $p_i = 1 - q_i$ the probability that it is hit. N_{hit} and N_{unhit} are the total number of hit and unhit counters in a given annulus.

Over a small range of core distances, the density ρ_μ can be considered to be constant. The probability of a counter being unhit is then

$$q_i = \exp\left(-N_{\mathrm{bkg}}\right) \exp\left(-\rho_\mu \epsilon_i A_i\right), \tag{5.8}$$

with N_{bkg} the expected number of noise hits in the event window, ϵ_i the efficiency of the i^{th} counter, and A_i its effective area. Taking these to be the same for each counter and maximising $\mathcal{L}$, we trivially obtain for ρ_μ

$$\rho_\mu = \frac{-\ln\left(1 - \frac{N_{\mathrm{hit}}}{N_{\mathrm{live}}}\right) - N_{\mathrm{bkg}}}{\epsilon A \cos\theta}, \tag{5.9}$$

with θ the zenith angle of the shower and $N_{\mathrm{live}} = N_{\mathrm{hit}} + N_{\mathrm{unhit}}$ the total number of active counters.

In order to reconstruct the total muon multiplicity of the shower, N_μ, it is inadvisable to simply integrate the densities ρ_μ obtained above, since there are generally not enough measurements for an accurate evaluation of the integral. Instead, one assumes some functional form for the muon lateral distribution function, and performs another log likelihood fit. The work of Kidd [134] demonstrated that the normalised lateral distribution from MIA densities measured by the on–off method is in excellent agreement with the AGASA LDF, Eq. 2.20. The latter was therefore used in the N_μ analysis. The log likelihood function to be maximised is the same as Eq. 5.7, except that we now have

$$q_i = \exp\left(-N_\mu \rho_\mu(R_i)\epsilon_i A_i\right) \exp\left(-N_{\rm bkg}\right). \tag{5.10}$$

$\rho_\mu(R_i)$ is the normalised muon density (*i.e.* Eq. 2.20 divided by N_μ) for counter i at core distance R_i.

The muon density at a core distance of 600m, $\rho_\mu(600)$, is also used as a composition estimator in this thesis. It is calculated in the following way. The hit counters are divided radially into logarithmic bins. The density in each bin is calculated according to Eq. 5.9. $\rho_\mu(600)$ is calculated by interpolating between density measurements on either side of 600m. Occasionally, only one bin will be populated by hit counters, or all muon measurements will lie beyond 600m from the core. In these instances, the shower is assigned a $\rho_\mu(600)$ of zero, even though N_μ is non–zero.

5.3.2 Energy and Depth of Maximum

The first step in extracting the longitudinal profile is to bin the signal along the shower track. Ideally, one would prefer to use the signals of individual PMTs for a profile fit. Unfortunately, the predicted signal used in the profile fitting χ^2 depends rather strongly on the offplane angle. Since the PMT pointing directions are not known to sufficient accuracy that this prediction would be reliable, one instead divides the track into bins of angular width 1°.

The program `bindata` was developed by Kidd [134] to bin the signal. This originally did not take account of the intrinsic shower width, but since HiRes–MIA events all have small R_p (otherwise they would not trigger MIA), the shower cannot be treated as a line source. Instead, one assumes that the shower lateral distribution is described by the NKG form, Eq. 2.6. This was incorporated into a new version, called `bin_lat`. A Gaisser–Hillas function (Eq. 2.10) with $X_0 = 0$, $X_{\rm max} = 650$ g/cm^2 ("typical" values of these parameters) is assumed at this stage for the longitudinal profile, so that an approximate shower age s can be determined as a function of depth. This is required as an input to the NKG function.

The track is decomposed into 1 degree bins along its length, and each tube in the shower is accordingly allotted a bin. Each tube lies in one bin only — the tube signal is not split between bins. A bin can contain more than one tube. In this case, the bin signal is obtained by taking a weighted average of the individual tube signals.

In order to correctly calculate the signal for each bin, `bin_lat` performs amplitude fitting for each mirror to get the best local plane fit. This requires an assumption about how the flux varies across the mirror. The analysis in this thesis assumed a linear variation, although the final results are largely independent of the functional form chosen [143].

`bin_lat` calculates the expected signal for the amplitude fit by taking into account fluorescence light production, Cherenkov light production, and the lateral distributions of charged particles (NKG function) and Cherenkov light. We use the simulation results of Patterson and Hillas [144] to determine the age and zenith angle dependence of the latter. Atmospheric attenuation is also taken into account. Once the expected signal has been calculated for each tube, it is used to weight each tube in the average signal for the bin (see above). The bin error is also calculated, this being a combination of uncertainties due to Poisson statistics and error in the mirror plane fit.

Once the bin signals and their errors have been obtained, a profile fit can be performed. One constructs a χ^2

$$\chi^2_{\rm pfl} = \sum_{i=1}^{\rm nbins} \frac{({\rm bin}_{\rm pred} - {\rm bin}_{\rm meas})^2}{\sigma^2_{\rm bin}}, \tag{5.11}$$

where $\rm bin_{meas}$ is the measured bin signal, and $\sigma_{\rm bin}$ is its error. $\rm bin_{pred}$ is the predicted bin signal at the detector. This is calculated by assuming a Gaisser–Hillas function for the longitudinal profile and modelling production and transport of fluorescence and Cherenkov light. In this way we can use the measured signal to infer the shower size at the track as a function of depth. The contributions of scintillation light, direct Cherenkov light and scattered Cherenkov light (both molecular and aerosol–scattered) are all taken into account.

A search is performed over ($N_{\rm max}$, $X_{\rm max}$) space to find the values of these parameters that minimise $\chi^2_{\rm pfl}$. The Gaisser–Hillas parameter λ is fixed at 70 g/cm^2, and X_0 is fixed at -20 g/cm^2. These parameters are often (erroneously) identified with the mean free path and first interaction depth, although they are largely insensitive to energy and composition and therefore of little use. If they are left as free parameters in the fit, they simply increase the chance of the fitting algorithm being trapped in a local minimum. It is therefore preferable to restrict them so that good estimates of $X_{\rm max}$ and $N_{\rm max}$ can be obtained.

Having found the values of $X_{\rm max}$ and $N_{\rm max}$ that best reproduce the data, we can determine the energy using the calorimetric method of Ref. [119] (see Chapter 3). The composition–independent missing energy correction, Eq. 3.10, is also applied.

Two example shower profiles are shown in Figs. 5.11 and 5.12. The first is a well–measured event for which most of the flux is fluorescence light. The second is an example of an event which is dominated by Cherenkov light (direct Cherenkov in this instance).

5.4 Detector Monte Carlo

In order to draw any sort of physics conclusions from the data, it is necessary to ensure that the operation of both detectors is well understood. To this end

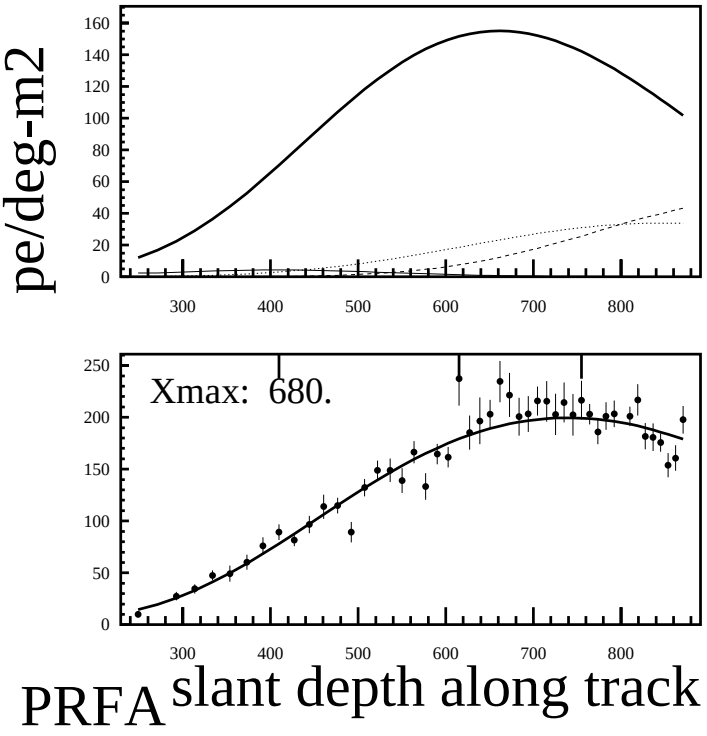

FIGURE 5.11. The top plot indicates the contributions to the signal from fluorescence light (heavy line), direct Cherenkov light (thin solid line), Rayleigh scattered Cherenkov light (dashed line) and Mie scattered Cherenkov light (dotted line). The bottom plot shows the total bin signal and associated errors, overlaid with a line showing the total fitted light.

a detailed Monte Carlo (MC) simulation of HiRes and MIA has been written. The code used in this work is similar to that used in Ref. [134], but with a more sophisticated treatment of the shower physics, particularly the muon component.

5.4.1 Generation of EAS

The first step in simulating the detector response to an EAS event is to generate the shower itself. This is done by parametrising the results of CORSIKA simulations.

We generated events at various zenith angles from 0° to 60° and energies from 3×10^{16} eV to 5×10^{18} eV, at a relative thinning level of 10^{-5}. 500 events were generated for each zenith angle and energy, using both the Sibyll and QGSJet

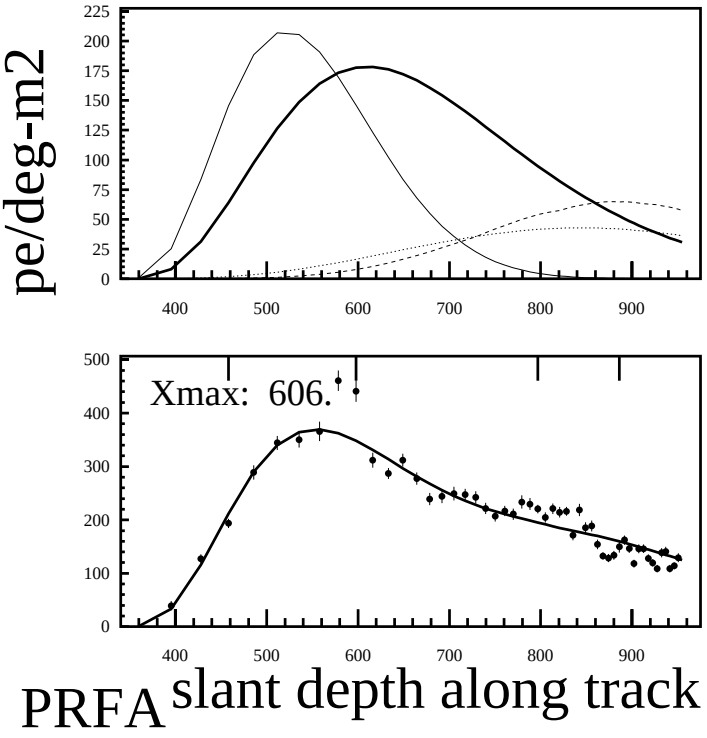

FIGURE 5.12. An event dominated by direct Cherenkov radiation.

interaction models. This allowed us to parametrise the first interaction depth X_1, the width parameter λ, depth of maximum $X_{\max}$ and size at maximum $N_{\max}$ in terms of zenith angle and energy. These parameters are all assumed to be normally distributed. Generating an EAS event therefore involves sampling from a gaussian for each parameter, taking into account the correlations between them.

The muon component of the shower, particularly its time structure, was rather more difficult to simulate. We assumed a lateral distribution function of the form

$$\rho_\mu(R) \propto \left(\frac{R}{R_0}\right)^{\alpha} \left(1+\frac{R}{R_0}\right)^{\beta}, \tag{5.12}$$

with R_0 being a lateral scale parameter. α and β are left as free parameters, depending on energy and zenith angle. CORSIKA simulations suggest that there is some correlation between them. This is incorporated into the detector MC. This functional form agrees quite well with the AGASA LDF except at small core distances, where it is more akin to the Greisen LDF [145].

The arrival time distribution of muons is parametrised by the following form:

$$\frac{dN}{dt} \propto t^a \exp\left(\frac{-t^b}{\tau}\right). \tag{5.13}$$

The parameters a, b and τ depend on energy, zenith angle and core distance. Correlations between these parameters are taken into account in the Monte Carlo.

5.4.2 Modelling detector response

The detector MC uses the parametrisations described above to randomly select the longitudinal behaviour and muon content of each shower. In addition, the event geometry (R_p and track vector) is randomised.

Since the HiRes/MIA system did not feature a genuine hybrid trigger, we do not implement hybrid triggering in the MC. Instead, we first check for a MIA trigger (since any event close enough to trigger MIA is almost certain to trigger HiRes), then for a HiRes trigger. If both detectors are triggered the event is kept.

The MIA part of the simulation is done by sampling the LDF parameters and calculating the resultant number of muons in each counter. This number is then Poisson–fluctuated. Each muon has its arrival time sampled according to the parametrisation of Eq. 5.13. Background muons are randomly generated at a mean rate of 5 Hz. The simulation takes account of dead counters and the counter efficiency of 93%.

The arrival times of all muons (shower and background) are sorted, taking into account cable length delays, and a test for a patch level trigger (3 triggered counters in a patch) is performed. The pulses from patch level triggers are time sorted and a detector level trigger is formed if the 6 patch requirement is met.

The HiRes part of the simulation begins by taking a Gaisser–Hillas function with parameters sampled according to the procedure described above. The production and transport of fluorescence and Cherenkov light is modelled in detail for points spaced 0.04° apart along the shower axis. We assume that the lateral structure of the shower follows the NKG formula, and accordingly calculate its

effect on the spot size, for the fluorescence component only. The lateral distribution of Cherenkov light was not incorporated into the simulation. The night sky background is also taken into account. We assume Poisson fluctuations in both the signal and the noise.

After modelling the light production, the MC calculates the number of photons at the tube face by means of a ray tracing method. The mirror efficiency and effective area (there is some obscuration by the PMT cluster) are taken into account, as are the PMT gain and quantum efficiency and the filter transmission (see Fig. 5.6). The MC then calculates charge integrals and triggering times for each tube, and implements the subcluster and mirror triggering conditions as described above.

If both HiRes and MIA are triggered, the event data for triggered tubes and muon counters are read out in the standard DST format. These events can then be reconstructed using the algorithms described above.

5.5 Detector Resolution

To study the detector resolution, we generated several thousand events using the hybrid MC. 8000 proton showers and 4000 iron showers were generated, with an artificially flat E^{-2} differential spectrum in order to obtain as many events for analysis as possible at the higher end of the available energy window. All results were later reweighted as appropriate to reflect the true spectrum ($\sim E^{-3}$). Events were generated over the range [3×10^{16} eV, 5×10^{18} eV]. More proton events than iron were generated because the intrinsic fluctuations for protons are greater.

Events were generated with random zenith, azimuth and core location. Shower cores were restricted to be within 1.5 km of the centre of MIA, as cores landing further out than this would have little chance of triggering MIA.

Several cuts were devised to optimise the detector resolution by eliminating poorly reconstructed events, taking care not to bias the parameters of interest.

5.5.1 Data Quality Cuts

The basic cuts, which eliminate obviously poor quality events, are as follows [134]:

- events pass the hybrid trajectory reconstruction procedure (`hbrd_traj`, described in section 5.2.3)
- number of hit MIA counters > 40
- track length (angle subtended by first and last tubes in event) $> 15^\circ$

In addition, the following standard cuts are applied:

- track length $> 20^\circ$. It was found that tightening the track length cut improved $X_{\rm max}$ resolution.
- $X_{\rm max}$ is bracketed, *i.e.* $X_{\rm low} < X_{\rm max} < X_{\rm high}$, where $X_{\rm low}$ and $X_{\rm high}$ are the shallowest and deepest points seen by the detector — this criterion ensures that $X_{\rm max}$ is contained within the detector field–of–view
- grammage subtended by track > 250 g/cm^2 — ensures that enough of the shower development curve is seen for a good profile fit
- estimated error in $X_{\rm max} < 50$ g/cm^2. There are two errors in $X_{\rm max}$. The first is the statistical error in the profile fit. The second results from the uncertainty in the reconstructed geometry. We require that both of these errors be less than 50 g/cm^2.
- $\chi^2_{\nu-2} < 10$, *i.e.* χ^2 per degree of freedom for profile fit is less than 10
- minimum viewing angle $> 10^\circ$ — removes events which are likely to have a large amount of Cherenkov light contamination. The minimum viewing angle is defined as the smallest angle between the shower axis and the tubes viewing the track.

- $R_P^{\rm MIA} < 2000$ m, *i.e.* distance from shower core to centre of MIA is less than 2 km. This ensures that events with good reconstructed geometry are retained, thus improving $X_{\rm max}$, energy and N_μ resolution.

Three further cuts ("muon cuts"), in addition to those above, can be imposed to improve the N_μ and $\rho_\mu(600)$ resolution:

- 300 m $< R_P^{\rm MIA} <$ 1000 m — this aids in accurate determination of $\rho_\mu(600)$. The lower bound removes events which saturate the detector (and therefore bias N_μ and $\rho_\mu(600)$), while the upper bound eliminates events which are likely to have poorly measured $\rho_\mu(600)$.

- nhit < 700 — nhit is the total number of hit counters (including accidental hits). This cut removes a reconstruction bias near detector saturation.

- nhit > 80 — this marginally improves N_μ and $\rho_\mu(600)$ resolution, but at the expense of reducing the small number of events available for analysis.

5.5.2 Resolution results

The resolution functions for several physically important parameters are shown below. The mean and sigma of each (resulting from a gaussian fit, unless otherwise stated) is given in Table 5.1. The convention employed here is that error = (reconstructed - MC) or (recon - MC)/MC, as appropriate. The results in this section were obtained under the assumptions of the QGSJet model, although the conclusions if Sibyll is used are not substantially different in this context.

Several points are worth noting here. It seems that HiRes/MIA systematically underestimates the muon content (both total muons and density at 600 m). This may be due in part to the assumptions made in the analysis regarding the muon lateral distribution.

The $\rho_\mu(600)$ resolution is not significantly improved by demanding 80 hit counters, and carries the cost of further reducing a sparse data set. For the real data,

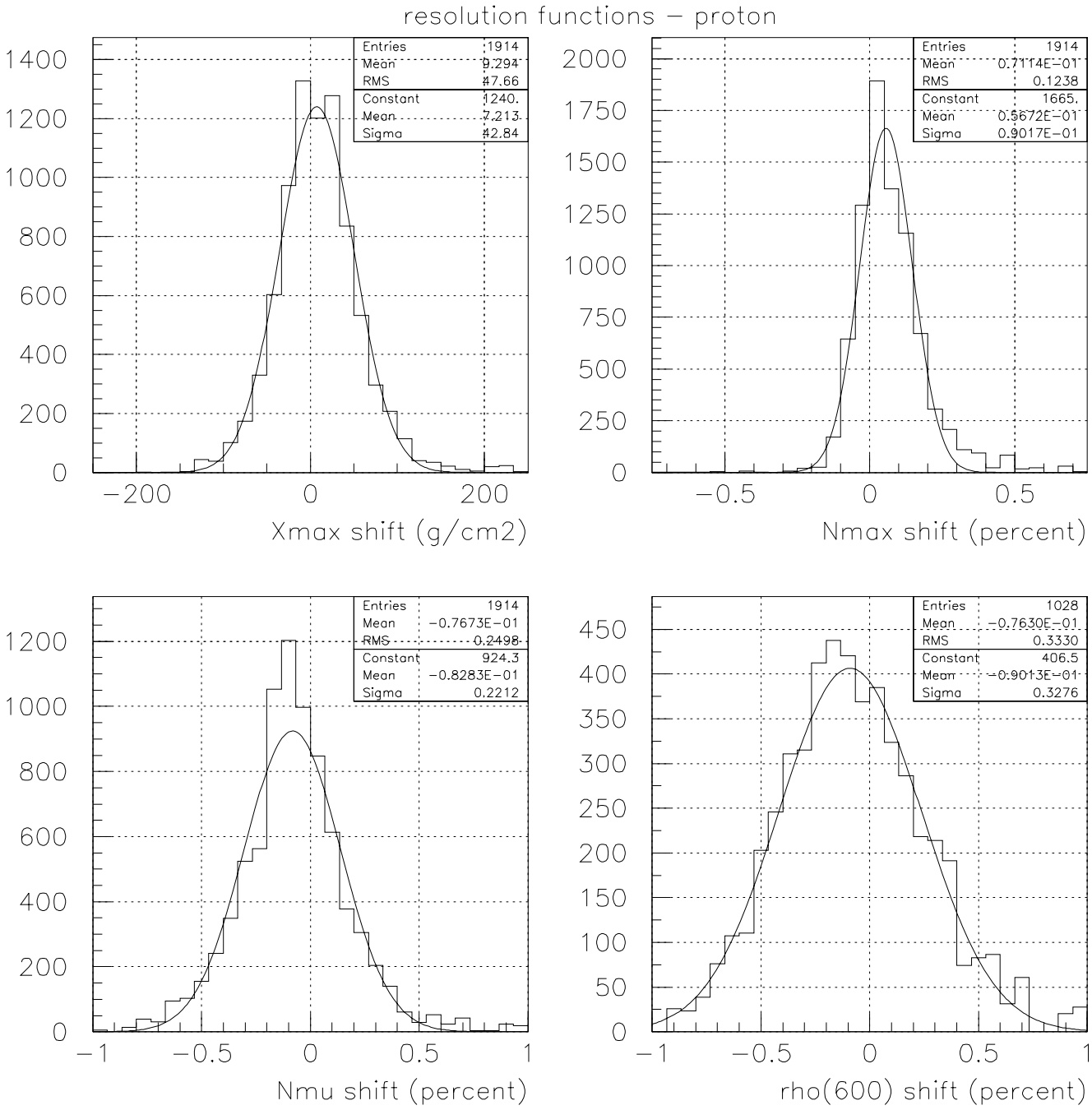

FIGURE 5.13. $X_{\max}$, $N_{\max}$, N_μ and $\rho_\mu(600)$ resolution for proton showers. 1914 of 4788 events passed the standard cuts of Section 5.5.1. Of those, 1028 returned non–zero values of $\rho_\mu(600)$ (see discussion in text).

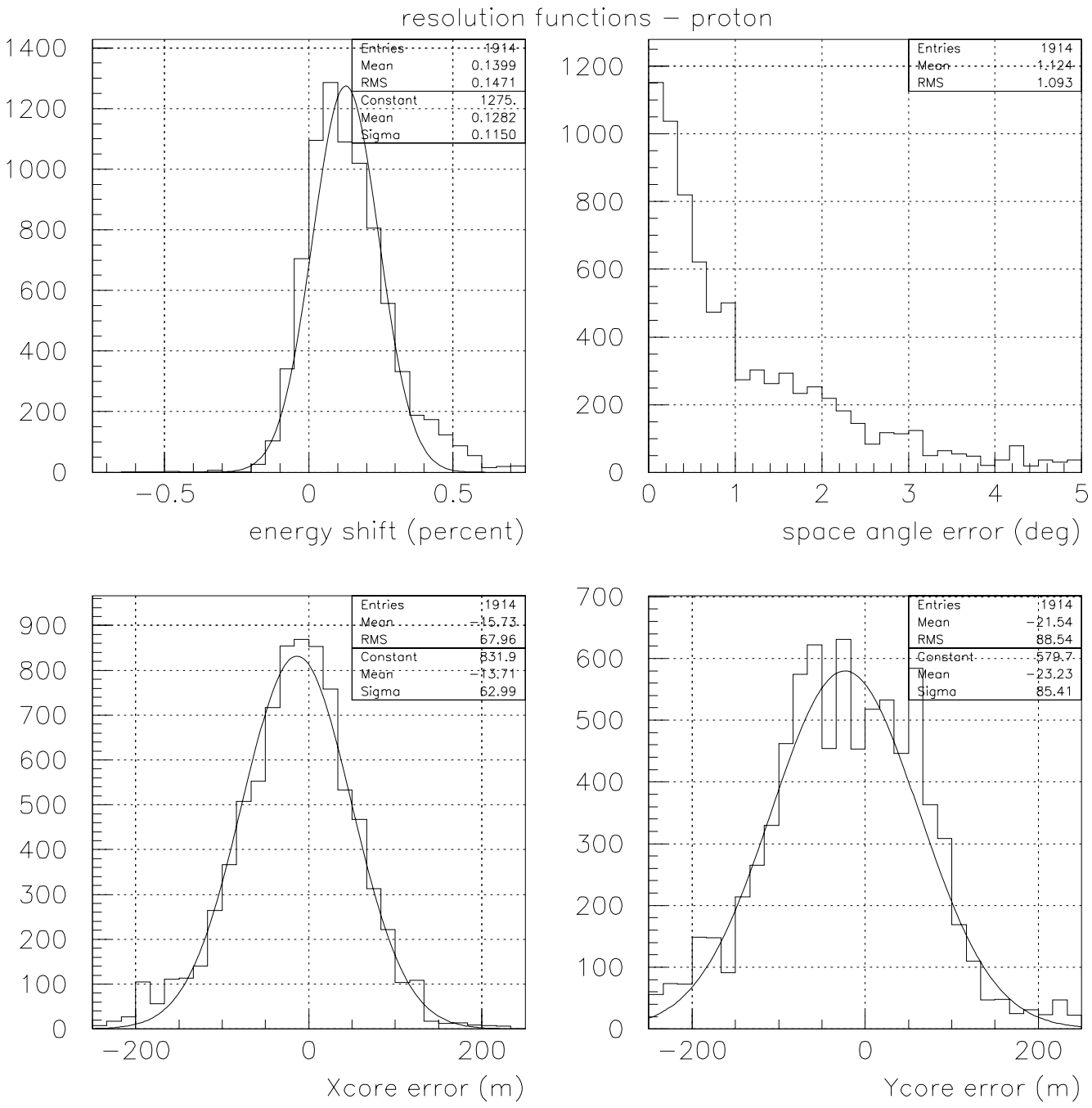

FIGURE 5.14. Proton again, but this time the energy resolution, as well as the core location error and space angle error, defined as the angle between the MC and reconstructed directions.

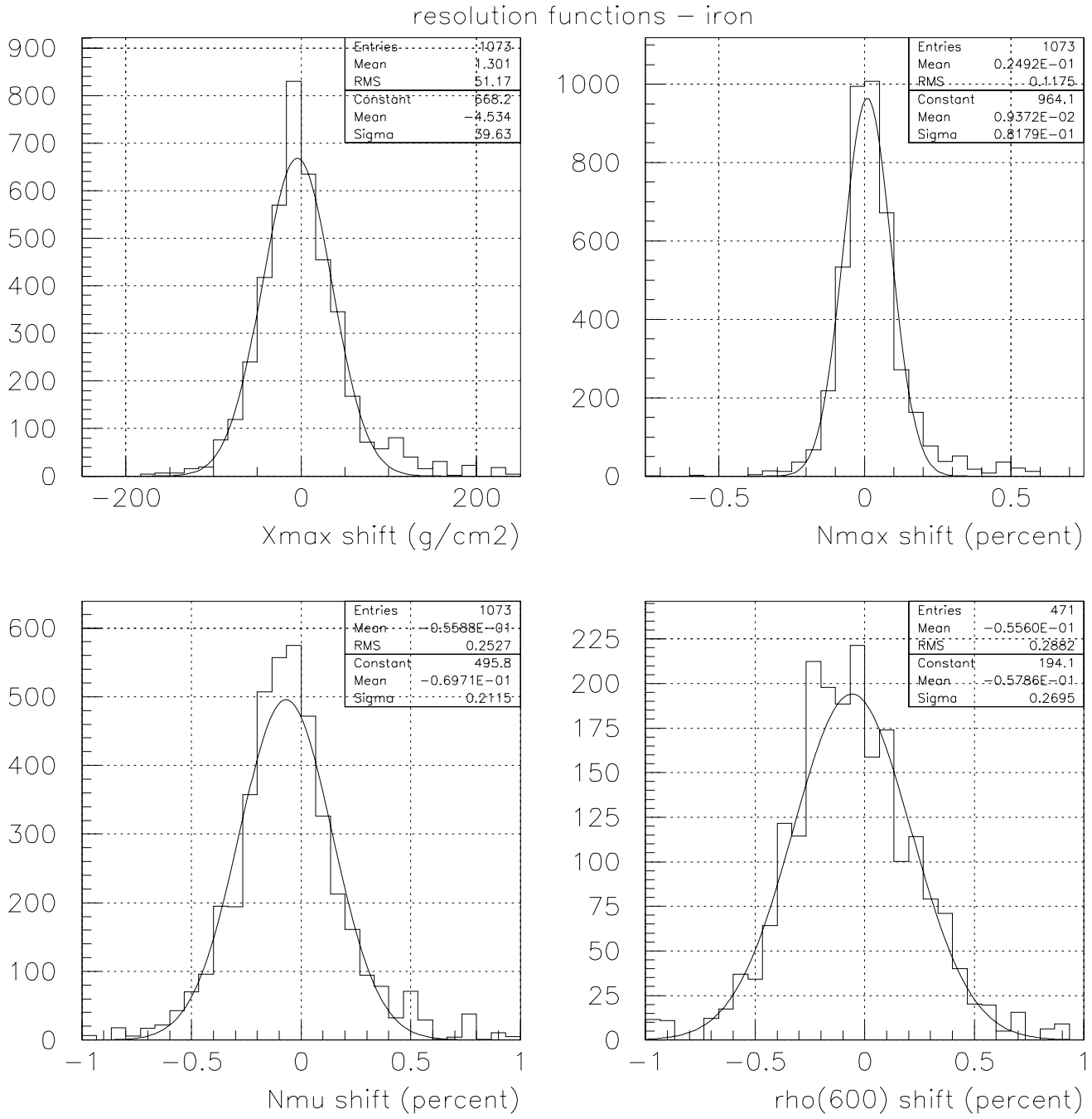

FIGURE 5.15. As for Fig. 5.13, but for iron showers. 1073 of 2698 events survive the standard cuts. Of these, only 471 have a non–zero $\rho_\mu(600)$.

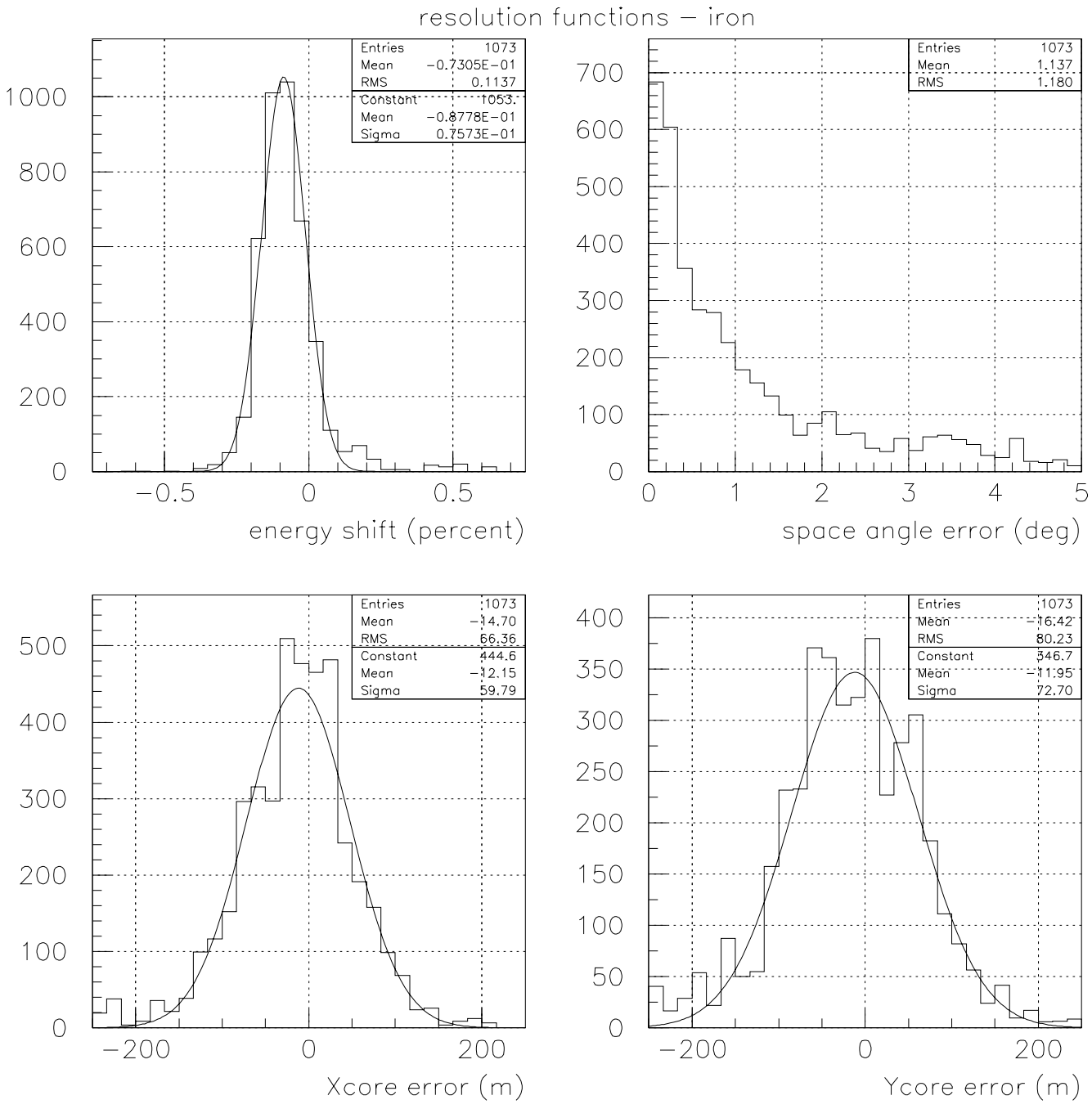

FIGURE 5.16. As for Fig. 5.14, but for iron showers.

	proton		iron	
	σ	mean	σ	mean
$X_{\max}$ (g/cm^2)	43	7.2	40	-4.5
energy (%)	11.5	13	7.6	-8.6
$N_{\max}$ (%)	9.0	5.7	8.2	0.93
$x_{\rm core}$ (m)	63	-14	60	-12
$y_{\rm core}$ (m)	85	-23	73	-12
N_μ (%)	22	-8.3	21	-7.0
$\rho_\mu(600)$ (%)	33	-9.0	27	-5.8
N_μ (nhit $>$ 80) (%)	17	-7.3	17	-5.8
$\rho_\mu(600)$ (nhit $>$ 80) (%)	29	-5.4	25	-5.3
median space angle	0.88°		0.83°	

TABLE 5.1. Mean and sigma of resolution functions for an E^{-3} differential spectrum under the standard cuts described in the text. nhit $>$ 80 indicates that an additional cut requiring 80 hit counters was imposed.

it is perhaps inadvisable to apply this cut. We do not apply it in achieving the composition results in this thesis.

The geometrical reconstruction accuracy is comparable to (but not quite as good as) that attained in the stereo reconstruction of prototype data by Wilkinson [118]. That study reconstructed laser shots viewed by both HiRes detectors.

The $X_{\max}$ and energy resolution obtained with HiRes/MIA are better than those obtained with the stereo Fly's Eye ($\sim$ 40 g/cm^2 and 10%, compared to $\sim$ 50 g/cm^2 [54] and 25% [146]). The opposite trends in the systematic energy shift for protons and iron are due to the composition–independent missing energy correction applied in the analysis. As a consequence, iron energies are systematically underestimated, while proton energies are systematically overestimated.

As a final remark, we compare the energy, R_p and zenith angle distributions for Monte Carlo events after reconstruction and cuts with the corresponding distribu-

tions for the data (Fig. 5.17, Fig. 5.18). Clearly there is good agreement between them, proving that the hybrid MC is an accurate depiction of the detector operation. There is a slight difference between the zenith angle distributions for proton and iron events, because the $X_{\max}$ bracketing cut introduces a slight bias against near–vertical proton showers.

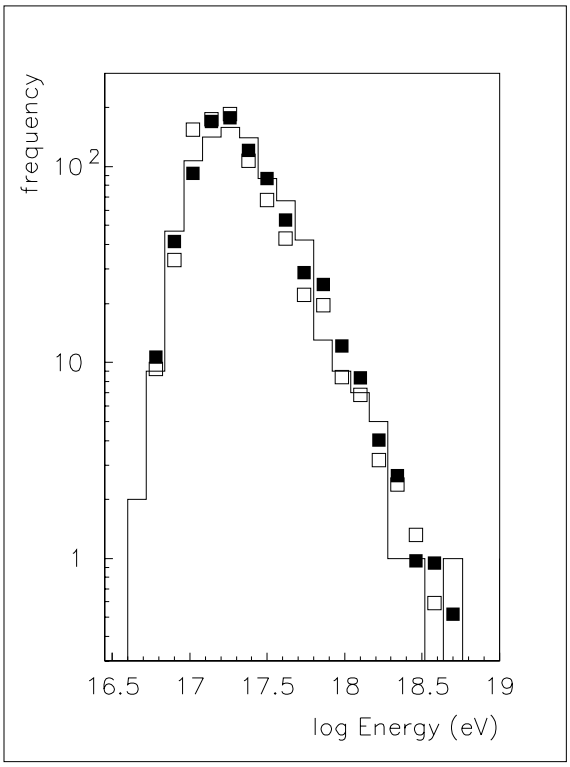

FIGURE 5.17. Energy spectrum for the HiRes/MIA data set (solid line) with proton showers (solid squares) and iron showers (open squares) superimposed. The MC histograms have been rescaled to have the same area as the data.

5.6 Study of tube pointing directions

For accurate reconstruction of EAS trajectories and energies, precise knowledge of the pointing direction of each tube in each PMT cluster is required. The usual technique employed by HiRes is to measure the mirror pointing direction using surveying equipment, and deduce the pointing directions of individual pixels

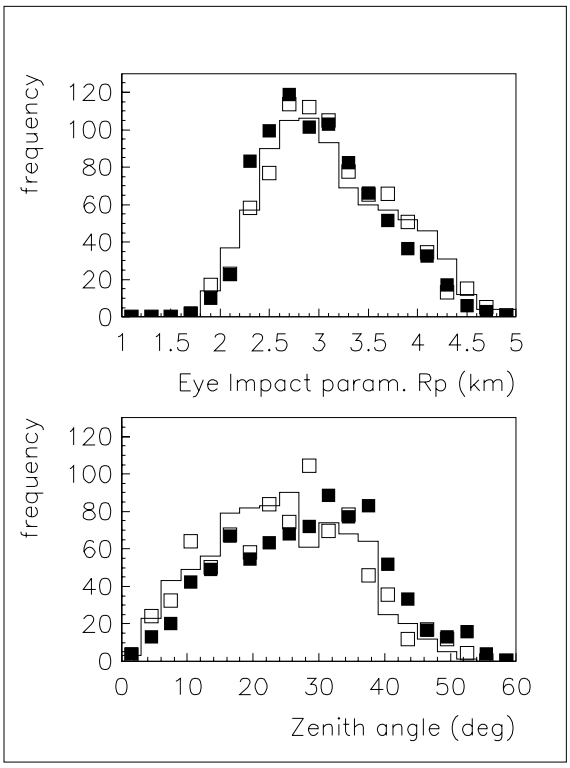

FIGURE 5.18. R_p and zenith angle distributions for data (solid lines) and simulations (points). Histograms have been scaled to have the same area.

accordingly by taking into account their position in the cluster and the distance of the cluster from the mirror. Unfortunately, this method cannot account for small shifts in the position of tubes within the cluster, or of the cluster as a whole. These shifts could have a significant effect on estimation of the fluorescence part of the signal recorded by each PMT, since the tube response profile is approximately gaussian as a function of off–plane angle if one ignores optical aberrations (in particular, coma). This being the case, the relative uncertainty in the tube signal is given by

$$\frac{\Delta S}{S} = -\frac{x\Delta x}{\sigma^2}, \tag{5.14}$$

S being the signal, x the offplane angle and σ the width of the PMT response function. Taking $\sigma = 0.3$ [147], it is seen that an error in tube pointing direction as small as a tenth of a degree can result in dramatic underestimation of the signal,

e.g. 22% at an offplane angle of 0.2°. For tubes far from the plane, this can pose a significant problem.

To study the accuracy or otherwise of the surveyed pointing directions, a device called the Laserscope was developed at the University of Adelaide [148]. Its primary function was to aid in monitoring the atmosphere within the detector volume, but it also proved useful in the context described here. The Laserscope consisted of a frequency–tripled YAG laser mounted on a Meade LX–200 telescope. The laser was housed with an energy probe inside a box which was attached to the telescope via a custom built frame. A 5kg counterweight was added to balance the weight of the laser box. The Laserscope pointing was calibrated by aligning the telescope with visible stars. The pointing accuracy attainable by this method was 5 arcmin [148].

5.6.1 The Wall of Fire

A survey of tube pointing directions using the Laserscope was carried out by firing a large number of laser shots across the field of view of the detector on several nights in 1996. The study described here uses data from March 21 and October 12. In the former case, the Laserscope was located at (1659.73, 2906.63, -131.5) in the standard HiRes coordinate system (all distances in metres from the origin on Five Mile Hill). Three shots were fired at each zenith angle, at an azimuth of 120°, and the Laserscope was moved in 0.1° steps. This "wall of fire" was repeated on October 12, when the Laserscope was placed at (1459.12, 6708.90, -2.50). On this occasion groups of ten shots were fired at trajectories spaced $\frac{1}{6}$th of a degree apart in the plane of the mirror. This was done to provide more even coverage of the mirrors in the upper ring, which were poorly sampled (very few events per PMT) in the March 21 sweep. These laser shots were also used to test the HiRes stereo reconstruction algorithms developed by Wilkinson [118].

The data from each sweep of the detector are passed through the standard HiRes filtering software to ensure that only "track–like" events are retained. Not all of these events will be laser shots — some (very few) real cosmic ray events

will also be recorded. The reduced data set is then used in further analysis.

5.6.2 Extracting tube pointing directions

Some typical PMT response profiles are shown in Fig. 5.19. In principle, the peak of the response should occur when the track passes through the tube centre, *i.e.* at an offplane angle of 0°. In practice, this is not observed — for example, tube 16 in Fig. 5.19 has its peak near 0.1°. This provides some indication of how far its true pointing direction differs from the direction assumed in the analysis software.

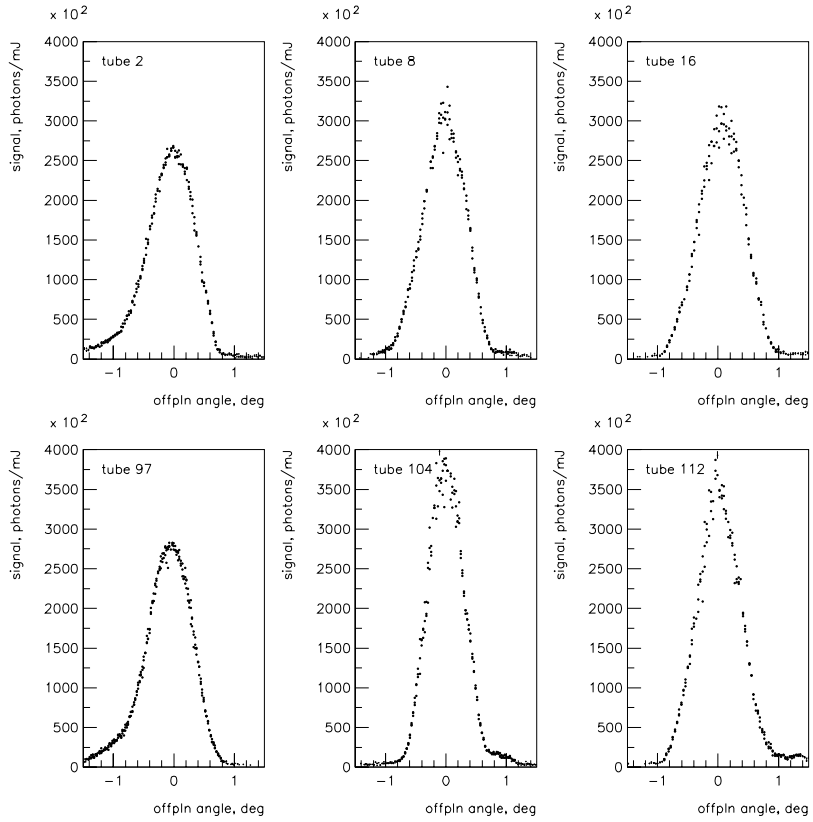

FIGURE 5.19. Tube response profiles for mirror 5 from the March 21st scan of the HiRes I prototype. The PHOB numbers have been scaled by the laser energy (as measured by the radiometer) to take account of fluctuations in the laser output.

For each tube in the detector, I match event times with the times recorded in

the laserscope firing log. Since the track geometry is known *a priori*, an offplane angle can be calculated for each shot using the nominal tube pointing direction. This allows one to plot signal (in photons, as recorded in the PHOB bank) as a function of offplane angle. Since the laser output varied over the course of the run (see Fig. 5.20), this had to be normalised to the laser energy for each shot. In a sense the absolute scale is not relevant for this study, since we are interested only in the shape of the tube response.

Supposing that we know the geometry of the track that produces the maximum tube signal for each of two Laserscope positions, we can calculate the true pointing direction by finding the intersection of the corresponding shower–detector planes. This is simply the normalised cross product of the two plane normals. By definition, this will produce an offplane angle of zero for both tracks, since the plane normals are mutually perpendicular to their cross product. The problem therefore reduces to finding the "maximum track" for each sweep for a given tube.

The tube response profiles are approximately gaussian near their peak. The offplane angle corresponding to the peak position can be found by performing a gaussian fit over the range $[-0.5°, 0.5°]$. Outside this range, the tails due to mirror aberration start to become important and can bias the fit.

Once the peak offplane angle is found, one can determine the zenith, θ, and azimuth, ϕ, of the maximum track. An immediate problem arises because we are trying to find two unknowns with only one constraint. However, we are saved by the fact that we know how the Laserscope moved between shots during each sweep. This allows us to interpolate in θ and ϕ between shots corresponding to angles either side of the maximum to find the geometry of the maximum track. This having been found for both sweeps, the true tube pointing direction can be calculated.

5.6.3 Pointing directions from Laserscope data

An example of tube pointing errors derived from Laserscope surveys are shown below. Mirror 7 is chosen here because it was the mirror which was best sur-

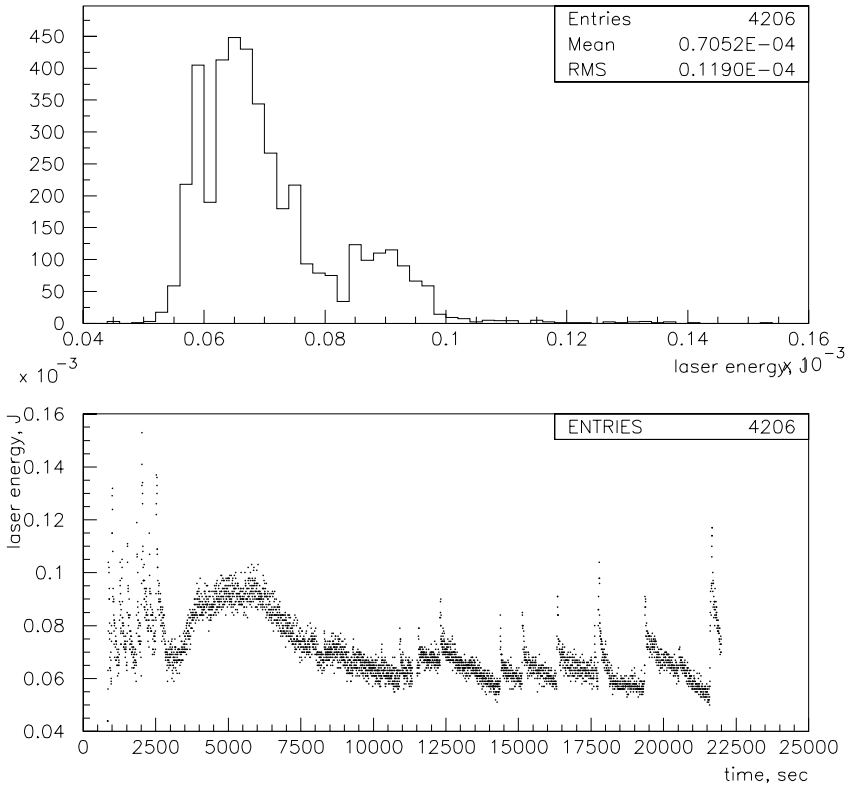

FIGURE 5.20. Distribution of laser energies (top) and output as a function of time (bottom) for the March 21st run of the Laserscope.

veyed. Two separate high resolution sweeps from different Laserscope positions were available for this mirror. In Figs. 5.21 and 5.22, we show the errors obtained assuming two different sets of nominal pointing directions. The first set assumed surveyed mirror directions which were used up until September 1995 (Fig. 5.21), while the other used a more recent result (Fig. 5.22). The improvement between the two surveys is emphasised by Fig. 5.23.

This study shows that, for mirror 7 at least, the surveyed directions are not too far removed from those derived from Laserscope sweeps. Unfortunately, there were several sources of error in this particular data set. The nature of the March 21st sweep meant that the lower ring mirrors were extremely well sampled, but the higher rings were not. The October 15th sweep attempted to rectify this by

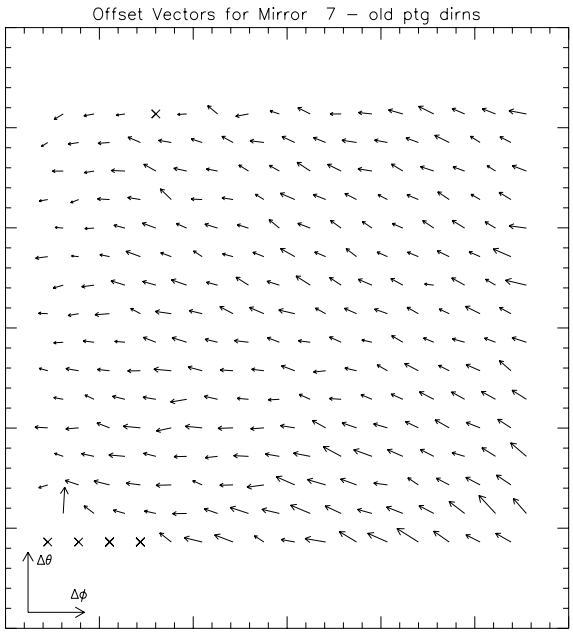

FIGURE 5.21. Error in tube pointing direction. The error for each tube is represented as a vector. The horizontal axis is the azimuth error, and the vertical axis the zenith angle error. The scale is such that each small division represents 0.25°. Crosses denote tubes for which the procedure described in the text failed.

using a constant step size in the plane of the mirror, but was hampered by "sag" in the Laserscope. The output of the YAG laser used on March 21st had dropped off dramatically enough that it was temporarily out of use, and so a Nitrogen laser was employed in its place. This was so heavy that it caused the Laserscope alignment to be out by up to several tenths of a degree, dependent on zenith angle (worse at large elevations). This meant that the derived pointing directions would be questionable at best.

Provided that good pointing accuracy of the Laserscope can be guaranteed, the technique discussed here is a good method of probing tube pointing directions. Other methods, such as using the positions of bright stars, are currently being investigated.

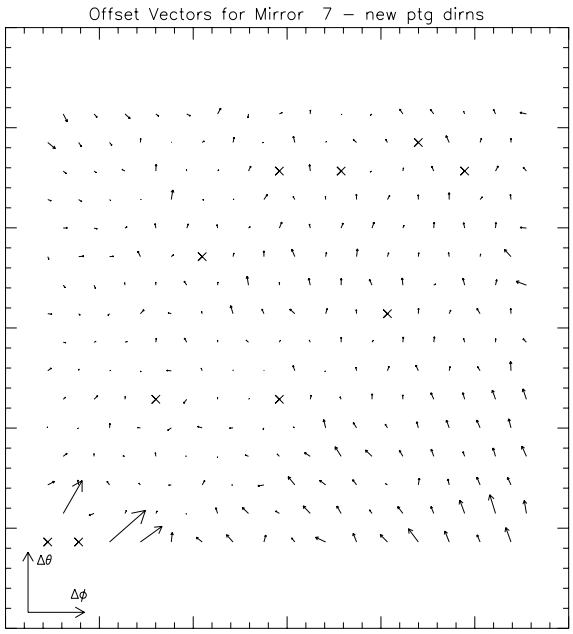

FIGURE 5.22. As for Fig. 5.21, but with the nominal directions derived from a later survey of mirror pointing directions.

5.6.4 Comparison with ray tracing calculation

A further use of Laserscope is examining the accuracy of the ray tracing table used in the analysis and detector Monte Carlo. Tube response profiles obtained from laser shot data can be compared with what would be expected from ray tracing (convolved with the intrinsic PMT response function, etc.). We show such comparisons in Figs. 5.24 and 5.25 below.

Note that the profiles have been normalised to unity in each case. Clearly the ray tracing does a reasonable job of reproducing the data, except at large offplane angles ($\pm 1°$). It is perhaps unsurprising that this is the case, since the error in the signal increases as a function of offplane angle (see Eq. 5.14). Additional effects such as multiple scattering and mirror defects complicate modelling of the signal at large offplane angles.

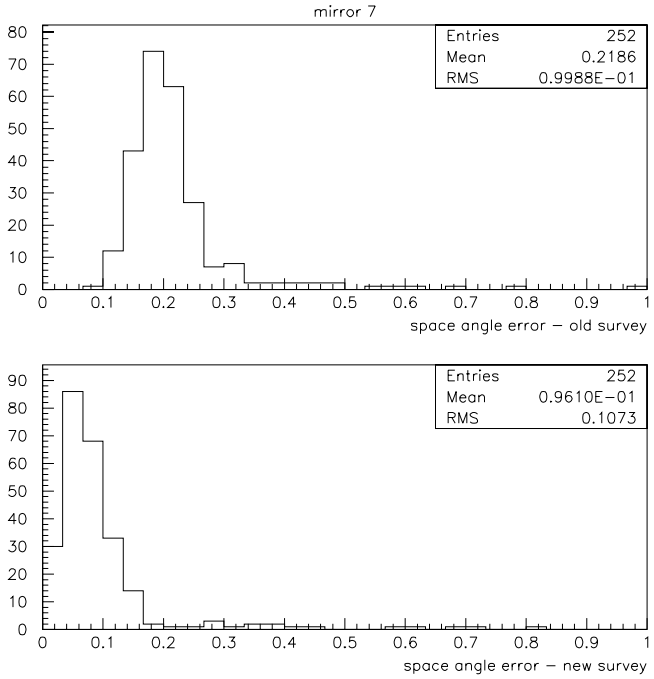

FIGURE 5.23. Distribution of space angle errors, defined as the angle between the nominal and "true" pointing directions.

5.7 Atmospheric density profile

The atmospheric density profile (pressure as a function of height) is required knowledge for HiRes reconstruction. HiRes measures the light flux as a function of height, but determination of $X_{\max}$ (composition) and energy requires the flux as a function of column density, or equivalently, atmospheric pressure. Usually some model atmosphere is assumed (US Standard Atmosphere, parametrisations of MODTRAN simulations), but often this does not take account of seasonal variation. An indication of the problem is given in Fig. 5.26.

The model value is derived from a parametrisation of the US Standard Atmosphere [72]. The data are obtained from Radiosonde measurements. These are taken every twelve hours by balloons released at Salt Lake City airport. The 'sondes directly record temperature, dewpoint, wind speed and direction, and pressure. Height is inferred by using the hydrostatic equation. This is the so–called

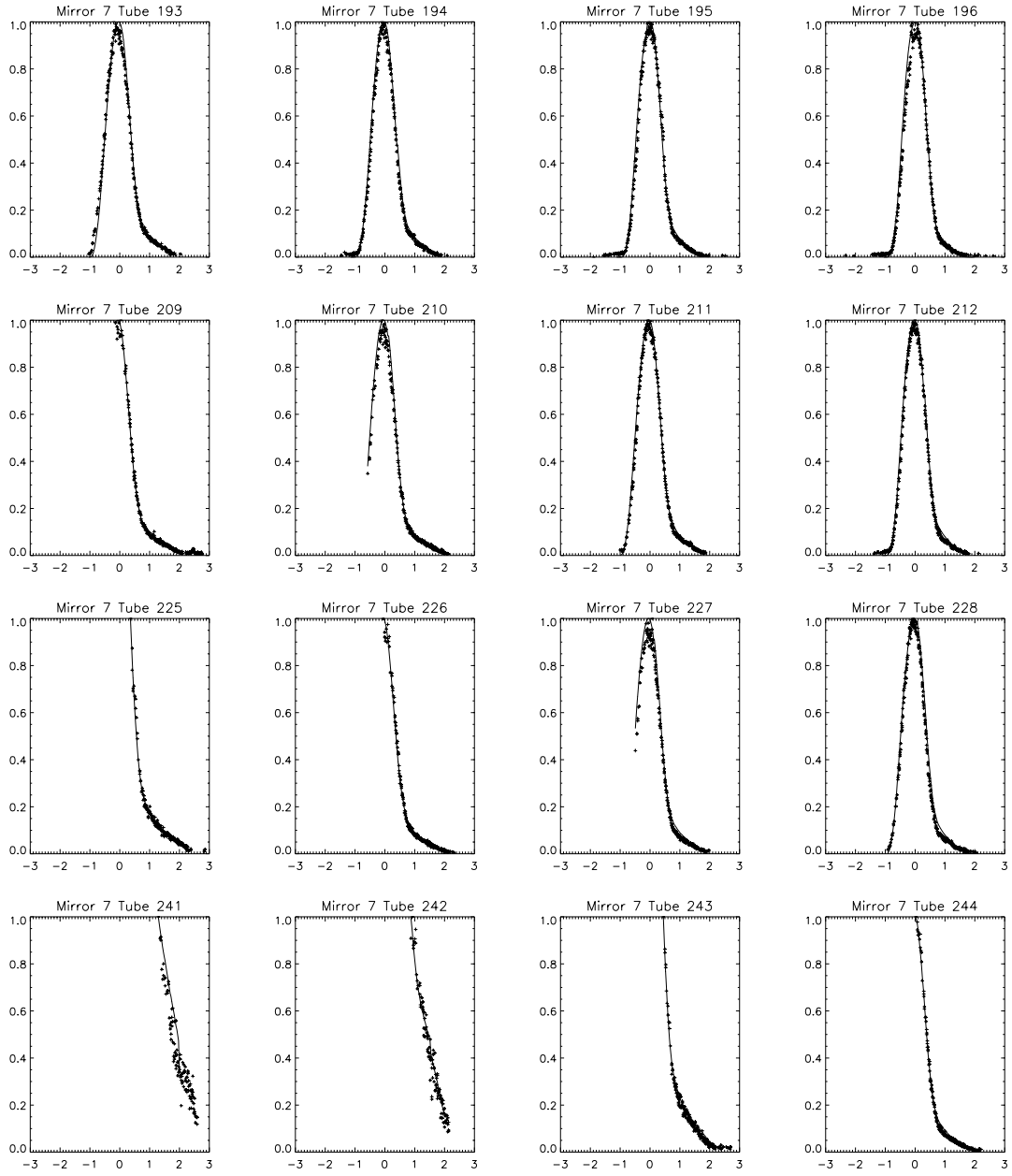

FIGURE 5.24. Comparison of measured tube profiles (+) and raytraced profiles (solid lines) for subcluster 13 of mirror 7. Profiles have been normalised to have unit height.

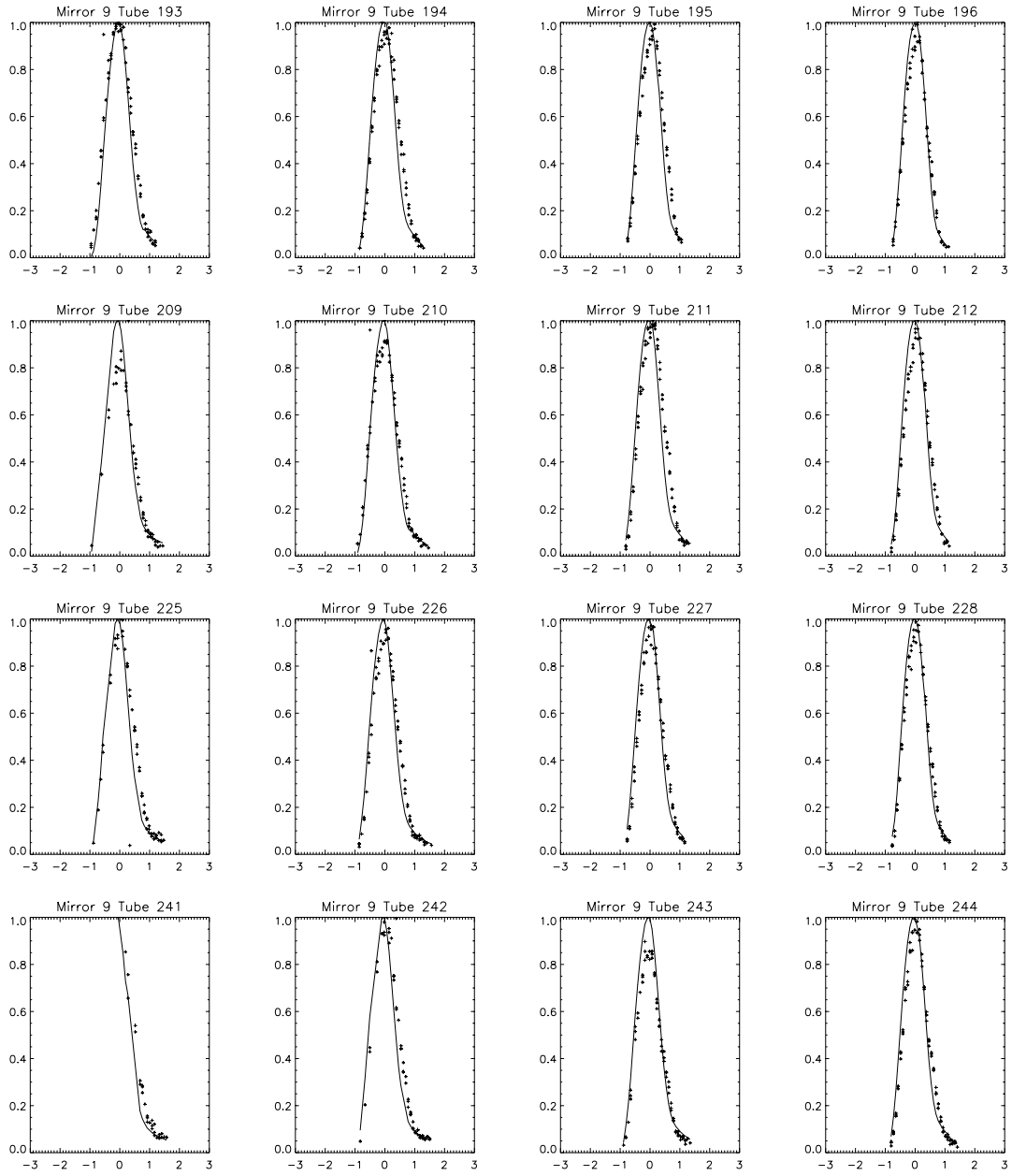

FIGURE 5.25. As for Fig. 5.24, but for subcluster 13 of mirror 9.

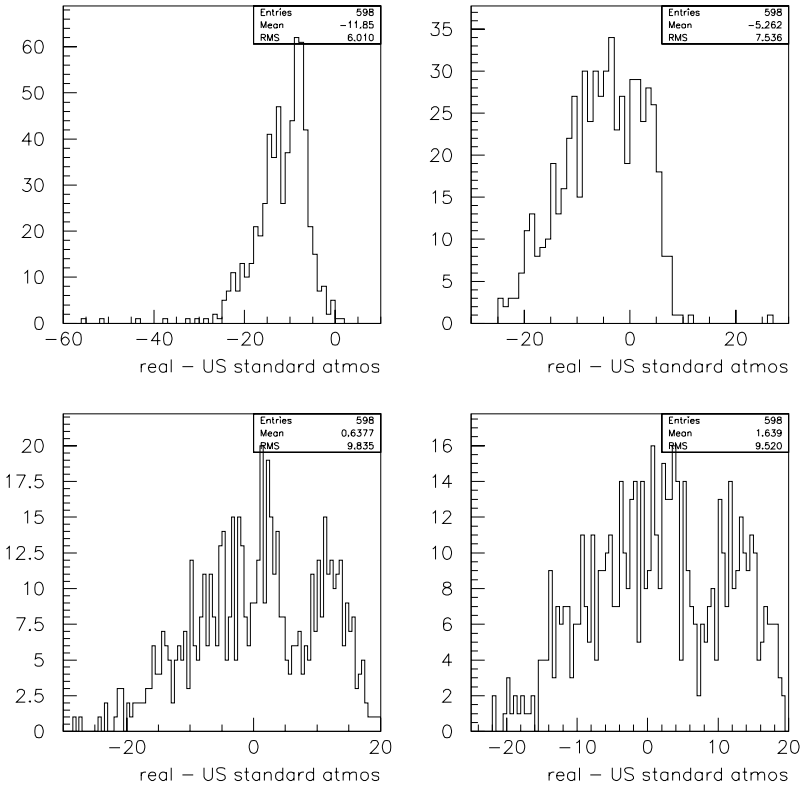

FIGURE 5.26. Measured atmospheric pressure minus the value predicted by a parametrisation of the US Standard Atmosphere (1976), in units of millibars. The four plots are for a height of 2km, 4km, 8km, 10km above sea level, respectively.

"geopotential height", which is almost identical to the geometrical height [149]. Fig. 5.26 represents a year's worth of data.

Since radiosonde measurements are available only every twelve hours, it is not practical to use only these data to obtain pressure profiles. However, if the ground pressure is known in the interim, it may be possible to infer the profile with a reasonable degree of accuracy. If one assumes that the ratio of the pressure at a given height h to the pressure at ground level is constant, then the value of this ratio from the most recent available radiosonde data can be used to scale the current value of the ground pressure, *i.e.*

$$P_h^{\rm now} = \frac{P_h^{\rm radiosonde}}{P_0^{\rm radiosonde}} P_0^{\rm now}. \qquad (5.15)$$

Fig. 5.27 shows the error resulting from this naïve assumption. Here we show the "renormalised" value obtained from Eq. 5.15 subtracted from the real value measured by radiosonde at four different heights above sea level. This demonstrates that the effect on $X_{\rm max}$ resolution would not be large. At a height of 4km, corresponding to a depth of approximately 600 g/cm^2 (a fairly typical value of $X_{\rm max}$ at 10^{17} eV), the standard deviation is 2 g/cm^2, with a systematic shift of less than 1 g/cm^2.

There is scope for improving this type of correction further by including extra local weather information (ground temperature, wind speed, etc.), although the effect on longitudinal profile fitting may not be large enough to warrant it. However, accounting for local atmospheric conditions is crucial for a proper calculation of the shower energy, since the atmosphere within the detector volume strongly affects modelling of the light flux.

5.8 Correlations between composition parameters

A hybrid experiment ought to, in principle, be able to measure composition better than either a surface array or fluorescence eye on its own. One way of doing this is to study correlations between parameters measured by the two different components. To understand what correlations might be present in the data, it is instructive to look at results from EAS simulations, without the detector response folded in. To this end we generated several hundred events using CORSIKA with QGSJet at different energies and zenith angles, and a thinning level of 10^{-5}. For each shower, we output the full list of muons reaching the ground and their weights, as well as their 3–momenta and the time at which they reached ground level (taken to be the HiRes depth of 860 g/cm^2). The fitted values of $X_{\rm max}$, X_0 and $N_{\rm max}$ were also output for each shower.

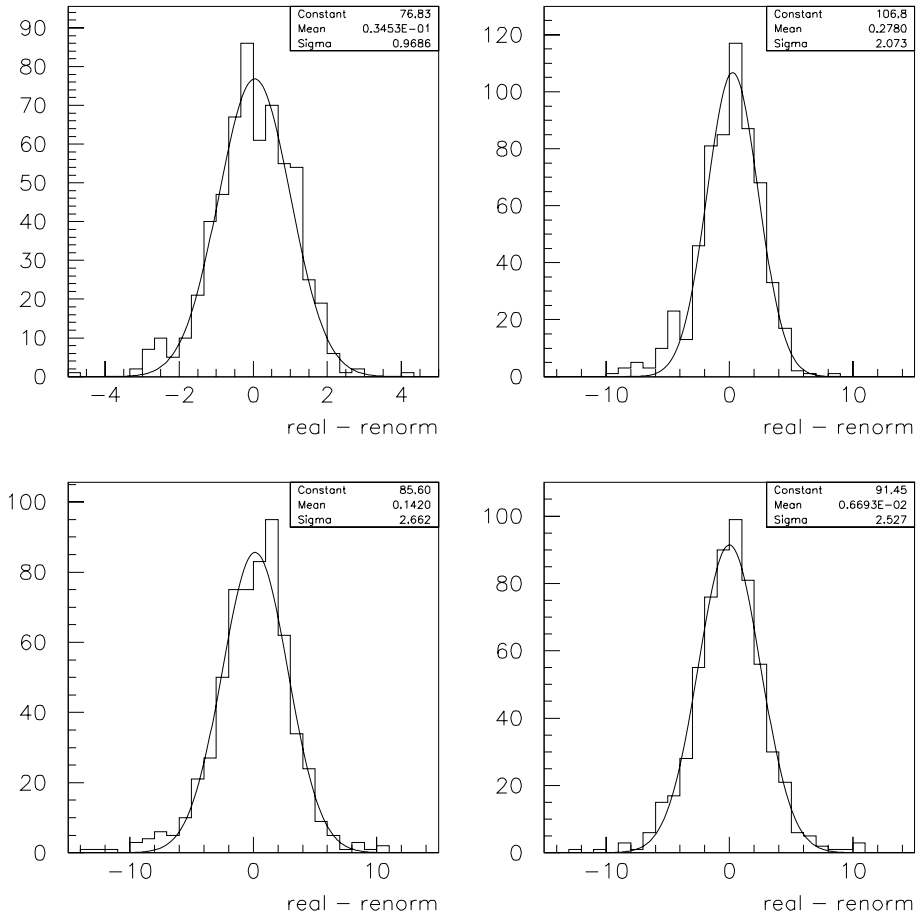

FIGURE 5.27. Error in pressure, in millibars, calculated according to Eq. 5.15, at 2km, 4km, 8km and 10km.

To investigate possible correlations between shower parameters, we calculated the curvature of the shower front for each event. We assumed that the departure from a plane front was quadratic, *i.e.* $\Delta t = ar + br^2$ where Δt is the mean delay from a plane front at core distance r. This form fits the CORSIKA data nicely. We also fit the lateral distribution to the AGASA LDF with the exponents of the various factors (α, β, δ) left as free parameters. The behaviour of the risetime (defined as the time taken to go from the 10% level to the 50% level in a particular radial bin) was also studied. We found from the CORSIKA data that risetime varies with core distance as a power law, *i.e.* risetime $\propto r^{\eta}$. The risetime at a core distance of 500m and the index η were calculated for each shower.

The pairwise correlations of all of the aforementioned muon parameters with each other and with $X_{\max}$, X_0 and $N_{\max}$ were examined. We found no strong correlation except between distance to $X_{\max}$ and risetime at 500 m, a and b respectively. This is illustrated in Figs. 5.28, 5.29, 5.30, 5.31, 5.32, 5.33. Here distance to $X_{\max}$ is calculated by assuming an exponential atmosphere with a scale height of 8 km, *i.e.*

$$d_{X_{\max}} = -H_0 \log\left(\frac{X_{\max}}{X_{\text{ground}}}\right) \sec\theta, \tag{5.16}$$

with $H_0 = 8$km the scale height, $X_{\text{ground}} = 860$ g/cm^2 the atmospheric depth at ground level, and θ the zenith angle of the shower.

A quantitative measure of the (linear) correlation between two parameters x and y is given by the Pearson coefficient:

$$r = \frac{\langle xy\rangle - \langle x\rangle\langle y\rangle}{\sigma_x \sigma_y}. \tag{5.17}$$

Parameters which are 100% correlated will have a Pearson coefficient of ± 1, while completely uncorrelated parameters will give $r = 0$. The probability that a random sample of N uncorrelated points gives a value of $|r|$ greater than that observed is [150]

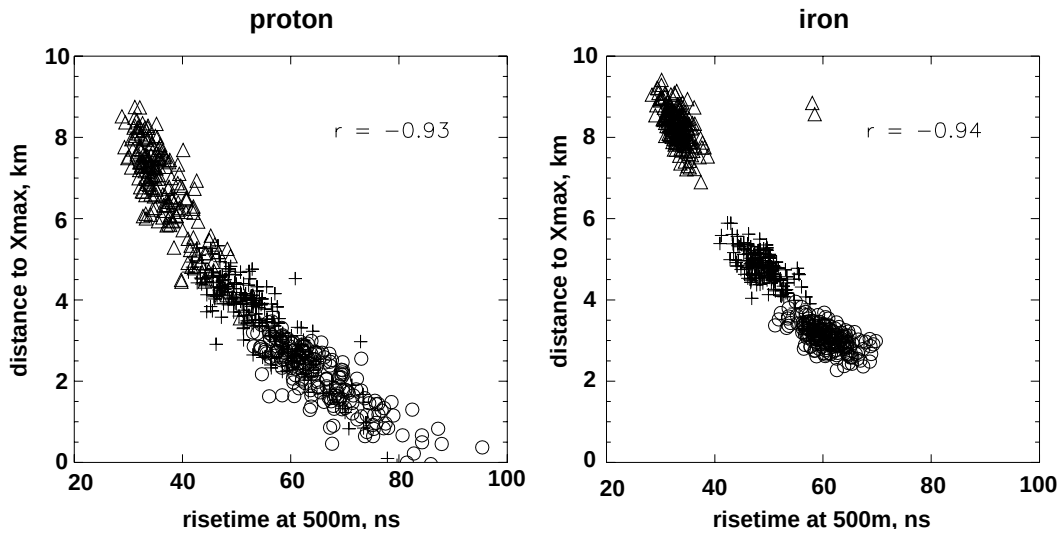

FIGURE 5.28. Distance to $X_{\max}$, $d_{X_{\max}}$, as a function of risetime at 500m from the core for proton (left) and iron (right) showers at 10^{17} eV. △: 0° zenith angle, +: 30°, ○: 45°.

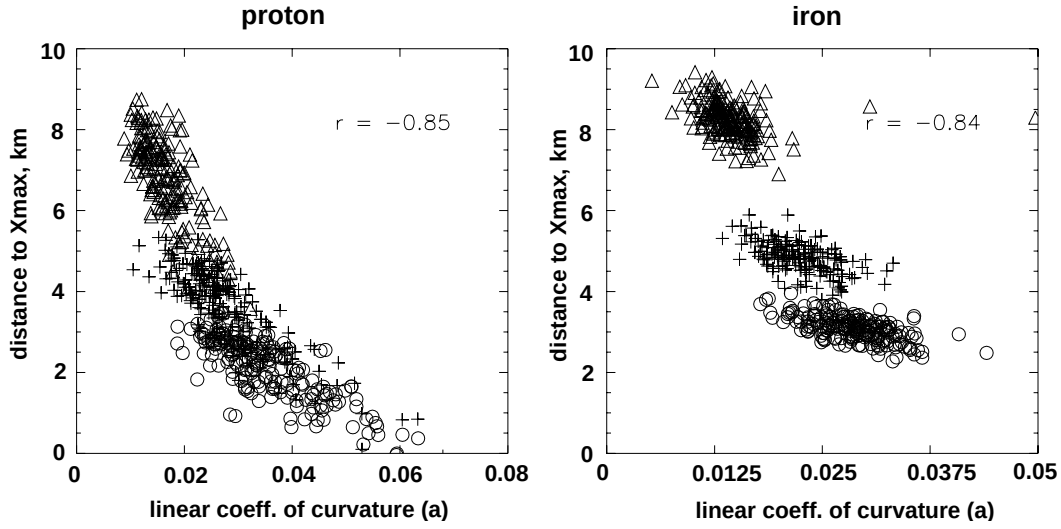

FIGURE 5.29. $d_{X_{\max}}$ *v.* linear part of the shower front curvature at 10^{17} eV.

$$P_c(r,N) = 2\int_{|r|}^{1} P_r(\rho,\nu)d\rho, \tag{5.18}$$

where

$$P_r(\rho,\nu) = \frac{1}{\sqrt{\pi}}\frac{\Gamma[(\nu+1)/2]}{\Gamma(\nu/2)}(1-\rho^2)^{(\nu-2)/2}. \tag{5.19}$$

$\nu = N-2$ is the number of degrees of freedom.

It is obvious by inspection that risetime, a and b are strongly correlated with distance to $X_{\max}$, independent of energy and composition. One can calculate a probability for each according to Eq. 5.18. Unsurprisingly, the probability that the correlation occurs purely by chance is less than 10^{-10} in each case.

As discussed previously in the context of risetime (Chapter 3), the correlation between distance to $X_{\max}$ and the temporal characteristics of the muon component is a geometrical effect. The time dispersion for showers that develop early (larger distance to $X_{\max}$) is smaller than for later–developing showers. As a consequence, early–developing showers will have smaller risetimes at a given core distance, and smaller delays with respect to a plane front.

To investigate whether the correlations observed in CORSIKA simulations would be measurable with HiRes/MIA, we took CORSIKA data and assumed an $X_{\max}$ resolution of 30 g/cm^2. Since the risetime resolution was not known, we varied it to see what effect it would have on the correlation. The CORSIKA values of $X_{\max}$ and risetime were fluctuated assuming a gaussian with a σ equal to the resolution for each parameter. The result is shown in Figs. 5.34 and 5.35. It appears that a risetime resolution of 15 ns or better is required for the correlation to be observable. We did not test whether the correlations with shower front curvature would be observable, since HiRes/MIA was unlikely to be sensitive to such effects. For example, the delay at a core distance of 300m for a shower with $X_{\max} \sim 600$ g/cm^2 would be of the order of 10 ns, not much more than the MIA TDC resolution of 4 ns.

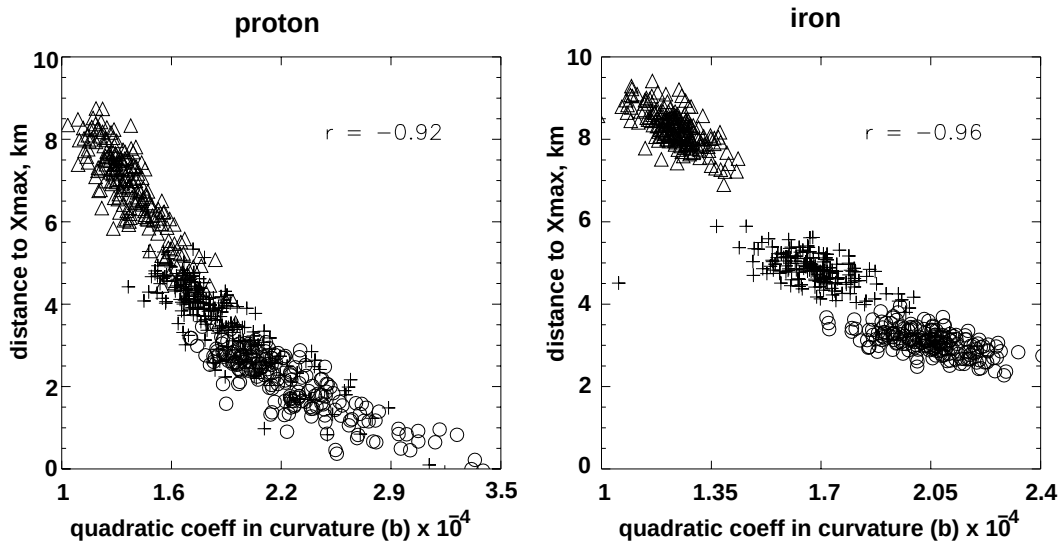

FIGURE 5.30. $d_{X_{\max}}$ *v.* quadratic part of the shower front curvature at 10^{17} eV.

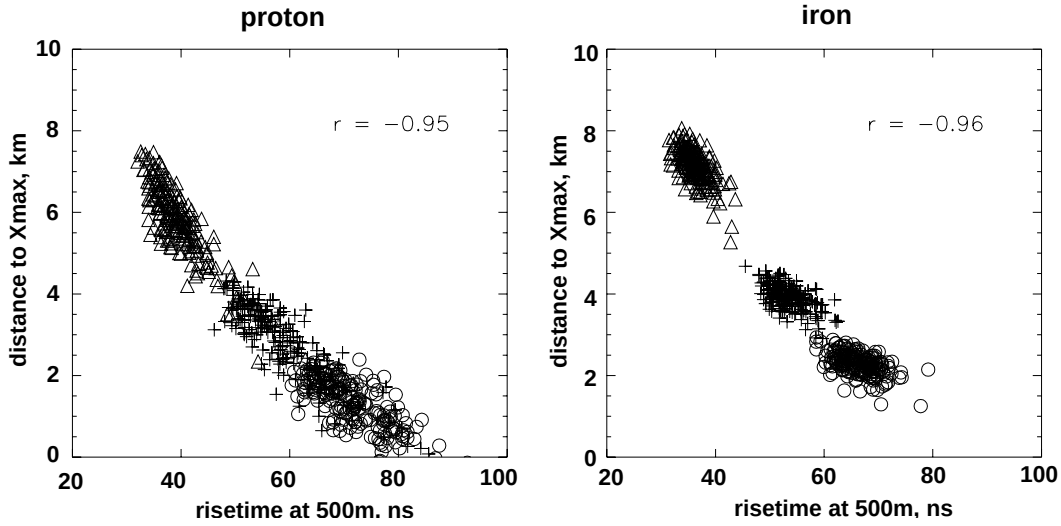

FIGURE 5.31. $d_{X_{\max}}$ *v.* risetime at 10^{18} eV.

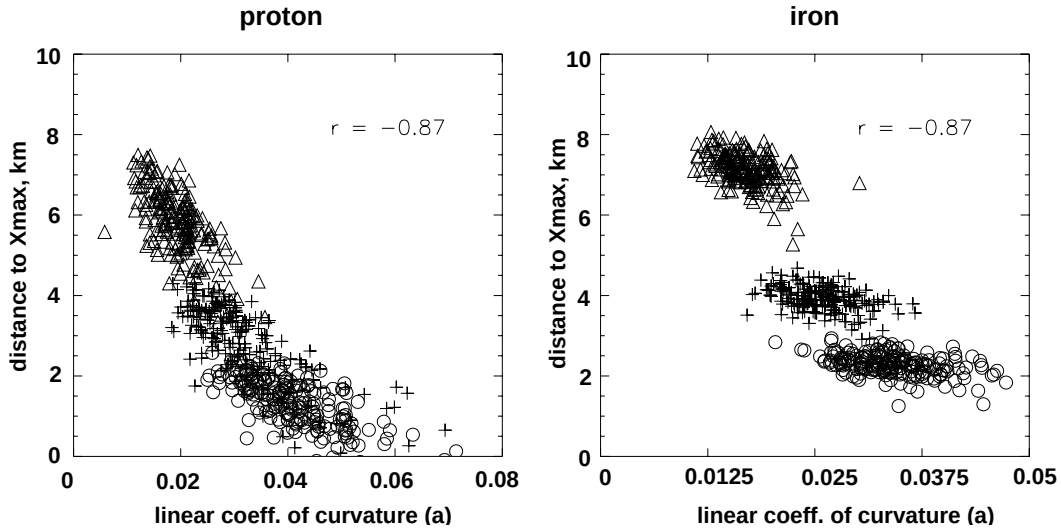

FIGURE 5.32. $d_{X_{\max}}$ *v.* linear part of the shower front curvature at 10^{18} eV.

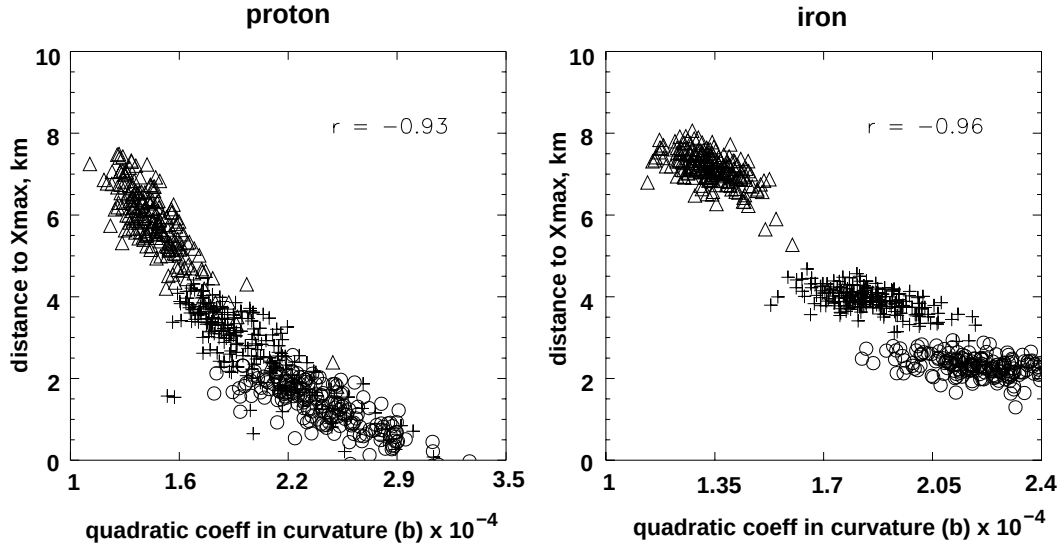

FIGURE 5.33. $d_{X_{\max}}$ *v.* quadratic part of the shower front curvature at 10^{18} eV.

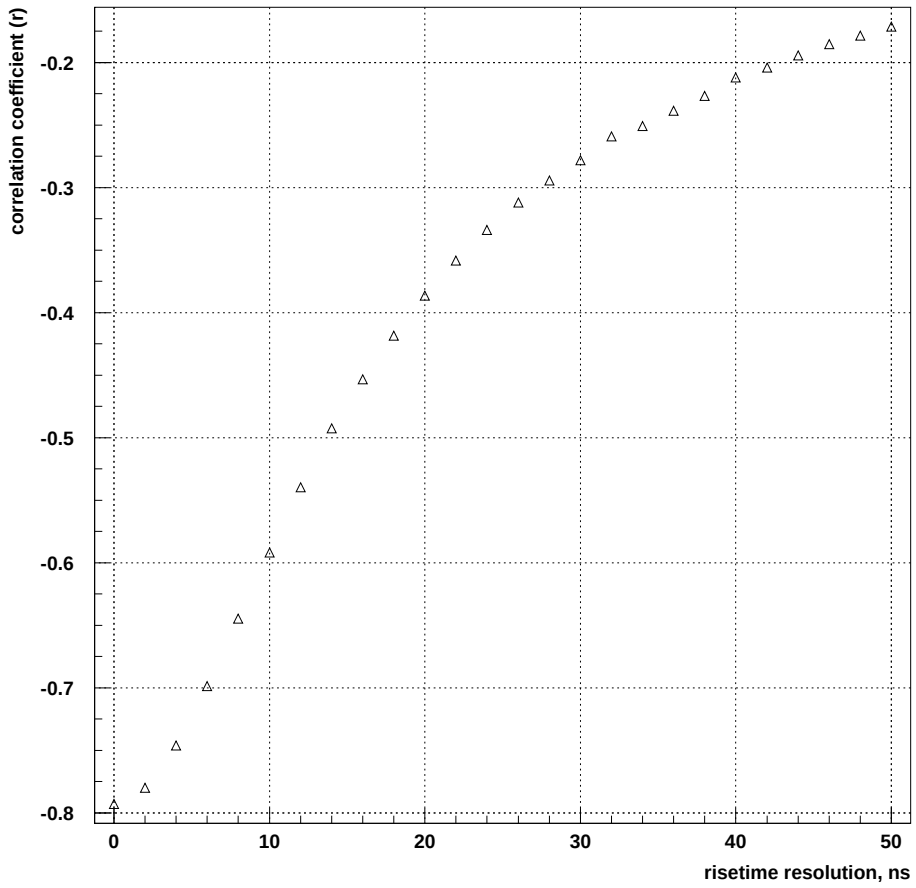

FIGURE 5.34. Correlation coefficient r as a function of risetime resolution.

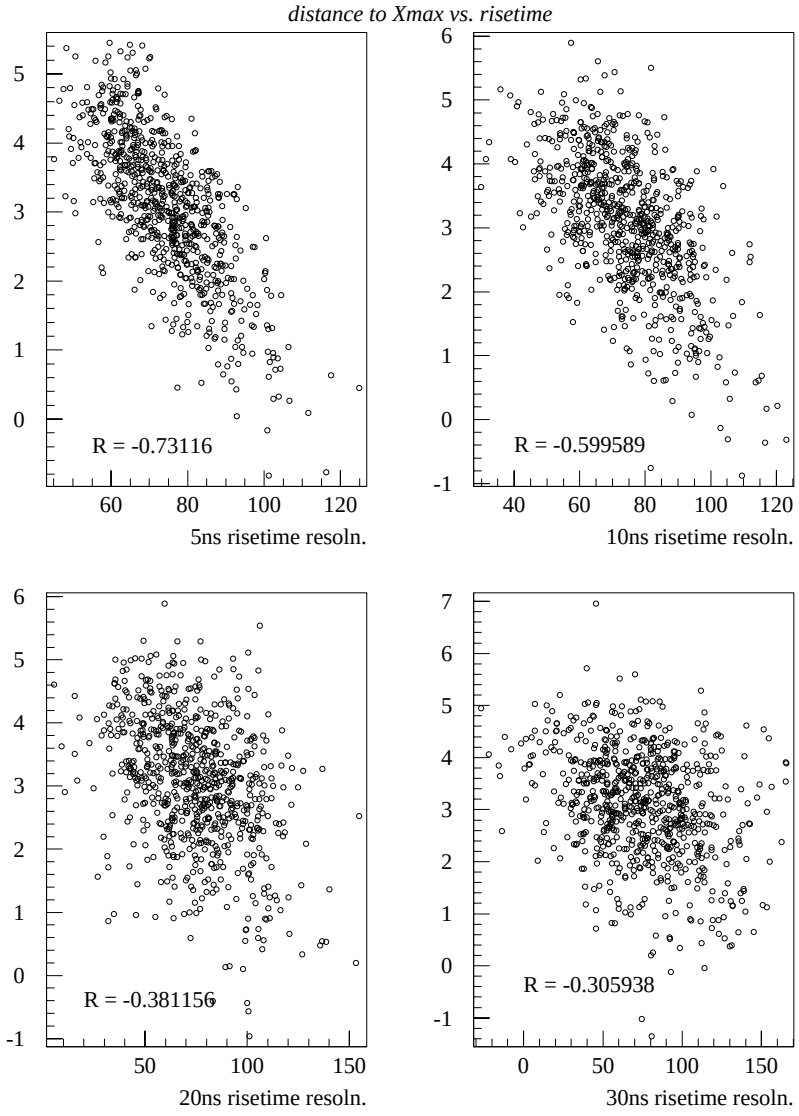

FIGURE 5.35. Correlation between distance to $X_{\max}$ and risetime under different assumptions about the risetime resolution.

5.9 Composition results

After the standard cuts are applied to the original hybrid data set comprising 2491 events, 898 high quality events remain. These are used to determine an $X_{\rm max}$ elongation rate (denoted as α in this section) and muon slope parameter β, defined as the slope of $\log_{10} N_\mu$ against $\log_{10} E$, or alternatively as that of $\log_{10} \rho_\mu(600)$ against $\log_{10} E$. The slope parameter can be regarded as a muon elongation rate (we will use the terms interchangeably). We also investigate correlations between $X_{\rm max}$ and parameters related to the muon component.

5.9.1 Elongation rates

The mean $X_{\rm max}$ as a function of energy is shown for Monte Carlo data (under the assumptions of two different hadronic generators, QGSJet and Sibyll) in Fig. 5.36. The elongation rate for iron under QGSJet is $\alpha = 58.5 \pm 1.3$ g/cm^2/decade, while for protons it is 60.9 ± 1.1 g/cm^2/decade. We find that there is no bias in reconstruction of the elongation rate. Sibyll predicts similar elongation rates, but with mean $X_{\rm max}$es some 25 g/cm^2 deeper. The elongation rate for the data, on the other hand, is $\alpha = 93.0 \pm 8.5$ (stat.) ± 10.5 (syst.). Examination of the QGSJet lines in Fig. 5.36 would suggest, on the basis of elongation rate arguments alone, that the composition is changing from a mixed one at 10^{17} eV to a predominantly light one at 10^{18} eV. The conclusion is slightly different in an absolute sense for Sibyll (heavy $\rightarrow$ mixed), but the gist is the same: the composition is changing over the energy range considered.

For $\rho_\mu(600)$, we find a slope parameter of $\beta = 0.83 \pm 0.01$ for both iron and protons under QGSJet, and 0.80 ± 0.02 (iron) and 0.81 ± 0.02 (proton) under Sibyll. However, Sibyll predicts significantly fewer muons for each composition. Fig. 5.37 suggests that the data are heavier than QGSJet iron until $\sim 4 \times 10^{17}$ eV, at which point they become iron–like until the highest observed energies. This indicates either a problem with the model, or the analysis, or both. The problem is even worse for Sibyll (simulation data not indicated here). The measured slope

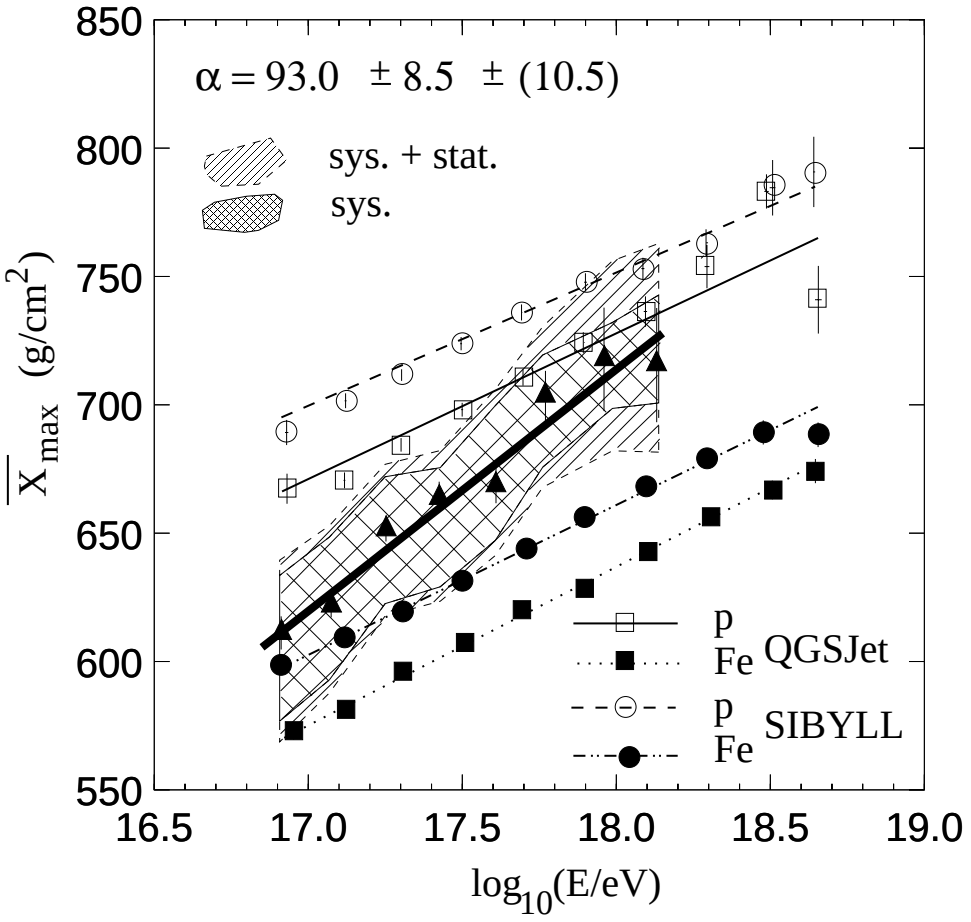

FIGURE 5.36. $X_{\max}$ as a function of energy. The data are depicted as triangles. The heavy line is the best fit to the data. The hatched area indicates the statistical error in $X_{\max}$, while the shaded area beyond that delineates the systematic error.

parameter is $\beta = 0.73 \pm 0.03$ (stat.) ± 0.02 (syst.). Therefore, on the basis of elongation rate, one could argue that there is weak indication for a lightening in composition.

A similar dilemma is present for the N_μ data (Fig. 5.38). The simulation data for QGSJet give $\beta = 0.85 \pm 0.04$ and $\beta = 0.80 \pm 0.03$ for iron and protons respectively, while Sibyll yields $\beta = 0.80 \pm 0.03$ and $\beta = 0.78 \pm 0.03$. The best fit to the data gives $\beta = 0.71 \pm 0.06$. Again, this might suggest weak evidence for a lightening composition, but the fact that the absolute muon numbers from the models all lie below the data makes such a conclusion tentative at best. Since the error bars for the measured and Monte Carlo values of β overlap, one might say

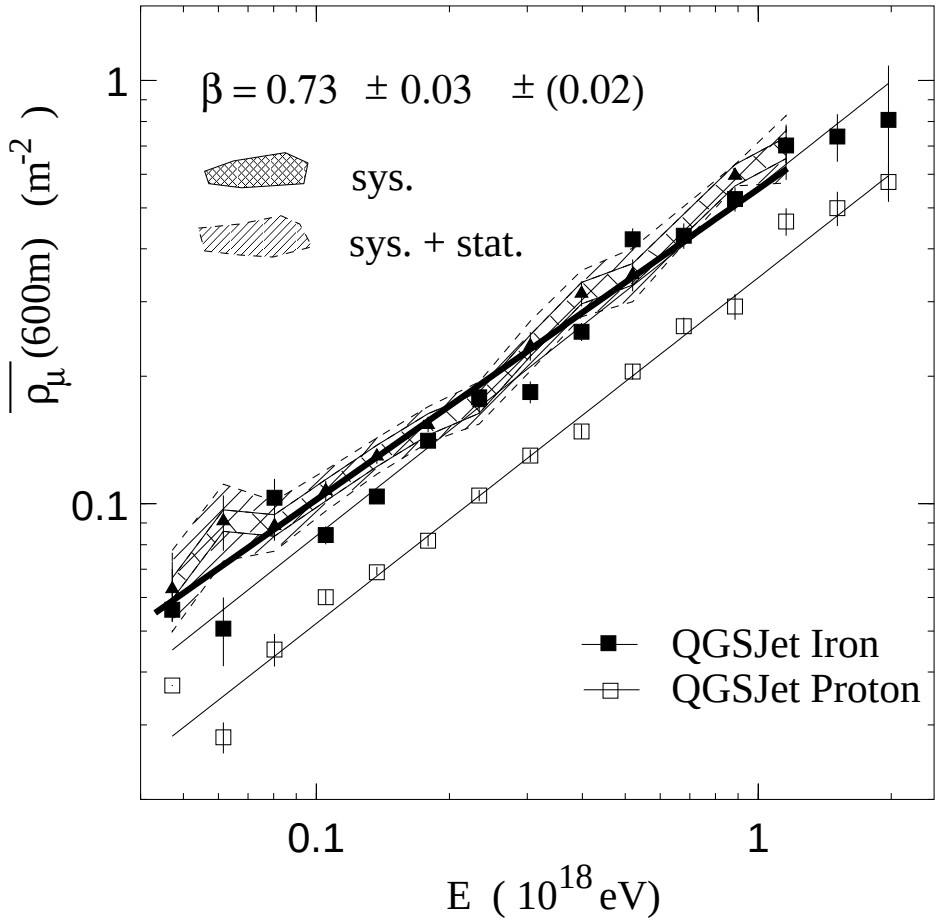

FIGURE 5.37. $\rho_\mu(600)$ as a function of energy for MC events under the QGSJet hadronic generator, and for the hybrid data set (triangles with error bars). Solid line is the best fit to the data, while hatched and shaded areas indicate statistical and systematic errors respectively.

that the data are consistent with an unchanging composition. Visual inspection of Fig. 5.38 would confirm this, ignoring for the moment that the data all lie above the line for QGSJet iron.

If considering elongation rates on their own, there is apparent consistency between the HiRes and MIA measured composition. However, the absolute scale of the muon component poses a problem. There are several possible reasons why the data appear heavier than iron. It is possible that the muon counter efficiencies are lower than the values used in the analysis. We took this into account when calculating the systematic error in the slope parameter, using the results of a 1995

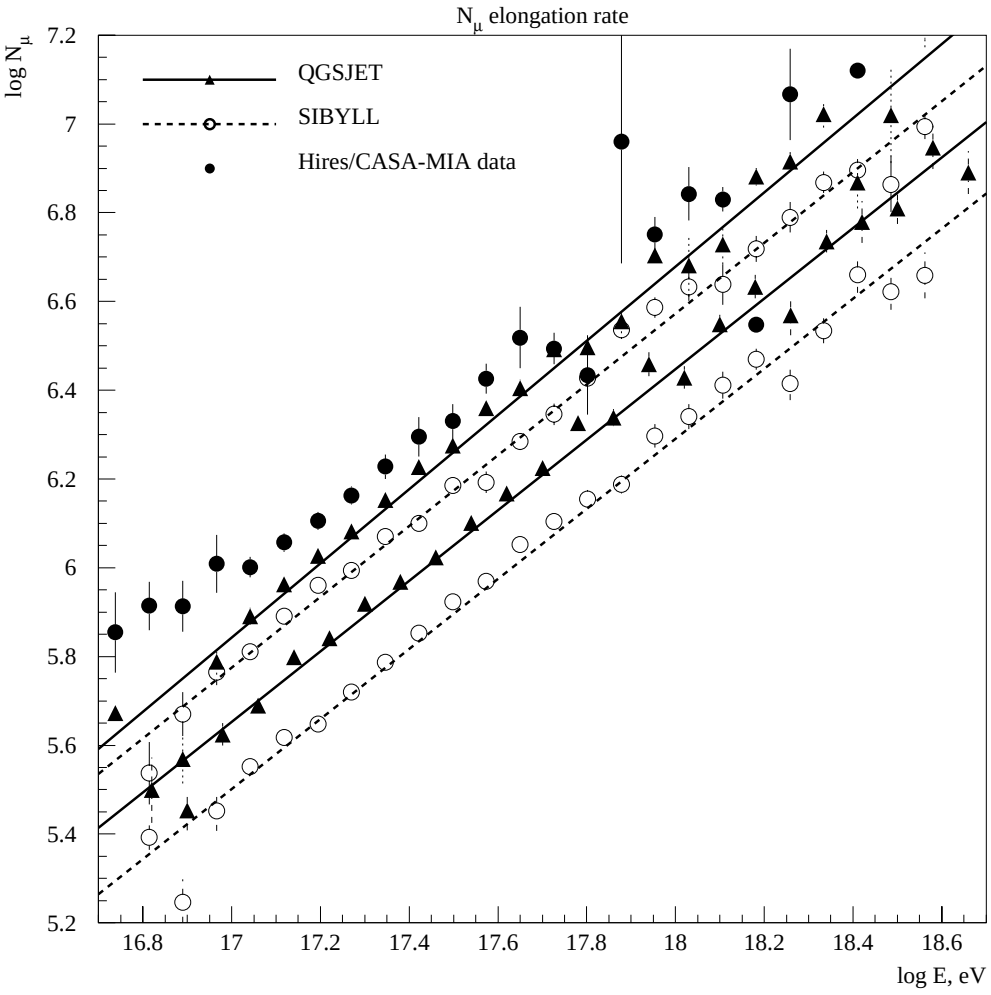

FIGURE 5.38. N_μ against energy for simulations (lines and points) and the HiRes/MIA data set (solid circles with error bars). The best fit to the data is not indicated here.

study [141]. This forms the biggest contribution to the systematic error. Other effects such as cross talk between MIA patches, background muons, electromagnetic punch through and variation in the overburden were investigated, but were found to have little effect on the counter energy threshold [137]. We find that at 3×10^{17} eV, our value of $\rho_\mu(600) = 0.24 \pm 0.02 \pm 0.02$ m^{-2} is consistent with the AGASA value of 0.25 m^{-2} [84]. Allowing for the differences in muon energy threshold and atmospheric depth, the AGASA–measured density ought to be higher than that for MIA by 0.027 m^{-2} at this energy [151]. It seems that there is a shortcoming in the models used here, at least with respect to muon production.

We further examined the data to look for possible correlations between fluorescence detector parameters and ground array parameters. The graph of $X_{\max}$ *v.* risetime at 600m is shown in Figs. 5.39 and 5.40 for the simulations, and Fig. 5.41 for the data. Only those events for which a risetime was calculable are included here. At least three radial bins with 10 hit counters were required for this to be the case, since the risetime at 600m was calculated via a least squares fit. Apparent correlation in the plots is slightly misleading as the events with large risetimes tend to compress the horizontal scale. Calculating the value of r via Eq. 5.17 gives values of -0.14 for protons, -0.16 for iron and -0.15 for the data. This suggests that the correlation has been almost completely washed out by detector resolution effects. Recall that the $X_{\max}$ resolution is somewhat larger than the value assumed in Section 5.8. It seems that the risetime resolution is also sufficiently poor that the correlation disappears for both the Monte Carlo events and for the real data.

A scatter plot of $X_{\max}$ against $\rho_\mu(600)$ for protons and iron shows a fairly clear boundary between the two populations, at least before detector response is folded in. This is illustrated in Figs. 5.42 and 5.43 for events at 10^{17} and 10^{18} eV. It should be possible, in principle, to derive some composition information from this fact. A KNN–type test, for example, as employed for CASA–MIA data [111], assigns probabilities that a given event belongs to one of two parameter sets. By examining the probability distribution as a function of energy, one can obtain information about the mean composition. This was not done here, but could

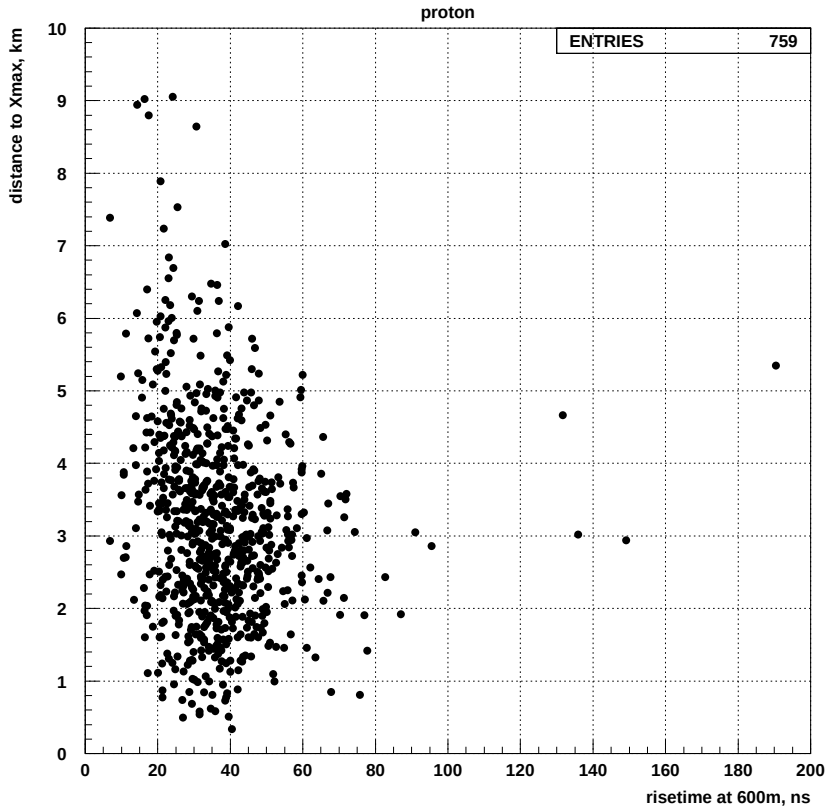

FIGURE 5.39. $X_{\max}$ against risetime at a core distance of 600m for proton Monte Carlo events.

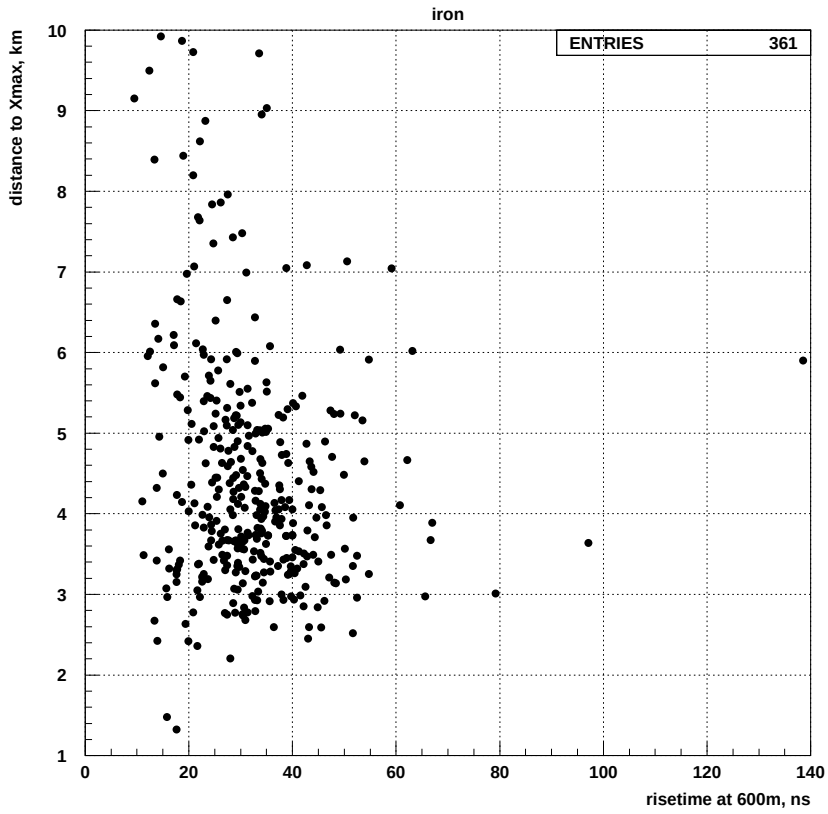

FIGURE 5.40. $X_{\max}$ against risetime at a core distance of 600m for iron Monte Carlo events.

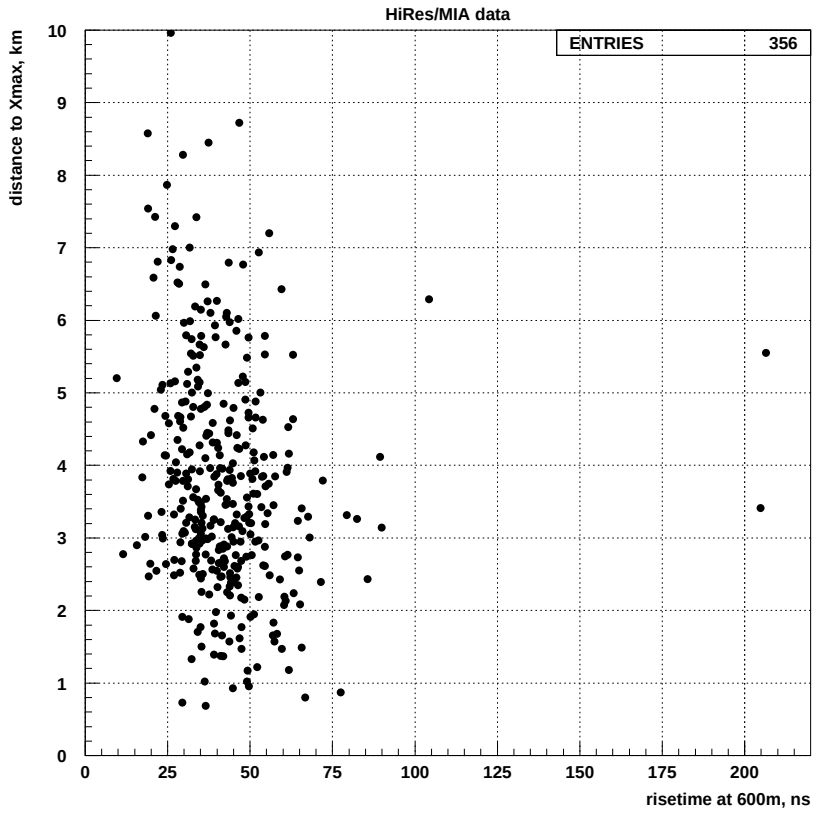

FIGURE 5.41. $X_{\max}$ against risetime at a core distance of 600m for the HiRes/MIA data.

be employed in future, perhaps in a reanalysis of the HiRes/MIA data set, and certainly in analysis of Auger data.

By inspection of Fig. 5.44, it seems as though there is no correlation between $X_{\rm max}$ and $\rho_\mu(600)$ in the data, an observation borne out by the fact that $r = 0.03$. However, this plot contains events with different energies and zenith angles. To account for this, we apply a correction to each data point such that

$$\begin{aligned} X'_{\rm max} &= X_{\rm max} - 58(\log_{10} E - 17.5) \\ \rho_\mu(600)' &= \rho_\mu(600) \times 10^{0.15(\sec\theta - 1)} \times 10^{0.894(17.5 - \log_{10} E)}, \end{aligned} \tag{5.20}$$

where energy E is in eV and θ is the zenith angle. By this procedure we correct the data such that they correspond to vertical showers at a single energy ($10^{17.5}$ eV). The parametrisations of Eq. 5.20 are obtained directly from CORSIKA data and are independent of composition. The result is shown in Fig. 5.45. Calculation shows that $r = 0.23$ after the correction. This suggests that any correlation is weak at best.

5.10 Summary

We have used the hybrid data set obtained by the HiRes and MIA detectors in coincidence to attempt to infer the cosmic ray composition over the energy range 10^{17} – 10^{18} eV. Measurements of the $X_{\rm max}$ and muon elongation rates suggest a lightening of composition over this range, independent of assumptions about hadronic interactions, but such a conclusion is considerably weakened by the fact that the currently available models appear to underestimate the muon content of the shower. We have examined the data for correlations between $X_{\rm max}$ and the muon component, but even when such correlations are present in the simulations, they appear to be destroyed by detector resolution effects.

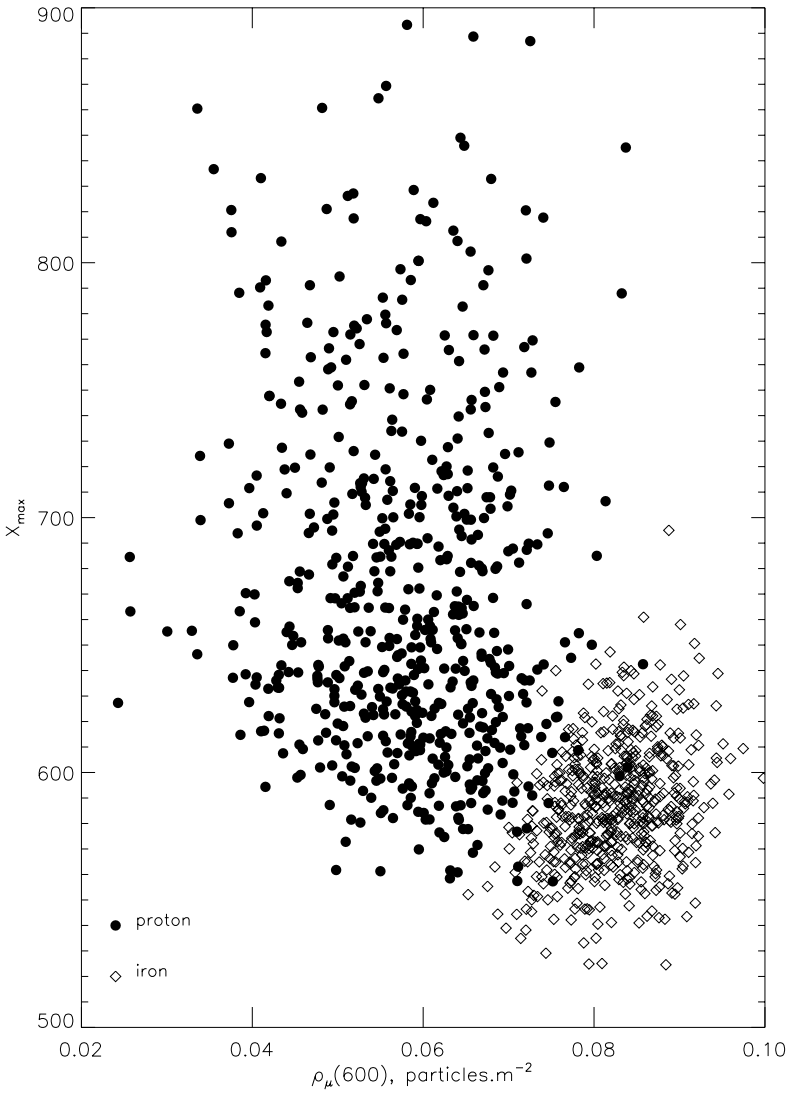

FIGURE 5.42. $X_{\max}$ *v.* $\rho_\mu(600)$ at 10^{17} eV.

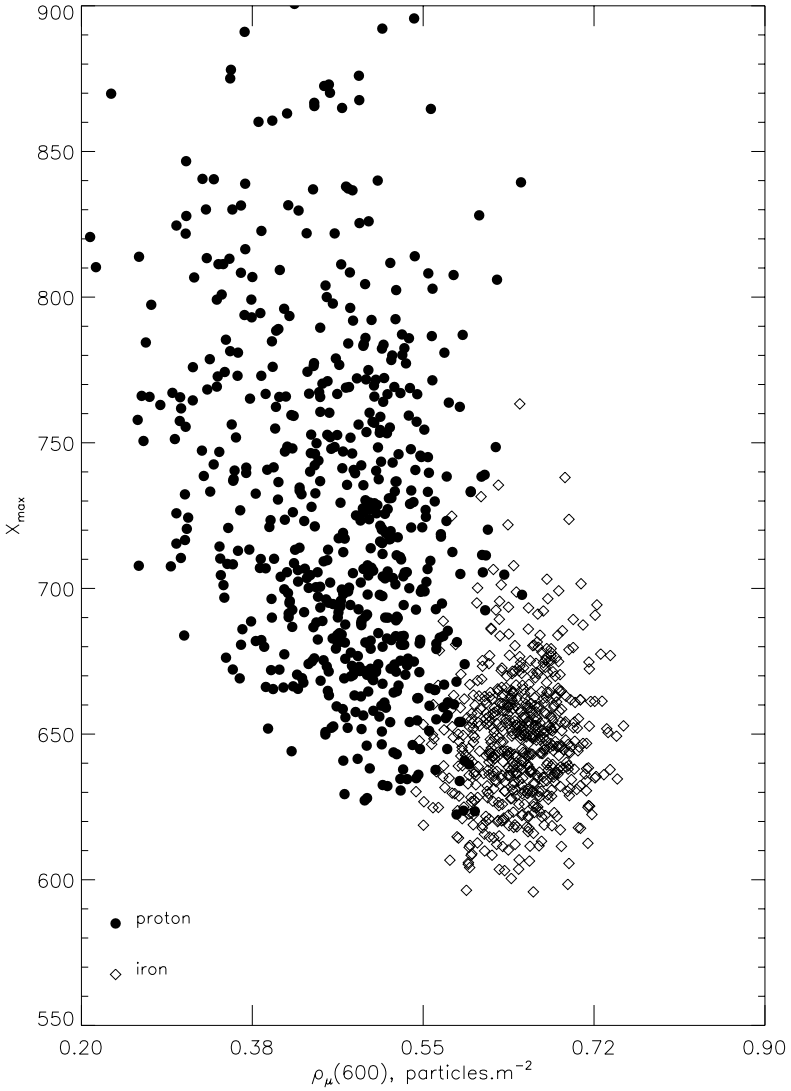

FIGURE 5.43. $X_{\max}$ *v.* $\rho_\mu(600)$ at 10^{18} eV.

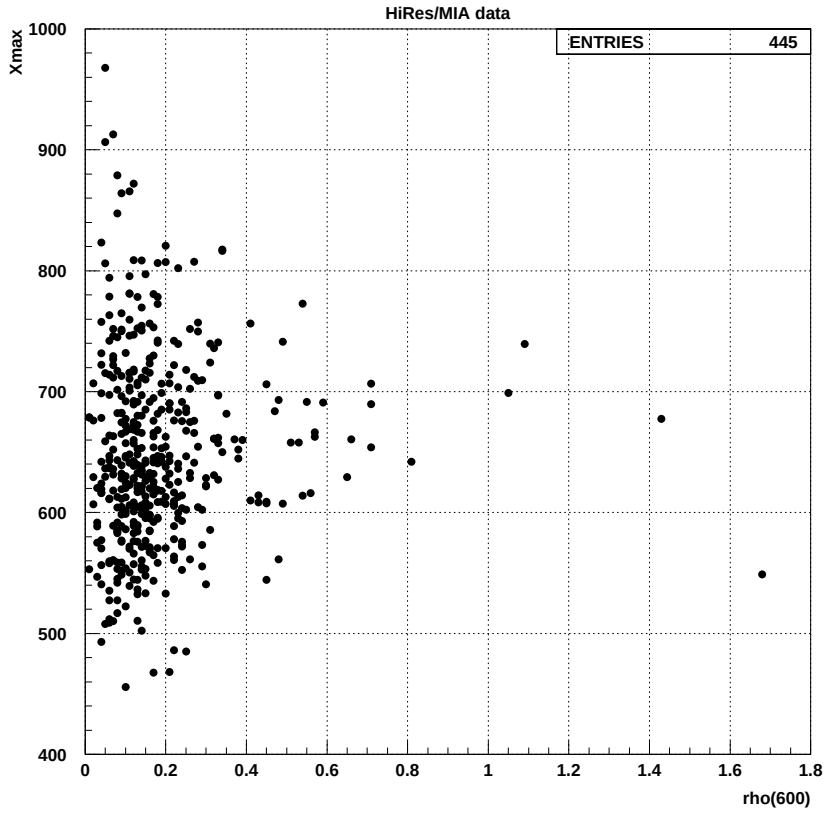

FIGURE 5.44. $X_{\max}$ against $\rho_\mu(600)$ for the real data. Different energies and zenith angles are mixed together here.

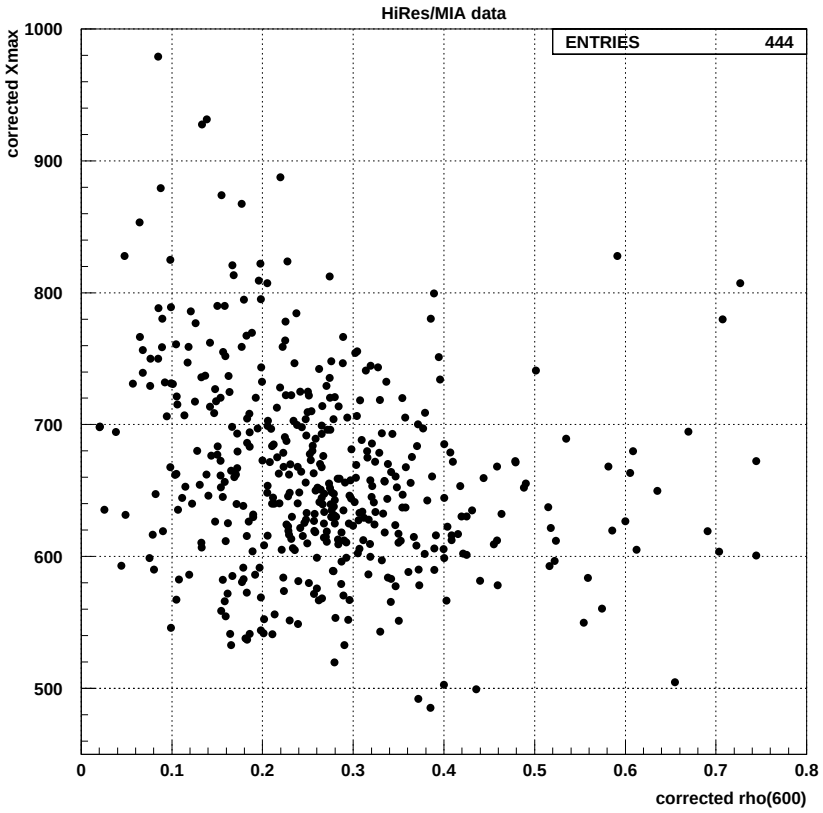

FIGURE 5.45. $X_{\max}$ against $\rho_\mu(600)$ for the real data, with the correction of Eq. 5.20 applied.

Chapter 6

The proton–proton cross section at cosmic ray energies

In this chapter I describe a technique for deriving the total proton–proton cross section, $\sigma_{pp}^{\rm tot}$, from the $X_{\rm max}$ data. Calculating the production part of the inelastic proton–air cross section, $\sigma_{p-{\rm air}}^{\rm prod}$, is relatively straightforward and has been discussed by several authors (see, for example, refs. [152, 153, 154]). Using this to find $\sigma_{pp}^{\rm tot}$ is considerably more challenging and model–dependent [155, 156, 157].

The method described here will be applied to the HiRes/MIA data set (discussed in Chapter 5) to calculate $\sigma_{p-{\rm air}}^{\rm prod}$ and $\sigma_{pp}^{\rm tot}$. Problems and potential systematic effects will be highlighted. The results obtained with this data set will be compared to results obtained previously by other cosmic ray experiments, and to accelerator data.

6.1 Calculating $\sigma_{p-{\rm air}}^{\rm prod}$ from air shower measurements

If air shower experiments could directly measure the distribution of depths of first interaction (X_1), it would be possible to directly determine the proton–air mean free path and hence the total cross section. In practice, this cannot be done. Surface arrays, by their very nature, do not measure the first interaction, and insufficient light is produced at the beginning of the shower for fluorescence and Cherenkov detectors to be able to measure X_1. In principle, X_1 could be inferred by a fit to some functional form (for example, the Gaisser–Hillas function), but such fits are phenomenological in nature and tend to yield unrealistic (or even negative) values of X_1. One must therefore turn to other methods to attempt a measurement of the cross section.

It is known from Monte Carlo simulations of air showers [153] that the attenuation length[1] of proton–induced air showers, Λ, is given by

$$\Lambda = \kappa \lambda_{p-\mathrm{air}}, \tag{6.1}$$

where $\lambda_{p-\mathrm{air}}$ is the mean free path for protons in air, and κ is a proportionality factor ($\kappa > 1$) which can depend in general on energy and on the hadronic interaction model used. The proportionality holds strictly only if $\lambda_{p-\mathrm{air}} > x_0$, where $x_0 = 37$ g/cm^2 is the radiation length in air. The relationship 6.1 results from the convolution of an exponential X_1 distribution with intrinsic shower development fluctuations. The value of κ, which can be viewed as the rate at which energy is dissipated into the EM component of the shower, will therefore be smaller for models with scaling violation than for those which incorporate hadronic scaling. This is because models with scaling violation tend to have larger multiplicity and inelasticity. Atmospheric cascades will therefore develop more rapidly and suffer smaller fluctuations.

κ is constrained to be in the range $1.1 < \kappa < 1.5$, where the lower bound is for models with extreme scaling violation, and the upper bound is for scaling models. Pryke [100] has demonstrated[2] that κ is independent of energy for the SIBYLL and QGSJet hadronic interaction drivers and for the splitting model of Hillas (as implemented in MOCCA92, see section 2.4.1).

Once the attenuation length Λ is known, the production cross section for protons on air can be calculated via

$$\sigma^{\mathrm{prod}}_{p-\mathrm{air}} = \frac{A m_p}{\lambda_{p-\mathrm{air}}}, \tag{6.2}$$

where A is the mass number of the target nuclei and m_p is the proton mass. For air we use an "average" value for A of 14.5, and using the relation between Λ and

[1] The term "attenuation length" sometimes refers to the logarithmic slope of the tail of an individual shower development curve. In this thesis it will always refer to a *beam* attenuation length, *i.e.* it describes the rate of attenuation of showers of a given energy arriving at a given zenith angle.

[2] No attempt to include the effects of detector resolution was made in that analysis.

$\lambda_{p-\mathrm{air}}$, obtain

$$\sigma^{\mathrm{prod}}_{p-\mathrm{air}}(\mathrm{mb}) = 2.41 \times 10^4 \frac{\kappa}{\Lambda(\mathrm{g/cm^2})}. \tag{6.3}$$

Note that the quantity measured by air shower experiments is the *production* part of the cross section, *i.e.* the inelastic cross section for processes in which at least one new hadron is produced in addition to nuclear fragments [158], rather than the total cross section. This is because processes such as elastic and quasi–elastic scattering and diffractive excitation do not contribute to cascade development. $\sigma^{\mathrm{prod}}_{p-\mathrm{air}}$ is often (incorrectly) identified with $\sigma^{\mathrm{inel}}_{p-\mathrm{air}}$ in the literature.

Before progressing to an explanation of how the more fundamental proton–proton cross section can be calculated, I note the following:

- Any attempt to calculate the cross section for *protons* on air obviously requires that the primary flux be mostly protons. Contamination by nuclei with $A > 1$ will tend to decrease the measured value of Λ and hence artificially increase $\sigma^{\mathrm{prod}}_{p-\mathrm{air}}$. In the analysis presented here, it is assumed that the primary flux is mostly protonic. The validity or otherwise of this assumption will be explored.

- This type of measurement requires excellent understanding of the experimental resolution. In particular, a non–gaussian tail in the resolution function will tend to decrease the measured value of Λ, thereby artificially increasing the cross section.

6.1.1 Λ from HiRes/MIA data

The data set used here is the hybrid HiRes/MIA one discussed in Chapter 5. The standard cuts as defined in section 5.5.1 are applied, meaning that 898 events are available for this analysis.

In order to select out the events with the highest probability of being protons, I restrict the fit for Λ to those showers which have X_{max} 100 g/cm^2 beyond the peak of the distribution. For the HiRes/MIA data, the peak occurs at approximately

620 g/cm^2. Simulations show that the expected contamination from helium nuclei above 720 g/cm^2 is of the order of 30–40%, assuming that cosmic rays of different composition arrive in equal numbers at the top of the atmosphere. This figure is estimated by generating a large number of events (approx. 10000) for proton, helium and iron primaries using the hybrid Monte Carlo described in section 5.4. These events were then passed through the same reconstruction procedure as the real data. The resultant $X_{\max}$ distributions are shown in Figure 6.1.

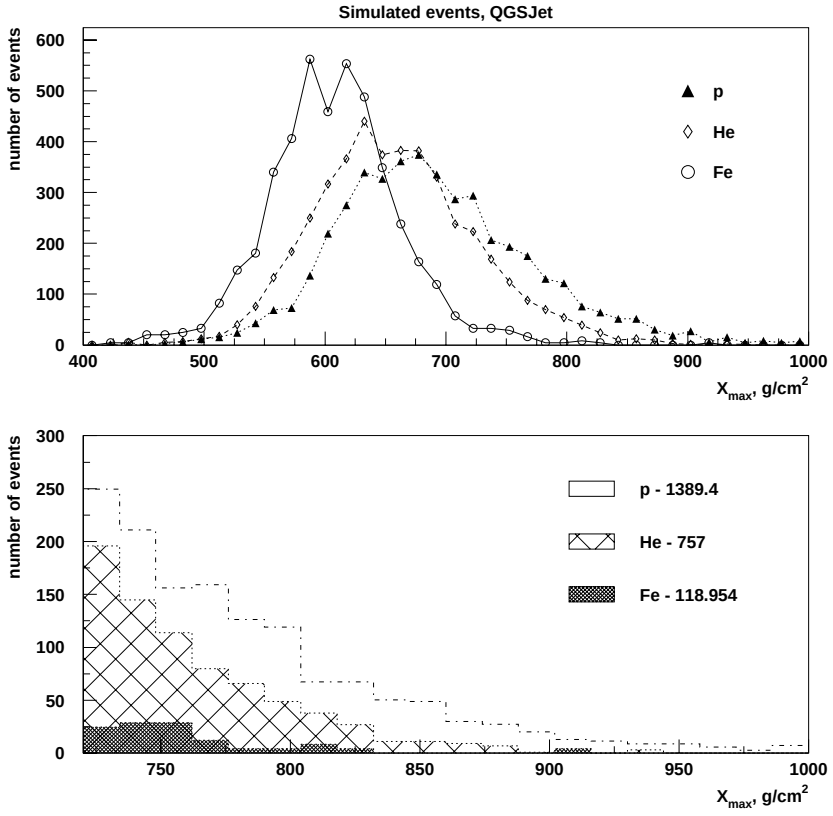

FIGURE 6.1. $X_{\max}$ distributions for simulated events, as generated by CORSIKA with the QGSJet driver. In the top plot the histograms have been normalised to contain the same number of events. The bottom plot shows the number of events of each composition that would be expected beyond 720 g/cm^2.

Some caution must be advised here, since different hadronic models will produce slightly different $X_{\max}$ distributions and hence different helium to proton ra-

tios in the $X_{\max}$ range considered. QGSJet is chosen here because of the currently used hadronic generators, it appears to be the most realistic [159]. In practice, the choice of model should have little effect in this context, as will be seen later.

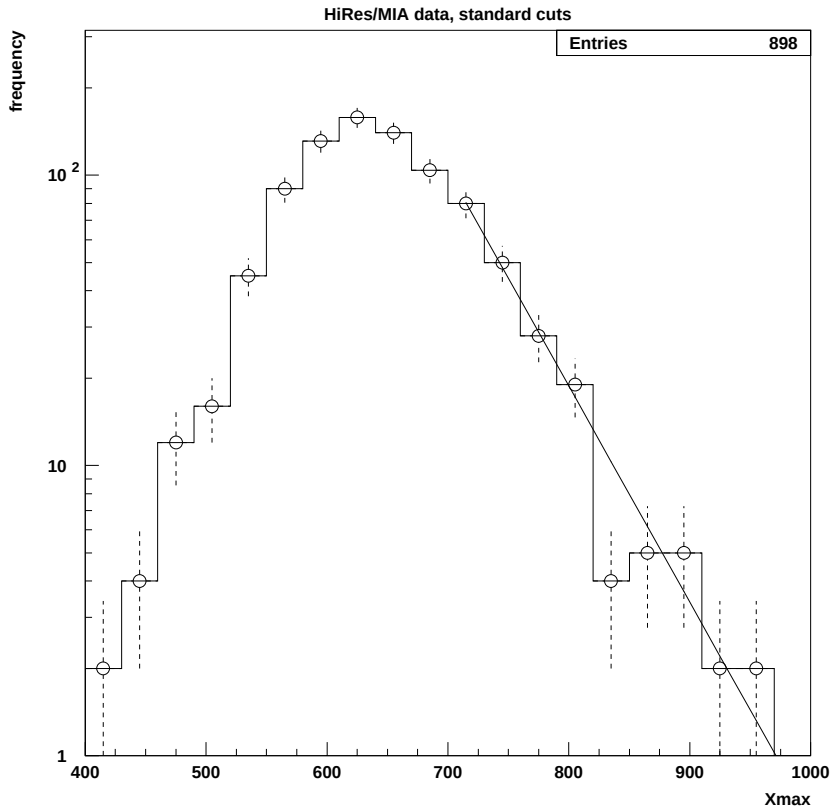

FIGURE 6.2. The $X_{\max}$ distribution measured by the HiRes/MIA experiment, and a fit to the exponential tail of the distribution.

In principle an even more stringent constraint on $X_{\max}$ could be placed on the fit, but this would further reduce an already sparse data set and is not done here.

An exponential fit to the $X_{\max}$ distribution beyond 720 g/cm^2 yields a slope of -0.017 $\pm$ 0.0014, or a value for Λ of 58.5 $\pm$ 5 g/cm^2 (see Figure 6.2). The fit is performed using the maximum likelihood method and assuming that the errors within each $X_{\max}$ bin are Poisson. The error in Λ is purely the error estimated by the fitting procedure.

Systematic errors in Λ The presence of nuclei in the primary beam will tend to steepen the tail of the $X_{\rm max}$ distribution and hence decrease the measured value of Λ. This effect was investigated for the HiRes/MIA experiment by generating large numbers of proton and helium showers and varying the fraction of helium in the artificial data set. Suppose that $N_{\rm p}$ and $N_{\rm He}$ events respectively pass the reconstruction procedure, and that we want a fraction f of the sample to be helium. This is done by selecting a number n of the generated helium events randomly, where

$$n = \frac{f}{1-f} N_{\rm p}. \tag{6.4}$$

These n events are added to the proton sample. The standard cuts are then applied, and Λ is calculated according to the procedure in Section 6.1.1.[3] This process is repeated 1000 times for each value of f. Note that the maximum possible value of f is $f_{\rm max} = N_{\rm He}/(N_{\rm p} + N_{\rm He})$, which happens to be slightly smaller than 0.5 in this case. If larger values are desired (higher fraction of helium), the reverse procedure can be applied, *i.e.* randomly select proton events and add them to the helium sample.

The variation of Λ with f is rather slow for small f, as shown in Fig. 6.3. Even if 50% of showers were helium–initiated, the value of Λ would decrease by only 6 g/cm^2.

The statistical errors in Fig. 6.3 can be understood qualitatively by noting that the proton $X_{\rm max}$ distribution contains somewhat more events than that of helium in the range selected for the fit For $f < f_{\rm max}$, the helium showers that are added do not have much effect, and the fluctuations from trial to trial are correspondingly small. The effect on Λ increases with f, but the fluctuations do not increase much since a higher fraction of the helium data set is being sampled. When $f = f_{\rm max}$, there are no fluctuations since the entire data set is being used. For $f > f_{\rm max}$, proton events are added to the helium data set. These have a larger effect on

[3]Note that the value of f after cuts are applied will in general not be the same as that beforehand.

the tail of the helium $X_{\max}$ distribution, and the fluctuations are correspondingly larger.

The presence of non–gaussian tails in the $X_{\max}$ resolution function can bias the measured value of Λ. By performing a fit to Monte Carlo data for protons using the procedure described above, one finds a value for Λ of 58.6±2.95 g/cm^2 for the reconstructed $X_{\max}$ distribution, compared to 51.5±1.34 g/cm^2 for the input $X_{\max}$ distribution (errors are statistical). This suggests that a small bias is introduced by the reconstruction procedure, although there is no strong indication of non–gaussian behaviour in the $X_{\max}$ resolution function.

The fact that the value of Λ for proton showers generated by CORSIKA with QGSJet agrees with the measured value is probably a numerical coincidence. If QGSJet is indeed an accurate depiction of hadronic physics at these energies, perhaps the agreement is more meaningful. Better measurements with much higher statistics are required before such a conclusion could be drawn.

6.1.2 Other methods of measuring Λ

In addition to the method described above, it is possible to extract the shower attenuation rate by studying the fluctuations of $X_{\max}$. This method, originally proposed by Linsley, is generally used when $X_{\max}$ itself is not well measured, as is the case for the Yakutsk experiment, for example [154]. Another technique, used by the AGASA experiment, is to measure the rate of showers arriving with a fixed muon and electron size, N_μ and N_e respectively, as a function of zenith angle. The AGASA group perform a fit to

$$f(N_e, N_\mu, \theta) = f(N_e, N_\mu, 0) \exp(-x_{\rm obs}(\sec\theta - 1)/\Lambda), \tag{6.5}$$

where $x_{\rm obs}$ is the observation depth (920 g/cm^2 for AGASA), and θ is the zenith angle. To ensure that the presence of nuclei in the primary flux is minimised, the AGASA group select, for fixed N_μ, the ten percent of events which have the largest values of N_e. These are the most likely events to be protons, since showers of a given energy ought to have attenuated less if they have larger N_e, and therefore

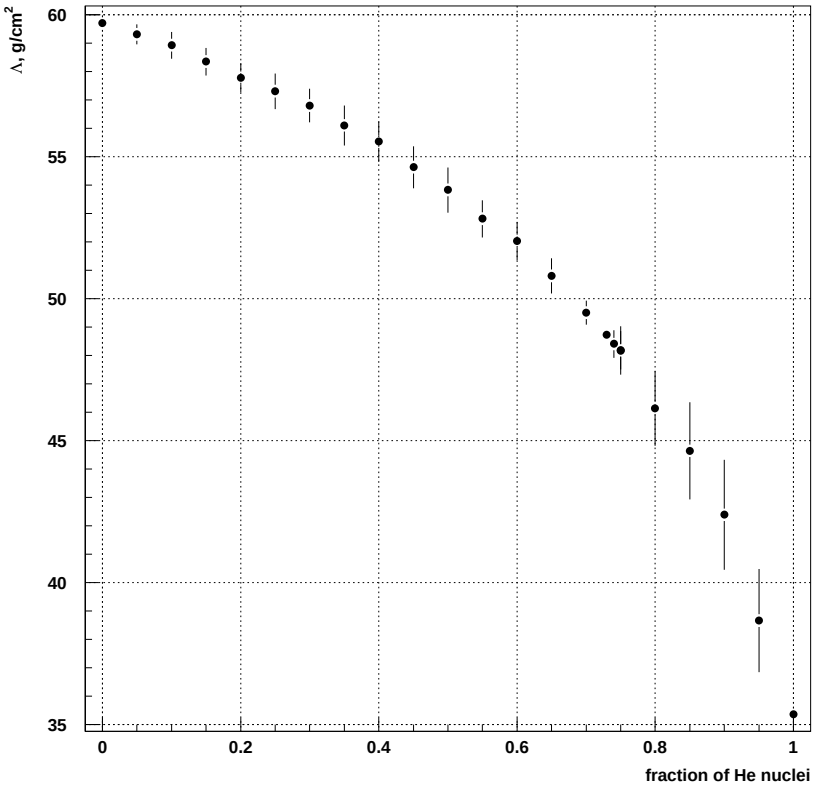

FIGURE 6.3. Effect of helium contamination on Λ.

must have penetrated deeper in the atmosphere. This assumes that $X_{\max}$ is above the observation level, generally true even for vertical showers in the energy range considered ($E \leq 10^{17.6}$ eV).

In principle, the AGASA technique could also be applied to the HiRes/MIA data set. This would enable a second, independent measurement of Λ and therefore a consistency check. Unfortunately, much higher statistics than are available for this data set are required. For example, the AGASA analysis used 553065 events with zenith angles less than 48.2° ($\sec\theta = 1.5$) [160], whereas a mere 573 events are available here after making suitable cuts.

In Figure 6.4, I plot measurements of Λ from AGASA, Fly's Eye (mono and stereo) and HiRes/MIA. Approximately 600 events were used in the Fly's Eye monocular analysis [161], while around 2500 events were available for the stereo

analysis [120]. Numerical values of Λ, and the energy ranges over which they apply, are given in Table 6.1.

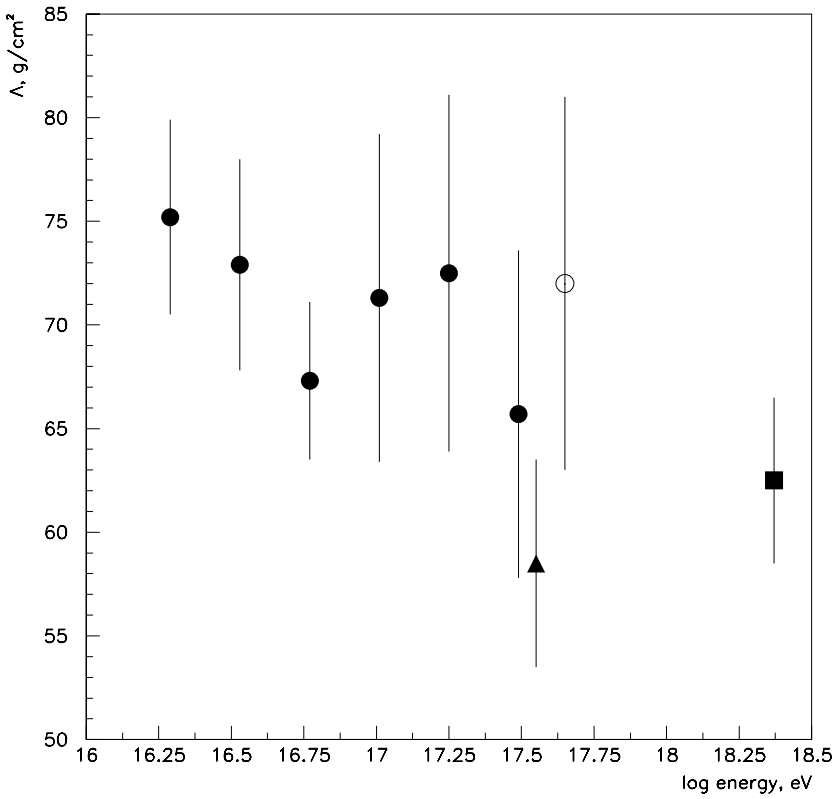

FIGURE 6.4. Attenuation length of air showers, as measured by AGASA [160] (•), Fly's Eye monocular [161] (○), Fly's Eye stereo [120] (■) and HiRes/MIA (▲). Points have been plotted at the midpoint of the (log) energy range in each case (see Table 6.1).

6.1.3 Extracting $\sigma_{pp}^{\rm tot}$

The production cross section, as measured by cosmic ray experiments, is given by [155]

$$\sigma_{p-\rm air}^{\rm prod} = \sigma_{p-\rm air}^{\rm tot} - \sigma_{p-\rm air}^{\rm el} - \sigma^{\rm q-el}. \tag{6.6}$$

experiment	range of $\log_{10} E$	Λ (g/cm^2)
AGASA	16.17 — 16.41	75.2 ± 4.7
	16.41 — 16.65	72.9 ± 5.1
	16.65 — 16.89	67.3 ± 3.8
	16.89 — 17.13	71.3 ± 7.9
	17.13 — 17.37	72.5 ± 8.6
	17.37 — 17.61	65.7 ± 7.9
Fly's Eye (mono)	17.0 — 18.3	72 ± 9
Fly's Eye (stereo)	17.75 — 19.0	62.5 ± 4
HiRes/MIA	17.0 — 18.1	58.5 ± 5

TABLE 6.1. Attenuation lengths measured by air shower experiments. References are given in the text.

Here $\sigma^{\mathrm{q-el}}$ represents the contribution due to quasi–elastic scattering, *i.e.* processes in which the nucleus fragments or is excited, but no new hadrons are created. Each term on the right hand side of Eq. 6.6 is calculable in Glauber theory, provided that the fundamental nucleon–nucleon scattering amplitude $f(\mathbf{q})$ is known[4].

The elastic scattering amplitude for nucleons on a nucleus of mass A, in the impact–parameter representation, is given in Glauber theory by [96]

$$F(q) = \frac{ik}{2\pi} \int d^2b\, e^{i\mathbf{q}\cdot\mathbf{b}} \int \prod_{i=1}^{A} d^3r_i\, \rho_i(r_i) \left[1 - \prod_{j=1}^{A} [1 - \Gamma(\mathbf{b} - \mathbf{r}_{\perp j})] \right]. \qquad (6.7)$$

Here $\mathbf{q} = \mathbf{k} - \mathbf{k}'$ is the 3–momentum transfer, $\mathbf{b}$ is the impact parameter vector (defined by the perpendicular drawn from the projectile to the horizontal axis), $\mathbf{k}$ and $\mathbf{k}'$ are the initial and final nucleon momentum respectively, ρ_i is the density profile of the i^{th} constituent nucleon (generally taken to be gaussian [155], although one can use density functions as given by the shell model [96])and $\mathbf{r}_i$ is its position

[4] All quantities are calculated in the centre–of–mass frame.

vector, and Γ is given by

$$\Gamma(\mathbf{b}) = \frac{1}{2\pi i k} \int d^2q\, e^{-i\mathbf{q}\cdot\mathbf{b}} f(\mathbf{q}), \tag{6.8}$$

i.e. it is the Fourier transform of the nucleon–nucleon elastic scattering amplitude.

Once $f(\mathbf{q})$ and hence $F(\mathbf{q})$ is known, the elastic and total cross sections for nucleons on air are easily calculated via

$$\begin{aligned} \sigma^{\rm el}_{p-{\rm air}} &= \int |F(\mathbf{q})|^2\, d\Omega_{\mathbf{k}'} \\ \sigma^{\rm tot}_{p-{\rm air}} &= \frac{4\pi}{k} {\rm Im}\, F(0), \end{aligned} \tag{6.9}$$

where the first relation follows from the definition of the elastic cross section and the second follows from the optical theorem.

The correction due to quasi–elastic scattering can be calculated in the Glauber formalism according to the procedure described in Ref. [155].

The pp elastic scattering amplitude is usually parametrised for small momentum transfer squared $t(=-q^2)$ as [162]

$$f(t) = \frac{k\sigma^{\rm tot}_{pp}}{4\pi}(\rho + i)e^{Bt/2}, \tag{6.10}$$

where ρ is the ratio of the real to imaginary parts of the forward amplitude, $\rho = {\rm Re}f(0)/{\rm Im}f(0)$, and B is the "forward nuclear slope parameter", defined by

$$B = \left(\frac{d}{dt} \ln \frac{d\sigma}{dt} \right)_{t=0}, \tag{6.11}$$

with $d\sigma/dt$ being the differential cross section, defined by $d\sigma/dt = (\pi/k^2)|f(t)|^2$. In general one ought to make B a function of t, but as long as t is small enough (< 0.1 GeV^2), the approximation is valid.

Eq. 6.10 is widely used because it contains three quantities which are (relatively) easily measurable at colliders, namely $\sigma^{\rm tot}_{pp}$, ρ and B. To apply this parametrisation for use in cosmic ray calculations, we need a way of extrapolating the measured values of these parameters by several orders of magnitude in energy. The most recent attempt to do this, by Block and coworkers [156, 163],

uses a QCD–inspired eikonal model which simultaneously fixes $\sigma_{pp}^{\rm tot}$, ρ and B, in contrast to previous work in which the three were allowed to vary independently [158, for example]. Once the amplitude is known, the proton–air cross section can be calculated in the Glauber formalism, as described above. $\sigma_{p-{\rm air}}^{\rm prod}$ is therefore uniquely determined by $\sigma_{pp}^{\rm tot}$ in this model, which contains very similar physics to that utilised by SIBYLL [96]. The relationship between $\sigma_{p-{\rm air}}^{\rm prod}$ and $\sigma_{pp}^{\rm tot}$ is plotted in Figure 6.5 below.

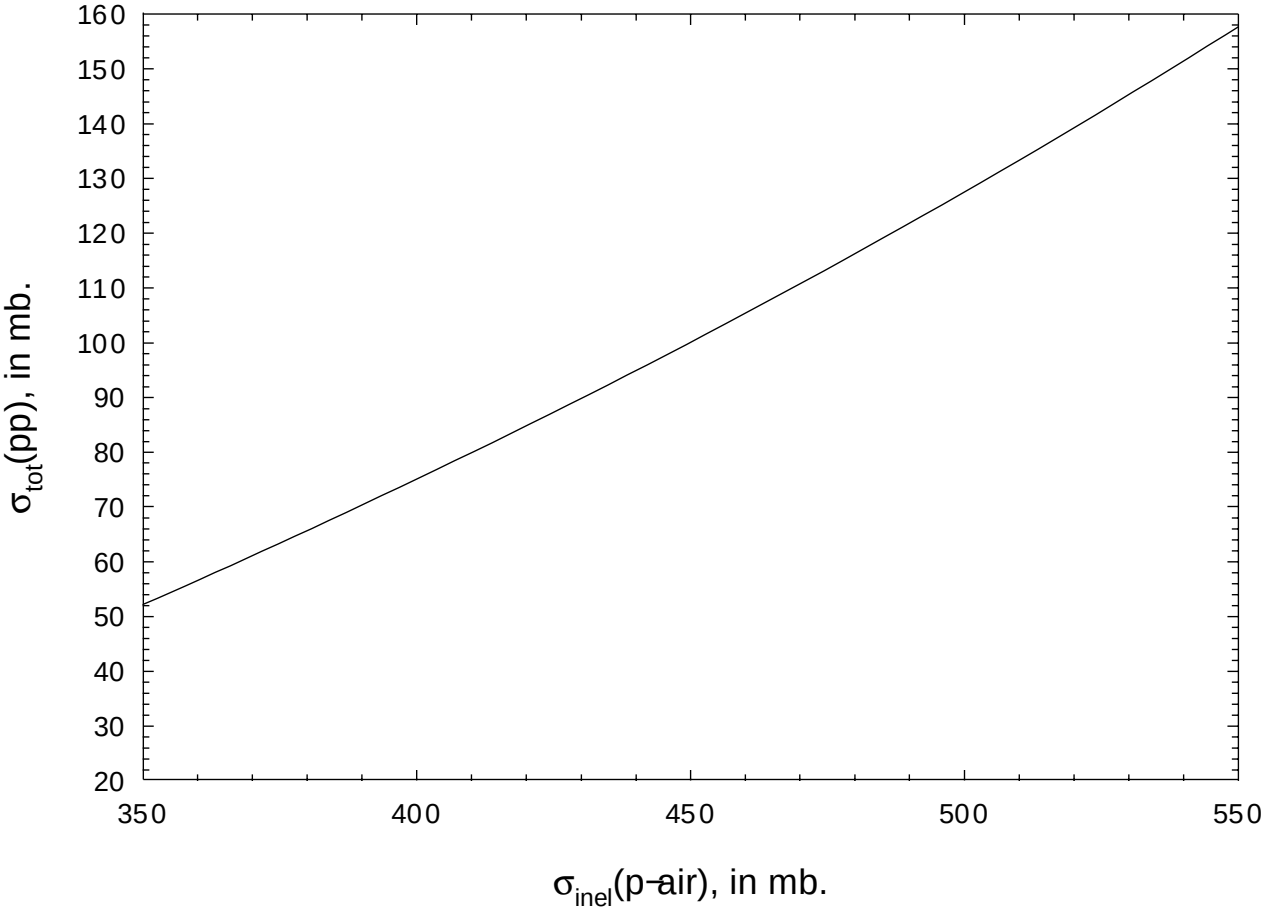

FIGURE 6.5. The relationship between $\sigma_{p-{\rm air}}^{\rm prod}$ and $\sigma_{pp}^{\rm tot}$ in the QCD–inspired eikonal model of Block *et al.* [163]

To apply the results of Fig. 6.5, we still require a value for the parameter κ. The value obtained by Block, Halzen and Stanev (BHS) [163], from a simultaneous fit to accelerator, AGASA and Fly's Eye monocular data, is $\kappa = 1.349 \pm 0.045({\rm statistical}) \pm 0.028({\rm systematic})$. This is consistent with the value

of 1.30 ± 0.04 obtained by Pryke [100] from a high–statistics study of $X_{\rm max}$ using QGSJet. Using the BHS model value with Eq. 6.3, I obtain

$$\sigma^{\rm prod}_{p-{\rm air}} = 556 \pm 51{\rm mb}. \tag{6.12}$$

In order to extract $\sigma^{\rm tot}_{pp}$ from Fig. 6.5, I digitised the curve and performed a fit to a quadratic using approximately 50 points, *i.e.*

$$\sigma^{\rm tot}_{pp} = a(\sigma^{\rm prod}_{p-{\rm air}})^2 + b(\sigma^{\rm prod}_{p-{\rm air}}) + c, \tag{6.13}$$

with $a = 0.48528 \times 10^{-3}$, $b = 0.089624$ and $c =$ -38.262. This then yields for the total cross section

$$\boxed{\sigma^{\rm tot}_{pp}({\rm HiRes/MIA}) = 161.6\,^{+33.4}_{-30.8}\,{\rm mb}}$$

In Fig. 6.6 below, I plot this result with the available accelerator measurements, the corrected results from AGASA and monocular Fly's Eye data, and the BHS model prediction.

As can be seen from Fig. 6.6, the inferred HiRes/MIA value for the pp cross section is considerably higher than the Fly's Eye monocular result at similar centre–of–mass energy, and is not quite consistent with the prediction of the BHS model.

6.2 Summary and Discussion

The production part of the proton–air cross section, $\sigma^{\rm prod}_{p-{\rm air}}$, has been extracted from the HiRes prototype/MIA hybrid data set. The value obtained here is barely consistent with the results obtained by AGASA and those from the Fly's Eye monocular data set, but is consistent (within errors) with the Fly's Eye stereo result, provided that the same hadronic model is used to interpret the data. This type of measurement, relying as it does on the tail of the $X_{\rm max}$ distribution, requires very high statistics and detailed knowledge of the detector resolution. Possible systematic effects on the measured cross section, particularly those due to

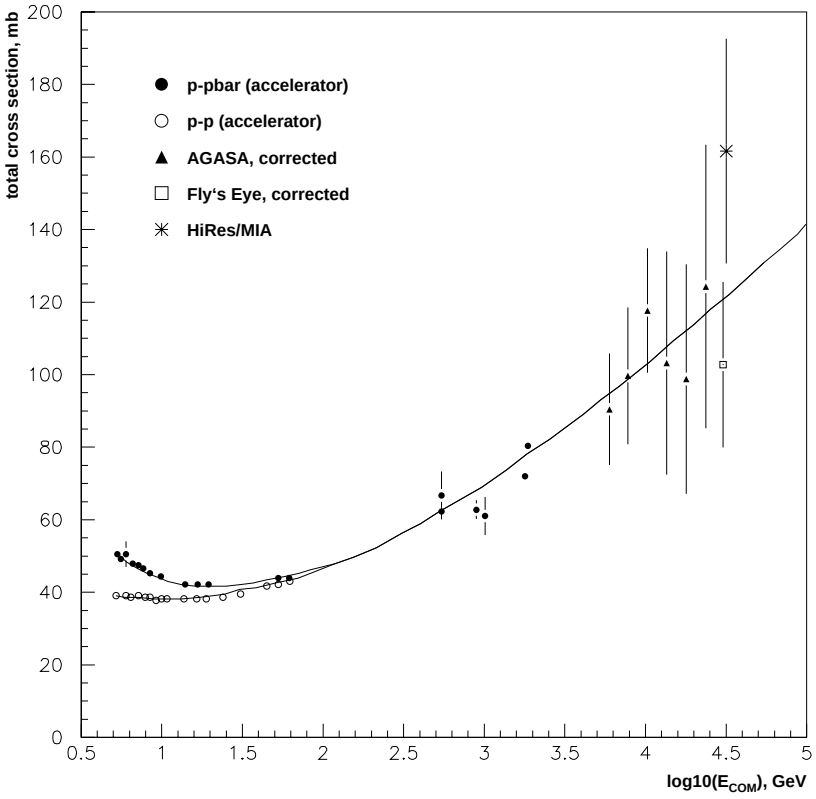

FIGURE 6.6. The total cross section from accelerator data, along with the published results from AGASA and Fly's Eye (monocular), corrected for the κ value used here. Lines are model predictions from Ref. [163]. The cross section result from the current work is also plotted (asterisk).

the presence of a non–protonic component in the primary flux, have been investigated. These effects are small compared to the uncertainties in extrapolations of hadronic models.

Attempting to infer the proton–proton total cross section, $\sigma_{pp}^{\rm tot}$, from a measurement of $\sigma_{p-{\rm air}}^{\rm prod}$ is highly model dependent. I have calculated $\sigma_{pp}^{\rm tot}$ here in the framework of the model of Block *et al.* [163]. The relatively large uncertainty in the measured value means that it is not possible to constrain all but the most extreme models of hadronic interactions, based on their extrapolation beyond accelerator energies. Indeed, it may not be possible to measure $\sigma_{pp}^{\rm tot}$ at all, since

$\sigma^{\rm prod}_{p-{\rm air}}$ may be rather insensitive to the value of $\sigma^{\rm tot}_{pp}$ at these energies. An unambiguous change with energy of $\sigma^{\rm prod}_{p-{\rm air}}$ would be a clear indication of new hadronic physics. Clearly a measurement of the energy dependence of $\sigma^{\rm prod}_{p-{\rm air}}$ requires an extremely high statistics, high quality data set, such as will be provided by the High Resolution Fly's Eye operating in stereo mode, or by the Auger detector. The latter has the advantage that the cross section can potentially be measured in two independent ways, and thereby checked for consistency.

Chapter 7

Conclusions and Further Work

The major results of this thesis are as follows. We have demonstrated in Chapter 4 that composition measurements from different experiments are consistent when the same assumptions about hadronic physics are made. This was seen most clearly for Fly's Eye and AGASA composition, where previously inconsistent results under different models were brought into good agreement by using the same hadronic model. The agreement was not complete, indicating either a deficiency in the model, or an unexplored systematic in either of the two experiments, or both. Under the assumptions of Sibyll, the composition appears to be changing from predominantly heavy to a mixed composition (approx. 50% iron for both experiments in a two–component model for composition).

A similar scenario was observed in the HiRes/MIA hybrid composition study (Chapter 5). In the case of HiRes, the elongation rate is far steeper than that predicted by any modern hadronic interaction generator. The data lie between the simulation lines for both the QGSJet and Sibyll generators without the need for any additional shift (as was necessary for the Fly's Eye data, due to a systematic that was originally unaccounted for). The $X_{\rm max}$ data illustrate a key point: when different models are used, different conclusions about the absolute composition are reached. Fig. 5.36 demonstrates that under QGSJet, the composition appears to be changing from mixed at 10^{17} eV to predominantly light above 10^{18} eV, while under Sibyll it appears to change from predominantly heavy to mixed. The latter is consistent with the Fly's Eye monocular result in Chap. 4.

For the muon component, we are faced with the problem that the data lie entirely above the iron simulation line at all energies. In Fig. 5.37 we show the results for QGSJet only. Sibyll predicts even fewer muons than QGSJet, thus

exacerbating the problem. We investigated the possibility that the muon energy threshold of MIA may have been different to that assumed when generating the MC events for comparison. Several systematic effects were taken into account, but none were large enough (even when applied together) to bring the data and MC into closer agreement. It is possible that an energy shift of 40% could do this, but this is much larger than the estimated systematic error of 25% [151]. The fact that the HiRes/MIA spectrum agrees quite closely with other experiments [145] also precludes such a large shift. It therefore seems that there is a deficiency in the muon production in these models.

Based on elongation rates alone for $X_{\rm max}$ and $\rho_\mu(600)$, HiRes and MIA both indicate a lightening of composition, although we cannot make a firm conclusion about the absolute composition measured by MIA, and therefore about the degree of agreement between the two experiments.

The HiRes/MIA data were used to measure Λ, the logarithmic decrement of the $X_{\rm max}$ distribution, which is directly related to the proton mean free path in air if the composition of deeply penetrating showers is protonic. Assuming from the results of Chap. 5 that this is the case (at least from the point of view of $X_{\rm max}$), we derived a value of Λ that was not quite consistent with previous measurements in a similar energy range. A MC study which assumed various degrees of contamination by helium nuclei showed that the systematic error might be as large as 5 g/cm^2 if the data were 50% helium. This would bring the result into better agreement with the AGASA result at the same energy. The inferred total proton–proton cross section, $\sigma_{pp}^{\rm tot}$, is not quite consistent with the parametrisation of Block, Halzen and Stanev [163], but would be consistent if this additional systematic shift were taken into account.

Several topics worthy of investigation were not explored in this thesis due to time constraints. In particular, discrepancies remain between the raytracing table used in the HiRes analysis software and the observed tube profiles as measured using laser shots. The discrepancies only show up in the tails of the profile, but can be significant for tubes that lie far from the track.

The composition analysis of Chapter 5 could have been improved by employing the KNN test (or something similar), which gives the probability that a given point belongs to a particular region of parameter space. This was not done for the HiRes/MIA data set due to the difficulty with the absolute scale of the muon measurements.

The energy dependence of the proton–proton cross section is of particular interest, but this could not be derived due to the limited size of the HiRes/MIA data set. Only 898 events passed all cuts, making it impossible to determine the energy dependence with any certainty.

There is much interesting physics to be derived from a hybrid experiment. It is anticipated that future high statistics measurements with experiments such as Auger will give us a better handle on cosmic ray composition, with the opportunity to simultaneously study a large number of composition–sensitive parameters. There is also excellent scope for probing particle physics above accelerator energies with such measurements, thus improving our models and composition resolution.

Appendix A

Terminology of high energy interactions

In this Appendix I define some of the terms used when describing hadronic interactions. The conventions here follow, for the most part, those used by Gaisser [72].

- The **centre of mass (COM) frame** is defined as the one in which the products of the interaction are mutually at rest, *i.e.* $\sum_i \vec{p}_i^* = 0$ where $\vec{p}_i^*$ is the 3–momentum of the i^{th} secondary in this frame.

- The **inelasticity** of an interaction is defined as that fraction of the energy not carried away by the leading particle, *i.e.* it is the energy available for production of secondary particles.

- The **multiplicity** is the number of secondary particles of a given type produced in a single interaction.

- The **leading** particle in an interaction is the one which carries the most energy away from the interaction. This is usually the incident hadron.

- The **n–particle inclusive cross section** is defined as

$$\sigma_n = \left(\prod_{i=1}^{n} E_i \right) \frac{d\sigma}{\prod_i d^3 p_i}, \tag{A.1}$$

  and is the multiply differential invariant cross section for finding one produced particle in each of the phase spaces d^3p_i/E_i, regardless of the other products [72]. The most important cross sections for cosmic ray cascades are σ_0, the total cross section, and σ_1, the cross section for the process

$$a + b \longrightarrow c + \text{anything}. \tag{A.2}$$

- It is possible to define a scaling variable $x_F = p^*_{||}/p^*_{||}(\max)$, where $p^*_{||}$ is the longitudinal momentum in the COM frame ($p^*_{||} = |\vec{p}^*| \sin\theta^*$). x_F is called **Feynman–x** and is approximately $2p^*_{||}/\sqrt{s}$ at high energies, s being the square of the total COM energy.

- The **rapidity** y of a particle is defined by $p_{||} = \mu_\perp \cosh y$, where $\mu_\perp = \sqrt{p_\perp^2 + m^2}$ is the "transverse mass". $p_\perp = |\vec{p}\,| \cos\theta$ is the (Lorentz–invariant) transverse momentum. For $p_\perp \gg m^2$, one has $y \to \eta = -\ln\tan\theta/2$, and η is called the **pseudorapidity**.

- Consider the inclusive process $a + b \longrightarrow c +$ anything at high energies. After Feynman [164], it is possible to visualise this in the parton picture[1] as follows: two extended objects (a and b) converge (in the COM frame) and "move through each other"[2]. As the interaction takes place, there occurs a process analogous to bremsstrahlung, sometimes termed "pionisation", in which many particles (mostly pions) are produced with small COM momentum, *i.e.* $x_F \sim 0$. This is referred to as the **central region**. The longitudinal momentum of c in the COM frame tends to be close to that of either the projectile a or the target b (depending on the sign of $p^*_{||}$), and can therefore be regarded as a fragment of either a or b. This is equivalent to saying that the rapidity is close to either its minimum or maximum value, respectively. For $y \sim y_{\min}$, we have $x_F \sim -1$, referred to as the **projectile** or **beam fragmentation region**, and $y \sim y_{\max} \Rightarrow x_F \sim 1$ is the **target fragmentation region**. At high energies $y \to \eta$ and the fragmentation region corresponds to the small–angle (forward) region.

- **Single diffractive** scattering is a process in which either the target or projectile is excited to a resonance, but no additional particles are produced,

[1] Partons are the pointlike constituents of hadrons, originally postulated by Feynman and nowadays identified with the quarks and gluons of QCD.

[2] As a consequence of this type of argument, the inclusive cross sections exhibit scaling at high energies; in particular, the total cross section $\sigma_0 \stackrel{\sqrt{s}\to\infty}{\longrightarrow}$ constant, and the one–particle inclusive cross section $f_{ac}^{(b)}$ becomes a function only of x_F, *i.e.* $f_{ac}^{(b)}(\sqrt{s}, p^*_{||}, p_\perp) \stackrel{\sqrt{s}\to\infty}{\longrightarrow} f_{ac}^{(b)}(x_F, p_\perp)$ [72]

e.g. $\pi + N \longrightarrow \pi + N^*$. In a **double diffractive** event, both particles are excited.

References

[1] A.M. Hillas. *Cosmic Rays*. Pergamon Press, 1972.

[2] P. Sokolsky, P. Sommers, and B. R. Dawson. Extremely High–Energy Cosmic Rays. *Phys. Rept.*, 217:225, 1992.

[3] S. Yoshida and H.Y. Dai. The extremely high energy cosmic rays. *J. Phys.*, G24:905, 1998.

[4] V.F. Hess. Observation of Penetrating Radiation in Seven Balloon Flights. *Z. Phys.*, 13:1084, 1912.

[5] V.F. Hess. On the Origin of Penetrating Radiation. *Z. Phys.*, 14:610, 1913.

[6] W. Kolhörster. *Deutsch. Phys. Gesell. Verh.*, 16:719, 1914.

[7] J. Clay. *Proc. Roy. Acad. of Amsterdam*, 30:1115, 1927.

[8] C.D. Anderson. The Apparent Existence of Easily Deflectable Positives. *Science*, 76:238, 1932.

[9] P.M.S. Blackett and G.P.S. Occhialini. Some Photographs of the Tracks of Penetrating Radiation. *Proc. Roy. Soc.*, A139:699, 1933.

[10] S.H. Neddermeyer and C.D. Anderson. Note on the Nature of Cosmic–Ray Particles. *Phys. Rev.*, 51:884, 1937.

[11] D.H. Perkins. Nuclear Disintegration by Meson Capture. *Nature*, 159:126, 1947.

[12] P. Auger, R. Maze, and T. Grivet-Mayer. *C.R. Acad. Sci. (Paris)*, 206:1721, 1938.

[13] P. Auger *et al.* Extensive Cosmic–ray Showers. *Rev. Mod. Phys.*, 11:288, 1939.

[14] G. Cocconi, A. Loverdo, and V. Tongiorgi. *Phys. Rev.*, 70:852, 1946.

[15] J. Daudin. *Ann. de Phys.*, 20:563, 1945.

[16] M.F. Kaplon, B. Peters, and H.L. Bradt. Evidence for Multiple Meson and γ–ray production in Cosmic–ray Stars. *Phys. Rev.*, 76:1735, 1949.

[17] G. Clark *et al.* An Experiment on Air Showers Produced by High–Energy Cosmic Rays. *Nature*, 180:353, 1957.

[18] B. Rossi. *Cosmic Rays.* McGraw–Hill, New York, 1964.

[19] J. Linsley, L. Scarsi, and B. Rossi. Energy Spectrum and Structure of Large Air Showers. *J. Phys. Soc. Japan*, 17(suppl. A–III):91, 1962.

[20] J. Linsley. Evidence for a Primary Cosmic–Ray Particle with energy 10^{20} eV. *Phys. Rev. Lett.*, 10:146, 1963.

[21] A.A. Penzias and R.W. Wilson. *Ap. J.*, 142:419, 1965.

[22] K. Greisen. End to the Cosmic Ray Spectrum? *Phys. Rev. Lett.*, 16:748, 1966.

[23] G.T. Zatsepin and V.A. Kuz'min. Upper Limit of the Spectrum of Cosmic Rays. *JETP Lett.*, 4:78, 1966.

[24] M.A. Lawrence, R.J.O. Reid, and A.A. Watson. The Cosmic Ray Energy Spectrum above 4×10^{17} eV as measured by the Haverah Park Array. *J. Phys.*, G17:733, 1991.

[25] A.M. Hillas. Measurement of the primary energy of air showers in the presence of fluctuations. In *Proc. 12th ICRC, Hobart*, volume 3, page 1001, 1971.

[26] M.M. Winn *et al.* The cosmic-ray energy spectrum above 10^{17} eV. *J. Phys.*, G12:653, 1986.

[27] B.N. Afanasiev *et al.* Recent Results from Yakutsk Experiment. In M. Nagano, editor, *Tokyo Workshop on Techniques for the Study of Extremely High Energy Cosmic Rays*, page 35, 1993.

[28] B.N. Afanasiev *et al.* Some Characteristics of EAS and Primary Cosmic Rays on Yakutsk Array Data. In M. Nagano, editor, *Proc. Int. Symp. on EHE Cosmic Rays*, page 32, 1996.

[29] T. Hara *et al.* The Akeno Air Shower Project. In *Proc. 16th ICRC, Kyoto*, volume 8, page 135, 1979.

[30] M. Teshima *et al.* Expanded Array for Giant Air Shower Observation at Akeno. *Nucl. Inst. Meth.*, A247:399, 1986.

[31] M. Teshima *et al.* Energy Spectrum of Primary Cosmic Rays above 10^{17} eV. In *Proc. 20th ICRC, Moscow*, volume 1, page 404, 1987.

[32] N. Chiba *et al.* Akeno Giant Air Shower Array (AGASA) covering 100 km^2 area. *Nucl. Inst. Meth.*, A311:338, 1992.

[33] N. Hayashida *et al.* Possible Clustering of the Most Energetic Cosmic Rays within a Limited Space Angle Observed by the Akeno Giant Air Shower Array. *Phys. Rev. Lett.*, 77:1000, 1996.

[34] R.M. Baltrusaitis *et al.* The Utah Fly's Eye Detector. *Nucl. Inst. Meth.*, A240:410, 1985.

[35] K. Suga. In *Proc. 5th Interamerican Seminar on Cosmic Rays, La Paz*, volume 2, page 49, 1962.

[36] A. Bunner. *The Atmosphere as a Cosmic Ray Scintillator.* PhD thesis, Cornell University, 1967.

[37] H. E. Bergeson *et al.* Measurement of light emission from remote cosmic ray air showers. *Phys. Rev. Lett.*, 39:847, 1977.

[38] G.L. Cassiday. Observatory for Ultra High–Energy Processes: The Fly's Eye. *Ann. Rev. Nucl. Part. Sci.*, 35:321, 1985.

[39] D.J. Bird *et al.* Detection of a Cosmic Ray with Measured Energy Well Beyond the Expected Spectral Cutoff Due to Cosmic Microwave Background. *Ap. J.*, 441:144, 1995.

[40] The Auger Collaboration. Pierre Auger Project Design Report, 2nd edition, 1997.

[41] The Auger Collaboration. Auger Collaboration Web Site (`www.auger.org`), 2000.

[42] D.E. Groom *et al.* Review of Particle Properties. *Eur. Phys. J.*, 15:1, 2000. Review of Cosmic Rays (update by T. Stanev and T.K. Gaisser).

[43] F.A. Aharonian and J.W. Cronin. Influence of the Universal Microwave Background Radiation on the Extragalactic Cosmic Ray Spectrum. *Phys. Rev.*, D50:1892, 1994.

[44] N. Hayashida *et al.* The Anisotropy of Cosmic Ray Arrival Direction around 10^{18} eV. In *Proc. 26th ICRC, Salt Lake City*, volume 3, page 256, 1999.

[45] J.A. Bellido *et al.* Southern Hemisphere Observations of a 10^{18} eV Cosmic Ray Source Near the Direction of the Galactic Centre. Submitted to Astroparticle Physics, 2000.

[46] D.J. Bird *et al.* Study of Broad Scale Anisotropy of Cosmic Ray Arrival Directions from 2×10^{17} eV to 10^{20} eV from Fly's Eye Data. e–print `astro-ph/9806096`, 1998.

[47] T. Stanev *et al.* Arrival Directions of the Most Energetic Cosmic Rays. *Phys. Rev. Lett.*, 75:3056, 1995.

[48] L.J. Kewley, R.W. Clay, and B.R.Dawson. Arrival Directions of the Southern Highest Energy Cosmic Rays. *Astropart. Phys.*, 5:69, 1996.

[49] N. Hayashida *et al.* Small–scale Anisotropy of Cosmic Rays above 10^{19} eV observed with AGASA. In *Proc. 26th ICRC, Salt Lake City*, volume 3, page 276, 1999.

[50] T.H. Burnett *et al.* Photon and Helium Spectra above 1 TeV for primary Cosmic Rays. *Phys. Rev. Lett.*, 51:1010, 1983.

[51] A.V. Apanasenko *et al.* Primary Cosmic Ray Spectra Observed by RUNJOB – proton and alpha spectra. In *Proc. 26th ICRC, Salt Lake City*, volume 3, page 163, 1999.

[52] A.V. Apanasenko *et al.* Primary Cosmic Ray Spectra Observed by RUNJOB – spectra for heavy and all particles. In *Proc. 26th ICRC, Salt Lake City*, volume 3, page 167, 1999.

[53] J.W. Fowler. *Composition and Spectrum of Cosmic Rays near the Knee measured by the CASA–BLANCA experiment.* PhD thesis, University of Chicago, 2000.

[54] D.J. Bird *et al.* Evidence for Correlated Changes in the Spectrum and Composition of Cosmic Rays at Extremely High Energies. *Phys. Rev. Lett.*, 71:3401, 1993.

[55] N. Hayashida *et al.* Muons ($\geq$ 1 GeV) in large Extensive Air Showers of energies between $10^{16.5}$ and 10^{19} eV observed at Akeno. *J. Phys.*, G21:1101, 1995.

[56] B.Z. Kopeliovich, N.N. Nikolaev, and I.K. Potashnikova. Rising Cross–sections in QCD and the Cosmic Ray Data. *Phys. Rev.*, D39:769, 1989.

[57] A.B. Kaidalov. The Quark–Gluon Structure of the Pomeron and the rise of Inclusive Spectra at High Energies. *Phys. Lett.*, B116:459, 1982.

[58] A.B. Kaidalov and K.A. Ter-Martirosyan. Pomeron as Quark–Gluon Strings and Multiple Hadron Production at SPS Collider Energies. *Phys. Lett.*, B117:247, 1982.

[59] A.A. Watson. Studies made at Haverah Park of the Energy Spectrum, Mass Composition and Anisotropy of Cosmic Rays above 4×10^{17} eV. In M. Nagano and F. Takahara, editors, *Proc. ICRR Int. Symp. on Astrophysical Aspects of the Most Energetic Cosmic Rays*, page 2. World Scientific, Singapore, 1991.

[60] A.M. Hillas. The origin of ultra–high energy cosmic rays. *Ann. Rev. Astron. Astrophys.*, 22:425, 1984.

[61] P.L. Biermann. The origin of the highest energy cosmic rays. *J. Phys.*, G23:1, 1997.

[62] P. Bhattacharjee and G. Sigl. Origin and Propagation of Extremely High Energy Cosmic Rays. *Phys. Rep.*, 327:109, 2000.

[63] E. Fermi. *Phys. Rev.*, 75:1169, 1949.

[64] M.S. Longair. *High Energy Astrophysics*, volume 2. Cambridge University Press, 2nd edition, 1994.

[65] R.J. Protheroe. Acceleration and Interaction of Ultra High Energy Cosmic Rays. In M.A. DuVernois, editor, *Topics in Cosmic Ray Astrophysics*. Nova Science Publishing, New York, 1999.

[66] L. O'C Drury. An introduction to the theory of diffusive shock acceleration of energetic particles in tenuous plasmas. *Phys. Rep.*, 46:973, 1983.

[67] P.O. Lagage and C.J. Cesarsky. The maximum energy of cosmic rays accelerated by supernova shocks. *Astron. and Astrophys.*, 125:249, 1983.

[68] J.P. Rachen and P.L. Biermann. Extragalactic ultra–high energy cosmic rays. *Astron. and Astrophys.*, 272:161, 1993.

[69] D. Fargion, B. Mele, and A. Salis. Ultrahigh-energy neutrino scattering onto relic light neutrinos in galactic halo as a possible source of highest energy extragalactic cosmic rays. *Ap. J.*, 517:725, 1999.

[70] T. Weiler. Cosmic ray neutrino annihilation on relic neutrinos revisited: a mechanism for generating air showers above the Greisen–Zatsepin–Kuzmin cutoff. *Astropart. Phys.*, 11:303, 1999.

[71] W. Heitler. *Quantum Theory of Radiation.* Oxford University Press, 2nd edition, 1944.

[72] T.K. Gaisser. *Cosmic Rays and Particle Physics.* Cambridge University Press, 1990.

[73] B. Rossi and K. Greisen. *Rev. Mod. Phys.*, 13:240, 1941.

[74] B. Rossi. *High Energy Particles.* Prentice Hall, 1952.

[75] J.F. Carlson and J.R. Oppenheimer. On Multiplicative Showers. *Phys. Rev.*, 51:220, 1937.

[76] K. Greisen. The Extensive Air Showers. *Prog. Elem. Part. Cos. Ray Phys.*, 3:1, 1956.

[77] K. Kamata and J. Nishimura. *Prog. Theor. Phys. Suppl.*, 6:93, 1958.

[78] C.L. Pryke. Asymmetry of Air Showers at Ground Level, 1998. Auger Project Technical Note GAP-98-034, available at `www.auger.org`.

[79] S. Yoshida *et al.* Charged particles in giant air showers above 1 EeV. *J. Phys.*, G20:651, 1994.

[80] T.K. Gaisser and A.M. Hillas. Reliability of the Method of Constant Intensity Cuts for Reconstructing the Average Development of Vertical Showers. In *Proc. 15th ICRC, Plovdiv*, volume 8, page 353, 1977.

[81] J. Linsley and A.A. Watson. Validity of scaling to 10^{20} eV and high-energy cosmic-ray composition. *Phys. Rev. Lett.*, 46:459, 1981.

[82] T.K. Gaisser *et al.* Elongation Rate of Air Showers and Implications for 10^{17}–10^{18} eV Particle Interactions. In *Proc. 16th ICRC, Kyoto*, volume 9, page 275, 1979.

[83] A.N. Cillis and S.J. Sciutto. Muon Bremsstrahlung and Muonic Pair Production in Air Showers. available at `http://xxx.lanl.gov/astro-ph/0006108`.

[84] N. Hayashida *et al.* Muons ($\geq$ 1 GeV) in Large Extensive Air Showers of Energies Between $10^{16.5}$ and $10^{19.5}$ Observed at Akeno. *J. Phys.*, G21:1101, 1995.

[85] K. Greisen. Cosmic Ray Showers. *Ann. Rev. Nucl. Part. Sci.*, 10:63, 1960.

[86] V. N. Gribov. A reggeon diagram technique. *Sov. Phys. JETP*, 26:414–422, 1968.

[87] T. Regge. Introduction to complex orbital momenta. *Nuovo Cim.*, 14:951, 1959.

[88] R. Omnés. *Introduction to Particle Physics.* Wiley–Interscience, London, 1971.

[89] A. Donnachie and P.V. Landshoff. Total cross sections. *Phys. Lett.*, B296:227, 1992.

[90] I. Ya. Pomeranchuk. *Sov. Phys. JETP*, 7:499, 1958.

[91] P.D.B. Collins and A.D. Martin. *Hadron Interactions.* Adam Hilger, Bristol, 1984.

[92] G. 't Hooft. A two-dimensional model for mesons. *Nucl. Phys.*, B75:461, 1974.

[93] G. Veneziano. Large N Expansion in Dual Models. *Phys. Lett.*, B52:220, 1974.

[94] G. Veneziano. Some aspects of a unified approach to gauge, dual and Gribov theories. *Nucl. Phys.*, B117:519–545, 1976.

[95] A. Capella *et al.* Dual parton model. *Phys. Rept.*, 236:225–329, 1994.

[96] R. S. Fletcher, T. K. Gaisser, P. Lipari, and T. Stanev. SIBYLL: An Event generator for simulation of high–energy cosmic ray cascades. *Phys. Rev.*, D50:5710, 1994.

[97] J. Ranft. Cosmic Ray particle production. available at `http://xxx.lanl.gov/hep-ph/9711334`.

[98] D. Heck *et al.* CORSIKA: A Monte Carlo code to simulate Extensive Air Showers. Technical report, University of Karlsruhe, 1998. Karlsruhe report no. FZKA–6019, available at `www-ik3.fzk.de`.

[99] J. Knapp, D. Heck, and G. Schatz. Inelastics Cross Sections and Their Influence on Air Shower Development. Technical report, University of Karlsruhe, 1997. preliminary (unpublished), available at `www-ik3.fzk.de`.

[100] C.L. Pryke. A comparative study of the depth of maximum of simulated air shower longitudinal profiles. available at `xxx.lanl.gov/astro-ph/0003442`.

[101] N.N. Kalmykov, S.S. Ostapchenko, and A.I. Pavlov. Quark–Gluon–String Model and EAS Simulation Problems at Ultra–High Energies. *Nucl. Phys. B (Proc. Suppl.)*, 52:17, 1997.

[102] J. Ranft. Dual Parton Model at Cosmic Ray Energies. *Phys. Rev.*, D51:64, 1995.

[103] J. Knapp. High Energy Interactions and Extensive Air Showers. In *Proc. 25th ICRC, Durban (Rapporteur Volume)*, 1997.

[104] A.M. Hillas. Two Interesting Techniques for Monte Carlo Simulation of Very High Energy Hadron Cascades. In *Proc. 17th ICRC, Paris*, volume 8, page 193, 1981.

[105] A.M. Hillas. Shower Simulation: Lessons from MOCCA. *Nucl. Phys. (Proc. Suppl.)*, B52:29, 1997.

[106] S.J. Sciutto. AIRES: A system for Air Shower simulations. User guide and manual, version 2.2.0. Technical report, University of La Plata, 1999. available at `www.fisica.unlp.edu.ar/auger/aires/doc/UsersManual.ps.gz`.

[107] M.T. Dova and S.J. Sciutto. Air Shower Simulations: Comparison Between AIRES and MOCCA, 1997. Auger Project Tech Note GAP-97-053, available at `www.auger.org`.

[108] H. Fesefeldt. The Simulation Of Hadronic Showers: Physics And Applications. Technical report, Tech. Hochschule Aachen, 1985. Report PITHA-85/02.

[109] W.R. Nelson, H. Hirayama, and D.W.O. Rogers. The EGS4 code system. Technical report, SLAC, 1985. report no. SLAC-265.

[110] H.Y. Dai *et al.* The energy estimation of ultra high energy cosmic rays. *J. Phys*, G14:135, 1988.

[111] M.A.K. Glasmacher *et al.* The cosmic ray composition between 10^{14} and 10^{16} eV. *Astropart. Phys.*, 12:1, 1999.

[112] K. Greisen. Highlights in Air–Shower Studies. In *Proc. 9th ICRC, London*, volume 2, page 609, 1965.

[113] L.G. Porter *et al.* A space–time detector for cosmic ray showers. *Nucl. Inst. Meth.*, 87:87, 1970.

[114] F. Kakimoto *et al.* A measurement of the air fluorescence yield. *Nucl. Inst. Meth.*, A372:527, 1995.

[115] X.Z. Zhang. The Multiply Scattering Effect on the Energy Measurement of UHE Cosmic Rays using Atmospheric Fluorescence Technique. unpublished, 2000.

[116] M.D. Roberts. private communication.

[117] G.L. Cassiday *et al.* Proposal to Construct a High Resolution EYE (HiRes) Detector. Technical report, University of Utah, 1990.

[118] C.R. Wilkinson. *The Application of High Precision Timing in the High Resolution Fly's Eye Cosmic Ray Detector.* PhD thesis, University of Adelaide, 1998.

[119] C. Song *et al.* Energy Estimation of UHE Cosmic Rays using the Atmospheric Fluorescence Technique. *Astropart. Phys.*, 14:7, 2000.

[120] T.K. Gaisser *et al.* Cosmic–ray composition around 10^{18} eV. *Phys. Rev.*, D47:1919, 1993.

[121] K.D. Green. *The Cosmic Ray Spectrum Above 0.3 EeV.* PhD thesis, University of Utah, 1992.

[122] M. Nagano *et al.* The Lateral Distribution of Electrons of Extensive Air Shower Observed at Akeno (920 g/cm^2). *J. Phys. Soc. Japan*, 53:1667, 1984.

[123] M. Nagano *et al.* Energy spectrum of primary cosmic rays between $10^{14.5}$ and 10^{18} eV. *J. Phys.*, G10:1295, 1984.

[124] M.H.A. Huang. *Anisotropy of Extremely High Energy Cosmic Rays.* PhD thesis, University of Utah, 1996.

[125] G.L. Cassiday *et al.* Measurements of Cosmic–Ray Air Shower Development at Energies above 10^{17} eV. *Ap. J.*, 356:669, 1990.

[126] N. Hayashida and T. Kifune. Proportional Counter for Air Shower Observation. *Nucl. Inst. Meth.*, 173:431, 1980.

[127] Y. Matsubara. private communication, 1997.

[128] S. Yoshida *et al.* The cosmic ray energy spectrum above 3×10^{18} eV measured by the Akeno Giant Air Shower Array. *Astropart. Phys.*, 3:105, 1995.

[129] B.R. Dawson, R. Meyhandan, and K.M. Simpson. A Comparison of Cosmic Ray Composition Measurements at the Highest Energies. *Astropart. Phys.*, 9:331, 1998.

[130] N. Hayashida *et al.* Muons in Giant Air Showers Observed by AGASA and its Implications. In *Proc. 25th ICRC, Durban*, volume 6, page 241, 1997.

[131] Y. Matsubara *et al.* Measurement of Low Energy Muons in EAS at Energy Region Larger than 10^{17} eV. In *Proc. 19th ICRC, La Jolla*, volume 7, page 119, 1985.

[132] L.K. Ding *et al.* Re–examination of cosmic–ray composition around 10^{18} eV from Fly's Eye data. *Ap. J.*, 474:490, 1997.

[133] M. Nagano *et al.* Comparison of AGASA Data with CORSIKA Simulations. *Astropart. Phys.*, 13:277, 2000.

[134] M.J. Kidd. *Properties of Extensive Air Showers around* 10^{17} *eV.* PhD thesis, University of Illinois, 1996.

[135] T.Z. Abu-Zayyad *et al.* The Prototype High Resolution Fly's Eye Cosmic Ray Detector. *Nucl. Inst. Meth.*, A450:253, 2000.

[136] M.A. Catanese. *A Search for Ultra–High Energy Gamma Rays from Active Galactic Nuclei.* PhD thesis, University of Michigan, 1994.

[137] A. Borione *et al.* A Large Air–Shower Array to Search for Astrophysical Sources Emitting γ–rays with Energies $\geq 10^{14}$ eV. *Nucl. Inst. Meth.*, A346:329, 1994.

[138] E.C. Loh. Fabrication of HiRes Mirrors. In M. Nagano, editor, *Proc. Tokyo Workshop on Techniques for the Study of Extremely High Energy Cosmic Rays*, page 219, 1993.

[139] J.W. Elbert. The HiRes filter and its effect on the aperture. In M. Nagano, editor, *Proc. Tokyo Workshop on Techniques for the Study of Extremely High Energy Cosmic Rays*, page 232, 1993.

[140] T.Z. Abu-Zayyad *et al.* The HiRes Detector: Absolute Calibration and Alignment. In *Proc. 25th ICRC, Durban*, volume 5, page 333, 1997.

[141] M. Pritchard. Technical report, University of Michigan, 1995.

[142] M.A.K. Glasmacher. *Cosmic Ray Composition Studies with CASA–MIA*. PhD thesis, University of Michigan, 1998.

[143] H.Y. Dai, 1998. private communication.

[144] J.R. Patterson and A.M. Hillas. The Relation of the Lateral Distribution of Cherenkov Light From Cosmic Ray Showers to the Distance of Maximum Development. *J. Phys.*, G9:1433, 1983.

[145] T.Z. Abu-Zayyad *et al.* Measurement of the Cosmic Ray Energy Spectrum and Composition from 10^{17} to $10^{18.3}$ eV Using a Hybrid Fluorescence Technique, 2001. Accepted for publication in Ap. J.

[146] D.J. Bird *et al.* The Cosmic–Ray Energy Spectrum Observed by the Fly's Eye. *Ap. J.*, 424:491, 1994.

[147] H.Y. Dai, 1997. private communication.

[148] T.Z. Abu-Zayyad *et al.* Testing the High Resolution Fly's Eye Using Laserscope. In *Proc. 25th ICRC, Durban*, volume 5, page 349, 1997.

[149] J. Stickland. private communication, 1997.

[150] P.R. Bevington. *Data Reduction and Error Analysis for the Physical Sciences*. McGraw–Hill, New York, 2nd edition, 1992.

[151] T. Abu-Zayyad, others (the HiRes, and MIA collaborations). Evidence for Changing of Cosmic Ray Composition Between 10^{17} and 10^{18} eV from Multicomponent Measurements. *Phys. Rev. Lett.*, 84:4276, 2000.

[152] V. Barger *et al.* Proton–Proton Total Cross Section above 10^4 GeV: Can Cosmic Rays Give the Answer? *Phys. Rev. Lett.*, 33:1051, 1974.

[153] R.W. Ellsworth *et al.* Ultrahigh–energy cross–section from study of longitudinal development of air showers. *Phys. Rev.*, D26:336, 1982.

[154] P. Sokolsky. *Introduction to Ultrahigh–Energy Cosmic Ray Physics.* Addison–Wesley, Redwood City, USA, 1989.

[155] T.K. Gaisser, U.P. Sukhatme, and G.B. Yodh. Hadron cross sections at ultrahigh energies and unitarity bounds on diffraction. *Phys. Rev.*, D36:1350, 1987.

[156] M.M. Block *et al.* Photon–proton and photon–photon scattering from nucleon–nucleon forward amplitudes. *Phys. Rev.*, D60:054024, 1999.

[157] M.M. Block *et al.* Breaking the barriers — uniting accelerator and cosmic ray $p-p$ cross sections. Northwestern University NUHEP report no. 708, 2000. e–print no. hep-ph/0003226.

[158] R. Engel *et al.* Proton–proton cross section at $\sqrt{s} \sim 30$ TeV. *Phys. Rev.*, D58:014019, 1998.

[159] T. Stanev. High Energy Interactions and Extensive Air Showers. In *Proc. 26th ICRC, Salt Lake City (Rapporteur volume)*, page 247, 1999.

[160] M. Honda *et al.* Inelastic Cross Section for p–Air Collisions from Air Shower Experiments and Total Cross Section for p–p Collisions up to $\sqrt{s}$=24 TeV. *Phys. Rev. Lett.*, 70:525, 1993.

[161] R.M. Baltrusaitis *et al.* Total Proton-Proton Cross Section at $s^{1/2} = 30$ TeV. *Phys. Rev. Lett.*, 52:1380, 1984.

[162] M.M. Block and R.N. Cahn. High energy $p\bar{p}$ and pp forward elastic scattering and total cross sections. *Rev. Mod. Phys.*, 57:563, 1985.

[163] M. M. Block, F. Halzen, and T. Stanev. Extending the frontiers: Reconciling accelerator and cosmic ray p-p cross sections. *Phys. Rev.*, D62:077501, 2000.

[164] R.P. Feynman. Hadronic Interactions at Very High Energies. *Phys. Rev. Lett.*, 23:1415, 1969.